ADSORPTION AND DIFFUSION OF GASES IN Cu-BTC

SHIMA NAJAFI NOBAR

(B.Sc, in Chem. Eng., Sharif University of Technology, Iran, Tehran)

A THESIS SUBMITTED

FOR THE DEGREE OF DOCTOR OF PHILOSOPHY

DEPARTMENT OF CHEMICAL AND BIOMOLECULAR ENGINEERING

NATIONAL UNIVERSITY OF SINGAPORE

2012

DECLARATION

I hereby declare that the thesis is my original work and it has been written by me in its entirety. I have duly acknowledged all the sources of information which have been used in the thesis.

This thesis has also not been submitted for any degree in any university previously.

Shima Najafi Nobar

24 April 2013

ACKNOWLEDGEMENT

First of all, I would like to express my sincere appreciation to Prof. Shamsuzzaman Farooq for his guidance and sincere help at every stage of this work. His valuable advice and assistance always guided me to conduct my research smoothly.

I am very much indebted to my lab mates and academic friends Dr. Vemula Rama Rao, Ms. Mona Khalighi, Mr. Shreenath Kishnamorthy, Mr. Hamed Sepehr and Mr. Reza Haghpanah for actively participating in the discussion and the help that they have provided during this research work. I am also immensely thankful to the laboratory technologists, Madam Sandy, Mr. Ng Kim Poi and Mr. Toh, for their timely cooperation and help while designing and conducting the experiments in the lab. I am very thankful to my past lab mate Dr. Ravi Marathe who helped and guided me in some aspects of my thesis.

Special thanks also due to my friends for their constant support and encouragement to finish this work. I am happy to express my gratitude to my parents and other family members for their affectionate love, understanding, support and encouragement in all my educational levels. I would like to specially thank my dear husband Dr. Alireza Rezvanpour for his continuous help and support in all my life.

Finally, the financial support from National University of Singapore in the form of a research scholarship is gratefully acknowledged.

TABLE OF CONTENTS

SUMMARY

In this study, several samples of Cu-BTC, a member of the MOF adsorbent family, were synthesized following synthesis routes that represent some modifications of published recipes. The effects of mixing, reaction temperature and duration, and concentrations of the precursors on the synthesized samples are discussed. The sample that gave stable adsorption capacity after several adsorption-desorption cycles was chosen for further study.

The equilibrium and kinetic measurements of natural gas and bio gas components, CO_2, CH_4 and N_2, were performed on this screened sample. Single component isotherm measurements of the aforementioned gases were conducted over a wide range of pressures and temperatures using a constant volume apparatus, designed to minimize the required amount of adsorbent. The experimental adsorption equilibrium data of all three gases have been fitted with a suitable isotherm model. The equilibrium data for the three gases are also compared with those on a commercial Cu-BTC sample, produced by BASF and marketed as Basolite® C300. In addition, extensive dynamic column breakthrough experiments were conducted with the synthesized sample to establish the gas transport mechanism. Detailed analyses of the breakthrough responses, carried out using a non-isothermal, axially dispersed plug flow model with independently estimated axial dispersion coefficient, linear driving force (LDF) representation of the inter-phase mass transfer and isotherm parameters obtained from measured equilibrium data, reveal a consistent transport mechanism of all three gases in Cu-BTC particles. Correction of the measured column dynamics for the extra-column dead volume is also discussed in details.

The advantage of using finite volume method over finite difference method in solving the partial differential equations related to non-isothermal, non-isobaric adsorber dynamics is demonstrated in this study. A mathematical model for a four-step vacuum swing adsorption (VSA) process has been developed, and the model equations solved using the finite volume method and a suitable ODE solver from MATLAB to simulate the cyclic process.

Binary breakthrough of N_2-CO_2 and N_2-CH_4 mixtures at different concentrations have also been experimentally and theoretically investigated to establish appropriate representation of mixture equilibrium and kinetics, and validate the model assumptions related to the prediction of mixture equilibrium and kinetics using single component parameters.

Detailed parametric studies have been carried out for CO_2 capture from post combustion power plant flue gas by a four-step VSA process on the Cu-BTC adsorbent synthesized and characterized in this study. Finally, the performance of Cu-BTC for CO_2 capture has been compared with 13X zeolite. While Cu-BTC gave better purity-recovery than 13X under similar operating conditions, the energy advantage of the former could not be established within the scope of the present simulation study. The full optimization study necessary for a definite conclusion is recommended for a future undertaking.

LIST OF FIGURES

LIST OF TABLES

NOMENCLATURE

Symbols:

A	Cross sectional area, cm^2
b	Lanmuir constant, $\frac{cc}{mmol}$
b_0	Pre-exponential constant, $\frac{cc}{mmol}$
c	Adsorbate concentration in the solid phase, $\frac{mmol}{cc}$
$\bar{c}$	Dimensionless adsorbate concentration in the solid phase
c_0	Feed concentration in the solid phase, $\frac{mmol}{cc}$
C_{pa}	specific heat capacity of the adsorbed phase, $\frac{J}{mol.K}$
C_{ps}	specific heat capacity of the adsorbent, $\frac{J}{mol.K}$
C_{pg}	specific heat capacity of the gas phase, $\frac{J}{kg.K}$
C	Total concentration (or density, ρ_g), $\frac{mmol}{cc}$
$C_N(t)$	Detector gas concentration (composite response)
d	Column diameter, m
D_c	Micropore diffusivity, $m^2 s^{-1}$
D_e	Effective macropore diffusivity, $m^2 s^{-1}$
D_L	Axial dispersion coefficient, $m^2 s^{-1}$
D_m	molecular diffusivity of the adsorbate in the carrier gas, $m^2 s^{-1}$

F	Feed flow rate, $\frac{ml}{min}$ / flux term
$\overline{F}$	Dimensionless flow rate
G	Numerical flux function
h_i	Inside heat transfer coefficient, $\frac{W}{m^2.K}$
ΔH	Change in enthalpy due to adsorption/desorption, $\frac{kJ}{mol}$
k	LDF rate constant, s^{-1}
k_{film}	Mass transfer coefficient across the external film around the adsorbent particles, s^{-1}
k_{fitted}	Fitted mass transfer coefficient, s^{-1}
k_{macro}	Macropore mass transfer coefficient, s^{-1}
K	Henry's constant
K_g	Adsorbates thermal conductivity, $\frac{W}{m.K}$
K_p	Adsorbent thermal conductivity, $\frac{W}{m.K}$
K_z	Effective gas thermal conductivity, $\frac{W}{m.K}$
L	Column length, *m*
M	Gas molecular weight
N	Flux of the adsorbable component, $\frac{mmol}{cm^2.s}$
P	Total pressure, *bar*
Pe	Peclet number
Pe'_{∞}	Limiting value of Peclet number at high Reynolds number

Pr	Prandtl number
Q_j	Variable in the j^{th} cell in finite volume method
$Q(t)$	Volumetric flow rate to the detector, $\frac{ml}{min}$
q	Adsorbate concentration in the solid phase, $\frac{mmol}{cc}$
$\bar{q}$	Average adsorbate concentration in the solid phase, $\frac{mmol}{cc}$
q^*	Equilibrium solid loading, $\frac{mmol}{cc}$
q_0^*	Adsorbate concentration in the adsorbent in equilibrium with $c_{0,}$ $\frac{mmol}{cc}$
q_s	Saturated equilibrium adsorbed phase concentration, $\frac{mmol}{cc}$
r_i	Inside radius of the column, m
r_c	Crystal radius, m
R_g	Universal gas constant, $8.314 \frac{J}{mol.K}$
Re	Reynolds number
R_p	Particle radius, m
Sh	Sherwood number
Sc	Schmidt number
t	Time, s
T	Temperature, K
T_w	Column wall temperature, K
u	Superficial velocity, $\frac{m}{s}$

ΔU Change in internal energy due to adsorption/desorption, $\frac{kJ}{mol}$

ΔU_s Isosteric heat of adsorption, $\frac{kJ}{mol}$

v Interstitial gas velocity, $\frac{m}{s}$

v_0 Interstitial velocity of the feed gas, $\frac{m}{s}$

V_p Pellet volume, cm^3

W Energy consumption

W_{cycle} Energy consumption of the cycle, $\frac{kWh}{tonne\ of\ CO_2\ captured}$

Wt_p Pellet weight after regeneration, gm

y Gas mole fraction

z Axial distance measured from the column inlet, m

Greek letters and symbols:

γ Adiabatic constant

γ_1 Coefficient

ε_b Bed voidage

γ_2 Coefficient

β Constant

μ viscosity of the feed, $Poise$

$\frac{\varepsilon_p}{\tau}$ Ratio of the particle voidage to the tortuosity

δ Constant

ψ_1 Constant

ψ_2 Constant

ρ_p Particle density, $\frac{kg}{m^3}$

θ Surface coverage, $\frac{q}{q_s}$

α_p Constant for rate of the pressure change, s^{-1}

η Compression efficiency

Subscripts:

i Component / inside / initial

f final

d Dose side

u Test side

0 Feed / initial value

p Particle / pressurization

c crystal

s Scale factor / Isosteric

j Tank number in TIS model / grid point / grid cell

b Bed / blow down

a Adsorption / adsorbent

e evacuation

H High

L Low

I Intermediate

CHAPTER 1

INTRODUCTION

Adsorption separation processes are in widespread industrial use, particularly in the petroleum refining and petrochemical industries. The heart of an adsorption process is the porous solid medium. The porous solid provides a very high surface area or high micropore volume and it is this high surface area or micropore volume that contributes to the high adsorptive capacity. The first major development in the adsorption industry was the invention of zeolites.

Adsorption processes can be classified based on the feed composition. Depending on the composition of the strongly adsorbed species in the mixture, the separation process may be divided into purification and bulk separation. A purification process involves removal of trace contaminants from a bulk stream. In a bulk separation, two or more components present in high proportions in a mixture are separated. Water removal from natural gas/air/syn gas, odor removal from air, removal of sulfur compounds from natural gas, etc., are examples of purification processes. Air separation, olefins/paraffin separation and CO_2 capture from flue gas are good representatives of bulk separation processes.

An adsorptive separation process can also be categorized based on the mechanism of gas separation, namely steric, kinetic and equilibrium separations. In steric mechanism, the size and shape of the gas molecule is important. This means that only the small molecules with proper shape can diffuse into the adsorbent. This effect can be seen in some zeolites with molecular sieving property. In case of kinetic separation, different molecules with different size and shape diffuse into the pores, but at different rates. Nitrogen production from air by

means of carbon molecular sieve adsorbent is one of the important industrial kinetic separation processes. In this process, oxygen diffuses much faster than nitrogen into the solid. In equilibrium based separation processes, the affinity of the adsorbent for some species is higher that the others. Therefore, the strongly adsorbed components are adsorbed on the solid and can be separated from the weakly adsorbed components. Oxygen production from air on 5A and LiX zeolites are commonly cited examples of equilibrium controlled adsorption separation (Ruthven, 1984; Yang, 1987).

Another way of classifying the adsorption processes is by the method of adsorbent regeneration such as Temperature Swing Adsorption (TSA), Pressure Swing Adsorption (PSA), inert gas purge, and displacement desorption. TSA and PSA are the more common industrial processes. There are other types of categorization of adsorption separation processes, such as based on modes of operation.

The industrial adsorbents are characterized in terms of porosity, surface area, thermal and chemical stability, pore volume, pore size distribution and material density. Activated carbon, synthetic and natural zeolites, silica gel, activated alumina and carbon molecular sieves are the most important industrial adsorbents (Ruthven, 1984; Yang, 2003).

From the very early days of crystal chemistry it was recognized that the structures of complex crystals could usefully be described in terms of units variously called modules, building units, structural units, or secondary building units. More recently, it has been realized that the assembly of building blocks yields extended structures with designed properties. Therefore, a logical and simple way to combinatorial search for novel materials is to link together molecular building blocks with desired properties (Dybtsev et al., 2004 ;Yaghi, 2007).

The explosive growth in the synthesis of porous metal–organic materials in recent years is an outcome of the combinatorial search for novel materials designed to perform specific and cooperative functions.

1.1 MOF: A New Family of Adsorbents

Metal-organic frameworks (MOF) structures, also known as porous coordination polymers, are extended 1, 2 or 3-dimensional porous structures composed of transition metal ions (or clusters) acting as joints, which are linked together by rigid rod-like organic linkers (Rowsell and Yaghi, 2004; Ockwig et al., 2005). Metal-organic frameworks are prepared as crystalline solids by solution reaction of metal ion salts with organic bridges. These novel materials were first investigated by Tomic (1965) as the thermally stable coordination polymers. He studied the formation of these polymers using three ligands, 1,5-dihydroxy-2,6-naphthalenedicarboxylic acid (1,5-N-2,6), pyromellitic acid (PMA) and 2,3,6,7-naphthalenetetracrboxylic acid (NT), and selected metal ions such as zinc, nickel, iron and aluminum. Thereafter, research interest in this field was stimulated by Yaghi and his coworkers. They first reported the design and synthesis of an exceptionally stable and highly porous metal-organic framework called MOF-5 (Li et al., 1999). Later, they introduced the concept of reticular design using different carboxylate linkers (Eddaoudi et al., 2002).

Metal-organic framework structures can be synthesized with a wide variety of metal ions and organic reagents. Therefore, the number of new MOFs is rapidly increasing every year. Wilmer et al. (2011) have recently discussed the possibility of creating 137,953 hypothetical MOFs from a library of 102 MOF building blocks. However, the total number of synthesized MOFs by all researchers up to now is around 12,000. The size and chemical environment of the resulting void spaces are defined by the length and functionalities of the organic ligands (Yaghi, 2007; Dybtsev et al., 2004). MOF materials are commonly named in chronological

order like MOF-n where n is an integer number. Recent extensive research interests on the design and synthesis of MOFs have led to numerous practical and conceptual developments in this area. Specifically, the chemistry of MOFs has provided an extensive class of crystalline materials with high stability, tunable metrics, organic functionality, and porosity (Yaghi et al., 2003; Stein et al., 1993). Examples of organic and inorganic units are shown in Figure 1.1.

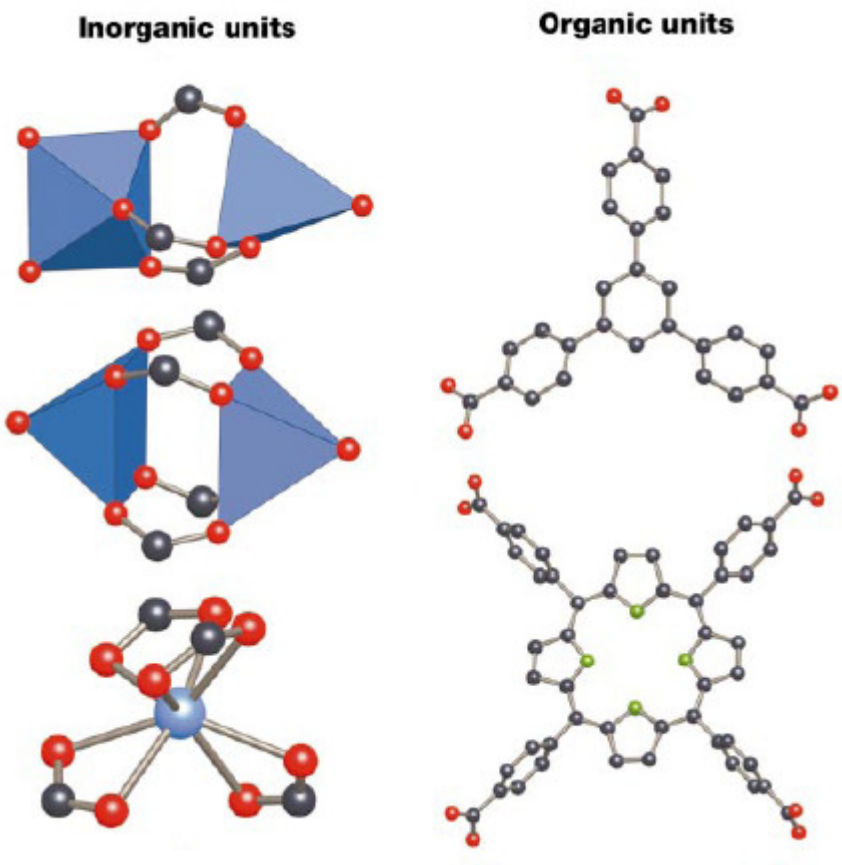

Figure 1.1 Examples of organic and inorganic units forming carboxylate MOFs. N: green; O: red; C: gray; blue: metal ion or metal cluster (Yaghi et al., 2003).

Porosity (which stands for the void volume fraction to total volume of the framework) and surface area are two of the most important properties of MOFs which have significant role in gas separation and storage. By sliming the organic linkers, the MOFs with ultrahigh porosity can be obtained (Chae et al., 2004; Rowsell et al., 2005). However, sliming the organic

linkers may be followed by framework instability or self-interpenetration inside the crystals (Chen et al., 2001; Lin et al., 2007; Schnobrich et al., 2010). Furukawa et al. (2010) have overcome the mentioned difficulties in the synthesis of four highly porous MOFs (MOF-180, MOF-200, MOF-205 and MOF-210). They have reported the highest surface area (BET: 6240 m^2g^{-1}, Langmuir: 10400 m^2g^{-1}) and pore volume for MOF-210 among all MOFs studied up to now.

According to the literature (Barman et al., 2011), incorporation of active sites in MOF structures can also improve the storage and catalytic performance of these materials. For example, removing coordinated solvent can create the open metal sites in some MOFs such as Cu-BTC, MOF-74 and MOF-648 and enhance the gas storage capacity.

In addition to high porosity, high surface area, absence of dead volume and 3-dimensional structure in metal-organic frameworks, some of them have flexible pore structure. The framework flexibility was known in other materials such as zeolites containing octahedral and tetrahedral motifs upon temperature change. However, some MOFs, such as MIL-53, show framework flexibility due to the adsorption and desorption of the guest molecules (Kitagawa et al., 2004; Liu et al., 2008; Volkringer et al., 2009; Finsy et al., 2009).

Among all MOF family members, MOF-199 or Cu-BTC is one of the rigid members which can be easily synthesized. It has a 3-dimensional structure with open metal sites and acceptable surface area and pore volume.

In late 2007, commercial Cu-BTC adsorbent called Basolite® C300 was marketed by Baden Aniline and Soda Factory (BASF). Thereafter, some studies focused on using this material in conducting equilibrium or kinetic measurements instead of synthesized Cu-BTC (Lamia et

al., 2009; Achmann et al., 2009; Brieva et al., 2010; Brieva et al., 2011; Frreira et al., 2011, Plaza et al., 2011). Brieva et al. (2010 and 2011) have studied the adsorption of some organo-sulfur compounds present in liquid fuels on some commercialized MOFs including Basolite® C300. According to their findings, adsorption capacity of Basolite® was much higher than some Y-type zeolites at ambient temperature.

1.2 Clean Energy Challenges

Clean energy can be defined as renewable or green energy which is usually obtained from renewable energy (RE) resources such as solar, wind, hydro, geo-thermal and tidal energies. Another definition for clean energy is energy produced with minimum environmental pollution. Security, sustainability and environmental impacts are important issues, which should be considered when an energy source is developed. Since approximately 1850, demand for fossil energy has steadily increased and this has led to steady increase of carbon dioxide level in the atmosphere. Carbon dioxide is an important member of Green House Gases (GHGs), which can absorb and emit radiation within the thermal infrared range and cause global warming, leading to sea level rise and some other undesirable impacts on the environment (Furukawa and Yaghi, 2009; IPCC Report, 2012).

There are different proposals for lowering GHG emissions while maintaining sufficient energy supply. For example, high-GHG carriers, such as coal and petroleum can be replaced by lower-GHG energy carriers, such as natural gas. Coal based power plant with provision for carbon dioxide capture and sequestration (CCS) can also lower GHG emission. Significant reduction in carbon footprint is possible if renewable and nuclear energy options are developed.

Biogas is a renewable energy, which is produced by anaerobic digestion or fermentation of biodegradable materials such as sewage sludge, manure, wet wastes and micro algae. Anaerobic digestion or fermentation is a biological process in which organic materials are broken down by microorganisms to produce methane, known as biogas. Therefore, biogas can provide a clean, easily controlled source of renewable energy from organic waste materials. Around 30% of biogas is carbon dioxide, which should be removed to upgrade and increase the heat content of this renewable energy source.

1.2.1 Carbon Capture and Sequestration (CCS)

CCS is advocated as an option for reducing green house gas (GHG) and hence, global warming and climate change (Report of the Interagency Task Force on Carbon Capture and Storage_Aug 2010). The idea is to capture and concentrate carbon dioxide (CO_2) from industrial effluent gases, and sequester in geological seams, such as depleted oil/gas fields, deep saline formation, and bottom of the ocean.

The large stationary CO_2 emitting sources around the world are coal fired power plants, steel mills, hydrogen and ammonia plants (IPCC Special Report on Carbon Dioxide Capture and Storage, 2005; Report of the Interagency Task Force on Carbon Capture and Storage, 2010). As may be seen from Figure 1.2, CO_2 capture and concentration are necessary for the pre- and post-combustions routes of power generation, as well as for the industrial processes. Oxyfuel combustion, which is currently in the developmental stage, uses pure oxygen for combustion. Hence, it produces pure CO_2, thus eliminating the need for a capture process. Over 70% world total CO_2 emission comes from post-combustion flue gas of coal-fired power plants (Report of the Interagency Task Force on Carbon Capture and Storage, 2010). The pre-combustion route of power generation employs the Integrated Gasification

Combined cycle (IGCC), which has been in commercial use since mid 1980s (DOE, 2011) is viewed as the future of coal fired power plants.

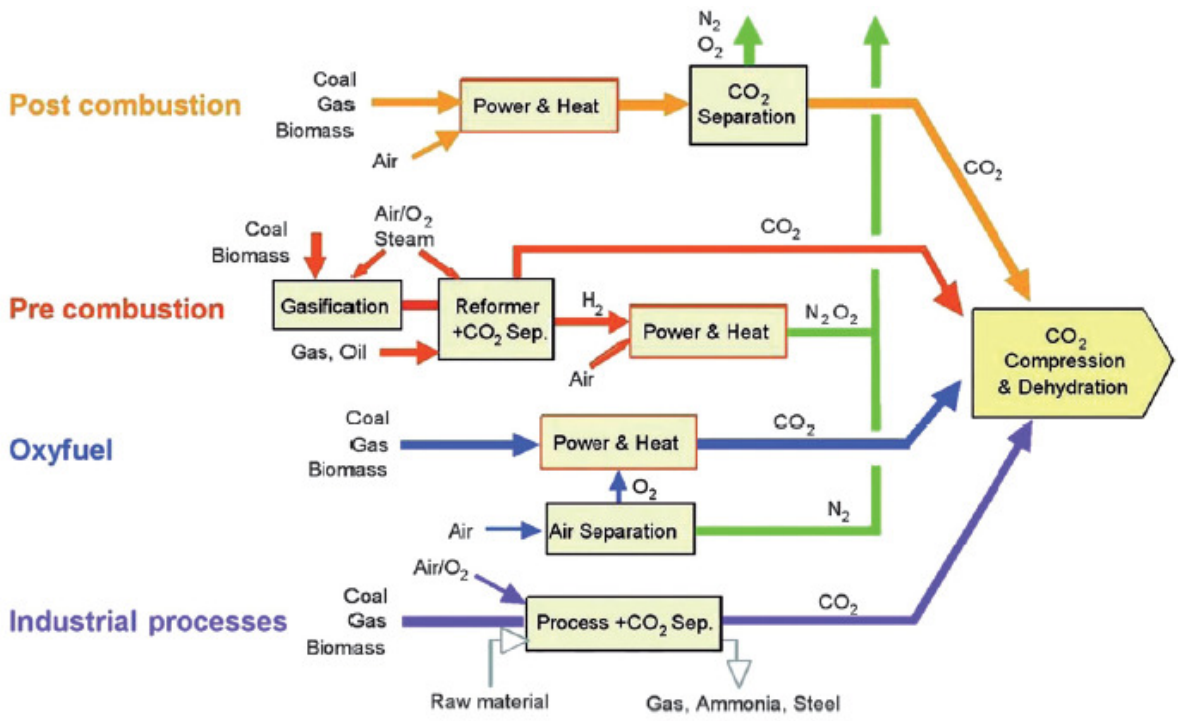

Figure 1.2 Overview of CO_2 capture processes (IPCC, Special Report on Carbon Capture and Storage, 2005, Prepared by Working Group III of the Intergovernmental Panel on Climate Change, Geneva, Switzerland).

Typical composition of post combustion flue gas from a coal fired power plant is 65-75% N_2, 12-15% CO_2, 7-18% H_2O, 2-7% O_2 and some trace components such as CO, NOx, SO_2 and C_xH_y (Xu et al., 2003; Sayari et al., 2011; Report of the Interagency Task Force on Carbon Capture and Storage. Aug 2010).

The energy required to run a CO_2 capture process is known as energy penalty. CO_2 capture and sequestration methods are compiled in Figure 1.3. The established technologies,

cryogenic distillation and amine based absorption, have high (60-80%) energy penalty. They are also matured technologies and scope for further improvement is limited. The challenge is to develop a technology that has lower energy penalty. In view of the very large amount of CO_2 that must be captured and concentrated, the plant size and capital cost are also important considerations. Adsorption based cyclic processes are emerging as energy efficient alternatives for industrial gas separation applications. They also offer economies of scale, unlike membrane processes. Hence adsorption technology is a potential candidate to offer lower energy solution for carbon capture and sequestration and other clean energy applications.

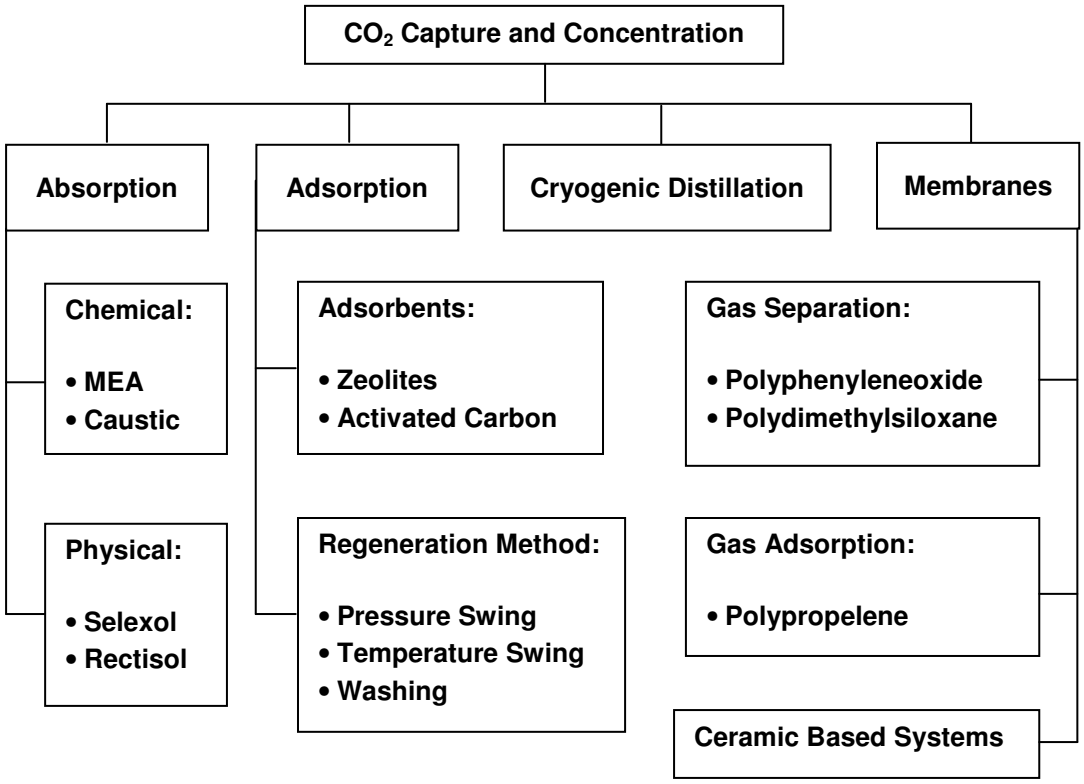

Figure 1.3 Technical options for CO_2 capture.

1.3 Cu-BTC

$[Cu_3(TMA)_2(H_2O)_3]_n$ or Cu-BTC in short, was first reported by Chui et al. (1999). According to them, Cu-BTC (also called HKUST-1) has a three dimensional channel system with a pore

size of 1 nanometer which is created by interconnection of $[Cu_2(O_2CR)_4]$ units. In fact, Cu^{2+} is the central cation and benzene-1,3,5-tricarbocylate (BTC) constitutes the linker.

Choice of Cu-BTC is due to its good thermal stability as well as reversible adsorption-desorption properties without any indication of damage to the crystal structure. In this material, the main pores of approximately 9 Å diameter form a cubic network with additional 3.5 Å (in diameter) side pockets (Wang et al., 2002). The resultant structure has big cavities and small octahedral cages. A Cu-BTC unit cell has cubic symmetry. This unit cell is formed by six side cages of octahedral shape (not symmetric) located at the vertices of the unit cell, and linked by the metal centers. BTC molecules placed in alternate faces form this octahedral structure. No molecule is placed in the rest of the faces, which form the windows and the side cages are accessible through these windows.

Several recipes for synthesis of Cu-BTC have been reported in the literature (Wang et al., 2002; Chowdhury et al., 2009; Lee et al., 2005; Dathe et al., 2005; Schlichte et al., 2004; Chui et al., 1999; Senkovska and Kaskal, 2008). These recipes have differences in the proportion of reagents, mixing of the organic and inorganic solutions before the reaction, duration and temperature of the reaction, and solvents used. Besides synthesis, most of the experimental studies on Cu-BTC have concentrated on gas adsorption equilibrium study using different methods. There are only a few experimental studies on the kinetics of adsorption of gases in Cu-BTC. Detailed review of synthesis recipes, and equilibrium and kinetic studies on Cu-BTC reported in the literature will be discussed in the next chapter.

1.4 Objective and Scope of the Work

Based on the review of Cu-BTC related studies in the previous section, it becomes obvious that no systematic study has been carried out to understand if the synthesis routine has any

effect on the gas capacity and its sustenance under repeated adsorption-desorption cycles. Therefore, several Cu-BTC were synthesized in the first step of this work following some variants of published recipes. Repeat CO_2 equilibrium capacity measurement was used to screen the recipes and identify the one that produced the most stable Cu-BTC sample.

In view of very low yield from these recipes, a new constant volume apparatus was designed, constructed and implemented that gave reproducible equilibrium data with only a few grams of adsorbent. Single component isotherms of CH_4, N_2, and CO_2 on both in-house Cu-BTC sample and Basolite® C300 have been measured over a wide range of pressures at different temperatures. The gases were chosen in view of their relevance in clean energy applications. In the absence of any clear jury on the mechanism of gas transport in Cu-BTC adsorbent particles, extensive adsorption and desorption breakthrough measurements of CH_4, N_2, and CO_2 on chosen in-house Cu-BTC sample have been carried out. A consistent transport mechanism has been proposed after a detailed analysis of the breakthrough responses. Binary breakthrough of N_2-CO_2 and N_2-CH_4 mixtures at different concentrations have also been experimentally and theoretically investigated to establish appropriate models for the prediction of mixture equilibrium and kinetics using only single component information.

Finally, a detailed modeling, simulation and optimization study was conducted to examine the suitability of Cu-BTC for CO_2 capture from (dry) post-combustion flue gas from a coal-based power plant.

1.5 Structure of the Thesis

A review of the available literature on structure, synthesis, equilibrium and kinetic behavior of gases in Cu-BTC is presented in chapter 2. In addition, some of the PSA and VSA studies have also been discussed in this chapter. Synthesis of Cu-BTC samples, sample selection,

physical characterization and preparation of the selected sample have been discussed in chapter 3. In chapter 4, experimental setup and procedure for unary adsorption equilibrium isotherm measurement are discussed together with measurement and analysis of these gases, namely N_2, CH_4 and CO_2 on Cu-BTC. Experimental unary and binary breakthrough results of these gases carried out with the view to establishing the transport mechanism and validating the binary equilibrium prediction are detailed in chapter 5. In chapter 6, the suitability of Cu-BTC for CO_2 capture from post combustion flue gas is theoretically investigated. Finally, in chapter 7 of the thesis, conclusions from the present study are drawn and recommendations for future studies are presented.

CHAPTER 2

LITERATURE REVIEW

Structure and synthesis of a wide variety of metal organic frameworks (MOFs) have been published in the open literature since 1990. Cu-BTC is the MOF of interest for the present study. In this chapter, a few interesting MOF structures are discussed first before reviewing published literature on synthesis and structural characterization of Cu-BTC and adsorption of gases on this material. The relevant literature on adsorption equilibrium and kinetics, and the potential of Cu-BTC in gas separation application are also discussed.

2.1 Structure of MOF

Recent extensive research on the design and synthesis of MOFs has led to significant conceptual and practical developments that have resulted in a class of crystalline materials with high stability, tunable metrics, organic functionality, and porosity. In addition, these materials can be synthesized in relatively pure form. Over 12,000 MOF structures have been reported in the Cambridge Structure Database (CSD) as of 2005, with the number of 3D MOFs doubling every 3.9 years (Yaghi et al., 2003; Liu et al., 2007; Tranchemontagne et al., 2008). The possibility of a finely controlled pore structure makes functionalized MOFs more attractive over the other microporous materials such as zeolites and microporous carbons (Vishnyakov et al., 2003).

Design of framework structures in which metal oxides clusters act as 'joints' and the organic linkers as 'struts' is essential to produce highly porous crystals with the lowest density ever recorded for a crystalline material. These significant properties are very useful, especially in gas storage and separation.

To have better understanding of MOF structures, MOFs with significant properties such as very high porosity (MOF-5, MOF-177), one dimensional pores (MOF-74), open metal sites (MOF-74) and breathing effect (MLI-53) are discussed in this section.

MOF-5: MOF-5 or ($Zn_4(O)(BDC)_3$), first reported by Li et al. in 1999, consists of Zn_4O units connected by linear 1,4-benzene dicarboxylate (BDC) struts to form a cubic network. The framework atoms in MOF-5 take up only a small fraction of the available space in the crystal. This MOF have also a high surface area of about 3909 m^2/g. The structure may be derived from a simple cubic six-connected net in two stages: first, the nodes (vertices) of the net are replaced by clusters of secondary building units; second, the links (edges) of the net are replaced by finite rods (struts) of BDC molecules. The core of the cluster consists of a single O atom bonded to four Zn atoms, forming a regular Zn_4O tetrahedron. Each edge of each Zn tetrahedron is then capped by a $–CO_2$ group to form a $Zn_4(O)(CO_2)_6$ cluster. The MOF-5 structure is shown in Figure 2.1 (Li et al., 1999; Tranchemontagne et al., 2008).

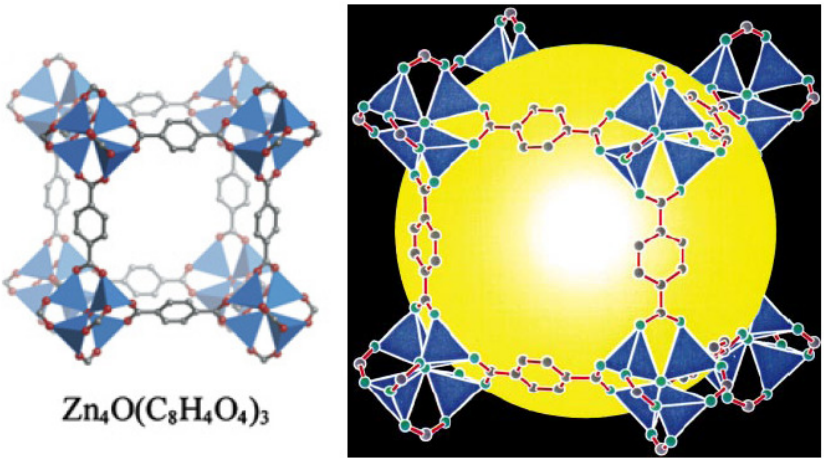

Figure 2.1 Structure of MOF-5 framework. O: green (right), red (left); C: gray; ZnO_4 tetrahedra: blue (Li et al., 1999; Tranchemontagne et al., 2008).

MOF-177: Chae et al. (2004) have reported a metal organic framework with high surface area of about 4500 m^2g^{-1}(Langmuir surface area). They have called this, MOF-177 which combines this exceptional level of surface area with an ordered structure that has extra-large pores capable of binding polycyclic organic guest molecules. In MOF-177 structure, A BTB or 1,3,5-benzentribenzoate ($C_{27}H_{15}O_6$) unit is linked to three Zn_4O units which is shown in Figure 2.2. The authors reported a pore volume of 1.59 cm^3g^{-1}. The narrowest dimension of the pores in MOF-177 is still in the microporous regime (10.8 Å<20 Å).

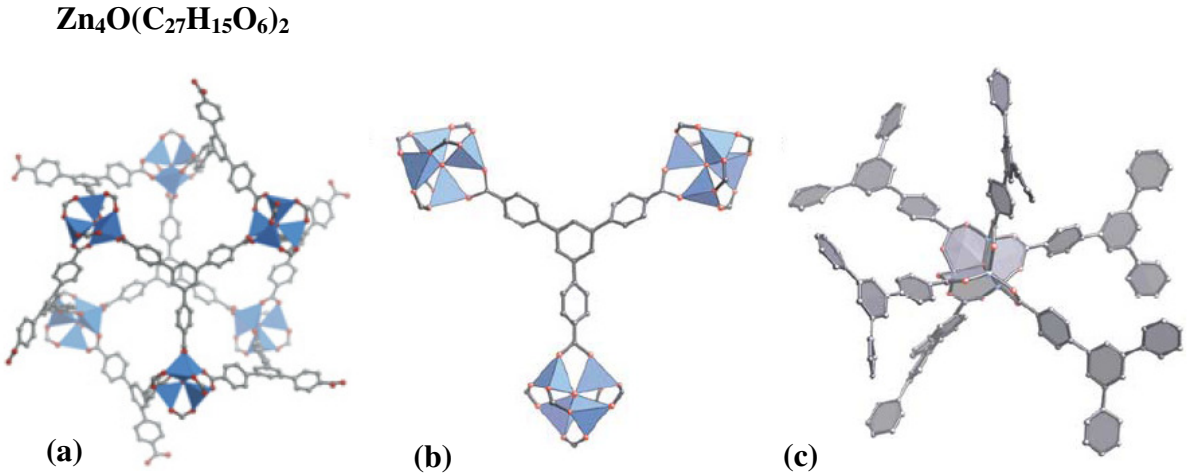

Figure 2.2 a: Structure of MOF-177. b: A BTB unit linked to three OZn_4 units (H atoms are omitted). ZnO_4 tetrahedra are shown in blue and O and C atoms are shown as red and black spheres, respectively. c: A fragment of the structure radiating from a central OZn_4: six-membered rings are shown as grey hexagons and Zn atoms as blue spheres (Chae et al., 2004; Tranchemontagne et al., 2008).

MOF-74: Rosi et al. (2005) synthesized some MOFs from rod-shaped secondary building units (SBU), MOF-74 is one such example. MOF-74 structure is based on coordinated carboxyl and hydroxy groups. Helical Zn-O-C rods of composition $[O_2Zn_2](CO_2)_2$ are constructed from 6-coordinated Zn(II) centers, where each Zn has three carboxyl groups. In addition, two hydroxy groups are bound as doubly bridging. The remaining coordination site has a terminal DMF or Dimethylformamide (C_3H_7NO) ligand. The rods consist of edge-

sharing ZnO_6 octahedra alternately opposite and next-neighbor to form a helix (Figure 2.3). The rods are linked by the benzene units of the 2,5-dihydroxy-1,4-benzenedicarboxylate (DHBDC) to produce **bnn** parallel rod packing as illustrated in Figure 2.3, and one-dimensional channels of dimensions 10.3 * 5.5 $Å^2$ in which terminal DMF molecules protrude and water guests reside. Considering just the carboxylate C atoms as points of extension, these form helices that are linked as in net **etb,** which is also shown in Figure 2.3. The only nets with one kind of vertex are known as **eta** and **etb**. The **eta** and **etb** nets contain helices of one hand and both hands, respectively. Roswell and Yaghi (2006) have reported Langmuir surface area of about 1132 m^2g^{-1}, BET surface area of about 783 m^2g^{-1} and pore volume of about 0.39 cm^3g^{-1} for MOF-74. The structure of MOF-74 is illustrated in Figure 2.4.

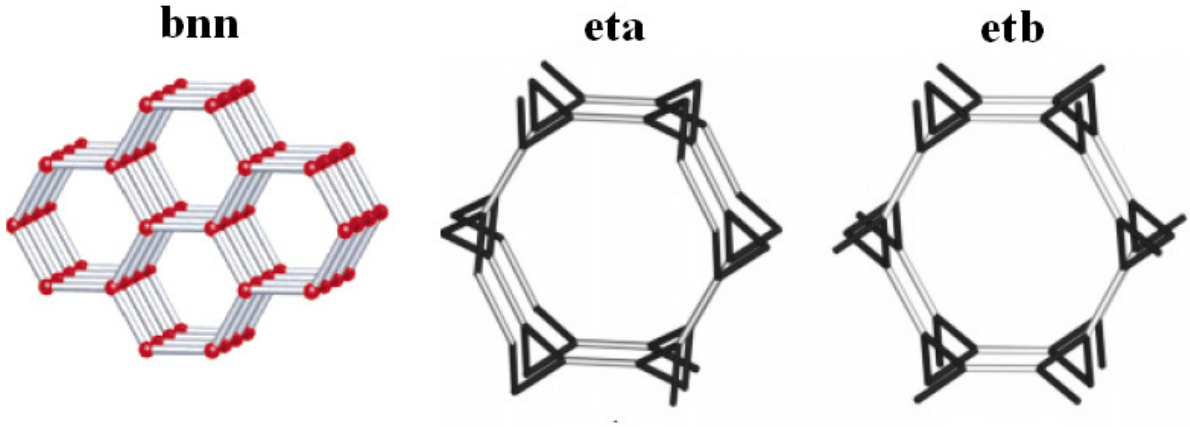

Figure 2.3 Interval rod packing (bnn); and nets formed by linking rods (linked helices: eta, etb) (Rosi et al., 2005).

MIL-53: Most of the stable porous open-frameworks have rigid organic multidentate carboxylate-type linkers with divalent transition metal cations (Cu^{2+}, Zn^{2+}, *etc.*). However, some are flexible such as MIL-53. Material from the Institute Lavoisier is called MIL in short. Flexibility means the pores can swell and shrink from adsorption and desorption. This behavior, shown in Figure 2.5, is called breathing effect in MOFs. Sorption of H_2, CO_2 and CH_4 have been studied to demonstrate the reversible swelling character of the porous MIL-53. The cell volume variation during breathing can reach up to 50%. It depends on the nature

and the size of the species encapsulated within the channels, but also on the nature of the metal. The breathing effect can also occur without the presence of any guest molecules (Liu et al., 2008). In MIL-53, a reversible structure transition between an open-pore and a closed-pore structure can be seen just as a function of temperature as well.

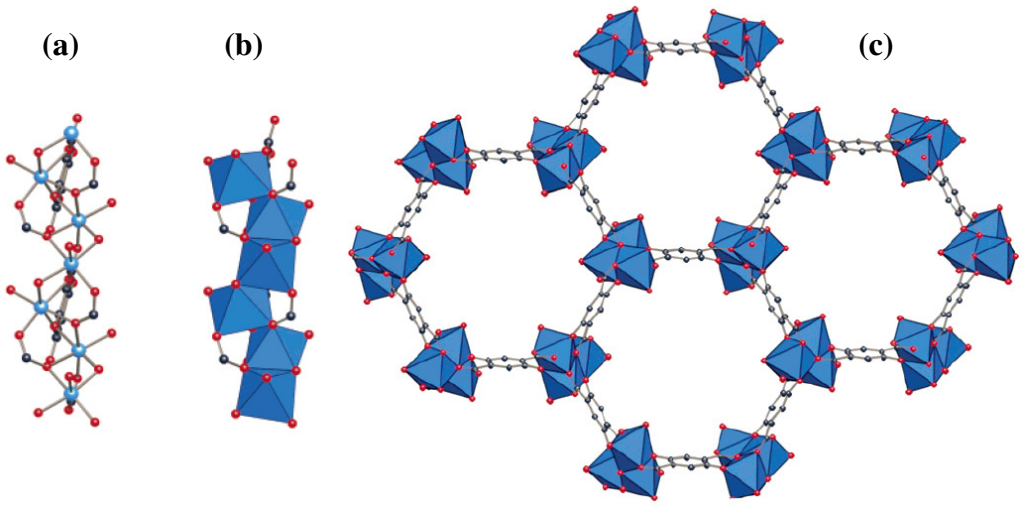

Figure 2.4 MOF-74: ball-and-stick representation of SBU (a); SBU with Zn shown as polyhedra (b); and view of crystalline framework with inorganic SBUs linked together via the benzene ring of 2,5-dihydroxybenzene-1,4-dicarboxylate (c) (DMF and H_2O guest molecules have been omitted for clarity). All drawing conditions are the same as in Figure 2.2, with Zn in blue (Rosi et al., 2005).

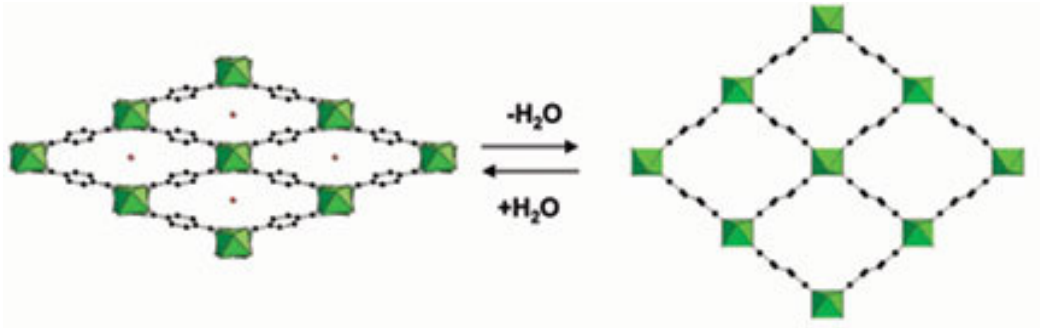

Figure 2.5. Breathing effect in MIL-53 MOF (Volkringer et al., 2009).

The term MIL-53 series refers to the structures resulting from different cations. The skeleton is formed of octahedral chains in which metals (Cr^{3+}, Al^{3+}, Fe^{3+}, Ga^{3+}) are connected by sharing corners (Livage et al., 2007). These chains are then linked in the other two directions by terephthalate ions to form a three-dimensional skeleton with lozenge-shaped channels. This MOF has already been marketed by the German company BASF under the name "Basolite". The terephthalate acid ions can be replaced with other ions like 2-amino terephthalate acid to improve adsorption properties of this material. Amino MIL-53 MOF is shown in Figure 2.6.

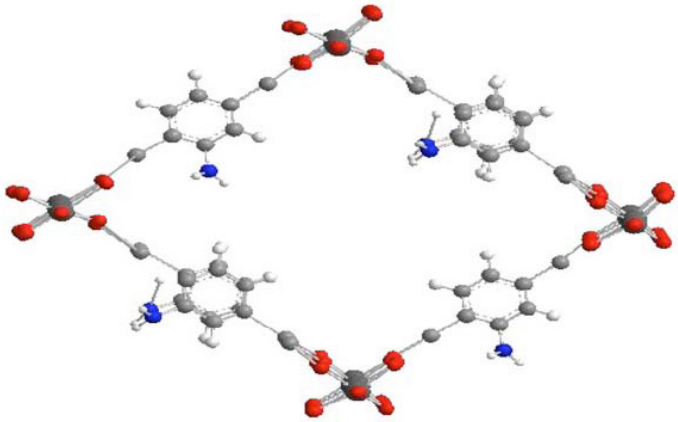

Figure 2.6. Amino MIL-53 (Al); red: oxygen atoms; light grey: carbon atoms; dark grey: Al atoms, and blue: nitrogen atoms (Gascon et al., 2009).

The flexibility of the MIL-53 network allows an adaptation of the skeleton to the size of the molecule trapped within the channels (Figure 2.7). However, the guest removal by heating leads either to an expansion (when the metal ion is Al or Ga, for example) or a contraction of the cell (when the metal ion is Fe, for example) (Volkringer et al., 2009).

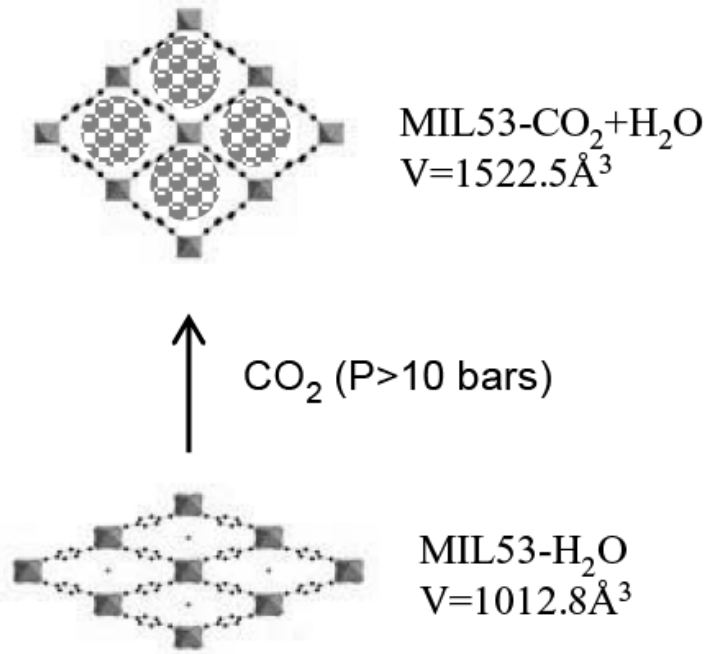

Figure 2.7. Adsorption of CO_2 on the hydrated MIL-53 (Cr) (Bourrelly et al., 2007).

MOF-210: Furukawa et al. (2010) have reported the synthesis procedure of a MOF material called MOF-210, with exceptionally high porosity (0.89 cm^3 cm^{-3} of MOF crystal) and surface area (BET: 6240 m^2 g^{-1}). According to them, the octahedral $Zn_4O(CO_2)$ building unit has an important role in MOFs with ultrahigh porosity. Joining these units with some organic linkers such as 4,4′,4″-benzene-1,3,5-triyltribenzoate (BTB), 4,4′,4″-(benzene-1,3,5-triyl-tris (ethyne-2,1-diyl)) tribenzoate (BTE), 4,4′,4″ (benzene-1,3,5-triyl-tris (benzene-4,1-diyl)) tribenzoate (BBC), 2,6-naphthalenedicarboxylate (NDC), biphenyl-4,4′-dicarboxylate (BPDC) and 1,4-benzenedicarboxylate (BDC) produce some MOFs with high surface area, porosity and pore volume (UMCM-2, MOF-177, MOF-180, MOF-200, MOF-205, MOF-210 and MOF-5 respectively). In addition to highest surface area and pore volume, MOF-210 shows the highest reported excess hydrogen uptake of 86 mg g^{-1} at 77 K (Hirscher, 2011). The organic and inorganic building units produced MOF-210 are shown in Figure 2.8.

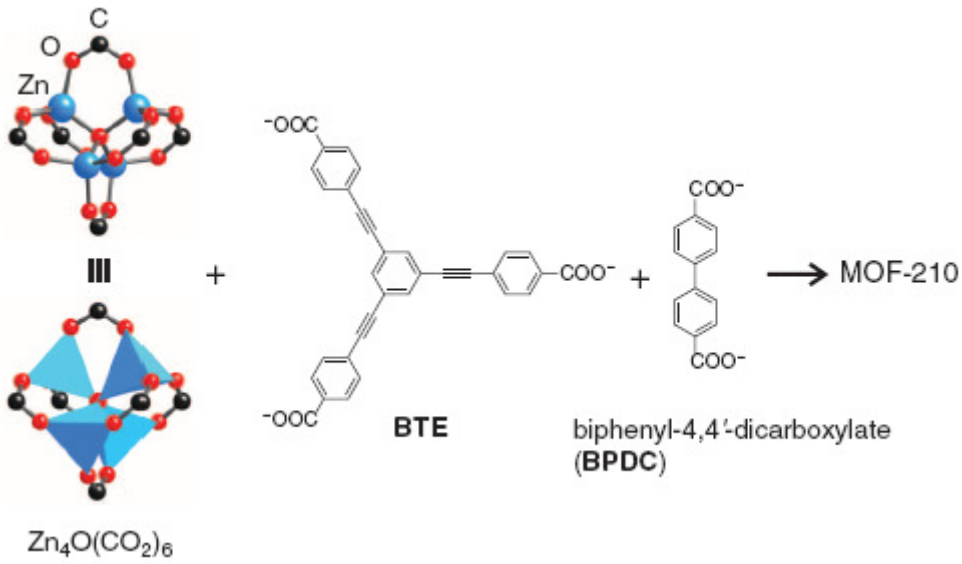

Figure 2.8. Organic and inorganic units produced MOF-210 (Furukawa et al., 2010).

2.2 Cu-BTC

Among the MOFs, Cu-BTC is one of the robust materials. One of its preparation methods is hydrothermal synthesis of Cu^{2+} as central cation and benzene-1,3,5-tricarbocylate (BTC) as linker. The main pores of approximately 9 Å diameter form a cube network with additional 3.5 Å (in diameter) side pockets (Dathe et al., 2005).

2.2.1 Structure of Cu-BTC

MOFs with the same type of coordinated metal ions show similar properties. For instance, the structures containing Zn have generally high affinity for moisture and the framework often collapses from adsorption-desorption of water. Cu-containing MOFs are mostly water stable. Several MOFs have open metal sites that are built into the pore walls in a repeating, regular order. Such sites are found in Cu-BTC and may impart catalytic behavior to the material. The partial positive charges on the metal sites in Cu-BTC can lead to enhanced adsorption properties (Karra et al., 2008).

Cu-BTC is composed of metal coordination polymers having Cu acting as joints and benzene-1,3,5-tricarboxylate (BTC) ligand as the linkers. The resultant structure has big cavities and small octahedral cages. A Cu-BTC unit cell has cubic symmetry. This unit cell is formed by six side cages of octahedral shape (not symmetric) located at the vertices of the unit cell, and linked by the metal centers. The octahedral structures are formed by BTC molecules placed in alternate faces. The rest of the faces are free of molecules, forming windows that allow the access to the side cages. Therefore, in the center of the unit cell there is a nearly spherical void space of 9 Å in diameter. Figure 2.9 shows the 3D structure of Cu-BTC. The main pore and side pockets are also shown in this figure.

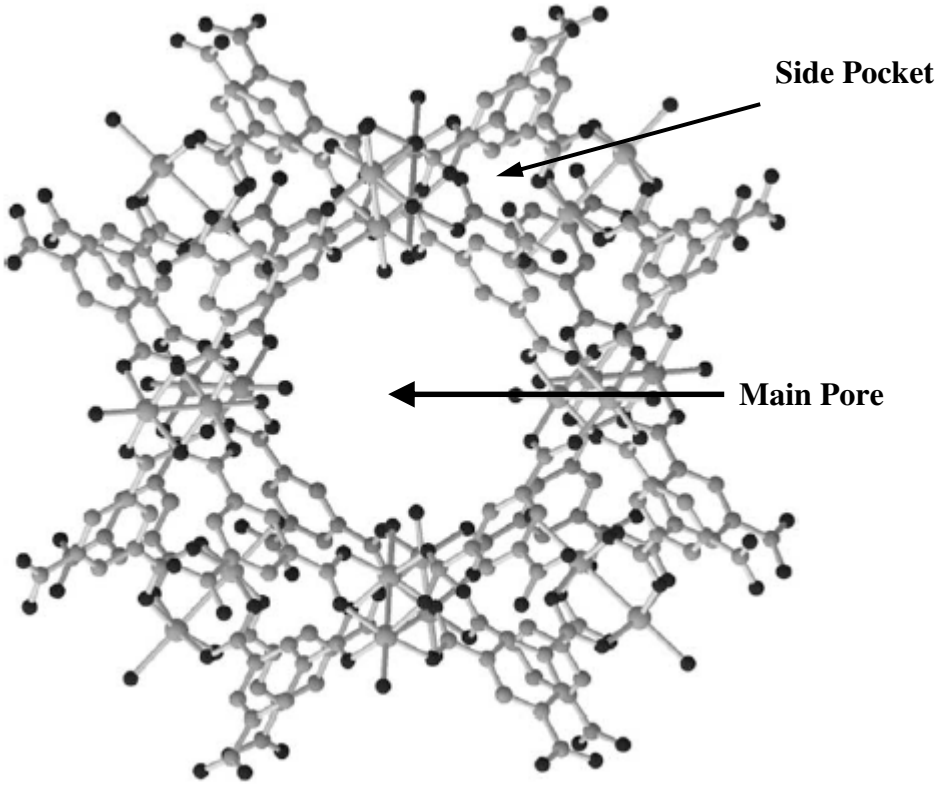

Figure 2.9 Crystal Structure of $Cu_3(BTC)_2(H_2O)_3$ (Schlichte et al., 2004).

Four types of adsorption sites have been identified for Cu-BTC structure, as shown in Figure 2.10. Type I site is close to the copper atoms and there are 48 of these sites in each unit cell. The location of site I' is in the big central cavity and each unit cell has 4 such adsorption

sites. Each unit cell has 8 site II located in the center of small octahedral cages. Type III sites, which are 8 per unit cell, are placed at the windows of the four open faces of the octahedral cages. The cutoff radius of sites I, II and III are 3 Å, 2 Å and 2 Å to 5.5 Å, respectively. The radius of site I' is measured by knowing the volume of this site, which is defined as the rest of the volume not contained in the other sites. Cu-BTC structure and its various adsorption sites are illustrated in Figures 2.10 (Garcı´a-Pe´rez et al., 2009; Castillo et al., 2008).

Some structural characteristics of Cu-BTC samples such as different densities, specific surface areas, pore volumes and accessible porosities reported in different literatures are also summarized in the Table 2.1.

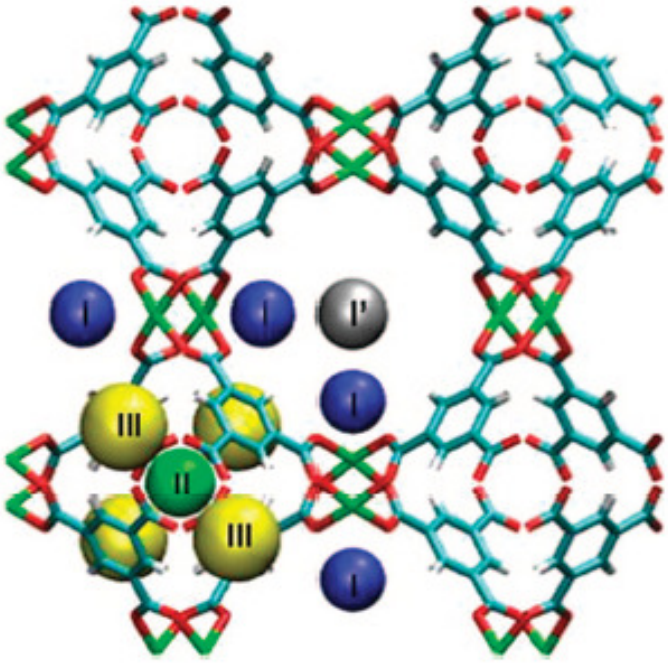

Figure 2.10 Structure of Cu-BTC showing the BTC molecules (blue) forming octahedra at the vertices linked by $Cu_2(COO)_4$ units. The adsorption sites are also shown in this figure (Castillo et al., 2008).

Table 2.1 Characteristics of Cu-BTC samples reported in the literature.

Reference	Surface Area ($m^2 g^{-1}$)	Pore volume ($cm^3 g^{-1}$)	Density ($g cm^{-3}$)
Chui et al. (1999)*	BET: 692.2 Langmuir: 917.16	Total: 0.333	1.22
Senkovska and Kaskel (2008)*	BET: 1502 Langmuir: 2216	0.76	Crystal: 0.88 Packing: 0.52
Wang et al. (2002)*	Synthesized @ 383 K: 964.5 Synthesized @ 423 K: 1333	-	-
Lee et al. (2005)*	-	0.4	-
Dathe et al. (2005)*	-	d > 16 Å: 0.1359 d = 4-20 Å: 0.417761	-
Liu et al. (2007)	(Solvent: Me-OH) BET: 1482 (Solvent: Me-OH) Langmuir: 2302 (Solvent: CH_2Cl_2) BET: 698 (Solvent: CH_2Cl_2) Langmuir: 1078 (Simulation) BET: 1635 (Simulation)Langmuir: 2205	0.828 (solvent: Me-OH) 0.39 (solvent: CH_2Cl_2) Simulation: 0.82	-
Garcı´a-Pe´rez et al. (2009)	1366	Micropore vol:0.55	-
Vishnyakov et al. (2003)	1500	Micropore vol: 0.34 Total pore vol: 0.37	-
Chowdhury et al. (2009)*	(Recipe 7A) BET: 857 (Recipe 7B) BET: 1482	(Recipe 7A) Total: 0.425 (Recipe 7B) Total: 0.753	(Recipe 7A): 0.793 (Recipe 7B): 0.495

* The recipes are given in section 2.2.2

2.2.2 Synthesis of Cu-BTC

Several recipes for the synthesis of Cu-BTC have been reported in the literature. These recipes have differences in the proportion of reagents, duration and temperature of reaction and solvent used. However, the last recipe has followed microwave reaction instead of hydrothermal or solvothermal route. Eight recipes are discussed below:

Recipe 1: Chui et al. (1999) were the first group to report synthesis of Cu-BTC. 1.8 mmol $Cu(NO_3)_2.3H_2O$ was heated with 1.0 mmol of trimesic acid in 12 ml of 50:50 de-ionized water-ethanol mixture at 453 K for 12 h in a 23 ml Teflon liner. The solid product was isolated by filtration, washed with water and ethanol and dried at ambient temperature in air. The authors have reported that higher reaction temperature led to higher dimensionality through the loss of terminal ancillary ligands.

Recipe 2: Wang et al. (2002) have developed an improved synthesis process for large scale production of highly porous Cu-BTC. Benzene-1,3,5-tricarboxylic acid (0.234 mol) was dissolved in 250 ml ethanol, and $Cu(NO_3)_2.2.5H_2O$ (0.466 mol) was dissolved in 250 ml water. Two solutions were then mixed together for 30 min and transferred into an autoclave and heated under hydrothermal conditions for 18 h. The effect of reaction temperature was investigated by heating at 383 K and 423 K. The blue crystals of Cu-BTC were isolated by filtration, washed with water and dried overnight at 383 K. The SEM images of the samples obtained at two different reaction temperatures are shown in Figure 2.11. The XRD patterns of the samples are shown in Figure 2.12.

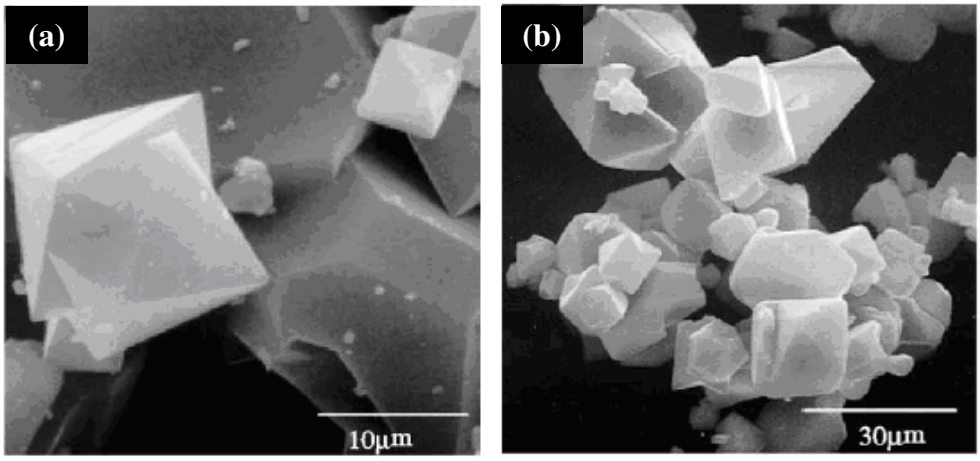

Figure 2.11 SEM micrographs of Cu-BTC synthesized at (a) 383 K and (b) 423 K (Wang et al., 2002).

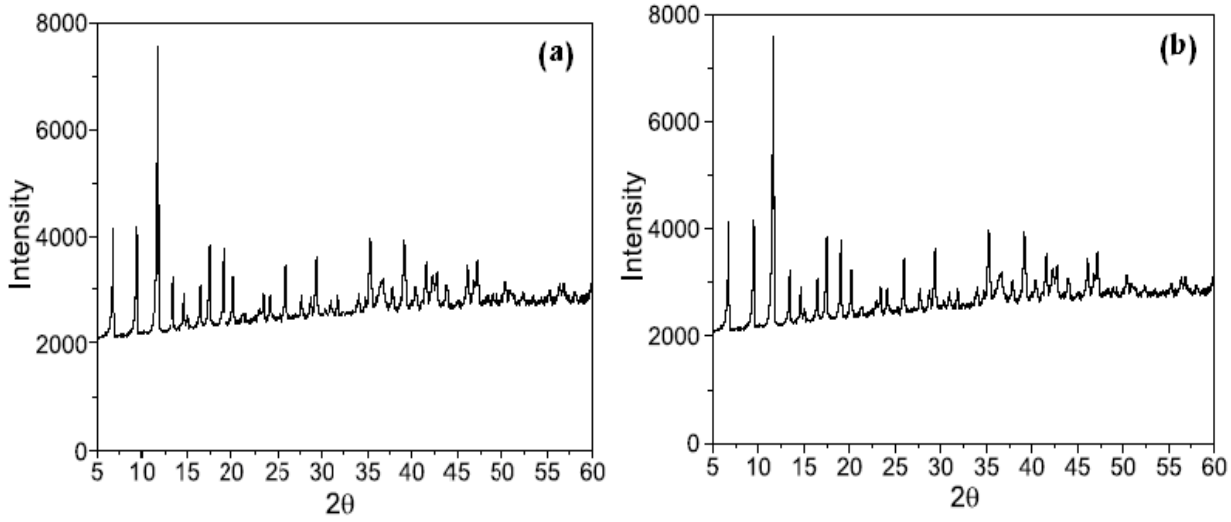

Figure 2.12 XRD pattern of Cu-BTC synthesized at (a) 383 K and (b) 423 K (Wang et al., 2002).

Recipe 3: Schlichate et al. (2004) have reported the synthesis of Cu_2O-free powder of Cu-BTC using trimesic acid (2.0 mmol) as the organic linker and $Cu(NO_3)_2.3H_2O$ (3.6 mmol) to create the metal cluster. They prepared their sample by dissolving $Cu(NO_3)_2.3H_2O$ in 12 ml deionized water and mixing with the solution of trimesic acid in 12 ml ethanol. The final solution was transferred into a 40 ml Teflon-lined autoclave and heated at 393 K for 12 h. The blue crystals of Cu-BTC were filtered and washed with de-ionized water and ethanol.

The product had a high specific pore volume of 0.41 $cm^3 g^{-1}$ and a pore diameter of 10.7 Å. It was found that higher reaction temperature led to the formation of impurities such as Cu_2O which significantly affected the catalytic properties of Cu-BTC. The experimental XRD pattern of the synthesized sample was compared with the theoretically calculated pattern and a very good agreement, as shown in Figure 2.13, was obtained. The authors have also explored the catalytic properties of synthesized Cu-BTC. Thermal stability of synthesized Cu-BTC was studied using TG/DTA and high temperature XRD. The continuous mass loss of 32% was seen up to 523 K due to dehydration of the material. A second weight change was observed due to the decomposition of network at 623 K.

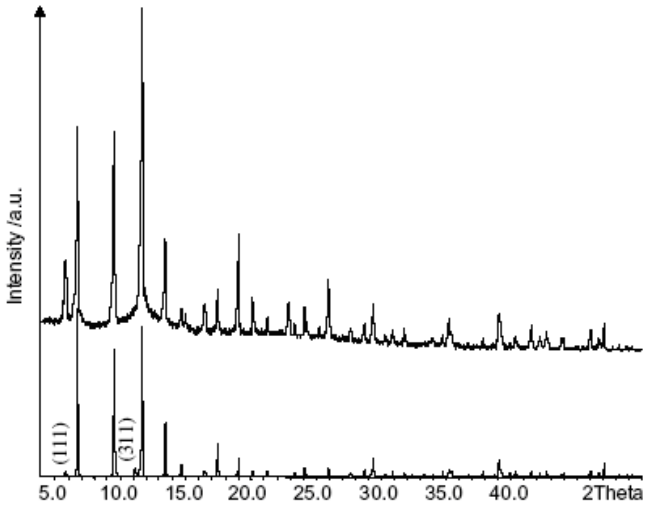

Figure 2.13 Observed (top) and calculated (bottom) XRD patterns of Cu-BTC synthesized according to recipe 3 (Schlichate et al., 2004).

Recipe 4: Dathe et al. (2005) have reported hydrothermal synthesis of Cu-BTC. Benzene-1,3,5-tricarboxylic acid (0.059 mol) was dissolved in 62.5 ml ethanol and $Cu(NO_3)_2.3H_2O$ (0.117 mol) in 62.5 ml water. The solutions was mixed at ambient temperature for 30 min and, then, transferred into a 120 cm^3 PTFE-lined stainless steel autoclave. The mixture was heated to 383 K under hydrothermal conditions for 18 h. Cu-BTC blue crystals were isolated by filtration and washed thoroughly with water. The solid product was dried overnight at 383 K. The yield was nearly 100%. The synthesized Cu-BTC was impregnated with barium salts (chloride, nitrate, acetate) to explore the role of the Ba^{2+} counter ion on SO_2 uptake.

Recipe 5: Lee et al. (2005) synthesized Cu-BTC by dissolving $Cu(NO_3)_2.3H_2O$ (1.8 mmol) in 6 ml de-ionized water and trimesic acid (0.5 mmol) was dissolved in 6 ml of ethanol. The reaction was carried out at 403 K for 12 h. The product was filtered and washed with de-ionized water and ethanol.

Recipe 6: Senkovska and Kaskel (2008) prepared Cu-BTC sample under solvothermal condition in ethanol-water solution. $Cu(NO_3)_2.3H_2O$ (14.49 mmol) was dissolved in 36 ml

de-ionized water and mixed with trimesic acid (9.9 mmol) dissolved in 36 ml ethanol. The mixture was then transferred into a 250 ml Teflon liner and heated at 393 K for 12 h. The solid product was filtered, washed with water and ethanol and dried at 423 K.

Recipe 7: In a more recent study, Chowdhury et al. (2009) have reported the synthesis of Cu-BTC (sample A) where they varied the solvent for dissolving the organic linker source. Benzene-1,3,5-tricarboxylic acid (0.009 mol) was added to 20 ml ethanol and mixed thoroughly. $Cu(NO_3)_2.3H_2O$ (0.018 mol) was dissolved in 10 ml de-ionized water in another flask. The two solutions were mixed together and stirred for 16 h. The resulting viscous mixture was then transferred into a Teflon-lined stainless steel autoclave and heated at 413 K for 48 h. Blue crystals of Cu-BTC were recovered by thorough washing and filtration with de-ionized water. The product was dried overnight at 358 K.

In the other synthesis (sample B), they used 1.0 g Benzene-1,3,5-tricarboxylic acid and dissolved in 30 ml of 1:1 mixture of ethanol/N,N-dimethylformamide (DMF). Moreover, 2.077g cupric nitrate trihydrate was dissolved in 15 ml water. The solutions were mixed together for 10 min, transferred into a Teflon-lined stainless steel autoclave, and heated to 373 K for 10 h. The resulting crystals were isolated by filtration and solvated DMF was removed by overnight extraction with methanol in a Soxhlet extractor. The product was dried at room temperature. SEM images and XRD patterns of the samples from the two synthesis route are shown in Figure 2.14 and 2.15.

Recipe 8: Besides common solvothermal and hydrothermal synthesis procedures, microwave-assisted hydrothermal synthesis of Cu-BTC was firstly reported by Seo et al. (2009). By using this method, rapid heating, faster kinetics, higher phase purity and product yield is obtained according to the literature (Komarneni et al., 1999; Hwang et al., 2005;

Tompset et al., 2006). Seo et al. (2009) have synthesized three different phases of Cu(II)-(BTC–H3) system using identical portion of organic and inorganic reaction mixtures. They have varied the reaction temperature and reaction time and, used a microwave oven with power of 300 W. Finally, they have found that 10 min reaction duration at 140ºC would give the best product yield and properties among the other trials. However, the conventional reaction procedure in common ovens showed higher product yield even according to their findings. The SEM, TGA and XRD results of the sample produced by recipe 8 are shown in Figure 2.16.

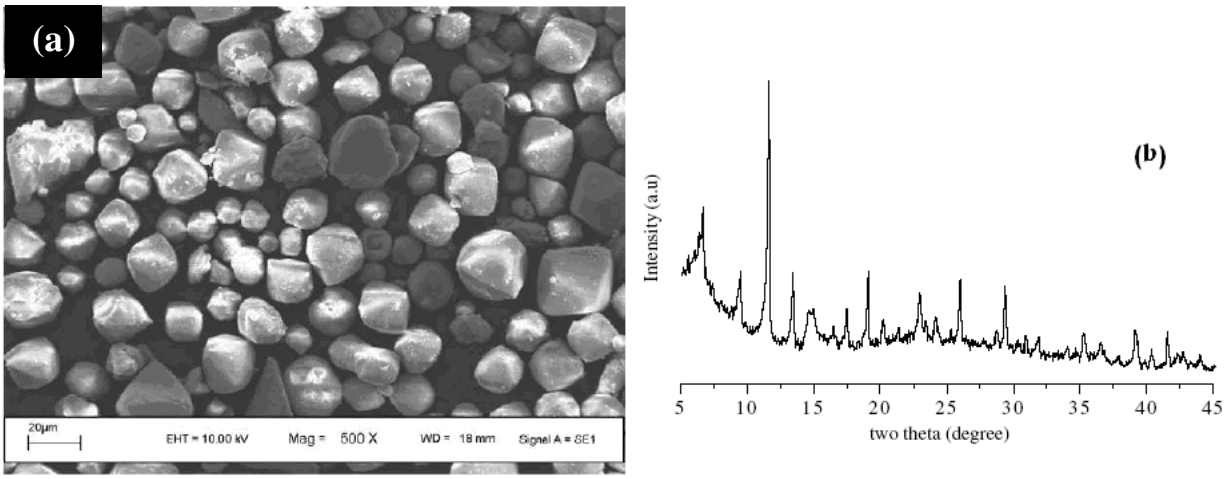

Figure 2.14 (a) SEM micrograph and (b) powder XRD pattern of Cu-BTC synthesized from recipe 7 (sample A) (Chowdhury et al., 2009).

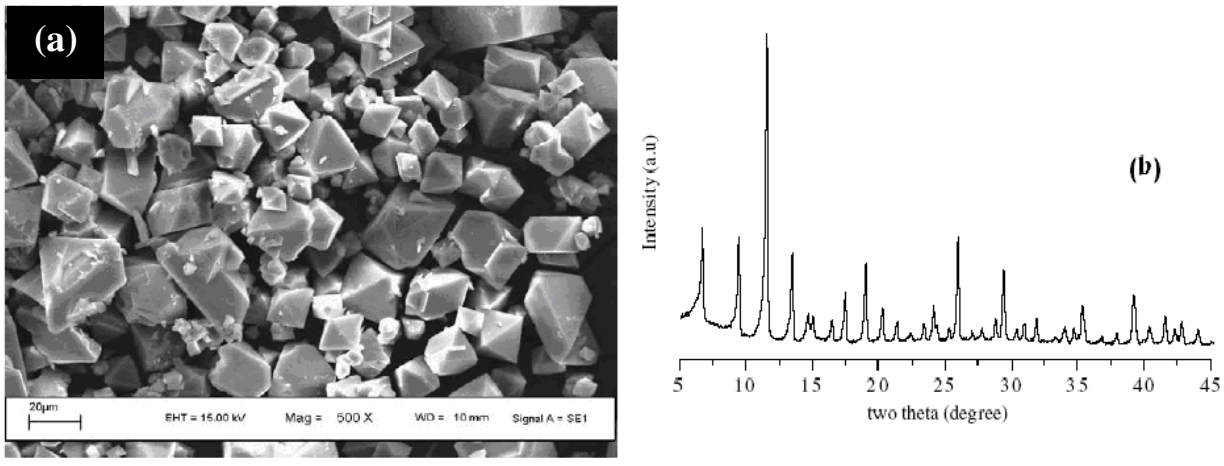

Figure 2.15 (a) SEM micrograph and (b) powder XRD pattern of Cu-BTC synthesized from recipe 7 (sample B) (Chowdhury et al., 2009).

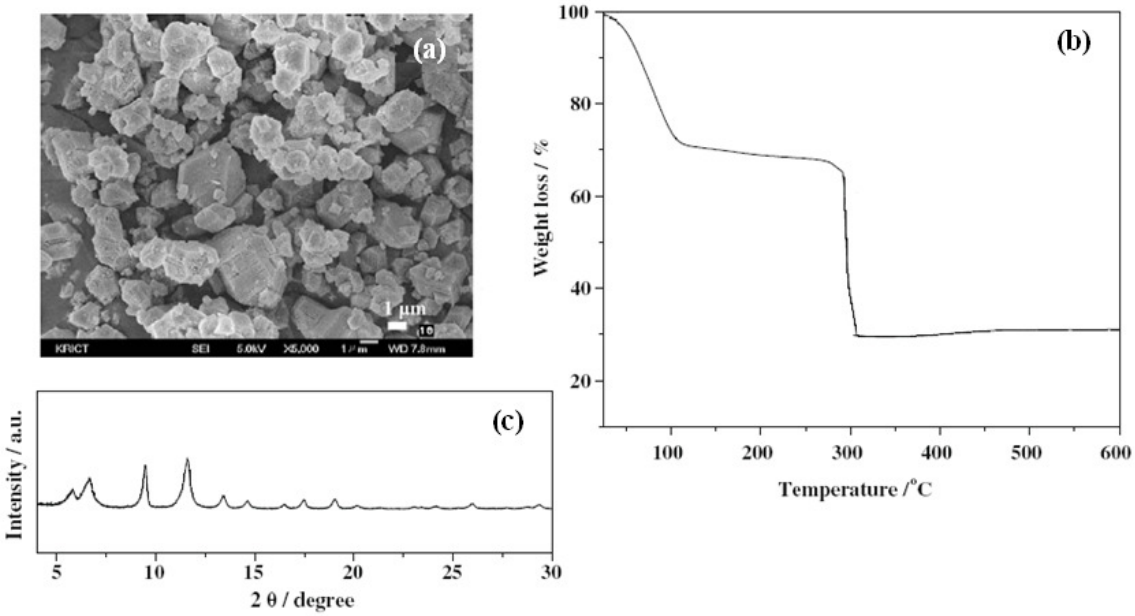

Figure 2.16 (a): SEM, (b): TGA and (c): XRD results of Cu-BTC product from recipe 8 (Seo et al. 2009).

2.2.3 Summary of the Synthesis Recipes

The published recipes for Cu-BTC synthesis discussed in section 2.2.2 have been summarized in Table 2.2. It is clear from the table that $Cu(NO_3)_2.3H_2O$ was used as the copper source in seven out of the eight recipes. In only one recipe, $Cu(NO_3)_2.2.5H_2O$ was used. Trimesic acid (Benzene-1,3,5-tricarboxylic) was the source of the organic linker in all the recipes. Similarly, de-ionized water was used to dissolve the copper source and, with the exception of one study, ethanol was used as the solvent for trimesic acid. A 50:50 mixture of ethanol and DMF was used to dissolve trimesic acid in one of the two versions of recipe 7. The molar ratio of $Cu(NO_3)_2.3H_2O$ to trimesic acid varied from 1.5 to 2 in most studies. The exception was recipe 5 where a ratio of 3.6 was used. Equal volumes of the two solvents were used in most studies. The exception was recipe 7 where the aqueous solvent was half the volume of organic solvent. The reaction temperature varied in the range 383 – 453 K. As for the reaction time, 12 h was used in 4 recipes (1, 3, 5 & 6), 18 h in two recipes (4 and one version of 2) and 1h in one recipe (recipe 8). Recipe 7 stands as an outlier in two aspects.

Table 2.2 Summary of synthesis recipes.

Recipe	Copper source (A)	Organic linker source (B)	Solvent for A (C)	Solvent for B (D)	Mole ratio A/B	ml of C/ gm of A	ml of D/ gm of B	Mixing the solutions before heating	Reaction temperature (K)	Reaction duration (h)	Product drying after filtration	Reference
1	$Cu(NO_3)_2.3H_2O$	Trimesic acid	De-ionized water	ethanol	1.8	13.8	28.6	No mixing	453	12	Not applicable	Chui et al. (1999)
2	$Cu(NO_3)_2.2.5H_2O$	Trimesic acid	De-ionized water	ethanol	2	2.3	5.1	30 min	383 423	18	Overnight at 383 K	Wang et al. (2002)
3	$Cu(NO_3)_2.3H_2O$	Trimesic acid	De-ionized water	ethanol	1.8	13.7	28.6	No mixing	393	12	Not applicable	Schlichte et al. (2004)
4	$Cu(NO_3)_2.3H_2O$	Trimesic acid	De-ionized water	ethanol	2	2.2	5.1	30 min	383	18	Overnight at 383 K	Dathe et al. (2005)
5	$Cu(NO_3)_2.3H_2O$	Trimesic acid	De-ionized water	ethanol	3.6	13.8	54.5	No mixing	403	12	Not applicable	Lee et al. (2005)
6	$Cu(NO_3)_2.3H_2O$	Trimesic acid	De-ionized water	ethanol	1.5	10.3	17.1	No mixing	393	12	at 423 K	Senkovska et al. (2008)
7	$Cu(NO_3)_2.3H_2O$	Trimesic acid	De-ionized water	ethanol	2	2.2	10.2	16 h	413	48	Overnight at 358 K	Chowdhury et al. (2009)
				1:1 mixture of ethanol/DMF	1.5	7.2	30	10 min	373	10	at room T	
8	$Cu(NO_3)_2.3H_2O$	Trimesic acid	1:1 mixture of water and ethanol		1.8	9.5	4.8	10 min	413 (in microwave oven)	1	Overnight at 373 K	Seo et al. (2009)

In one version of this recipe, the reagents were mixed for 16 h before heating in an autoclave for 48 h at 413 K, although all the chemical ingredients were same in the other recipes. In the other version of this recipe, the same research group reduced the molar ratio of $Cu(NO_3)_2.3H_2O$ to trimesic acid from 2 to 1.5 and used a mixture (50:50 by volume) of ethanol and DMF as the organic solvent, and reduced the mixing time to 10 min and reaction time to 10 h. Recipe 8 followed a different way of reaction procedure and it was using microwave oven instead of conventional ovens. Comparing the product yield of reaction using different types of oven (Seo. et al., 2009), conventional oven showed higher value.

2.3 Equilibrium and Kinetic Data of Gases on Cu-BTC

Most of the studies on MOF adsorbents, particularly Cu-BTC, have focused on molecular simulation; while the experimental studies on this adsorbent have mostly concentrated on gas adsorption equilibrium using different methods.

2.3.1 Equilibrium Studies

Wang et al. (2002) have studied adsorption of nitrogen, oxygen, carbon monoxide, carbon dioxide, nitrous oxide, methane, ethylene, ethane, n-dodecane and water on Cu-BTC. They used sorption-isosteric method (SIM) to investigate the sorption thermodynamics of carbon-dioxide. Constant-volume-variable-pressure sorption method was used to perform isotherm measurements of the above gases, except n-dodecane at 295 K. A home-built microbalance system was also used to measure CO and CO_2 isotherms at 298 K (Figure 2.17). Furthermore, a volumetric high-pressure analyzer (HPA) was used for high-pressure sorption isotherms of CO_2. Sorption breakthrough experiments using a typical home-built apparatus were conducted for n-dodecane.

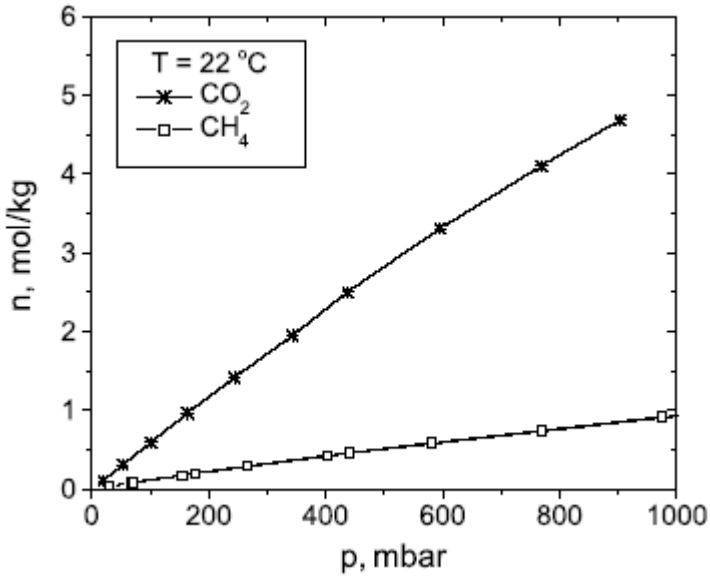

Figure 2.17 Sorption isotherms of CO_2 and CH_4 on Cu-BTC sample (Wang et al. 2002).

Chowdhury et al. (2009) have compared adsorption isotherms of N_2, O_2, Ar, CO_2, C_3H_8 and SF_6 at two temperatures (298.25 K and 315.15 K) on two Cu-BTC samples synthesized according to the recipe 7, discussed in section 2.2. The isotherm experiments were carried out gravimetrically on a Rubotherm magnetic suspension balance. For all gases, the adsorption capacities in the sample B was higher than these in sample A. The difference was attributed to the difference in surface area. In addition, the authors used Langmuir model for SF_6 and C_3H_8, and Virial isotherm model for fitting experimental data of N_2, O_2, Ar and CO_2. The isothermal experimental results for CO_2 at two different temperatures are shown in Figure 2.18.

Senkovska and Kaskel (2008) have evaluated three porous coordination polymers including Cu-BTC for methane storage. They measured excess adsorption isotherms of methane on the three adsorbents using gravimetric method at 303 K up to 200 bar. The effective volumetric storage capacity was measured by means of a volumetric miniature tank system. In the volumetric method, after regeneration of the sample loaded in the tank, the tank was filled

with methane up to the desired pressure. Then, methane was depressurized and the amount of desorbed gas was determined with a gas flow meter. In addition, pressure was monitored during the gas desorption by means of a digital pressure indicator. The schematic diagram of volumetric experimental setup used in this study is shown in Figure 2.19. The adsorption experimental results of methane on three adsorbents are also shown in Figure 2.20.

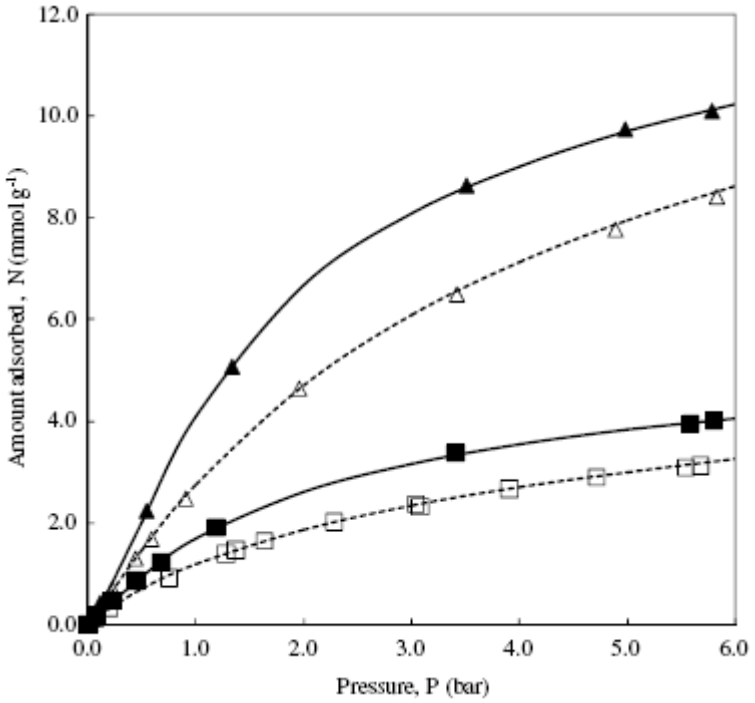

Figure 2.18 Adsorption isotherms for CO_2 on Cu-BTC sample A (squares) and sample B (triangles) at 295.25 K (close symbols) and 318.15 K (open symbols). Lines represent the Virial isotherm model (Chowdhury et al., 2009).

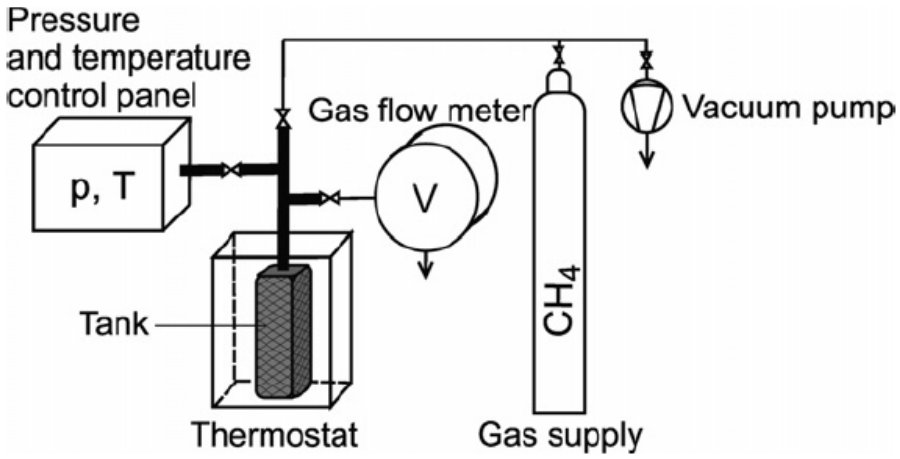

Figure 2.19 Schematic diagram of volumetric setup for high pressure measurements (Senkovska and Kaskel, 2008).

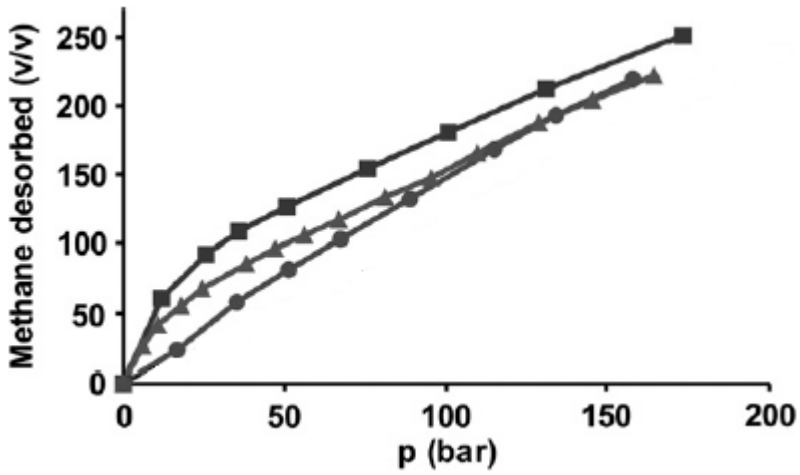

Figure 2.20 CH_4 adsorption isotherms on Cu-BTC (squares), Zn2(bdc)2(dabco) (triangles) and MIL-101 (circles) (Senkovska and Kaskel, 2008).

Lee et al. (2005) have conducted low-temperature gas sorption study on some microporous metal organic frameworks such as Cu-BTC. They used an automated micropore gas analyzer to carry out the adsorption-desorption experiments of H_2 and Ar on Cu-BTC. It can be clearly seen from Figure 2.21 that no hysteresis is occurred in sorption of H_2 on Cu-BTC sample at low temperatures.

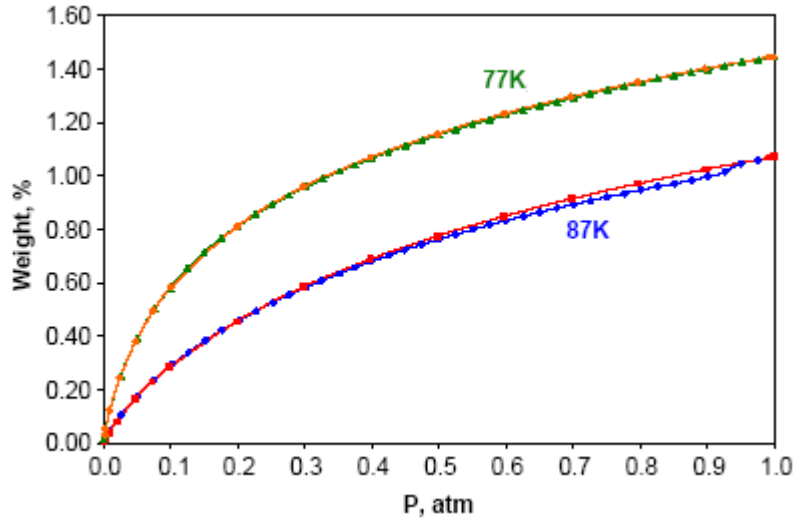

Figure 2.21 Adsorption and desorption of H_2 at 77 K and 87 K on Cu-BTC (Lee et al., 2005).

Aprea et al. (2010) have also reported the adsorption equilibrium of CO_2 on Cu-BTC at low pressure range and compared it with Zeolite 13X results by means of volumetric technique. According to the Figure 2.22, they have reported less nonlinearity of CO_2 isotherms on Cu-BTC samples which is an advantage in adsorption-desorption processes.

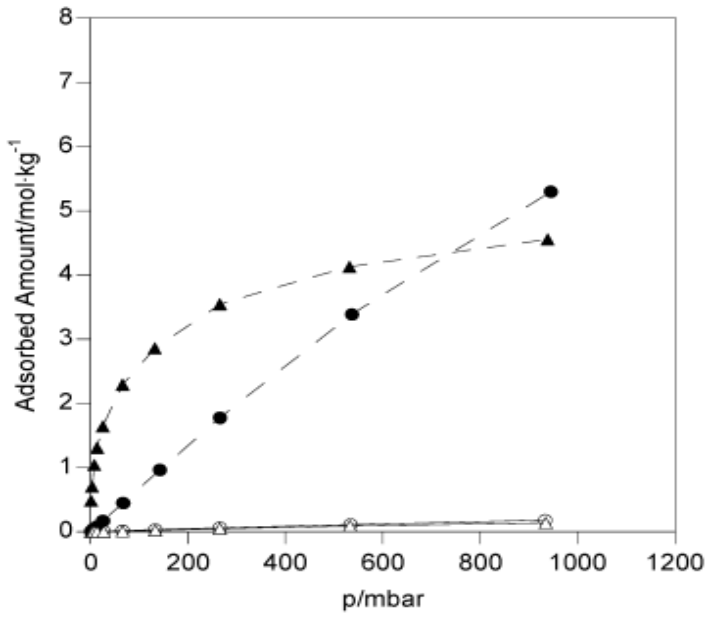

Figure 2.22 Adsorption isotherms of CO_2 (close symbols) and N_2 (open symbols) on Cu-BTC (circles) and Zeolite 13X (triangles) at low range pressure and 293 K (Apea et al., 2010).

Moreover, a comparison between experimental and molecular simulation of CO_2, CO and N_2 gas adsorption on Cu-BTC (Figure 2.23) has been reported by Karra and Walton (2010). They employed Grand Canonical Monte Carlo (GCMC) simulation to identify strategies in designing MOFs for CO_2, CH_4 and H_2 storage.

Hartmann et al. (2008) have carried out the adsorption measurements of isobutene and isobutane on different Cu-BTC samples in the temperature range 303-323 K. They conducted the isotherm experiments in a home-built volumetric apparatus. It was found that Langmuir-type I isotherm represented the isobutene data well and isobutane data was better represented by type V isotherm. Single component breakthrough responses, based on equilibrium model,

were also calculated. The results were encouraging for low pressure separation of isobutene and isobutane due to the peculiar shape of the isobutane isotherm (Figure 2.24).

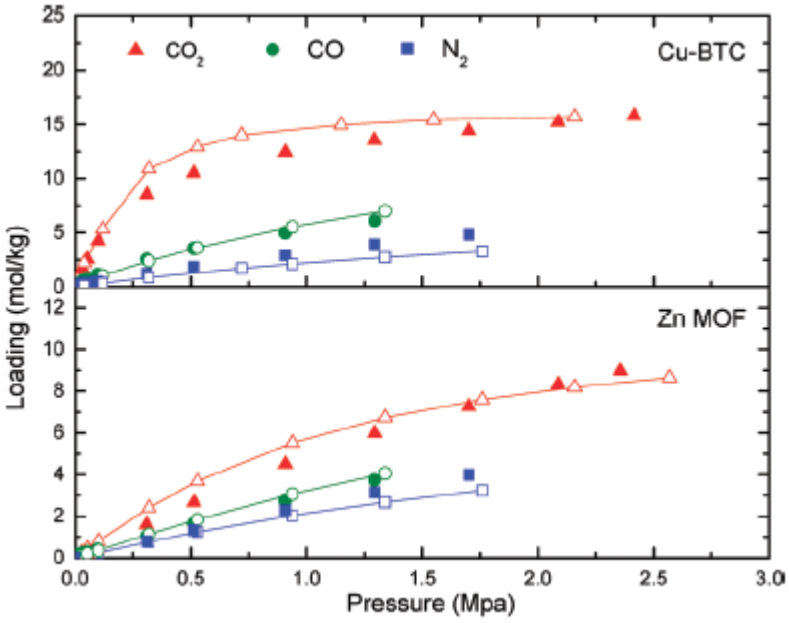

Figure 2.23 Experimental (close symbols) and computed (open symbols) adsorption isotherms of CO_2 (triangles), CO (circles) and N_2 (squares) on Cu-BTC and Zn MOF (Karra and Walton, 2010).

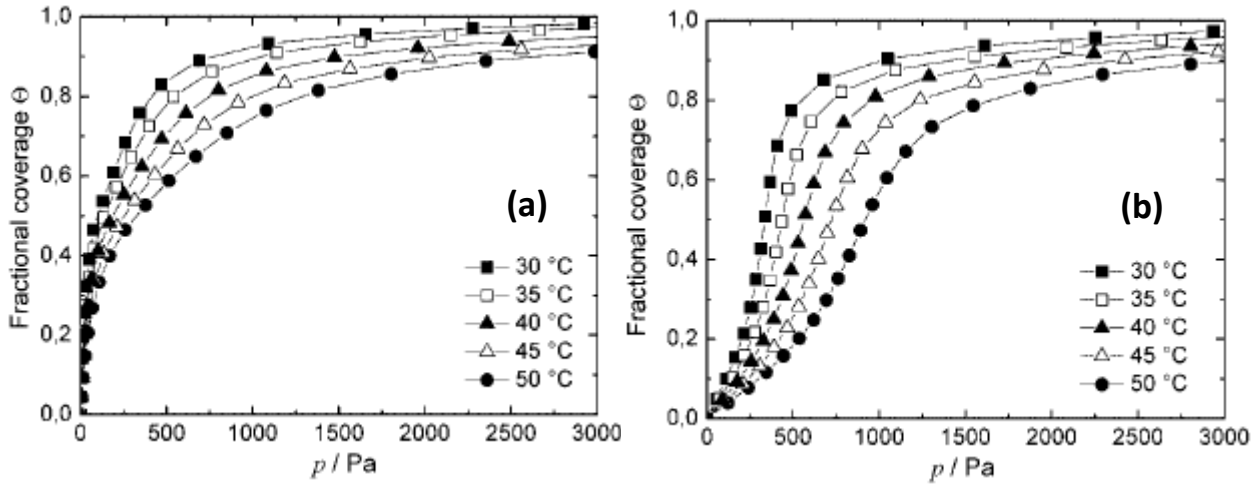

Figure 2.24 (a) isobutene and (b) isobutane adsorption on Cu-BTC sample at different temperatures (Hartmann et al., 2008).

Lamia et al. (2009) have explored the possibility of using Cu-BTC in adsorptive separation of propane/propylene, particularly in a simulated moving bed (SMB) process with isobutane as a desorbent. Cu-BTC powder, only recently marketed by BASF as Basolite® C300, was used in this study. Gravimetric method was used to conduct the low pressure isotherm measurements of propane, propylene and isobutane over a temperature range of 323 K to 423 K. The gravimetric method was selected because of its sensitivity, high accuracy and the possibility of checking the activation state of a sorbent sample.

The authors have also compared the experimental measurements to molecular simulation results. Propane adsorbed preferentially in the small octahedral side pockets of Cu-BTC framework, while large cages contained adsorbate molecules at high pressures. Propane and propylene adsorption capacity represented in this study were higher relative to the wildly used adsorbents such as zeolite 13X and CMS 4A. Adsorption isotherms of propylene, propane and isobutane on Cu-BTC are shown in Figure 2.25.

2.3.2 Kinetic Studies

There have been a few experimental studies on adsorption kinetics of gases in Cu-BTC. Kinetics and equilibrium behavior of Ar and CF_4 gases in Cu-BTC have been qualitatively reported by Krungleviciute et al. (2008) on a synthesized and a commercially available Cu-BTC samples. Similar relative temperatures ($T/T_{critical}$) were used to perform kinetic experiments on both adsorbents. A custom built adsorption setup was used to carrying out the measurements. The authors have presented 50 to 100 equilibrium points in the pressure interval between the beginning of the measurements and the saturation point. The isotherm results on Cu-BTC are shown in Figure 2.26.

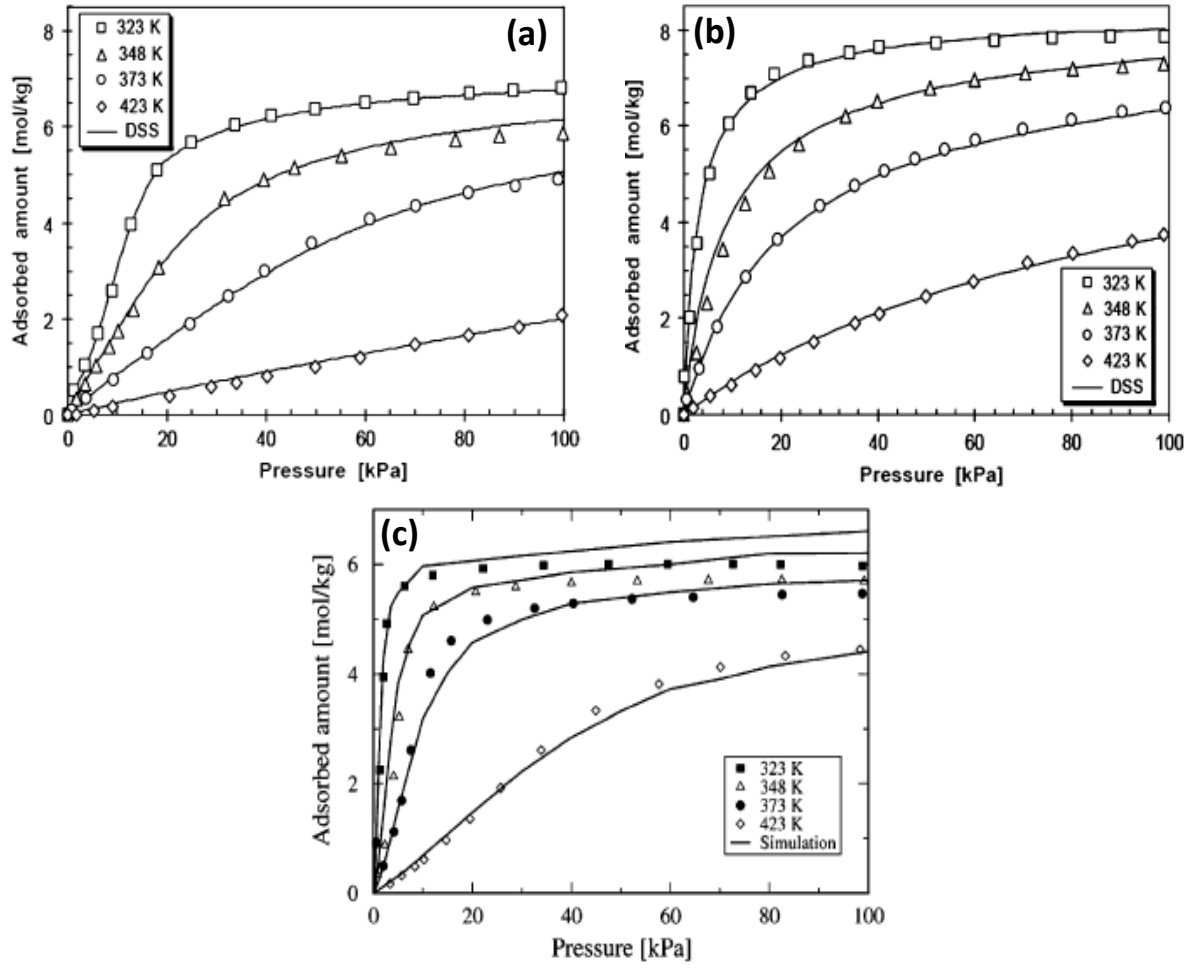

Figure 2.25 Experimental adsorption isotherms of (a) propane and (b) propylene. The solid lines represent the Dual Site Sips model. (c) Symbols show the experimental adsorption isotherms of isobutane and lines represent molecular simulation results (Lamia et al., 2009).

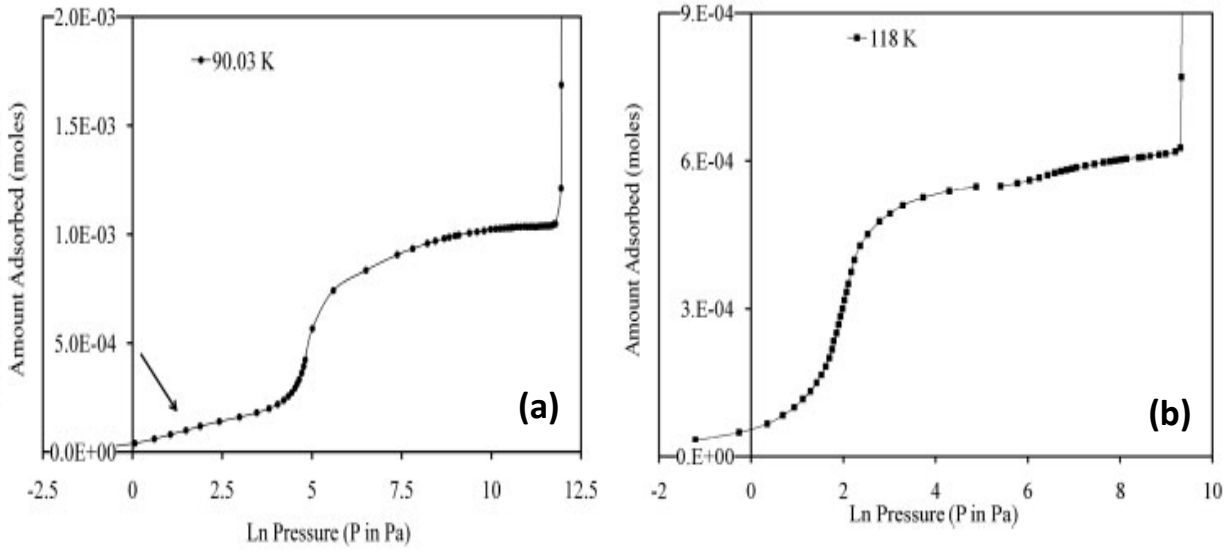

Figure 2.26 Adsorption isotherms of (a) Ar and (b) CF_4 on Cu-BTC (Krungleviciute et al., 2008).

During each equilibrium measurement, the decrease in pressure was recorded every 10 seconds to get the kinetic information. The results suggested that there were some sites in Cu-BTC which were not accessible to CF_4 molecules but were accessible for Ar molecules. However, the authors reported the same time duration (Figure 2.27) for both Ar and CF_4 to be adsorbed and reach the equilibrium on Cu-BTC as long as the main pore size in this adsorbent is much greater than the kinetic diameter of both the adsorbate species.

Hamon et al. (2010) have also reported the experimentally measured binary and ternary breakthrough of CO_2, CH_4 and CO at 303 K using Cu-BTC powder adsorbent. They have assumed both film and micropore resistances in this material. Although the binary breakthroughs of CO_2-CH_4 were experimentally measured at three different compositions, the simulation results did not capture the experimental data in this study (Figure 2.28). The authors have also experimentally measured the ternary breakthrough of CO_2-CH_4-CO but did not attempt to model the results.

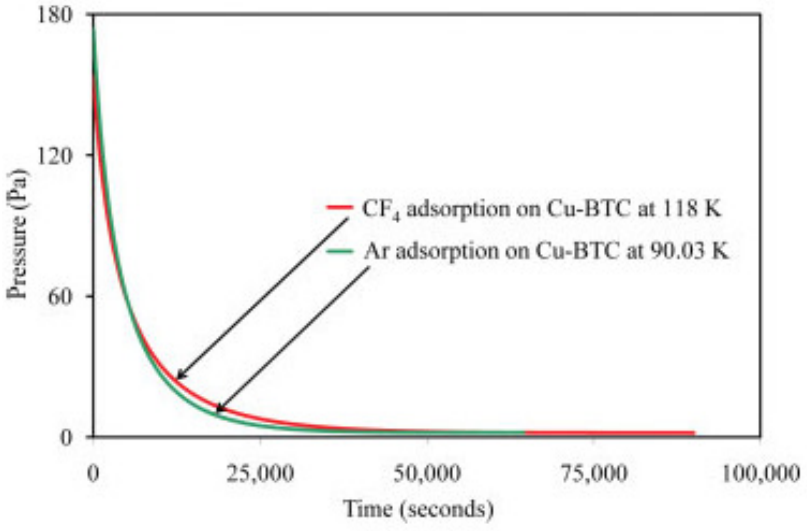

Figure 2.27 Pressure decrease as a function of time for Ar and CF_4 adsorption on Cu-BTC adsorbent (Krungleviciute et al., 2008).

Ferreira et al. (2011) have studied the separation and kinetics of propane-propylene by breakthrough experiments in a column packed with the commercial Cu-BTC (Basolite®

C300) extrudates. The objective was appraising the potential of Cu-BTC for using in Vacuum Swing Adsorption (VSA) and Simulated Moving Bed (SMB) processes. However, there was no modeling and simulation to explain their experimental results (Figure 2.29).

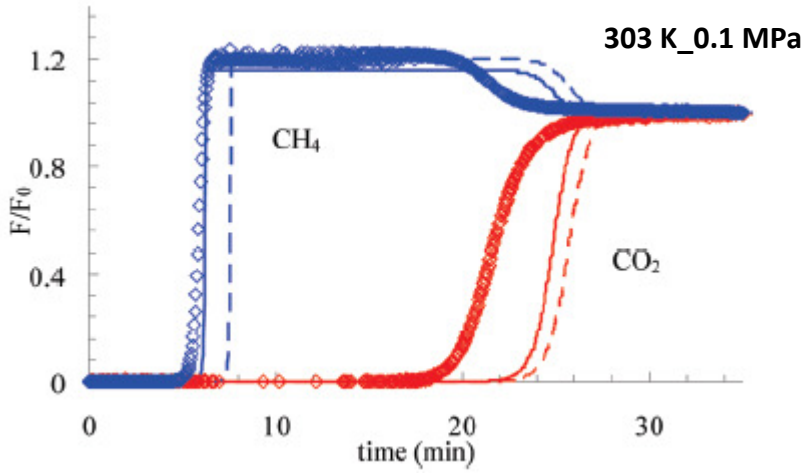

Figure 2.28 Breakthrough curves of the CO_2-CH_4 equimolar mixture on Cu-BTC. Symbols are experimental data, dashed lines and solid lines represent the simulated data based on single component and coadsorption isotherms respectively (Hamon et al., 2010).

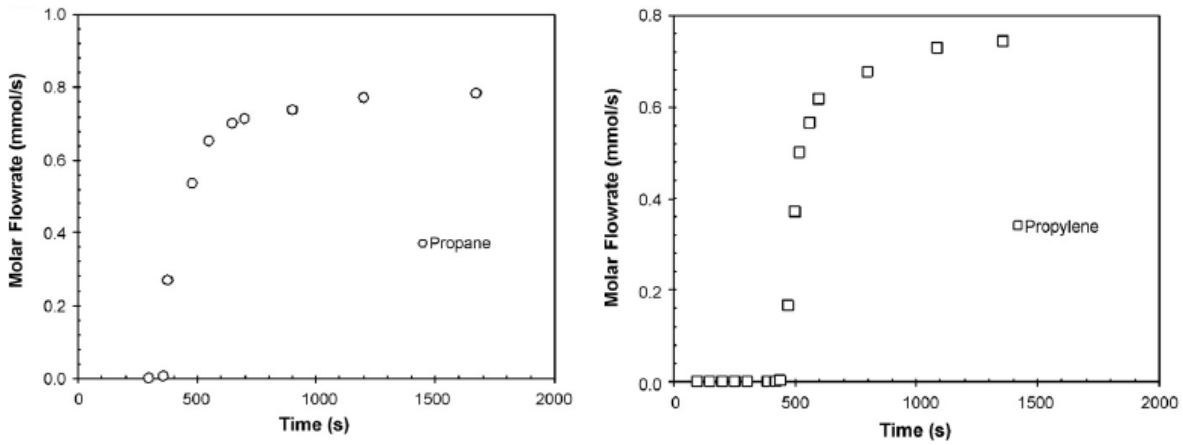

Figure 2.29 Breakthrough curves of the propane and propylene on Basolite® C300 at 373 K and 150 KPa (Ferreira et al., 2011).

2.4 Pressure Swing Adsorption (PSA) Technology

Pressure Swing Adsorption (PSA) and Vacuum Swing Adsorption (VSA) are wildly used industrial gas separation technologies based on the principles of adsorption. PSA has been

wildly used for hydrogen purification, air separation (both oxygen and nitrogen production) and natural gas purification.

2.4.1 Basic Cycle and Definitions

The original design of a PSA process was developed by Skarstrom (Skarstrom, 1960 & 1972), which was a two-bed, four-step cycle using silica gel desiccant for air drying. There are four steps in a Skarstrom PSA cycle, namely pressurization, high pressure adsorption, blowdown and purge, as shown in Figure 2.30. In step I, Bed 1 is pressurized to the high pressure and bed 2 is blown down to the low pressure. In step II, high pressure adsorption occurs in bed 1, while bed 2 is purged at the low pressure with part of the raffinate product from bed 1 undergoing high pressure adsorption. In the next two steps, the roles of the two beds are interchanged. In step III, after the high pressure adsorption step, bed 1 is blown down to the low pressure. At the same time, the high pressure feed stream is switched to bed 2 to repressurize it. In step IV, high pressure adsorption takes place in bed 2 and, bed 1 is purged at the low pressure using part of the product from the other bed. The cyclic operation on each bed continues and after a while the beds reach cyclic steady state when both beds produce same quality product in every cycle.

Several modifications to the existing Skarstrom cycle have been implemented to develop the better process performance. Introducing co-current depressurization, adding pressure equalization before the blowdown step, and having multi-bed PSA process instead of the simple two-bed process are some of the improvements implemented on the basic Skarstrom cycle (Yang, 2003).

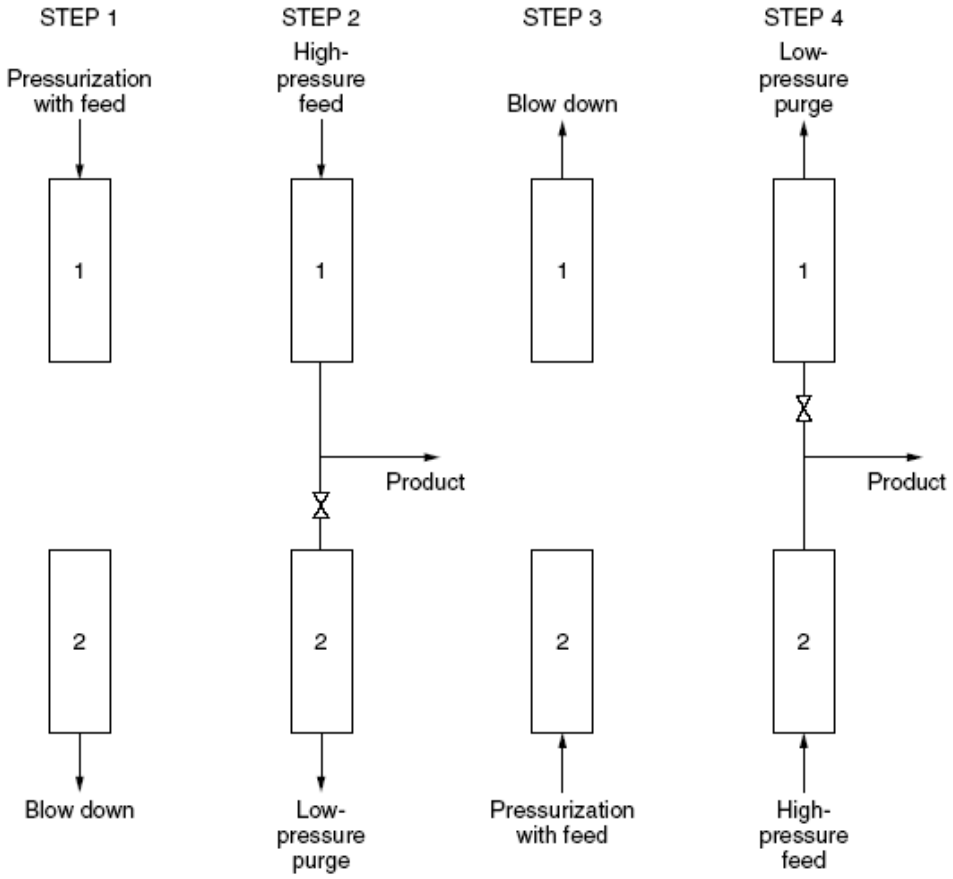

Figure 2.30 The sequence of steps in the basic Skarstrom PSA cycle (Yang, 2003).

In a PSA process, less strongly adsorbed component is called raffinate and more strongly adsorbed component is called extract. The former is also called light product while the latter is called heavy product. Product purity, product recovery and adsorbent productivity are used to evaluate the performance of a PSA cycle. Product purity is the integrated average concentration of the target component in the product stream over the period of collection. Product recovery measures the amount of target component in the product stream divided by the amount of the same component fed to the system during pressurization and high pressure adsorption. Adsorbent productivity is described by the amount of the target component obtained in the product stream per unit adsorbent amount (mass of volume) per unit time.

2.4.2 Equilibrium and Kinetically Controlled Separation

Depending on the adsorption mechanism, PSA separation processes can be categorized into two groups: equilibrium-controlled and kinetic-controlled processes (Shin and Knaebel, 1988, Ruthven et al, 1994). An equilibrium separation process is based on the difference in adsorbent affinity for the feed components to be separated. Kinetic separation is based on the difference in diffusion rates of gas components to be separated from the feed mixture. For equilibrium separation, the permanent dipole moment, polarizability, quadrupole moment, etc., often determine the affinities of the adsorbate molecules for the adsorbents. In a kinetically controlled separation, the adsorbent pore size is the key and should be in the range between the kinetic diameters of two competing adsorbate molecules. Many microporous adsorbents such as MOFs and molecular sieves with tailored pore structure have been synthesized for different applications (Hartman and Kevan, 1999). The kinetic separation factor is defined as the product of the equilibrium separation factor (the ratio of equilibrium loading in the adsorbed phase and corresponding adsorbate concentration for component 1 divided by the same ratio in component 2) and the square root of the diffusivity ratio of two competing adsorbates (Ruthven et al., 1994).

Air separation for oxygen production and hydrogen purification from refinery fuel gas are examples of equilibrium separation process. An example of kinetically controlled industrial PSA separation process is air separation for nitrogen production on carbon molecular sieves.

2.5 Modeling and Simulation of Adsorption Separation Processes

Modeling and simulation to understand the potential of new adsorbent for a given separation is increasingly becoming the first step before undertaking experimental work. Only promising adsorbents can then be taken to next stage of experimental validation. A process simulation

model validated with small scale experiments can be further used study scale-up economics before investing in pilot scale investigation.

The simplest approach to understand an equilibrium controlled separation is using equilibrium theory. In equilibrium theory, local instantaneous equilibrium is assumed for simplification of modeling. The adsorbate behavior can be qualitatively and quantitatively to some extent, represented using equilibrium theory. Local equilibrium is an ideal assumption that tells us the best possible performance.

Another approach is using dynamic modeling, which is more realistic since it accounts for finite mass transfer rate and other dispersions in the system. The model equations constitute a system of coupled, nonlinear partial differential equations that are numerically solved to simulate the process. This approach is more common in the contemporary PSA/VSA studies. Depending on the nature of resistance in the adsorbent particles, two main models, namely pore diffusion model and linear driving Force force (LDF) model, have been commonly used for describing the adsorption kinetics within the adsorbent particles. In the pore diffusion model, which is shown in Equation (2-1) (Yang and Doong, 1985), detailed diffusion equation within the spherical adsorbent particle is solved to obtain the local rate of solid loading (q_i) change.

$$\frac{\partial q_i}{\partial t} = \frac{1}{r^2}\frac{\partial}{\partial r}\left(D_{p,i} r^2 \frac{\partial q_i}{\partial r} \right), \qquad \forall r \in \left(0, r_p\right), \qquad i = 1,...,N \tag{2-1}$$

$D_{p,i}$ is the effective diffusivity of the i^{th} component in the adsorbent pores and r_p is the pore radius. If a parabolic solution profile is assumed, the uptake rate calculated from Equation (2-

1) becomes equal to the uptake obtained by making a linear driving force (LDF) approximation given by Equation (2-2) (Glueckauf and Coates, 1947).

$$\frac{\partial \bar{q}_i}{\partial t} = k_i \left(q_i^* - \bar{q}_i \right), \qquad i = 1, \ldots, N \qquad (2-2)$$

In the above equation, k_i represents the lumped mass transfer coefficient for i^{th} component. The LDF model has been successfully used to capture breakthrough dynamics of an adsorption column for all forms of diffusional transport in adsorbent pores, namely macropore and micropore diffusion. Further, it also allows distinction among the modes of transport in the macropores, such as molecular, Knudsen and surface diffusion. Moreover, equations have been reported in the literature that allow estimation of the LDF rate constant in Equation (2-1) from the appropriate intraparticle diffusional time constant of the adsorbate and available physical characteristics of the adsorbent. The equations for estimating LDF constants for macropore and micropore controlled diffusional transport are given below:

$$k_i = 15 \frac{\varepsilon_p D_p}{R_p^2} \frac{c_0}{q_0} \qquad (macropore\ control) \qquad (2-3)$$

$$k_i = 15 \frac{D_c}{r_c^2} \frac{c_0}{q_0} \qquad (micropore\ control) \qquad (2-4)$$

15 in the above equations is replaced by Ω_i in PSA/VSA process simulation. It has been shown in the literature that Ω_i depends on the cycling frequency of PSA/VSA cycles in order to match the LDF model solution to that obtained using the pore diffusion. Correlations have been proposed to calculate its value based on the controlling diffusional time constant and cycle time (Glueckauf and Coates, 1947). For most equilibrium controlled separation processes, even for very fast cycling frequency, $\Omega_i = 15$ is adequate. (Rama Rao et al., 2010). In case of kinetically controlled processes, where the controlling resistance is in the micropores, the diffusional time constant is strongly concentration dependent. The

correlations, developed assuming constant diffusivity, are not strictly valid for kinetically controlled processes. In such cases, either the full diffusion model including concentration dependence of micropore diffusivity should be used (Farooq and Ruthven, 1991; Farooq et al., 1993; Bhadra and Farooq, 2011; Khalighi et al., 2012), or the correlation should be calibrated separately for each system with limited experimental data (Kapoor and Yang, 1989).

2.6 New Challenges in Separation

Among the new adsorbents, there are some materials which show the potential for using in PSA/VSA processes for gas separation and purification, especially for clean energy applications such as CO_2 capture from flue gas, natural gas/bio gas upgrading, CH_4 and H_2 storage, etc. Currently, water washing membrane and amine scrubbing are the common methods being tried for upgrading natural gas and biogas (Cavenati et al., 2008; Rasi, 2008).

Recently, several MOF materials have been reported for CO_2 capture (Chen et al., 2009; Keskin and Sholl, 2009; Bae et al., 2008). Many of the MOFs are synthesized from nonrenewable precursors and harmful solvents such as DMF. Jeremiah et al. (2011) have proposed a routine for synthesis of a highly selective green MOF called CD-MOF-2. They have reported the isothermal capacity of this adsorbent for capturing CO_2 and CH_4.

Hamon et al. (2009) have studied co-adsorption and separation of CO_2-CH_4 mixtures using MIL-53(Cr) MOF material. They have also investigated the possibility of using this adsorbent in a PSA process for CO_2-CH_4 separation. Selectivity of this material for CO_2-CH_4 separation at different concentrations is shown in Figure 2.31.

Mason et al. (2011) have studied the characteristics of two MOFs, namely MOF-177 and Mg_2(dobdc), in post-combustion CO_2 capture using temperature swing adsorption (TSA). Sayari et al. (2011) have also reviewed the main contributions in the field of new adsorbents (mainly MOFs) for post-combustion CO_2 capture. Ma and Zhou (2009) have also reviewed the storage capacities of CO_2, H_2 and CH_4 in more than 20 MOFs. They have also compared the highest CO_2 capacity, which belongs to MOF-177 at high pressures (more than 15 bar), with the CO_2 capacity at the same pressures in 13X zeolite and MAXIZORB carbon powder. According to their report, MOF-177 has higher CO_2 capacity than the two commercial adsorbents.

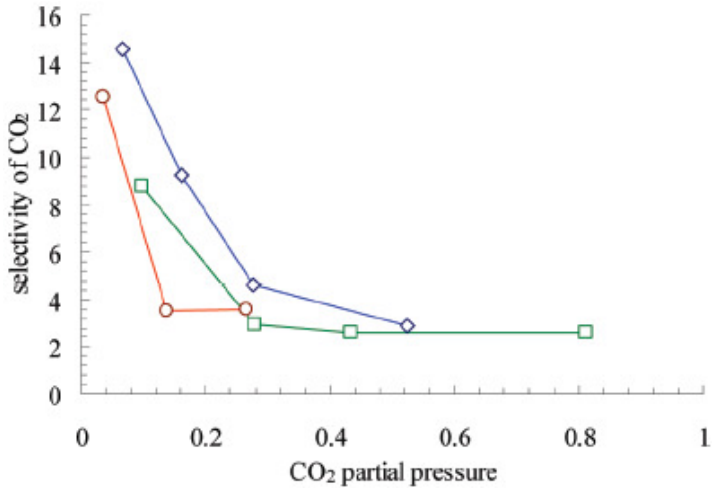

Figure 2.31 Selectivity of MIL-53 for CO_2-CH_4 from breakthrough measurements at different gas feed concentrations. 75-25 (square), 50-50 (diamond), 25-75 (circle) (Hamon et al., 2009).

Yang et al. (2011) have kinetically and thermodynamically investigated the co-adsorption of CO_2 and CH_4 in the zirconium terephtalate UiO-66(Zr) material. The authors have also discussed the possible use of this MOF in a PSA process instead of NaX Faujasite due to its good selectivity, high working capacity and easy regeneration of the adsorbent.

There are some trace compounds such as sulfur compounds, halogenated compounds and organic silicon compounds which should also be removed from biogas. These impurities can be removed sequentially, starting with sulfur compound, nitrogen, water and CO_2 respectively (Knaebel and Reinhold, 2003). According to the literature (Cavenati et al., 2008; Yang et al., 2007), Cu-BTC is a promising adsorbent for biogas purification due to the high capacity for CO_2 and modest curvature of the isotherm. Cavenati and coworkers (2008) have evaluated the CO_2 and CH_4 adsorption on Cu-BTC at different temperature and reported the selectivity for these two gases. They have also stated that applying this material in a VSA process for biogas upgrading would reduce the power consumption and size of the plant.

2.7 Chapter Summary

Structures of Cu-BTC and its various synthesis recipes published in the literature have been reviewed in this chapter. An account of available information on gas adsorption studies on this MOF has also been presented. A brief review of the PSA/VSA technology, and modeling and simulation of PSA/VSA processes has also been presented. . Recent developments of MOF adsorbents for clean energy applications have also been discussed.

Although there are numerous studies on MOF, most of them end in synthesis and equilibrium capacity measurement. A comprehensive study that takes a promising adsorbent from synthesis, through characterization of equilibrium and transport, to process development is missing, which is addressed in this study.

CHAPTER 3

SYNTHESIS, CHARACTERIZATION AND SAMPLE PREPARATION

In this chapter, synthesis, characterization and preparation of Cu-BTC samples are discussed. Several published recipes for the synthesis of Cu-BTC have been discussed in details in section 2.1.1 (Wang et al., 2002; Chowdhury et al., 2009; Lee et al., 2005; Dathe et al., 2005; Schlichte et al., 2004; Chui et al., 1999; Senkovska and Kaskal, 2008), and the key features were summarized in Table 2.1. Synthesis and XRD characterization of Cu-BTC samples carried out in the present study are presented. Sample selection for adsorption and diffusion study and further characterization of the selected sample are also discussed. Basolite® C300, a commercial Cu-BTC sample, has also been characterized and prepared for further analysis with the selected synthesized sample.

3.1 Samples Synthesized in the Present Study

Based on the summary of Cu-BTC synthesis reported in the literature given in Table 2.1, it was decided to study the effect of the following on the synthesized product: (i) mixing of the two solutions containing the two precursors before carrying out the reaction at a constant (high) temperature, (ii) reaction temperature, and (iii) duration of the reaction. Accordingly, five samples were synthesized according to the conditions detailed in Table 3.1. Copper nitrate trihydrate ($Cu(NO_3)_2.3H_2O$) (STREM CHEMICALS) and trimesic acid (Benzene-1,3,5-tricarboxylic) (SIGMA-ALDRICH) were used as the copper and organic linker precursors, respectively. The aqueous solvent used to dissolve copper nitrate trihydrate was

de-ionized water and the organic solvent to dissolve trimesic acid was ethanol. The following general synthesis protocol was followed:

1. A reference amount of copper nitrate trihydrate was accurately measured and dissolved in de-ionized water according to the ratio specified in Table 3.1 for the sample.
2. The next step was to accurately measure the trimesic acid in desired proportion and dissolve in ethanol according to specified ratio for the sample being synthesized.
3. Depending on which sample was being synthesized, the two solutions were either mixed for 15 / 30 min and then transferred to a Teflon-lined autoclave or the two solutions were directly transferred to the autoclave one after another without prior mixing. 50 ml or 100 ml autoclave was used depending on the total solution volume.
4. The Teflon-lined autoclave was put into a Furnace (LENTON THERMAL DESIGNS LTD/ENGLAND) at the desired temperature and duration given in Table 3.1.
5. The light blue supernatant liquid was decanted, and, the blue crystals of Cu-BTC were isolated by filtration, washed with de-ionized water and ethanol, and dried in air at room temperature or in an oven at 383 K.

3.2 Screening of the Synthesis Recipes

The five synthesized samples were numbered S1 to S5. They were systematically screened in order to find the best routine for Cu-BTC synthesis procedure, which are discussed next.

3.2.1 XRD Patterns

When X-rays interact with a crystalline solid phase, a diffraction pattern is obtained. Every crystalline substance gives a unique pattern. The X-ray diffraction pattern of a pure substance

Table 3.1 Summary of the Cu-BTC samples synthesized in this study.

Sample	Copper source (A)	Organic linker source (B)	Solvent for A (C)	Solvent for B (D)	Molar ratio of A/B	Weight ratio of A/B	ml of C/ gm of A	ml of D/ gm of B	Mixing the solutions before heating	T of reaction (K)	Reaction duration (h)	Product drying after filtration
S1	$Cu(NO_3)_2.3H_2O$	Trimesic acid	De-ionized water	ethanol	1.8	2.1	13.7	28.6	No mixing	393	12	Air drying at room temperature
S2	$Cu(NO_3)_2.3H_2O$	Trimesic acid	De-ionized water	ethanol	1.8	2.1	13.7	28.6	15 min	393	12	Air drying at room temperature
S3	$Cu(NO_3)_2.3H_2O$	Trimesic acid	De-ionized water	ethanol	1.8	2.1	13.8	28.6	No mixing	453	12	Air drying at room temperature
S4	$Cu(NO_3)_2.3H_2O$	Trimesic acid	De-ionized water	ethanol	2	2.3	2.2	5.1	30 min	383	18	Air drying overnight at 383 K in the oven
S5	$Cu(NO_3)_2.2.5H_2O$	Trimesic acid	De-ionized water	ethanol	2	2.2	2.3	5.1	30 min	423	18	Air drying overnight at 383 K in the oven

is, therefore, like a fingerprint of the substance. The powder diffraction method is thus ideally suited for characterization and identification of polycrystalline phases.

The main use of powder diffraction is to identify components in a sample by a search/match procedure. Furthermore, the areas under the peak are related to the amount of each phase present in the sample. In powder or polycrystalline diffraction it is important to have a sample with a smooth plane surface. Typically, the sample is ground down to particles of about 0.002 to 0.005 mm cross section. The ideal sample is homogeneous and the crystallites are randomly distributed. The sample is pressed into a sample holder to obtain a smooth flat surface.

A typical diffraction spectrum consists of a plot of reflected intensities versus the detector angle 2θ or θ depending on the goniometer configuration. The 2θ values corresponding to the peaks depend on the wavelength of the anode material of the X-ray tube. The d-spacing is obtained as a function of 2θ from Bragg's law:

$$d-spacing = \frac{n\lambda}{2Sin\theta} \qquad (3-1)$$

where n is an integer number determined by the order of the reflection; λ is the wavelength of X-rays, and moving electrons, protons and neutrons. d represents the spacing between the planes in the atomic lattice, and θ shows the angle between the incident ray and the scattering planes.

X-ray diffraction (XRD) data for the five Cu-BTC samples synthesized in this study and the commercial Basolite® C300 sample were obtained using Cu Kα radiation in the 5-45 degrees 2θ range with a scanning rate of 5 degrees/min using a Shimadzu X-ray diffractometer (model Lab-X600). Cu Kα radiation was bombarded on the dry powder samples to get the

diffraction signals. Cu-BTC samples were very fine powder which helped minimize the effect of preferred orientation on the XRD pattern. The measured XRD results together with representative Cu-BTC XRD signature published in the literature are shown in Figure 3.1 where good agreement is observed with all of them showing distinct peaks at $2\theta = 6.7^{\circ}$, 9.5°, 11.65°, 13.5°, 19.3° and 26°. Some of the synthesized samples contained very small amount of CuO impurity, typically appearing at $2\theta = 35.5$, 38.7°, or Cu_2O impurity, indicated by the small peak at $2\theta = 36.43^{\circ}$.

Sample S1 and S2 were synthesized by the same recipe. However, the organic and inorganic solutions in S2 were thoroughly mixed before reaction for about 15 min until the light blue jelly mixture appeared. The characteristic peaks of Cu-BTC were intact in location with or without pre-mixing of the two solutions, but the peaks at 6.7°, 11.65°, 13.5° and 26° had higher intensities in S1. CuO impurity was also seen in sample S1.

The precursors, solvents and the synthesis conditions except the reaction temperature were the same in S1 and S3. Cu_2O impurity could be seen in S3, which had higher reaction temperature. Similarly, the reaction temperatures in S4 and S5 were different, while the other conditions were practically the same. However, the solvent volume to precursor mass ratios were much higher in S4 and S5 compared to those in S1 and S3. Cu_2O appeared in the XRD pattern of S5, which had the higher reaction temperature, whereas CuO was seen in S4.

The reaction temperatures of S2 and S4 differed by a nominal 10 K. Considering this difference as negligible, the other important differences were duration of reaction and solvent volume to precursor mass ratio. Longer reaction time and high concentration of the

precursors in the reaction mixtures seem to have reduced the intensity of the first distinct peak at 2θ = 6.7° in S4. However, Cu_2O impurity was minimum in this sample.

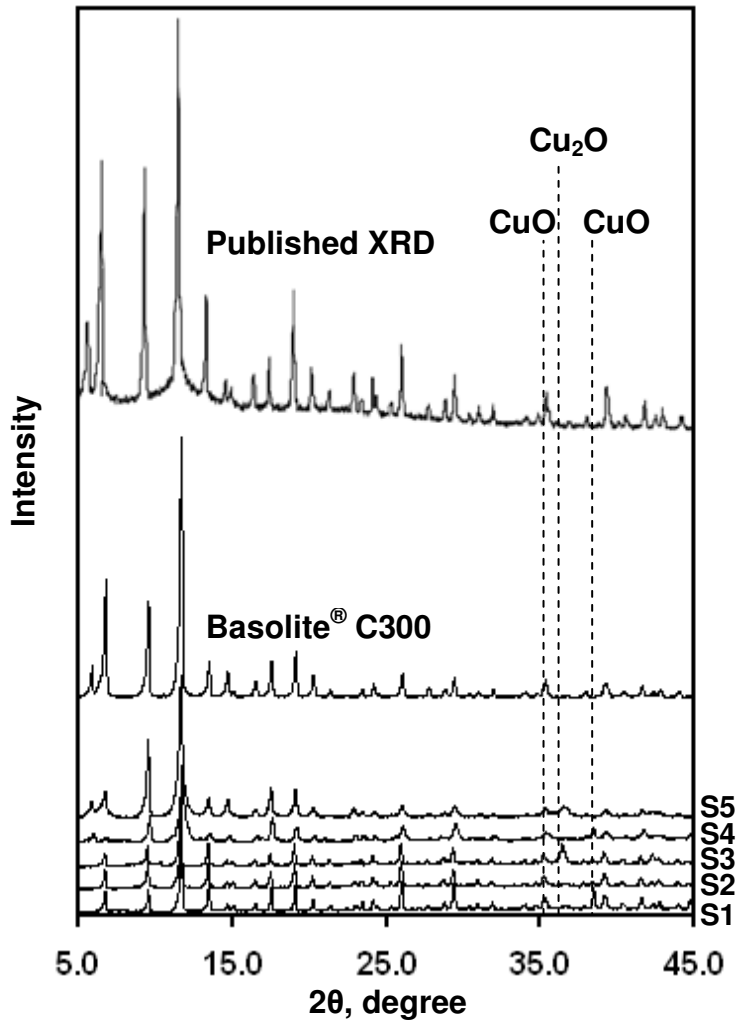

Figure 3.1 XRD patterns for the five synthesized Cu-BTC samples compared with that obtained for the commercial Basolite C300 sample and a representative Cu-BTC XRD pattern reported in the literature (Schlichte et al., 2004).

Modest reaction temperature and duration, and higher dilution of precursors appear to have favored better crystallinity measured by the relatively higher characteristic peak intensities in samples S1 and S2. The somewhat lower peak intensities in S2 over S1 as a result of pre-mixing the two solutions is, however, counter intuitive and not fully understood at this time.

3.2.2 Equilibrium Isotherms Measured on the Synthesized Samples

The XRD results suggest that all the five samples synthesized produced good crystalline materials. Next, equilibrium isotherms of CO_2 were measured in all five synthesized samples to assess which sample (and hence which recipe) would be most suitable for the intended study of adsorption and diffusion of gases in Cu-BTC. Carbon dioxide was chosen since it, due to its strong quadruple moment, is known to have strong isotherms in most MOFs. The constant volume method was used to measure the equilibrium isotherms.

The carbon dioxide isotherms measured on the five synthesized samples at one temperature are shown in Figure 3.2. It is interesting to note that despite confirmation of good crystallinity from the XRD results CO_2 capacities in samples S3 to S5 were much lower. Therefore, samples S1 and S2, based on relatively higher CO_2 capacity, were chosen to conduct further investigation. In order to assess stability and reproducibility, these two samples were subjected to multiple regeneration-adsorption cycling. The results are summarized in Figure 3.3. There was a significant drop in CO_2 adsorption capacity of sample S1 after the fourth regeneration. A possible reason may be structural damage from repeated regeneration at high temperature (423.15 K). On the other hand, sample S2 had somewhat lower CO_2 capacity compared to the initial capacity obtained in S1, but unlike S1 the capacity of S2 remained stable even after 15 cycles of repeat measurements. Therefore, sample S2 was selected to carry out detailed equilibrium and kinetic measurements.

3.3 Further Physical Characterization of Sample S2 and Basolite® C300

Thermo gravimetric analysis (TGA) and scanning electron microscope (SEM) were used for further physical characterization of sample S2 (chosen from the synthesized Cu-BTC samples) and the commercial Cu-BTC sample, Basolite® C300.

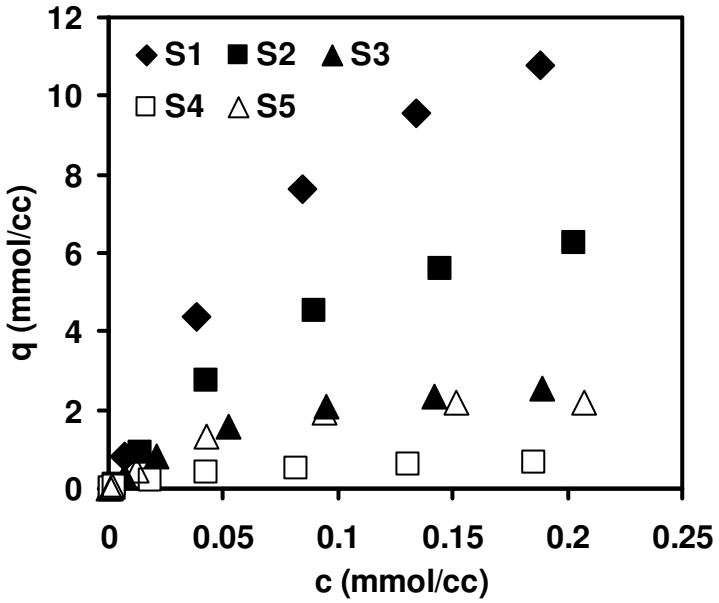

Figure 3.2 CO_2 isotherms on S1, S2, S3, S4 and S5 at 296.15 K.

3.3.1 Thermo Gravimetric Analysis

Thermo gravimetric Analysis (TGA) is a type of testing that is performed on samples to determine changes in weight in relation to change in temperature. A derivative weight loss curve can be used to tell the point at which weight loss is most apparent.

The results from TGA (Shimadzu, model DTG-60 AH), carried out at atmospheric pressure under helium flow from room temperature to 400°C, are shown in Figure 3.4. The weight loss patterns for the two samples were very similar. 40% weight loss up to 100°C gave a measure of water content in the fully hydrated Cu-BTC crystals. Both the samples were stable up to 300°C.

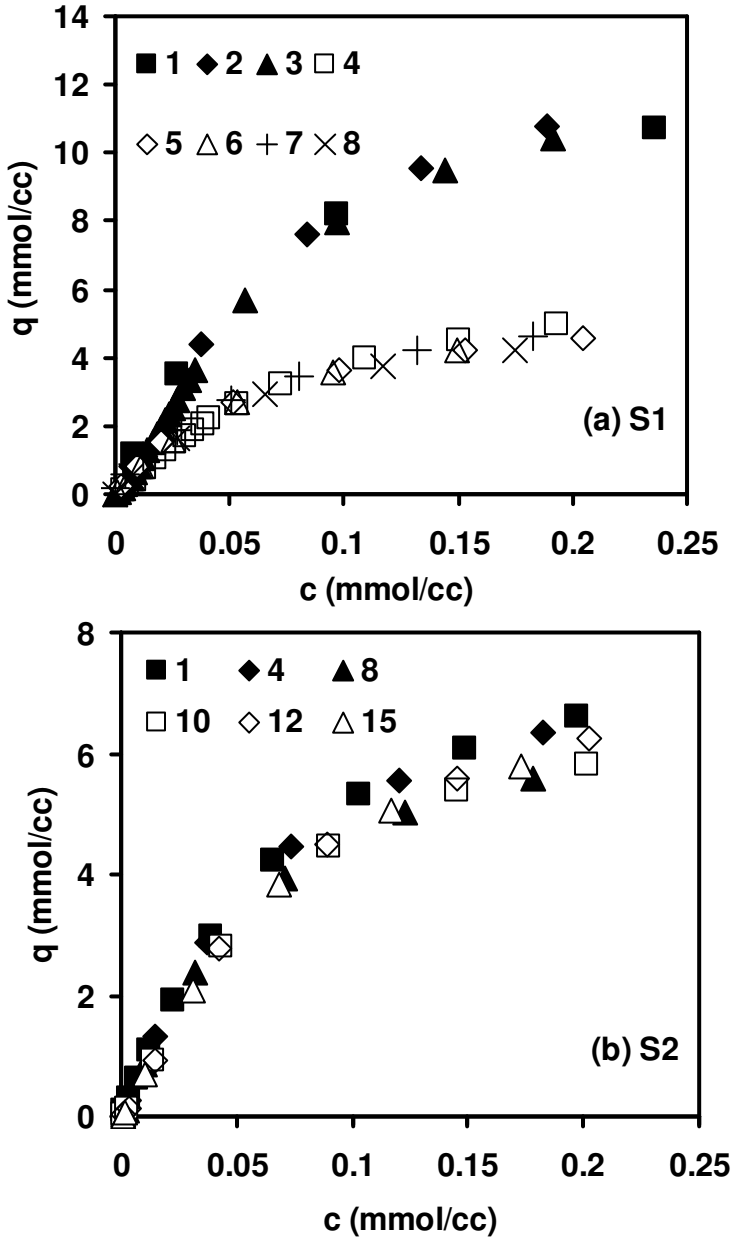

Figure 3.3 Repeat CO_2 isotherms measured on S1 and S2 Cu-BTC samples at 296.15 K.

3.3.2 Scanning Electron Microscope

In a Scanning Electron Microscope (SEM), high energy beam of electrons in a raster scan pattern is used to scan the sample surface. The electrons interact with the surface atoms which contain some information about the topography, electrical conductivity and other properties of sample surface.

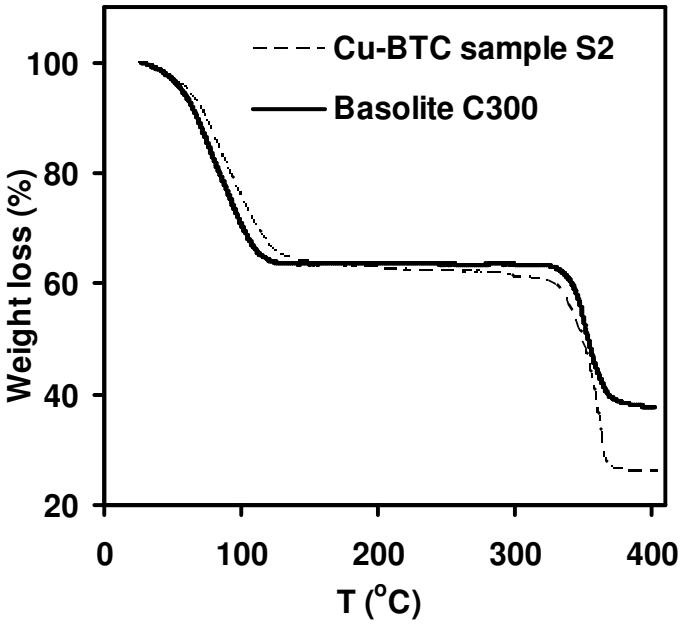

Figure 3.4 TGA results compared for the synthesized Cu-BTC sample S2 and Basolite® C300.

The crystal morphologies of the two samples obtained from SEM (JEOL, model 5600LV) study are shown in Figure 3.5. The octahedral shape of sample S2 crystals is clearly seen in the figure. The crystals of Basolite® C300 were less clearly defined and were also somewhat smaller in size compared to the sample S2 crystals. There is a good agreement between the XRD pattern of S2 and its polycrystalline shape seen in the SEM picture. The morphology of the synthesized Cu-BTC is consistent with other SEM images published for this material (Wang et al., 2002; Chowdhury et al., 2009; Dathe et al., 2005). The SEM images in Figure 3.5 also suggest less impurity in the synthesized material compared to the commercial material.

3.4 Adsorbent Preparation and Pellet Density Measurement

The dried Cu-BTC samples had to be prepared before conducting any adsorption-desorption experiment. The synthesized adsorbent powder was pelletized in a pellet die set (1.3 cm in diameter) using a hydraulic pelletizer (Carvier, model 3912) under a load of 8.5 metric tons. The pellets were then cut into small pieces. In mass transfer rate calculations, the cut pellets

were approximated as equivalent spheres of same area to volume ratio. The equivalent radius obtained was 0.147 cm.

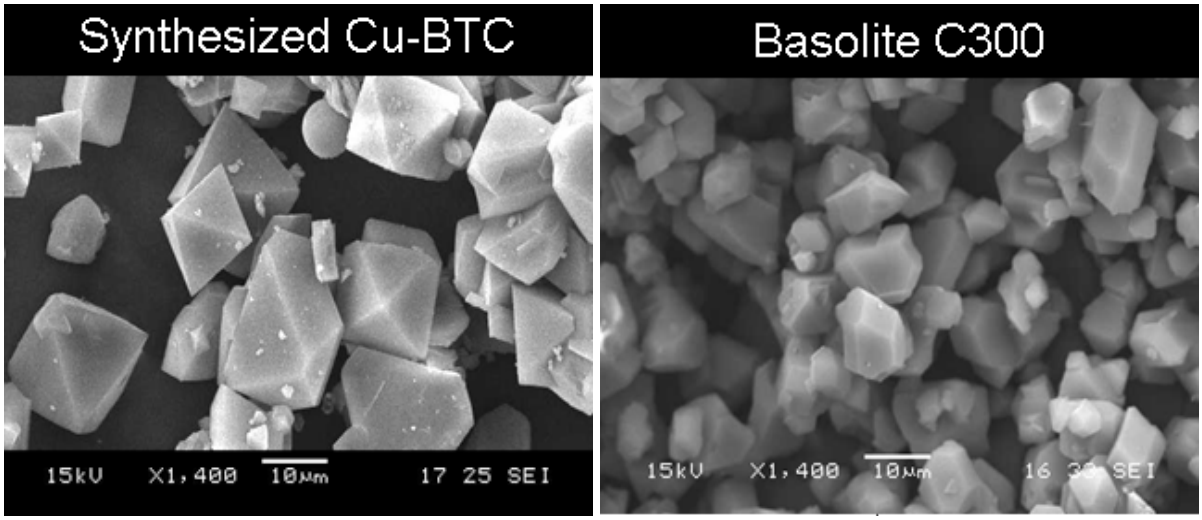

Figure 3.5 SEM images of synthesized Cu-BTC and Basolite® C300.

For conducting the equilibrium and kinetic calculations, we need to know the volume of adsorbent loaded in the test chamber of the constant volume apparatus. Therefore, the pellet density of the Cu-BTC sample chosen for the present study must be known. To carry our pellet density measurement, a pellet with known dimensions was prepared and, then, it was regenerated in a small cylinder placed in a small heater block and heated to 423 K (150°C) overnight under vacuum. The same regeneration condition was applied before starting any series of measurements. The pellet weight was measured immediately after bringing it out from the small cylinder to prevent any moisture adsorption. The same weight measurements were also conducted in a magnetic suspension balance after in situ regeneration and the same results were obtained.

The pellet densities of Cu-BTC and Basolite® C300, calculated according to the following equation, were 1.00 g cm^{-3} and 1.26 g cm^{-3} respectively.

$$\rho_p = \frac{Wt_p}{V_p}$$

$$(3-2)$$

Wt_p represents the pellet weight after regeneration and V_p represents the measured pellet volume.

3.5 Heat Effect on Physical Characteristics of Sample S2 and Basolite® C300

In order to investigate the thermal stability of the crystal structure upon heating, the hot plate XRD (Bruker-AXS Smart Apex CCD single-crystal diffractometers) was used. Absence of main peaks or presence of new peaks in XRD pattern can show the crystal instability of the sample. In addition, change in peak intensities and positions are indicators of change in chemical composition of the substance or structural inversion from crystal to amorphous. The hot plate XRD patterns of Basolite® C300 at different temperatures are shown in Figure 3.6.

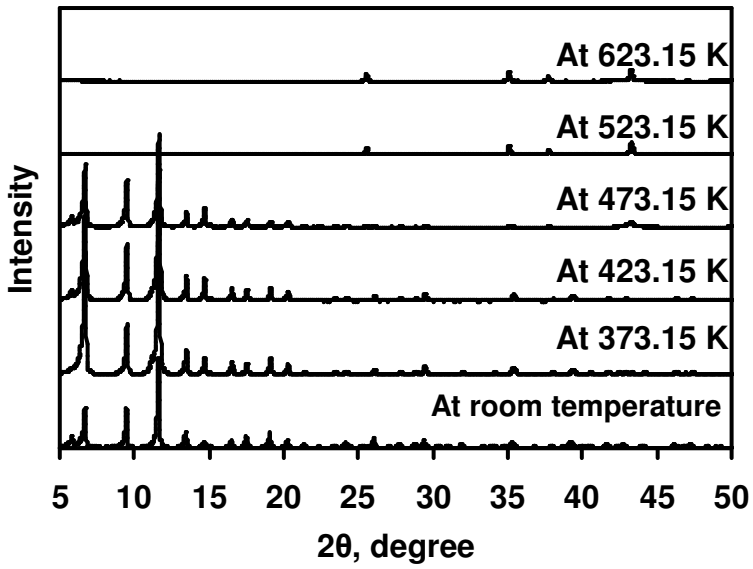

Figure 3.6 XRD pattern of heated Basolite® C300 using hot plate XRD device.

As can be clearly seen from this figure, the indicative peaks intensities of the crystal framework decreased at temperatures higher than 423.15 K and completely disappeared at

523.15 K. At this temperature, some new peaks were seen in the XRD pattern, which could be because of formation of new species or impurities in the crystal framework as a result of heat treatment.

As shown in Figure 3.4, after the first drop because of moisture evaporation, both synthesized Cu-BTC sample (S2) and Basolite® C300 had roughly stable weight until 300ºC. The two samples were heated at this temperature for 2 hours in presence of He and, the XRD patterns of the heated samples are shown in Figure 3.7. The main peaks in Basolite® C300 XRD pattern completely disappeared at this temperature while the main peaks of S2 sample were still intact. This can be due to the higher structural stability of the synthesized Cu-BTC sample at 573.15 K (300ºC) compared with the commercial Basolite® C300.

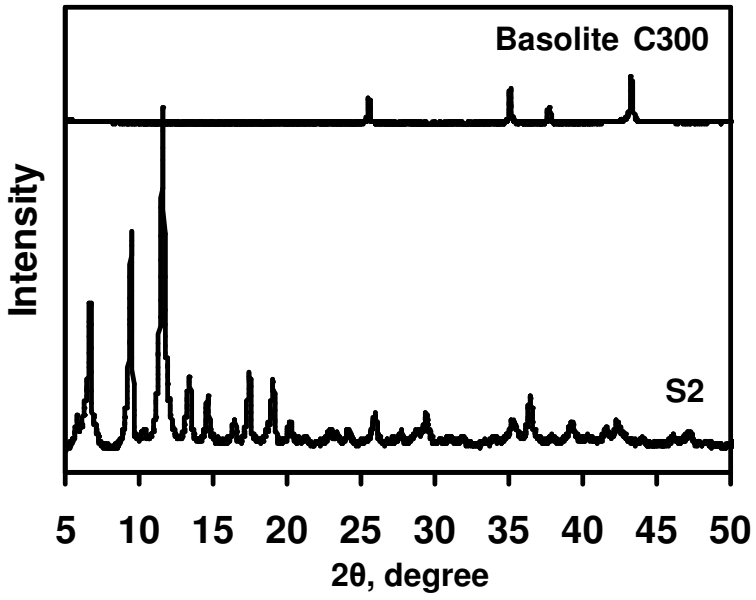

Figure 3.7 XRD pattern of sample S2 and Basolite® C300 after heating at 573.15 K (300ºC).

3.6 Finding the Best Adsorbent Regeneration Condition

The approximate temperature for effective regeneration of the adsorbent samples was determined by regenerating at several temperatures in the range 398-523 K, with increment of

10 to 20 K. An adsorbent sample was first placed in the test chamber of the constant volume apparatus and then subjected to alternate helium flushing and evacuation at least three times. Next, the sample was heated overnight at a temperature in the mentioned range under vacuum. The sample was then cooled to 296.15 (±0.5) K and CO_2 isotherm was measured over a wide pressure range. The entire procedure was repeated at other regeneration temperatures. The capacity peaked at 423.15 K and then decreased with further increase in the regeneration temperature. Representative CO_2 isotherms on a sample regenerated at three different temperatures are shown in Figure 3.8.

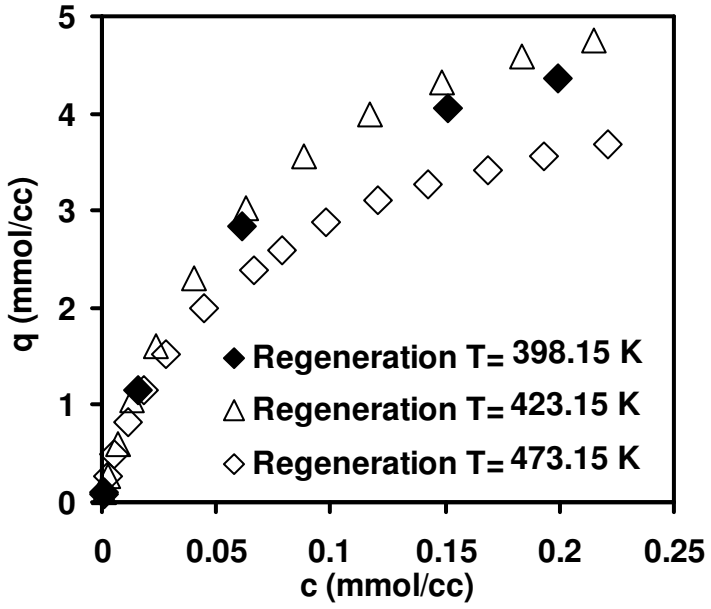

Figure 3.8 CO_2 adsorption capacity of Basolite® C300 samples regenerated at 398.15 K (125°C), 423.15 K (150°C) and 473.15 K (200°C).

According to the Figure 3.9, the crystalline blue color of the samples faded and ultimately turned black when regenerated at temperatures beyond 423.15 K. This observation is particularly interesting since the onset of second weight change in TGA (see Figure 3.4) was > 573.15 K (300°C). However, the XRD results obtained by heating in-situ at different temperatures, shown in Figure 3.6, confirm that the change in color from heating beyond 423.15 K was indeed accompanied by diminishing intensity of some of the characteristic

peaks, and therefore decreasing crystallinity, which explain the drop in the measured isotherms. Based on these observations, 423.15 K (150°C) was chosen as the adsorbent regeneration temperature in this study.

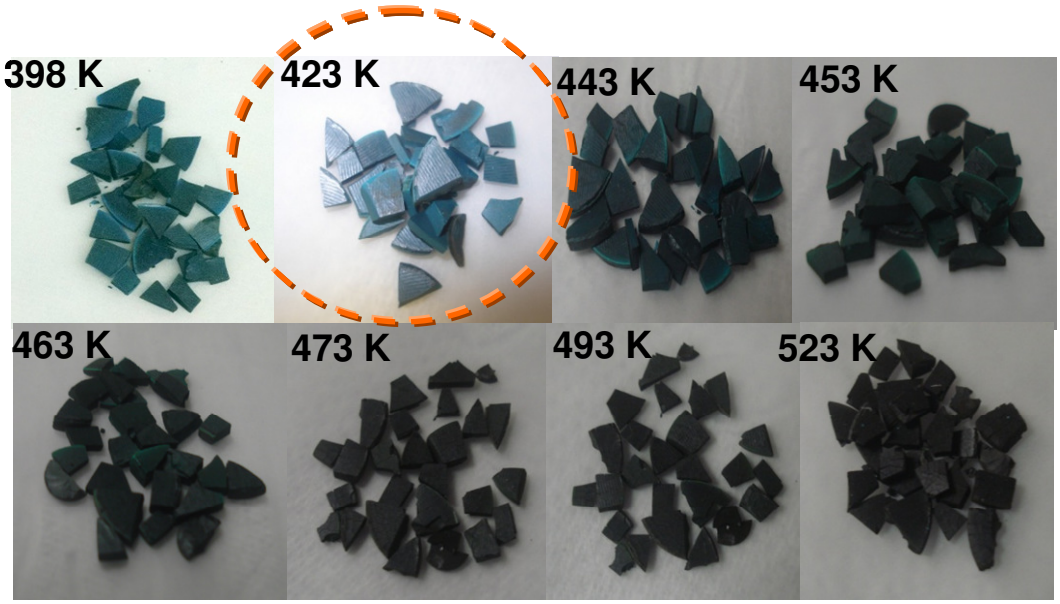

Figure 3.9 Basolite® C300 sample regenerated at different temperatures.

3.7 Chapter Summary

Five Cu-BTC samples were successfully synthesized using the same precursors at different conditions. The samples were screened by subjecting to repeated adsorption-desorption cycles of CO_2 isotherm measurement. Pre-mixing of the solutions containing the precursors, modest reaction temperature and duration, and higher dilution of the precursors gave the most stable sample S2, which survived the screening test. The optimum regeneration temperature was determined to be 423.15 K (150°C) for both in-house and Basolite® C300 samples.

CHAPTER 4

ADSORPTION EQUILIBRIUM STUDIES

A systematic protocol for finding out the best conditions for synthesis of Cu-BTC was outlined in chapter 3. In addition, physical characteristics of in-house Cu-BTC sample and commercial Basolite® C300 were reported in the same chapter. In this chapter, detailed measurements of single component equilibrium isotherms for carbon dioxide, methane and nitrogen on the synthesized Cu-BTC sample and Basolite® C300 up to about 6 bar pressure at four temperatures ranging from 282.15 K (9 °C) to 333.15 K (60 °C) are presented. Moreover, adsorbent homogeneity will be examined using isosteric heat of adsorption calculation. Gas equilibrium selectivity of both adsorbents for clean energy related applications will also be compared with some reported values at the end of this chapter.

4.1 Adsorption Equilibrium Experiments

For carrying out the isotherm experiments, the adsorbent particles were prepared, and the experimental apparatus was designed and calibrated. Adsorbent preparation, constant volume device calibration, experimental data processing and experimental isotherm data will be discussed in following sections.

4.1.1 Adsorbent Preparation

Sample S2 and Basolite® C300 were chosen for detailed equilibrium measurements in this study. These samples were in powder form and were not suitable for volumetric adsorption studies. Therefore, as we discussed in section 3.5, the powder samples had to be prepared before conducting any adsorption-desorption experiment. The powder was pelletized in a pellet die set (1.3 cm in diameter) using a hydraulic pelletizer (Carvier, model 3912) under a

load of 8.5 metric tons. Each pellet was then cut into four smaller pieces. In mass transfer rate calculations (which will be discussed in chapter 5), the cut pellets were approximated as equivalent spheres of same area to volume ratio. The equivalent radius obtained was 0.147 cm in this study The hydraulic pelletizer used and preparation of Cu-BTC particles are shown in Figures 4.1 (a) and 4.1 (b), respectively.

4.1.2 Constant Volume Method

The constant volume method has been extensively used in our laboratory for equilibrium isotherm measurement, and measurement of relatively slow micropore controlled uptake (Marathe et al., 2004). It is a simple and inexpensive method, which allows easy measurements over a wide pressure and temperature range. Experimental data processing is also straightforward using this method. Other common methods for similar measurements are gravimetric method, chromatographic method and differential adsorption bed (DAB) method. The DAB method is very tedious but gives very reliable mixture equilibrium data.

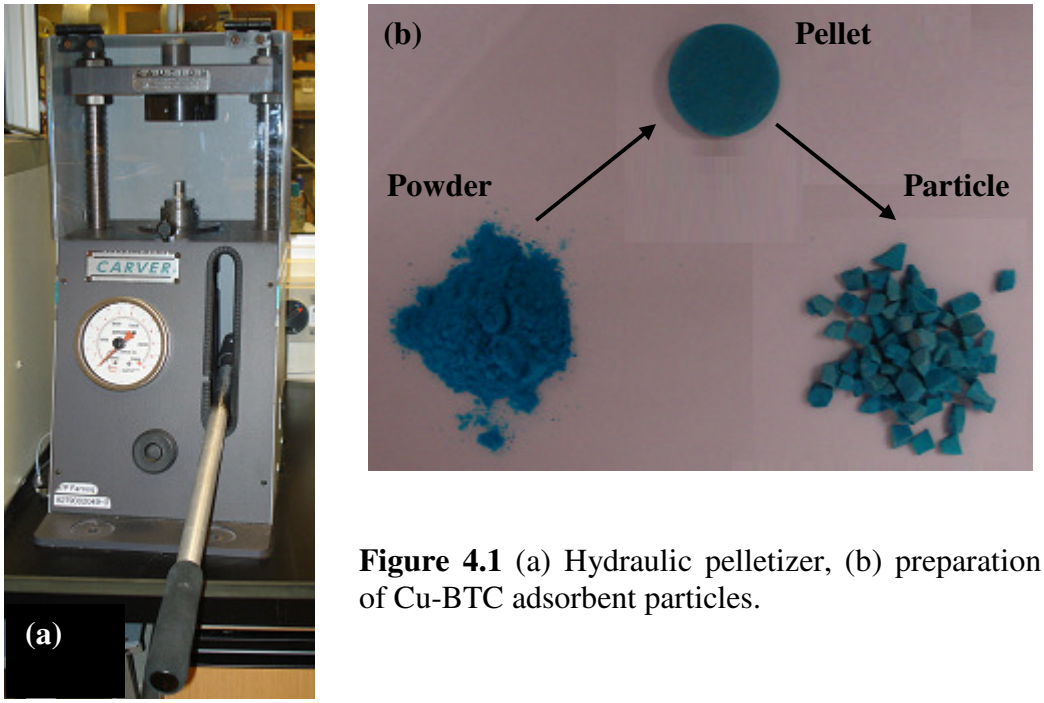

Figure 4.1 (a) Hydraulic pelletizer, (b) preparation of Cu-BTC adsorbent particles.

In this study, the constant volume apparatus was redesigned to further reduce the dead volume (compared to the previous versions used in this laboratory) in order to operate with only a few grams of an adsorbent sample. The set-up was constructed in the workshop of the Chemical and Biomolecular Engineering Department at NUS. A schematic diagram of the set-up is shown in Figure 4.2. In the description that follows, various components of the constant volume apparatus are identified with numbers used in Figure 4.2.

The constant volume apparatus basically consisted of two cylindrical chambers, called test and dose chambers, connected by an on/off solenoid valve (CKD; Model AB42-02-2) controlled with a DC power supply (Topward; Model 3303D).

An absolute pressure transducer (Endress+Hauser; model PMP131-A2201R4S, 0-5 bar gauge) was connected to the dose side to measure the initial and final system pressures, which were needed to carry out the mass balance and calculate the equilibrium adsorbed amount. The absolute pressure transducer (2) was connected to a voltmeter (HEWLETT PACKARD; Model 34401A) to read the voltage. In addition to this absolute pressure transducer, two differential pressure transmitters (VALIDYNE; Model P55D), (5) and (9), were installed on the dose and the test sides with the reference ports connected to the reference cylinder. The differential pressure transducers were necessary to track the change in pressure on the two sides of the solenoid valve until the system reached new equilibrium following the introduction of a known pressure step. This arrangement is necessary to measure both equilibrium and uptake in the same experimental run. However, uptake measurements could not be implemented using constant volume apparatus in this study because of the fast uptake rate of gases in Cu-BTC.

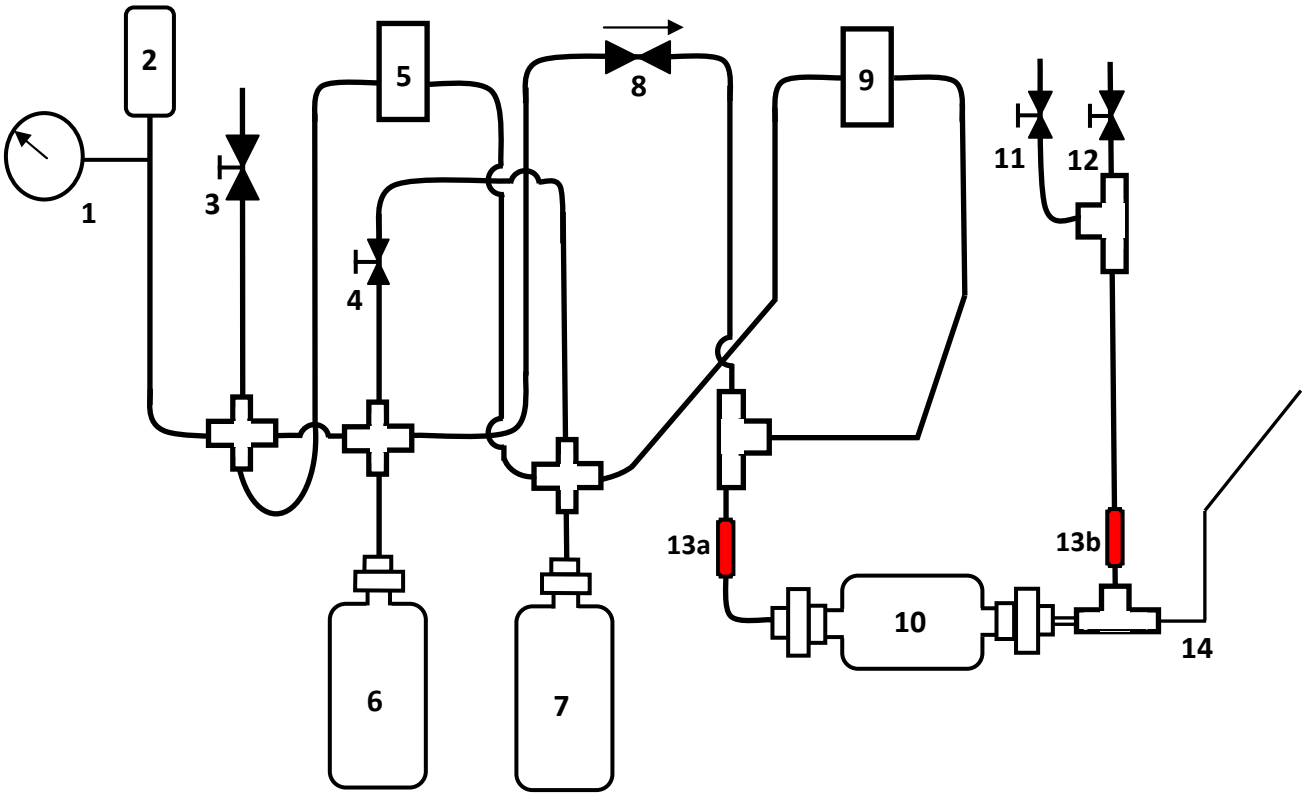

(1) Pressure gauge
(2) Absolute pressure transducer (APT)
(3) Inlet valve
(4) The valve separating dose and reference side
(5) Differential pressure transducer (DPT)
(6) Dose cylinder
(7) Reference cylinder
(8) Solenoid valve
(9) Differential pressure transducer (DPT)
(10) Test cylinder
(11) Gas release valve
(12) The valve connecting to the vacuum pump
(13a, 13b) Quick fit
(14) Thermocouple

Figure 4.2. Schematic diagram of the constant volume apparatus.

The experimental temperature was measured with a thermocouple inside the test chamber. In order to control the experimental temperature, the whole system (excluding the transducers and solenoid valve) was immersed in a water bath during the experiment. The water bath temperature was controlled by a heavy-duty digital temperature controller (Lauda; Model RK 8 KS). A picture of the constant volume setup in our laboratory is shown in Figure 4.3.

4.1.2.1 System Volume Measurement

The calculation of equilibrium data from constant volume experiments depends on the system volume. Therefore, the volumes of different main parts of the constant volume apparatus including the associated tubing were carefully measured using a bubble flow meter (see Figure 4.4).

Each part of the experimental setup namely dose, reference and test side was separated from the other parts for measuring its volume. As it was shown in Figure 4.2, the dose and test sides were separated from each other by means of the solenoid valve (number 8). Moreover, the dose and reference sides were separated by valve number 4. The black plastic bulb which is in the bottom part of the calibrated tube (volumetrically graded) was filled with the soap water solution. The does/test/reference side was firstly pressurized by an inert gas (N_2 or He). Then, the gas was gradually released from the setup into the bottom part of the calibrated tube via the plastic pipe. The soap bubbles were created once the gas entered the calibrated tube. The initial pressure of the setup was recorded when specific bubble was passing the zero point (0cc) indicated on the calibrated tube. Some amount of gas from the setup was slowly introduced to the calibrated tube up to a level that the indicator bubble reached to 100cc. The final pressure of the setup was also recorded. The number of gas moles inside the setup could be calculated based on the setup pressure and temperature (Equation (4-1)). In addition, the number of moles released from the setup into the calibrated column at atmospheric pressure and temperature could also been calculated according to the Equation (4-2).

$$n_i = \frac{P_i V}{R_g T_i} \quad \& \quad n_f = \frac{P_f V}{R_g T_f} \tag{4-1}$$

$$\Delta n = \frac{P_{atm} \Delta V}{R_g T_{atm}} \qquad (\Delta V = V_2 - V_1 = 100 - 0 = 100\,\text{cc}) \tag{4-2}$$

According to the above equations, the setup volume (each part) can be calculated based on the below equation:

$$n_i = \frac{P_i V}{R_g T_i} \quad \& \quad n_f = \frac{P_f V}{R_g T_f}$$

$$\Delta n = (n_i - n_f) \xrightarrow{T_i = T_f = T} \frac{P_{atm}\,\Delta V}{R_g T_{atm}} = \frac{(P_i - P_f)V}{R_g T} \Rightarrow V = \frac{T\,P_{atm}\,\Delta V}{(P_i - P_f)\,T_{atm}} \qquad (4-3)$$

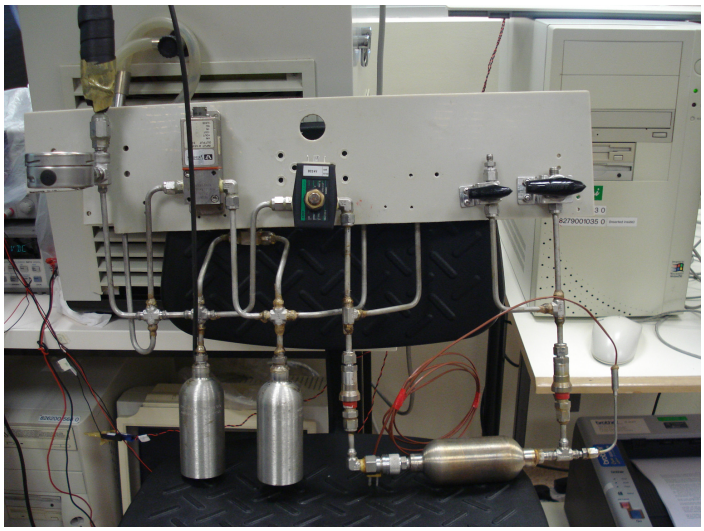

Figure 4.3 The picture of the constant volume apparatus used in this study.

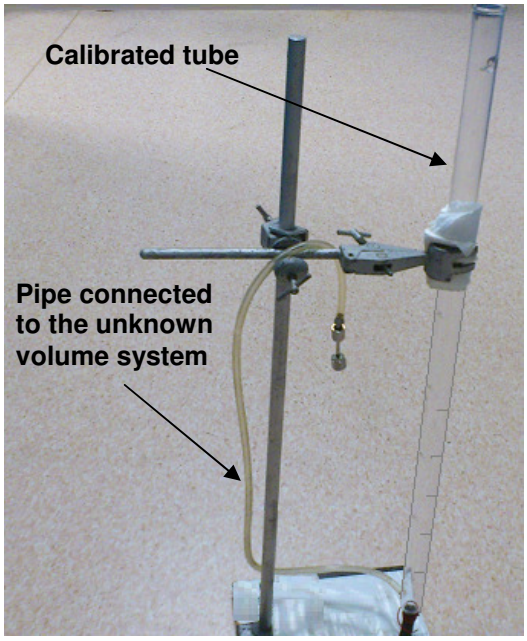

Figure 4.4 The picture of the bubble flow meter used to test and dose side volumes of the constant volume apparatus.

The volumes of dose, test and reference sides were found to be 177.9 cc, 166.6 cc and 164.2 cc, respectively. The volume measurements were conducted at least ten times to improve accuracy.

4.1.2.2 Pressure Transducer Calibration

Both types of transducers were calibrated using a digital pressure calibrator (Fluke, Model 700P07). The calibration procedure was implemented in the following way. The pressure calibrator was connected to the exit line of valve (3) for calibrating the absolute pressure transducer (2), while valves (3) and (12) were closed. Around 0.03 bar gas was introduced to the system by slightly opening of valve (3) which was connected to the helium cylinder. The absolute pressure of the system and the corresponding voltage were recorded by means of the pressure calibrator and volt meter, respectively. Step changes were introduced to the system up to 6 bar in increments of 0.03-0.05 bar. Finally, a calibration curve was found for pressure data versus voltage data. The calibration curves for pressure below atmosphere and above atmosphere are given in Table 4.1.

Table 4.1. Calibration curves for pressure transducers.

P (bar)	Calibration curve (APT no. 2)	
0-1	$P = 1.191V^{*} - 0.136$	
1-6	$P = 1.201V - 0.152$	
0-6	$P = 1.198V - 0.142$	
ΔP *(bar)*	Calibration curve (DPT no. 5)	Calibration curve (DPT no. 9)
0-0.58	$\Delta P = 0.1023\,\Delta V + 0.0007$	$\Delta P = 0.106\,\Delta V + 0.0014$

* Voltage unit: *volts (v)*

For calibration of the differential pressure transducers, the whole system was first pressurized up to a certain pressure (2.5 bar). Then, the reference side was separated from the other parts

of the setup by closing the valve (4) shown in Figure 4.2. Pressure steps in increments of 0.01 to 0.05 bar were gradually introduced to the system until the pressure deference between the reference and dose/test side reached 0.6 bar. Differential voltages of dose side and test side were captured simultaneously using a data acquisition card connected to the computer using LabVIEW program. Finally, the best fitted lines of differential pressure versus differential voltage of dose and test sides were found.

4.1.2.3 Experimental Procedure for Equilibrium Measurement

Before starting any experiment, we should be certain that the whole system is leak proof. For this purpose, the setup (without adsorbent) was pressurized with helium up to 5 bar and immersed in the water bath. The temperature of the water bath was set near to the ambient temperature. There was no change of the pressure reading even after 24 h, which confirmed that the leak was indeed negligible. In fact, such a long test is not necessary for systems and conditions where equilibrium is very quickly attained.

The adsorbent was prepared before putting in the test chamber as explained in section 4.1.1. About 3-5 g of a Cu-BTC sample was used. The sample was first regenerated externally and weighted before introducing in the test chamber. After introducing the known amount of adsorbent sample in the test chamber, it was regenerated at 423.15 K (150 °C) under vacuum. After regeneration of a particular sample placed on the test side, the valve (12) connecting the cylinders to the vacuum pump, discharging to a fume hood, was closed, and the system was brought to the desired experimental temperature using the constant-temperature bath. The setup was usually kept in the water bath for about 2 hours before starting any measurement to ensure that the desired temperature was uniformly attained in all parts of the system as well as by the adsorbent particles inside the test chamber. A steady voltage output from the

absolute pressure transducer was taken as the measure of thermal equilibrium. The system pressure and temperature were noted, and the solenoid valve was closed to separate the test side from the dose side. A known amount of adsorbate gas was then added to the dose side through the inlet valve (3), and some time was allowed for the gas to attain the system temperature. Let this new pressure of the dose side be denoted by $P_d^{0+}(j)$ when the temperature stabilized to T_s. The solenoid valve (8) was de-energized to open and left in that position to allow the pressures on the dose and test sides to be equalized, and the system to reach new equilibrium. For equilibrium measurements, the step size was limited by the desired frequency of data points in the experimental pressure range of the isotherm. Hence, the step size was limited to 0.05-1 bar when the target was only to obtain equilibrium data points.

4.1.2.4 Processing of Equilibrium Data

The ideal gas law is assumed to be valid in the experimental pressure range. The mass balance applicable for the *j*th equilibrium step is given by:

$$\left(P_d^{\,0+}(j)-P_d^{\,\infty}(j)\right)\frac{V_d}{R_g T_s}=\left(P_u^{\,\infty}(j)-P_u^{\,\infty}(j-1)\right)\frac{(V_u-V_a)}{R_g T_s}+\Delta n(j) \qquad (4-4)$$

$$\Delta n(j)=n(j)-n(j-1) \qquad (4-5)$$

V_d , V_u and V_a indicate dose side, test side and adsorbent volume respectively. j = 1, 2, 3, … shows the step number, $\Delta n(j)$ represents the number of moles adsorbed in j^{th} step and $n(j)$ is the total number of moles adsorbed by the adsorbent particles up to the j^{th} step. *d, u, a* and ∞ represent dose side, test side, adsorbent and equilibrium condition respectively.

$P_d^{+0}(j)$ is the dose side absolute pressure just before opening the solenoid valve. $P_d^{\infty}(j)$ is the dose side absolute pressure when equilibrium is reached at the end of stage j and pressure on the dose and test sides become equal $\left(P_d^{\infty}(j) = P_u^{\infty}(j) = P^{\infty}(j)\right)$. V_a gives the external particle volume of the adsorbent, which is calculated from the initial adsorbent mass (after regeneration) and density of adsorbent particles density. q_p is the capacity of the adsorbent particles in the solid phase corresponding to the gas pressure at equilibrium and it is calculated from Equation (4-6).

$$q_p = \frac{n(j)}{V_a} \qquad (4-6)$$

All isotherms measured are presented as q_p vs. c in this thesis. c is the gas phase adsorbate concentration at the equilibrium pressure, which is obtained by Equation (4-7).

$$c = \frac{P^{\infty}(j)}{R_g T_s} \qquad (4-7)$$

4.1.3 Adsorption Equilibrium Isotherms

Single component isotherms of carbon dioxide, methane and nitrogen on synthesized Cu-BTC and Basolite® C300 were measured at four different temperatures (282.15 K, 296.15, 313.15 and 333.15 K) over a pressure range from 0 to 6 bar. The data were analyzed according to the procedure mentioned in section 4.1.2.4. The isotherm experimental data details are presented in Appendix 1 of this study.

Representative adsorption isotherms for carbon dioxide, methane and nitrogen on Cu-BTC sample S2 and Basolite® C300 in the temperature range 282.15 K to 333.15 K are shown in Figure 4.5. In the pressure range covered in this study, carbon dioxide had the highest

adsorption capacity followed by methane and nitrogen. All the three gases are polarizable. In addition, CO_2 and N_2 have quadruple moments, but CH_4 is nonpolar. The polarizability and quadruple moment values for these gases are given in Table 4.2. Strong adsorption of CO_2 most likely results from its strong interactions with the Cu-BTC framework due to both polazalibility and quadruple moment effects. In the adsorption of CH_4 and N_2, it seems that the quadruple moment of N_2 is less dominant than the higher polarizability of CH_4. Although the polarizability of CO_2 is comparable with that of CH_4, the appreciable quadrupole moment of the former appears to have contributed to its higher heat of adsorption (heat of adsorption will be discussed is section 4.3). As can be seen from Figure 4.5, sample S2 has higher capacity than Basolite® C300 for all measured gases.

Table 4.2 Polarizability and quadropole moment of CO_2, CH_4 and N_2 (Sircar, 2006).

Gas	Polarizability (cm^3) ($*10^{25}$)	Quadropole moment ($esu.cm^2$) ($*10^{26}$)
CO_2	26.5	4.3
CH_4	26.0	0
N_2	17.6	1.52

4.2 Modeling of Adsorption Equilibrium

Adsorption equilibrium data is the most important piece of information in understanding an adsorption process. Experimental data have been explained by many equilibrium isotherm models proposed over the years. These models are discussed in details by Do (1998). Langmuir isotherm was used to analyze the single component experimental equilibrium data measured in this study and the results are presented in the following sections.

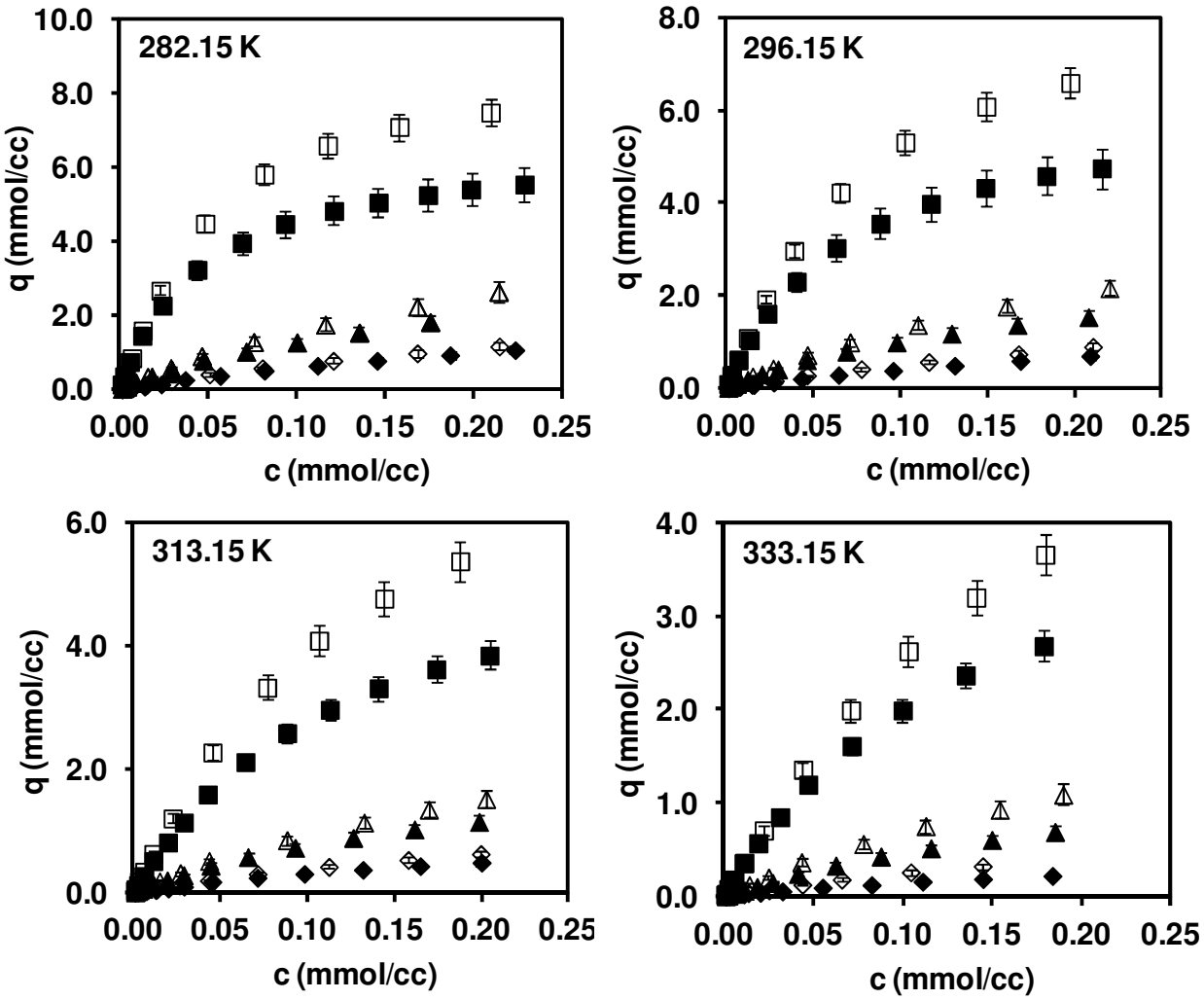

Figure 4.5. Experimental equilibrium data of CO_2 (□, ■), CH_4 (△, ▲) and N_2 (◇, ◆) on synthesized Cu-BTC sample S2 (open symbols) and Basolite® C300 (filled symbols).

4.2.1 Langmuir Isotherm

The most basic theory in adsorption is Langmuir theory (1918), which is widely used due to its mathematical simplicity, thermodynamic consistency and its ability to fit isotherm data for a wide variety of systems. Langmuir model is based on the following assumptions:

1) Monolayer adsorption.
2) Adsorbent surface has a fixed number of well-defined localized adsorption sites.
3) Each site can hold only one adsorbate molecule.
4) The adsorbent surface is energetically homogeneous.
5) There is no adsorbate-adsorbate interaction.

The Langmuir isotherm has the following form:

$$\frac{q_p}{q_s} = \frac{bc}{1+bc} \tag{4-8}$$

$$b\,q_s = K \tag{4-9}$$

$$b = b_0 \exp\left(\frac{-\Delta U}{R_g T}\right) \tag{4-10}$$

In the above equations, K is the dimensionless Henry's constant, q_s (mmol/cc) is temperature independent saturation capacity for each adsorbate in the solid phase and b (cc/mmol) is the Langmuir constant which depends on temperature according to Equation (4-10). b_0 represents the pre-exponential factor in the Arrhenius type temperature dependence of b. ΔU (kJ/mol) is the internal energy change due to adsorption. The Langmuir isotherm parameters, b_0, ΔU and q_s are obtained by simultaneous nonlinear regression of experimental isotherm data measured at different temperatures.

The Langmuir isotherm fits are shown in Figure 4.6 and, corresponding parameters have been compiled in Table 4.3. These parameters were obtained separately for each gas by simultaneous nonlinear regression of data at all temperatures subjected to the constraint of a temperature independent monolayer saturation capacity, q_s. R^2, the regression residual is normally used as a quantitative measure of how good is the fit ($R^2 = \left[q_{theoretical} - q_{experimental}\right]^2$).

The extended Langmuir isotherm model, given by Equation (4-11), can be used for modeling of multi-component systems using single component parameters in Table 4.3. However, the extended Langmuir model is thermodynamically consistent only when all the species have the same q_s value. .

$$\frac{q_A}{q_s} = \frac{(bc)_A}{1+\sum_{i=A}^{Z}(bc)_i} \qquad (4-11)$$

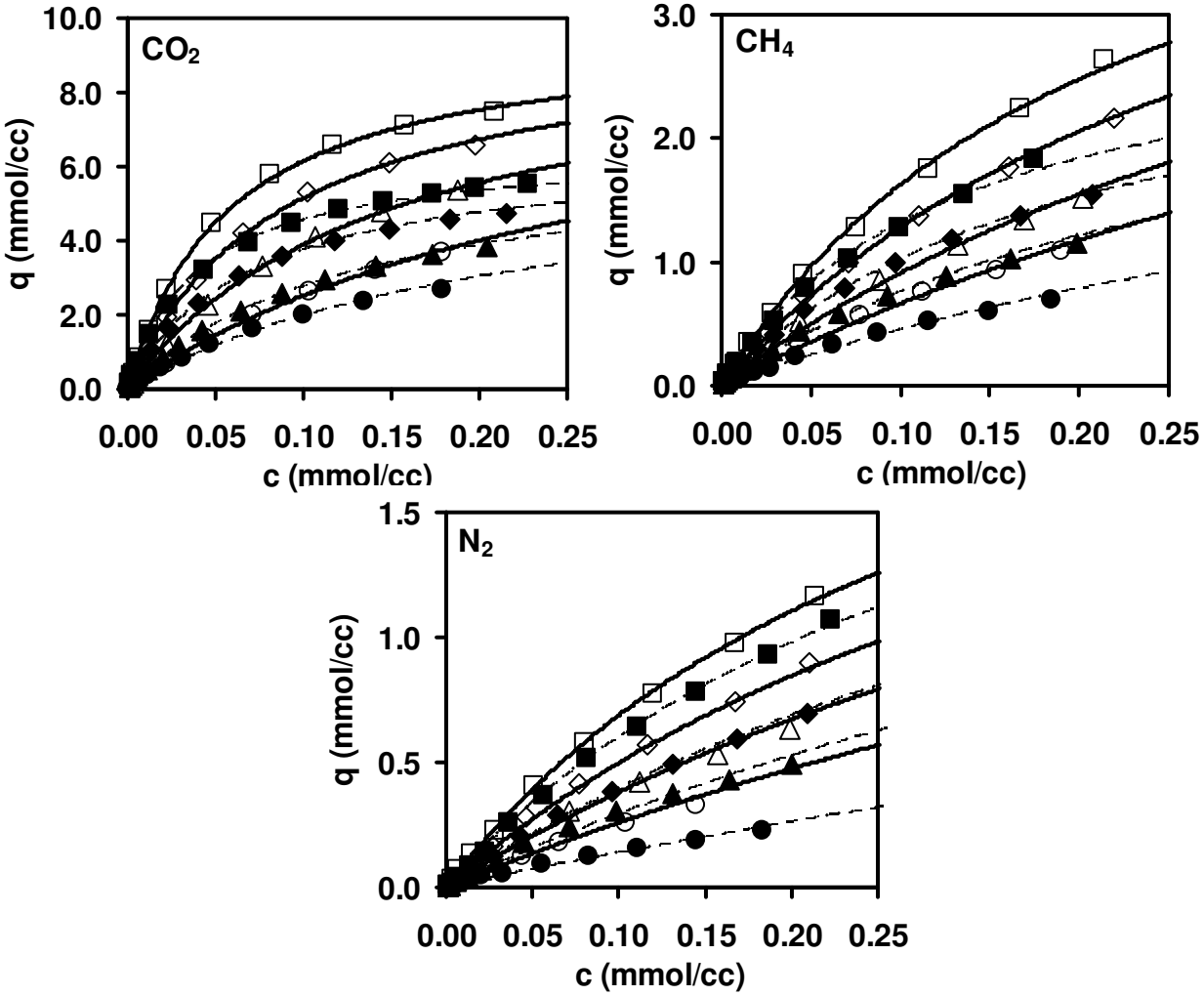

Figure 4.6. Experimental equilibrium data of CO_2, CH_4 and N_2 on synthesized Cu-BTC sample S2 (open symbols) and Basolite® C300 (filled symbols) and their Langmuir model fits. The Langmuir fits are shown with solid lines for sample S2 and broken lines for Basolite® C300. Squares, lozenges, triangles and circles represent temperatures of 282.15 K, 296.15 K, 313.15 K and 333.15 K, respectively.

Ideal adsorbed solution theory (Myer and Prausnitz, 1965; Sircar, 1995) is often used for mixture calculation in systems where the components have significantly different saturation capacities. However, it requires iterative solution of implicit equations, which adds significantly to the computational burden in process simulations. Computationally, there is no problem in using component specific q_s values in mixture calculations using extended

Langmuir isotherms, which has been adopted in the published literature with good quantitative success (Bai and Yang, 2001 & 2002).

Table 4.3. Langmuir isotherm parameters for adsorption of gases on Cu-BTC.

Synthesized sample S2				
Adsorbate gas	$q_s\left(\frac{mmol}{cc}\right)$	$b_0\left(\frac{cc}{mmol}\right)$	$-\Delta U\left(\frac{kJ}{mol}\right)$	R^2
CO_2	9.7	5.2e-4	24.5	0.170
CH_4	5.2	2.4e-3	17.7	0.020
N_2	2.8	1.8e-3	17.5	0.003
Basolite® C300				
Adsorbate gas	$q_s\left(\frac{mmol}{cc}\right)$	$b_0\left(\frac{cc}{mmol}\right)$	$-\Delta U\left(\frac{kJ}{mol}\right)$	R^2
CO_2	6.25	3.00e-4	26.7	0.191
CH_4	3.06	6.00e-4	22.3	0.031
N_2	2.85	2.00e-4	22.1	0.017

4.3 Heat of Adsorption

The change in internal energy due to the adsorption $(-\Delta U)$ for CO_2, CH_4 and N_2, obtained by nonlinear regression of the equilibrium data to fit the Langmuir isotherm are given in Table 4.3. If energetic heterogeneity is present in an adsorbent, then the higher energy sites, if accessible by an adsorbate, are occupied first. Hence, comparing the internal energy obtained from the temperature dependency of the Henry's constant, *K*, given by Equation (4-12), with that obtained from nonlinear regression of the isotherm data over a wide pressure range can be a useful first step to assess adsorbent heterogeneity.

$$K = K_0 \exp\left(-\Delta U \big/ R_g T\right) \qquad (4-12)$$

where $K_0 = b_0 q_s$.

For a heterogeneous adsorbent, the internal energy obtained from nonlinear regression of the isotherm data over a wide range gives the average value and hence is expected to be lower than the value obtained from the linear range data. The temperature dependence of the Henry's constants for CO_2, CH_4 and N_2 in the two adsorbent samples plotted according to equation (4-12) and the corresponding internal energy values obtained from the slopes of the plots are shown in Figure 4.7. The internal energy values given in Figure 4.7 and Table 4.3 are very close for CO_2 and the former values are marginally higher for the other two gases, which seem to suggest that both the Cu-BTC samples are practically homogeneous for the adsorption of CO_2, CH_4 and N_2.

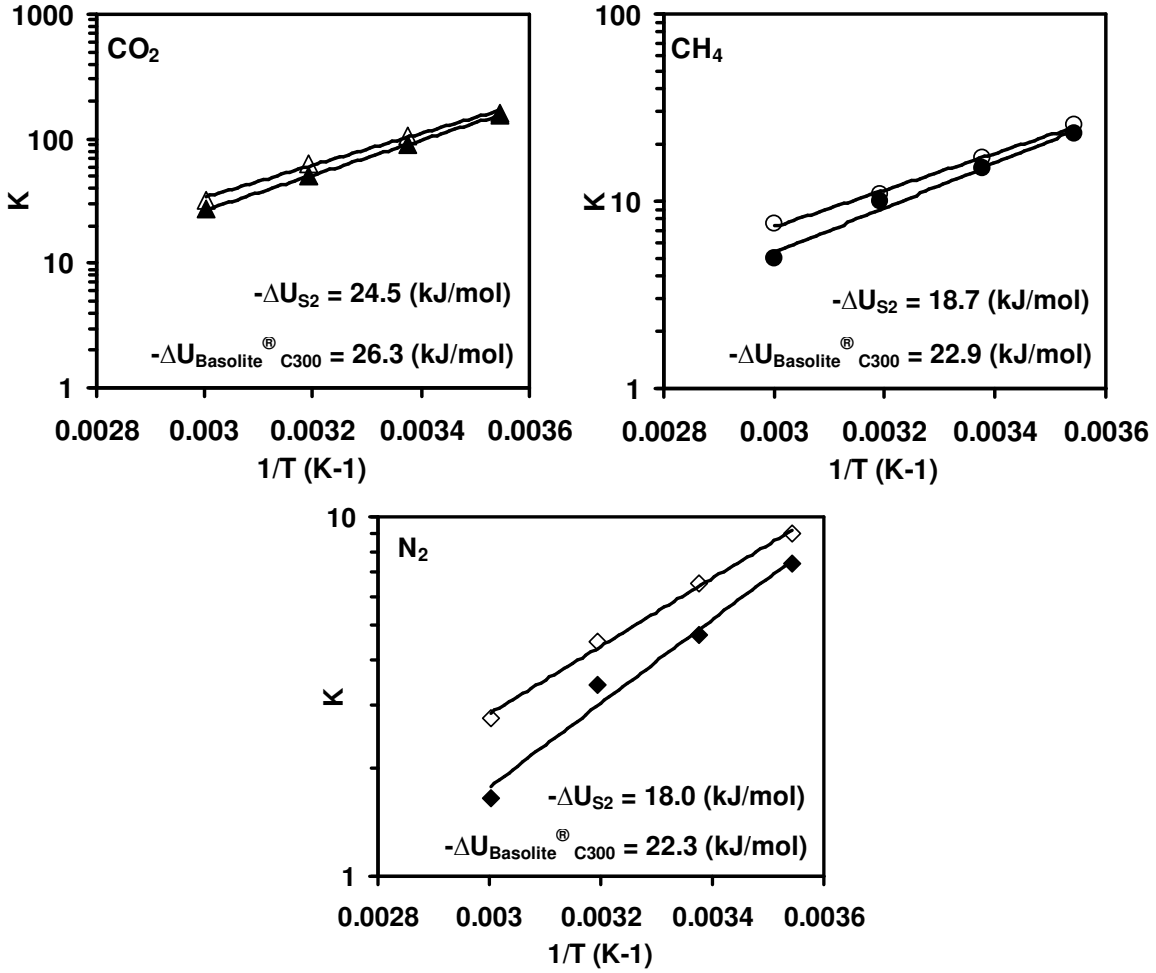

Figure 4.7. Temperature dependency of Henry's constant in linear range of the isotherms. Open symbols and filled symbols represent data for S2 and Basolite® C300, respectively.

4.4 Isosteric Heat of Adsorption

Studying the isosteric heat of adsorption (ΔU_s) is another way of understanding energetic heterogeneity in the adsorbents. Isosteric heat of adsorption, which is independent of temperature, is given by Equation (4-13) (Sircar, 1985).

$$\Delta U_s = R_g T^2 \left(\frac{\partial ln\, P}{\partial T} \right)_q \qquad (4-13)$$

The integrated form of Equation (4-13) is shown in Equation (4-14):

$$ln\, P = \frac{\Delta U_s}{R_g T} + constant \qquad (4-14)$$

The following procedure was implemented to find isosteric heat of adsorption at different levels of loading. Firstly, at each fixed solid loading (q_p), gas concentration (or pressure) was found corresponding to each temperature at which equilibrium was measured. Then, the *P* versus *1/T* data were plotted on a semi logarithmic scale at different loading for each gas. These plots are shown in Figure 4.8 and, ΔU_s was obtained from the slope of each data set. Finally, the calculated isosteric heats were plotted against the corresponding solid loadings (surface coverage, $\theta = \frac{q}{q_s}$). ΔU_s decreases with increasing the surface coverage in a heterogeneous adsorbent. ΔU_s increases with increasing the surface coverage (Marathe et al., 2005) if there is lateral interaction between adsorbed molecules. According to the Figure 4.9, the isosteric heat of adsorption is practically independent of θ for all three gases in both Cu-BTC samples. Further confirming that both the Cu-BTC samples are energetically homogeneous for the adsorption of CO_2, CH_4 and N_2 in the pressure range covered in this study.

4.5 Equilibrium Selectivity

Separation factor or selectivity is an important parameter in preliminary selection of promising adsorbents for separation of a specific gas mixture. The simplest measure of equilibrium selectivity of two adsorbates on an adsorbent is the ratio of Henry's constants of the two gases.

$$\eta_{A/B} = \frac{K_A}{K_B} = \frac{K_{0A}\exp\left(-\Delta U_A / R_g T\right)}{K_{0B}\exp\left(-\Delta U_B / R_g T\right)} = \frac{b_{0A}\, q_s \exp\left(-\Delta U_A / R_g T\right)}{b_{0B}\, q_s \exp\left(-\Delta U_B / R_g T\right)} \qquad (4-15)$$

In the Equation (4-15), $\eta_{A/B}$ is the equilibrium selectivity of adsorbate *A* over adsorbate *B*, and K_A and K_B are the Henry's constants of the two gases in the adsorbent under consideration. The pre-exponential term (b_0) and saturation capacity (q_s) of gases are shown in Table 4.3. Equilibrium selectivity defined as a ratio of Henry's constants is also the true selectivity for a system where the mixture equilibrium follows extended Langmuir isotherm. For a non-Langmuirian system, it is still useful for initial screening of separation potential of different adsorbents for the separation of a given mixture. The temperature effect on equilibrium selectivity (ratio of Henry's constants for gases that follow Langmuir isotherm) of CO_2/N_2 and CO_2/CH_4 gas pairs in synthesized Cu-BTC sample S2 is shown in Figure 4.10, which looks encouraging for further investigation. In addition, the selectivity of these gas pairs in different adsorbents published in the literature are shown in Figures 4.11 and 4.12 and compared with the values obtained in this study.

Sircar et al. (1996) reported a very high selectivity for CO_2/N_2 in 5A zeolite at one temperature, which is the highest among the adsorbents shown in Figure 4.11. Selectivity for CO_2/N_2 in 13X zeolite has been reported in a number of studies but the results differ almost

by an order of magnitude. The selectivity for CO_2/N_2 in Cu-BTC obtained in the present study is consistent with available literature data. While somewhat lower than in 13X, selectivity in Cu-BTC is better than the published results in silicalite and activated carbon.

Sircar et al. (1996) also reported a very high selectivity for CO_2/CH_4 in 5A zeolite at one temperature, which is the highest among the adsorbents shown in Figure 4.12. The selectivity for this gas pair obtained in the present study is also in good agreement with the available literature data for Cu-BTC. This selectivity is better than in activated carbon and MOF-5, but somewhat lower than in 13X zeolite and zirconium pillared clays.

Overall, the selectivity of a gas pair on various adsorbents depends on different factors such as adsorbent structure, surface polarity of the adsorbent, and relative magnitudes of the polarizability, dipole moment and quadrupole moment of each adsorbate gas. The types and concentration of cations present in the adsorbent framework and their accessibility to the adsorbate gases also affect selectivity of the gas pairs on adsorbents. In MOF adsorbents, the pore size and structure, and existence of open metal sites are important factors affecting selectivity.

4.6 Chapter summary

In this chapter, the experimental procedures and the results of adsorption equilibrium studies using constant volume apparatus have been presented. Experimental isotherms of CO_2, CH_4 and N_2 at four temperatures (282.15 K, 296.15 K, 313.15 K and 333.15 K) over the pressure range of 0-6 bar in two adsorbents namely, synthesized Cu-BTC (S2) and Basolite® C300, have been conducted and the results are reported in this chapter. Langmuir isotherm model is able to adequately capture the experimental isotherm data. By analyzing the isosteric heats of

adsorption (ΔU_s), it has been confirmed that both the Cu-BTC samples are energetically homogeneous for the adsorption of CO_2, CH_4 and N_2 in the pressure range covered in this study.

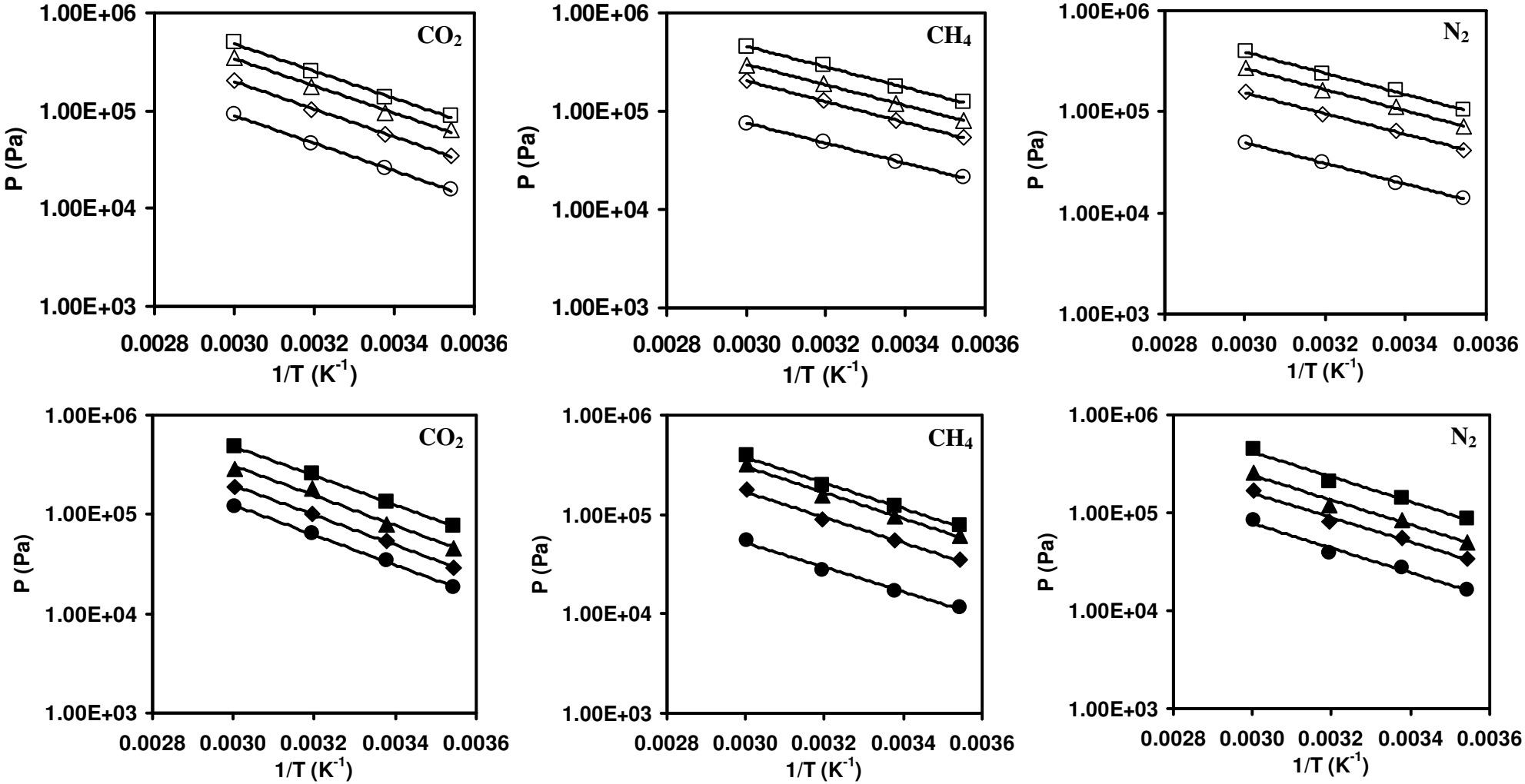

Figure 4.8. Adsorption isosters of CO_2, CH_4 and N_2 on sample S2 (open symbols) and Basolite® C300 (filled symbols).

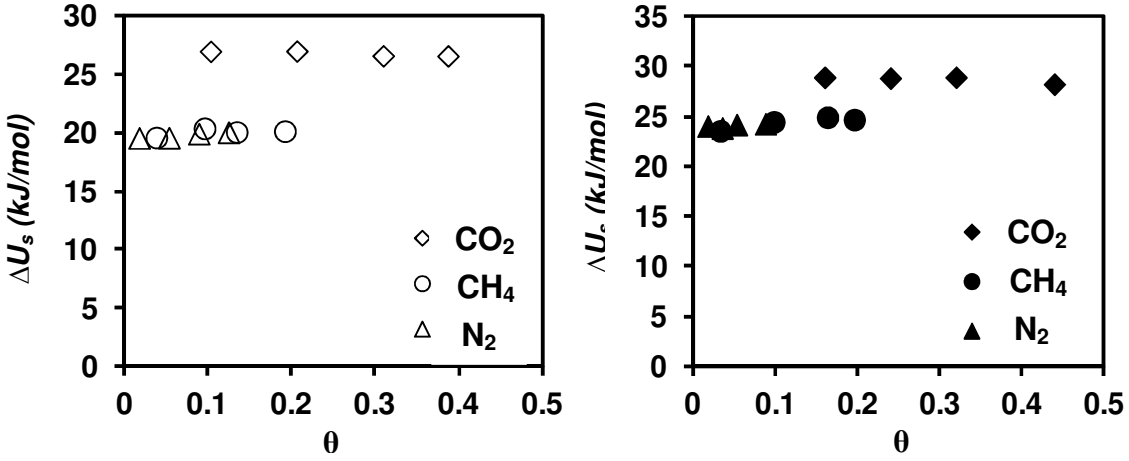

Figure 4.9. Isosteric heat of adsorption dependency on surface coverage for adsorption of CO_2, CH_4 and N_2 on sample S2 (open symbols) and Basolite® C300 (filled symbols).

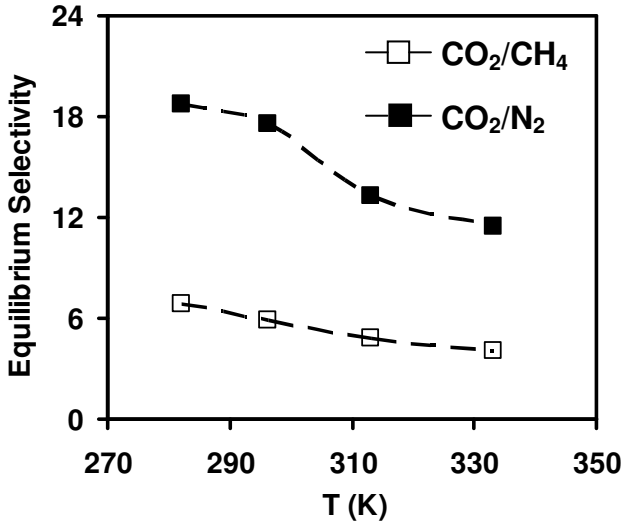

Figure 4.10. Effect of temperature on equilibrium selectivity of gases in Cu-BTC.

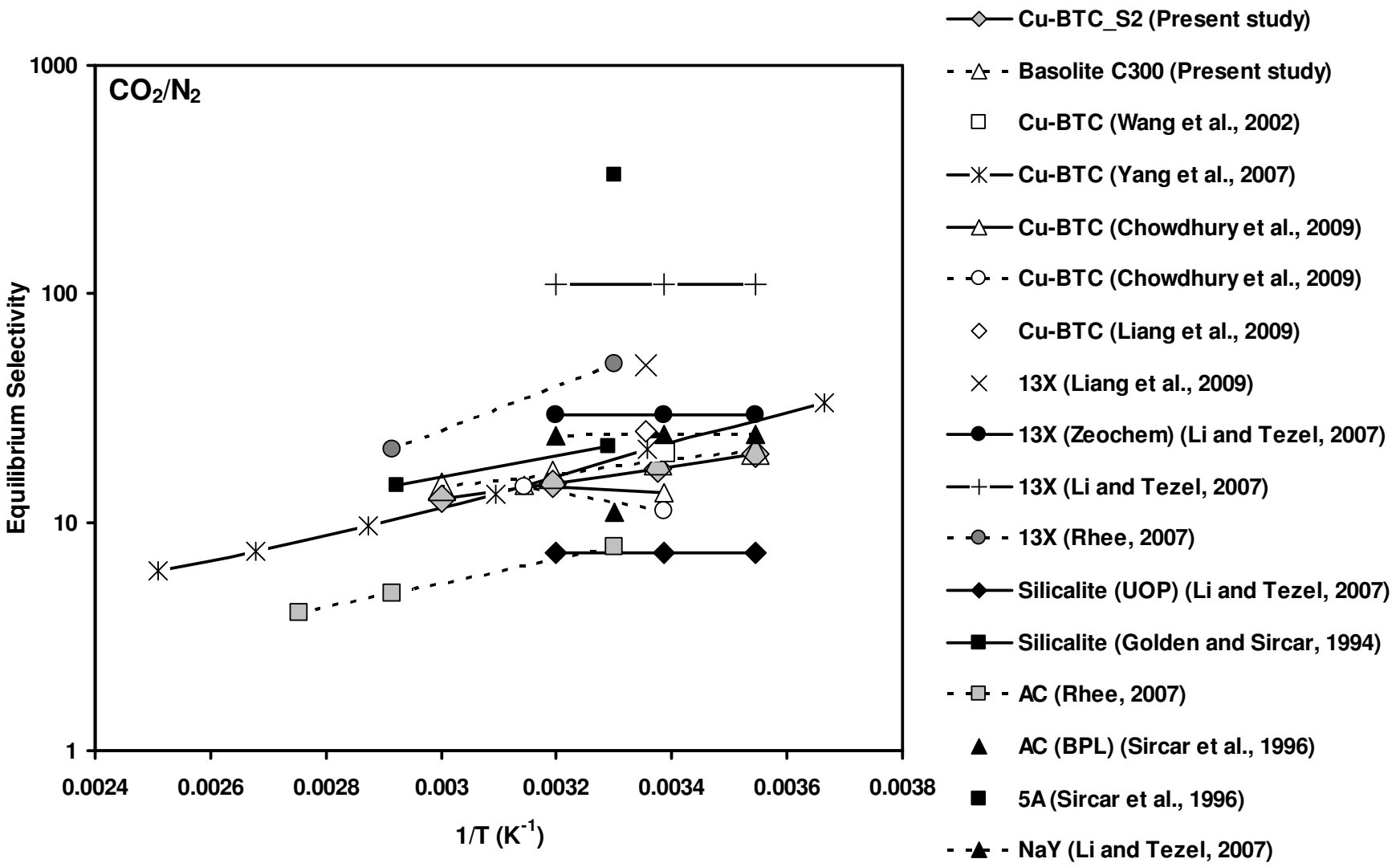

Figure 4.11 Equilibrium selectivity of CO_2/N_2 in sample S2 and Basolite® C300 compared with different published data on various adsorbents.

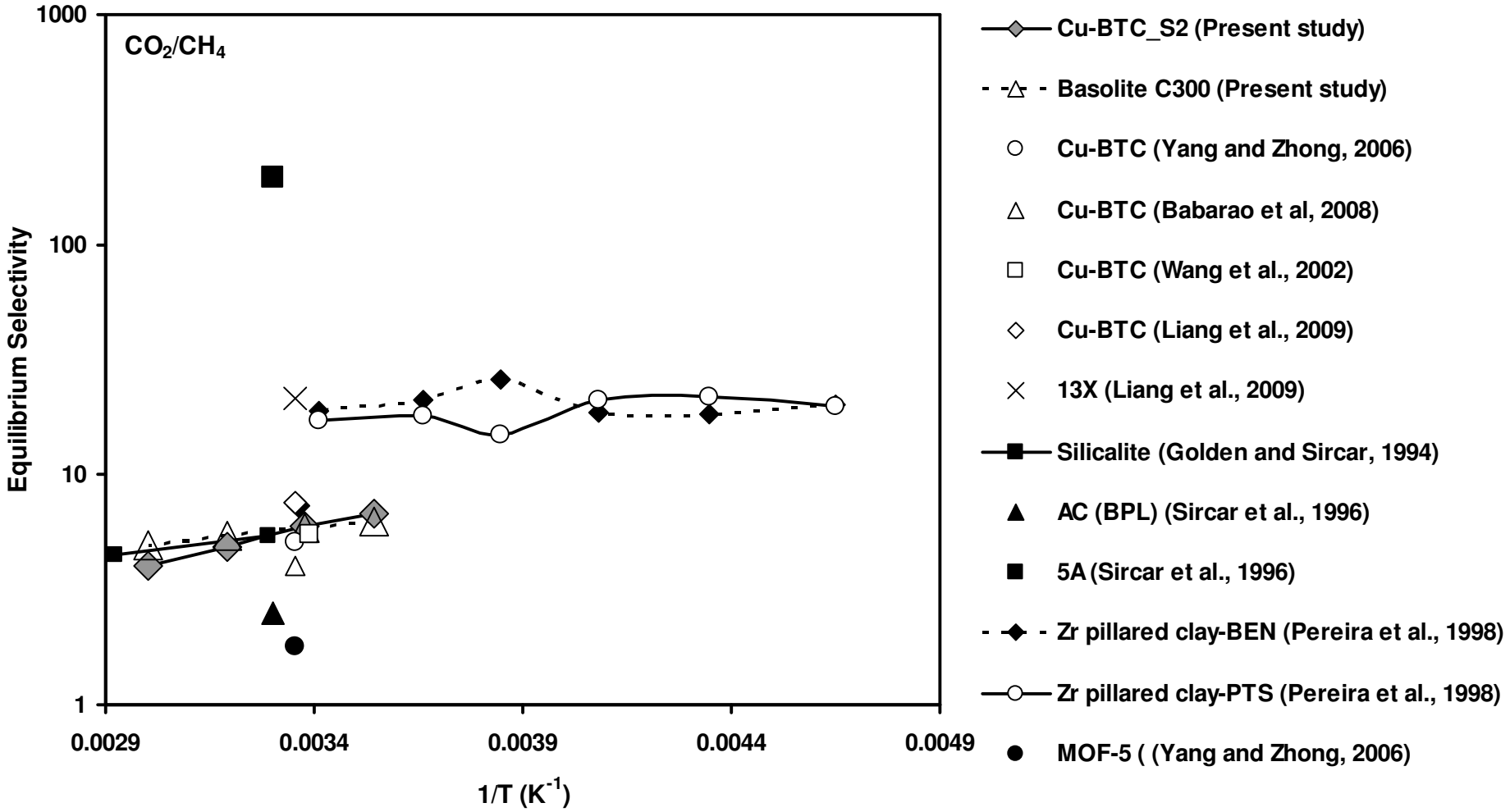

Figure 4.12 Equilibrium selectivity of CO_2/CH_4 in sample S2 and Basolite® C300 compared with different published data on various adsorbents.

CHAPTER 5

TRANSPORT MECHANISM

Single component adsorption equilibrium isotherm measurements for CO_2, CH_4 and N_2 on two Cu-BTC samples, one synthesized and one commercial, over a wide range of temperatures and pressures, and modeling of the measured data were discussed in chapter 4. In this chapter, the gas transport mechanism in the chosen synthesized Cu-BTC sample, S2, is established from extensive unary (feed is a mixture of an adsorbable component and helium) dynamic column breakthrough experiments. Correction of the measured column dynamics for the extra-column dead volume is discussed.

5.1 Experiments to Characterize Adsorption Kinetics

In this study, a total of 54 single component adsorption and desorption breakthrough runs were conducted for the three adsorbate gases, CO_2, CH_4 and N_2, at two temperatures (296.15 K and 313.15 K), four total pressures (2, 4, 6 an 8 bar) and two adsorbate mole fractions (0.1 and 0.24 in balance helium). Reproducibility of the results was confirmed by repeating several of these runs.

5.1.1 Dynamic Column Breakthrough Apparatus

An existing dynamic column breakthrough (DCB) apparatus in our laboratory was redesigned and modified for kinetic measurements. The dead volume was reduced as much as possible so that a small column containing about 17g of the synthesized sample S2 would yield meaningful breakthrough results. Reliable equilibrium and kinetic measurements using less adsorbent is important because of the low product yield of the adsorbent synthesis procedure. The column was filled with the adsorbent particles prepared by the same method detailed in

section 4.1.1. The schematic diagram of the DCB apparatus is shown in Figure 5.1.

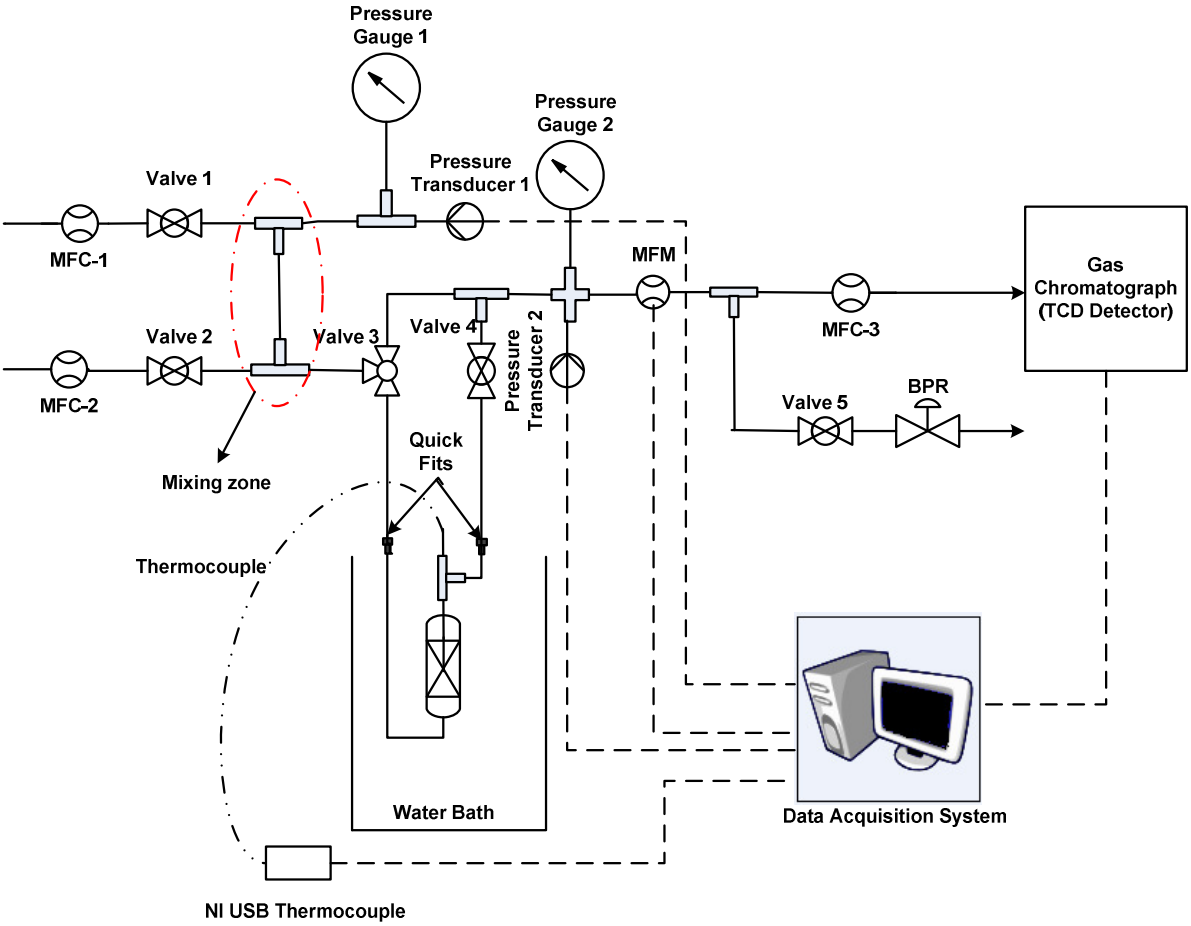

Figure 5.1. Schematic diagram of the breakthrough apparatus.

Two mass flow controllers (Brooks 5850E, powered and operated from Brooks 0151E), MFC-1 and MFC-2, were used to supply the feed at a constant rate by mixing the carrier (helium) and the adsorbate gas (CO_2, CH_4 or N_2) in the desired proportion. In this study, the adsorbate gas proportion was varied from 10-24 volume %. A mass flow meter (Brooks 5860i, powered directly from the 220 V supply) was placed very close to the adsorption column outlet to measure the exit flow rate. Pressure transducers (Honeywell, model 40PC150G2A, 0-150 psig) were installed at the inlet and outlet of the column. The pressure transducers were direct current operated that was supplied from a portable unit (Topward Electric Instrument, model TPS-4000). Pressure gauges (Wika, model EN 837-1) were also

installed with the pressure transducers for the convenience of visual checks for initial adjustments and during the runs. A K-type thermocouple, inserted in the packed bed from the top, was used to record the mid-point (along the length) temperature during the breakthrough measurements. A mechanical back-pressure regulator (GO Regulator, BP3, 0-50 psi) was installed at the column outlet to maintain the desired operating column pressure. A third flow controller (Porter, model 911139), MFC-3, was used to divert part of the gas from the adsorber exit at a fixed rate directly to the thermal conductivity detector (TCD) of a gas chromatograph (Perkin Elmer, model 0993-8559 REV-M) for analysis. The adsorption column was immersed in an insulated water bath and its temperature was controlled with a thermostat (Poly Science, model 9101). Valve 2 was used to introduce step changes in feed concentration for the adsorption and desorption runs. Valve 3 allowed bypassing the adsorption column to measure the blank response. The output signals from the mass flow meter, pressure transducers and TCD were connected to a data acquisition card (National Instruments, model SCB-68). The thermocouple was connected to a USB device (National Instruments, model TC01), which acted like a data acquisition card. During the adsorption and desorption runs, the signals from the pressure, flow, composition and temperature sensors received by the data acquisition cards were captured at pre-assigned rates and stored in a desktop computer using a LabVIEW data acquisition system (version 9.0). The flow controllers and meters, pressure transducers, thermocouple and TCD were adequately calibrated against appropriate standards prior to conducting breakthrough experiments. The calibration procedures are detailed in Appendix 2.

5.1.1.1 Breakthrough Experimental Procedure

The preparation procedure for the adsorbent placed in the column was the same as the procedure for equilibrium isotherm measurement in the constant volume apparatus. However,

the column was regenerated outside in a furnace and reattached to the DCB set-up using the quick fits shown in Figure 5.1. The column was equilibrated with the water bath set at the chosen experimental temperature for at least 2 hours before starting a breakthrough measurement. The carrier (helium) gas flowed through the column during this period.

The Gas Chromatograph (GC) apparatus had to be switched on and the Thermal Conductivity Detector (TCD) had to be prepared at least two hours before conducting any breakthrough experiment. All the while, the reference gas which was the same as the carrier gas (He) was flowing through the detector at a specific flow rate (30 ml/min). The carrier gas flowing through the column was partly diverted through the GC and it was also controlled at the same flow rate as the reference gas flow (30 ml/min). Helium gas was selected as the carrier and reference gas due to its high conductivity among the other gases and inert behavior in Cu-BTC adsorbent. The reference and carrier gas were introduced through the TCD before switching on the GC device. The oven and detector heaters had to be turned on as the first step to set up the TCD. The TCD bridge current was then set and balanced based on the criteria mentioned in the GC manual.

The required operating pressure of the system was set by adjusting back-pressure regulator. The upstream pressure at the gas cylinder head was kept sufficiently high for the flow controller to function properly. The minimum pressure drop required across the mass flow controller used in the experimental set up was 15 psi.

The adsorption runs were initiated by opening valve 2 to introduce the adsorbate gas to the carrier flow. The targeted concentration of the mixture gas could be obtained by changing the carrier and the main gas inlet flow rates. Care was taken to have the same discharge

pressure at two gas cylinders. The LabVIEW program was also started simultaneously with the opening of the main gas inlet valve 2 to capture all the necessary data. The data acquisition system collected data until the breakthrough was complete. Similarly, after the adsorption breakthrough was complete, valve 2 was closed to withdraw the adsorbate gas from the feed and begin the desorption run. The desorption data was stored in a separate file. The data collection continued until the TCD signal returned to the helium baseline. The valves 3 and 4 were open during the adsorption and desorption runs.

5.1.2 Data Processing of Breakthrough Experiments

As mentioned in sections 5.1.1 and 5.1.1.1, the voltage signals for pressure, exit gas flow rate, column mid-point temperature and the gas concentration during the adsorption and desorption measurements were captured and stored in a PC using LabVIEW data acquisition system (version 9.0). The recorded signals corresponding to each of the above variables at each time were converted to the actual value using the calibration equations given in Appendix 2. The ideal gas law was applied to convert pressure to concentration.

5.1.3 Mixing of the Feed Components

In the new design, two flow controllers (MFC-1 and MFC-2) were used to prepare a feed mixture (one adsorbate in helium for unary runs) in the desired ratio. This will be called post-mixed for easy reference. Therefore, having pre-mixed gas cylinders at different concentrations was not necessary. By conducting breakthrough experiments using the two flow controllers to produce a desired mixture (for example, equimolar N_2/He mixture) and repeating the same experiment with pre-mixed feed of the same composition, it was confirmed that mixing in the shortened upstream section connecting the flow controllers to the adsorber inlet was adequate. The comparison between the blank adsorption-desorption

breakthrough of pre-mixed and post-mixed gas is shown in Figure 5.2. The blank run measurement procedure was similar to the breakthrough runs detailed in section 5.1.1, but the valves 3 and 4 were closed to bypass the adsorber.

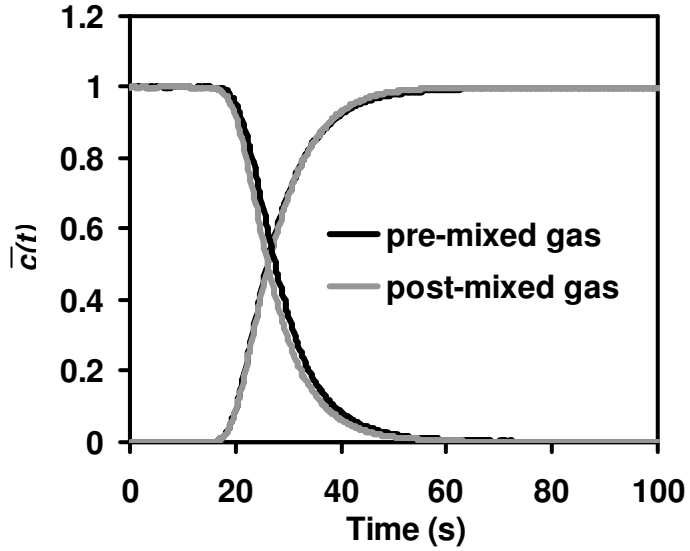

Figure 5.2. Non-adsorbing breakthrough experiments with equimolar N_2/He pre-mixed and post-mixed feed.

5.1.4 Blank Correction: TIS vs. PBP Methods

The length of tubes between the flow controllers, MFC-1 and MFC-2, and the adsorber inlet were shortened to reduce the upstream dead volume. In section 5.1.3 it was confirmed that mixing in the shortened upstream section was adequate. Similarly, in order to reduce the downstream dead volume the detector inlet was connected as close to the exit as possible. Nevertheless, the blank runs bypassing the adsorption column showed significant spreading of responses corresponding to step inputs at the detector inlet. Therefore, the breakthrough responses obtained with the adsorption column were carefully corrected from the corresponding blank responses conducted bypassing the column under the same conditions.

The blank correction methods discussed in the literature, namely point by point (PBP) and tank-in-series (TIS) methods were examined. The PBP method is based on linear additively

of the column and blank responses, an assumption that Rajendran et al. (2008) have shown to be inappropriate using synthetic data. Instead, they proposed to represent the blank response as a collection of several completely mixed tanks in series, where the actual number of tanks and equivalent total tank volume are determined by fitting the TIS model solution to the experimentally measured blank response. Tanks in series (TIS) model can describe the mixing in tubing, fittings and analyzer in the post-column section of the breakthrough apparatus. The TIS model representation of the blank in our breakthrough experimental system is schematically shown in Figure 5.3.

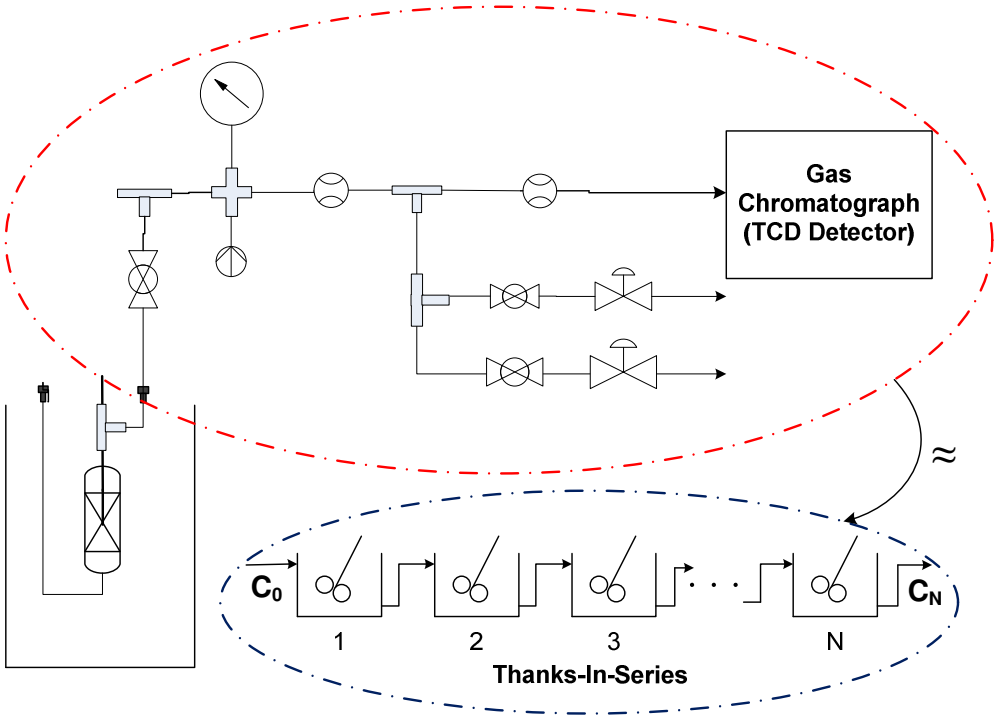

Figure 5.3. Schematic of the TIS model for description of dead volume effect.

The mass balance around the j[th] tank is represented by the following equations in the TIS model:

$$\frac{dC_j}{dt} = \frac{Q(t)}{V_{dead}/N}\left(C_{j-1}(t) - C_j(t)\right)$$

$$= \frac{1}{\tau(t)}\left(C_{j-1}(t) - C_j(t)\right), \quad j = 1,2,...,N \qquad (5-1)$$

The exit dead volumes including fitting, tubing, detector, etc., are assumed equal to V_{dead} in Equation (5-1). τ (t) represents the tank residence time and $Q(t)$ is the volumetric flow rate to the detector, which was kept constant. $C_N(t)$ is the detector outlet gas concentration (composite response).

It was discussed earlier that TIS model can be used for the description of the dispersion in the tubing, fitting and detector after the column exit. The true response of the system can be obtained by correcting the composite response from "extra column" effects. This means that by using the TIS model, what goes into the tank can be found based on information of what comes out of the tank. The following discussion will clarify the method further.

Equation (5-1) can be re-arranged to the following form:

$$C_{j-1}(t) = C_j(t) + \tau(t)\frac{\mathrm{d}C_j}{\mathrm{d}t}, \quad j = 1,2,...,N \qquad (5-2)$$

Equation (5-2) indicates that by measuring the $C_N(t)$ response and using finite difference approximation of the derivative term in the same equation, $C_{N-1}(t)$ can be calculated. The same approach can be implemented for $C_{N-2}(t)$, $C_{N-3}(t)$, … and finally to compute $C_0(t)$ which represents the input to the first tank i.e., adsorption column output (true response).

For several runs, both total and blank responses were measured by varying the controlled constant flow rate to the detector. The corrected responses from the PBP method did not converge, as may be seen from Figure 5.4, which provided direct experimental support that the column and blank responses were not additive. Therefore, the TIS method of blank

correction was applied in this study. A representative blank response from the present study and its fit by the tanks in series model is shown in Figure 5.5.

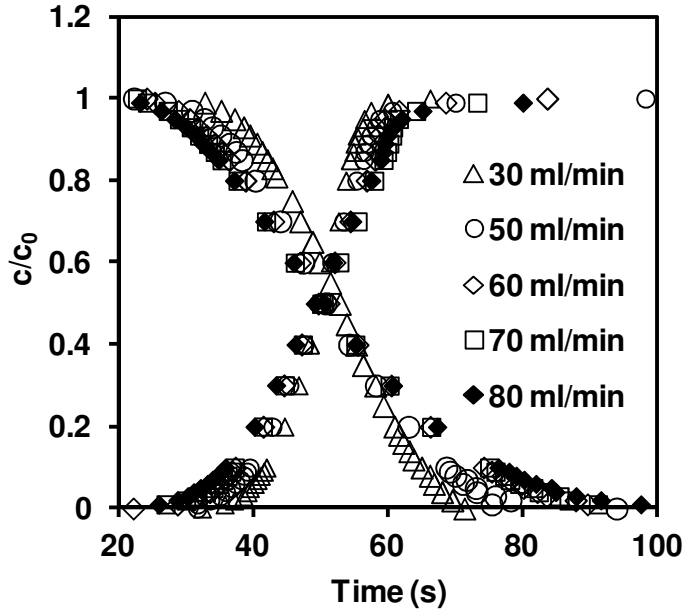

Figure 5.4. Comparison of PBP blank correction method using different TCD inlet flow rates.

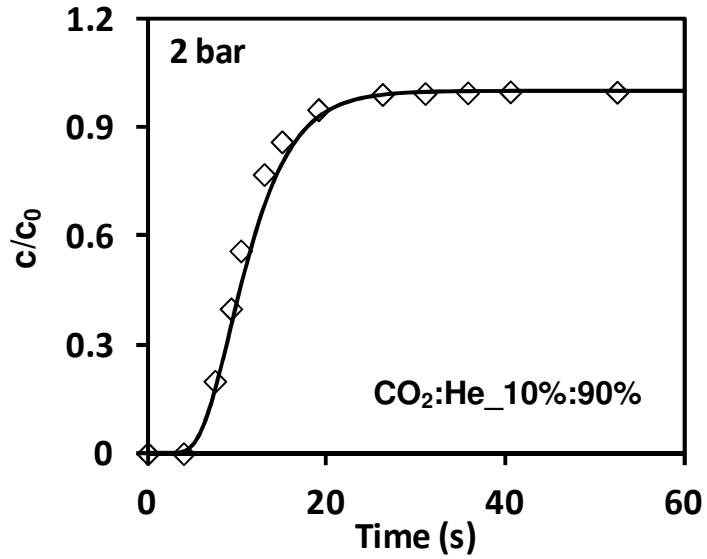

Figure 5.5. Fitting of the experimental blank response (symbols) by TIS model (solid line).

In an isothermal adsorption/desorption run, the change in exit flow rate is entirely due to the concentration change of the adsorbable component. Hence, in an isothermal

adsorption/desorption breakthrough run, the plot of $\frac{c(t)}{c_f}$ (c_f is feed gas concentration) *vs.* time should map exactly on the normalized exit flow rate, $\frac{F(t)-F_{\min}}{F_{\max}-F_{\min}}$, plotted as a function of time. Representative results from a nearly isothermal adsorption breakthrough run from the present study are shown in Figure 5.6 where the normalized concentration breakthrough corrected according to the two models are compared with the change in normalized exit flow rate. The agreement between the breakthrough result corrected by the TIS model and the change in normalize exit flow rate provides experimental support for the TIS model, which was validated only with synthetic data by its proposers.

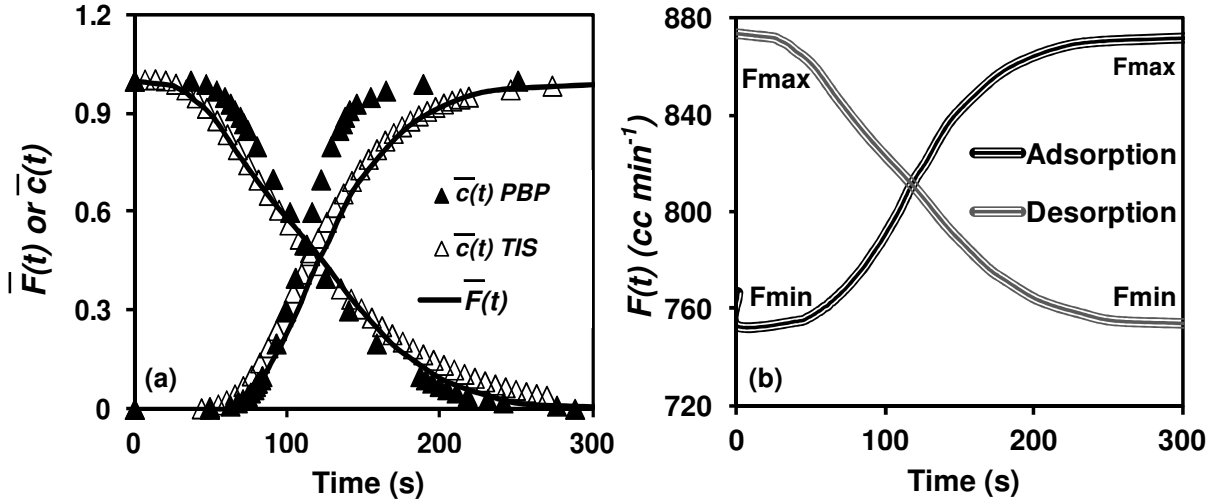

Figure 5.6 (a) Comparison of $\bar{c}(t)$ obtained by correcting with PBP and TIS models with $\bar{F}(t)$ plotted as function of time and (b) corresponding $F(t)$ *vs.* time plot showing $F_{\max}$ and $F_{\min}$. $\bar{c}(t)=\frac{c(t)}{c_f}$, $\bar{F}(t)=\frac{F(t)-F_{\min}}{F_{\max}-F_{\min}}$. The results are for 10% CH_4 in helium at 8 bar and 313.15 K.

5.1.5 Equilibrium Capacity from Corrected Breakthrough Responses

After blank correction of the composite breakthrough response with the TIS model, the corresponding flow rate at each point on the corrected breakthrough curve and, therefore, the velocity at each point could be obtained by Equation (5-3).

$$v\left(t\right)=\frac{F\left(t\right)}{P\,\varepsilon_b\,A} \qquad (5-3)$$

The equilibrium capacity of the adsorbent $\left(q_{equilibrium}\right)$ corresponding to the adsorbate concentration in the feed can also be obtained from each corrected breakthrough response. The following conservation of mass applies for the entire period of a breakthrough run:

$$\left(Moles\ in\right)-\left(Moles\ out\right)=\left(Accumulation\right) \qquad (5-4)$$

where

$$\left(Moles\ in\right)=\int_0^{t_a} A\,\varepsilon_b\,v_0\,c_0\,dt \qquad (5-5)$$

$$\left(Moles\ out\right)=\int_0^{t_a} A\,\varepsilon_b\,v\left(t\right)\,c\left(t\right)\,dt \qquad (5-6)$$

$$\left(Accumulation\right)=A\,L\left[\varepsilon_b\,c_0+\left(1-\varepsilon_b\right)q_{equilibrium}\right] \qquad (5-7)$$

Substituting (5-5) to (5-7) in (5-4) and rearranging, the following equation is obtained:

$$\left(q_{equilibrium}\right)_{ads}=\left[\int_0^{t_a}\left(1-\frac{v\left(t\right)c\left(t\right)}{v_0\,c_0}\right)dt-\frac{L}{v_0}\right].\left[\frac{v_0\,c_0\,\varepsilon_b}{L\left(1-\varepsilon_b\right)}\right] \qquad (5-8)$$

For desorption from a saturated bed, (*Moles in)* = 0 and mass balance equation takes the following form:

$$\left(q_{equilibrium}\right)_{des}=\left[\int_0^{t_d}\left(\frac{v\left(t\right)c\left(t\right)}{v_0\,c_0}\right)dt-\frac{L}{v_0}\right].\left[\frac{v_0\,c_0\,\varepsilon_b}{L\left(1-\varepsilon_b\right)}\right] \qquad (5-9)$$

In the above equation, $v(t)$ represents the gas interstitial velocity at the exit of the adsorber and v_0 is the interstitial velocity of the feed gas. Similarly, $c(t)$ is the concentration of the adsorbate in the stream leaving the column. Moreover, A, L and ε_b are column cross sectional area, column length and bed voidage, respectively. The term $\left(\frac{c(t)v(t)}{c_0 v_0}\right)$ can be calculated at each time and the integral may be evaluated numerically for the duration of the adsorption/desorption run to calculate $q_{equilibrium}$ from the breakthrough runs. The equilibrium data thus obtained are compared with the equilibrium data from the volumetric measurement in Figure 5.7 where very good agreement is observed.

5.2 Breakthrough Modeling

The spreading of the adsorption breakthrough response for a step input is due to the combined effects of axial dispersion, mass transfer resistance and heat effect. By simulating the experimental breakthrough runs using an appropriate model it is possible to shed light on the nature of the mass transfer resistance and quantify it for subsequent use in process design.

Despite using a small column diameter and water circulation around the column, the change in temperature due to adsorption/desorption was not always negligible. Therefore, a nonisothermal model was used to simulate the experimental adsorption and desorption breakthrough runs. The temperature change was in the range 1-16 degrees, the higher changes were for the CO_2 runs, as expected due to its higher capacity and ΔH values. The nonisothermal simulation results will also be compared with the results in the isotherm limit in order to assess the extent of heat effect.

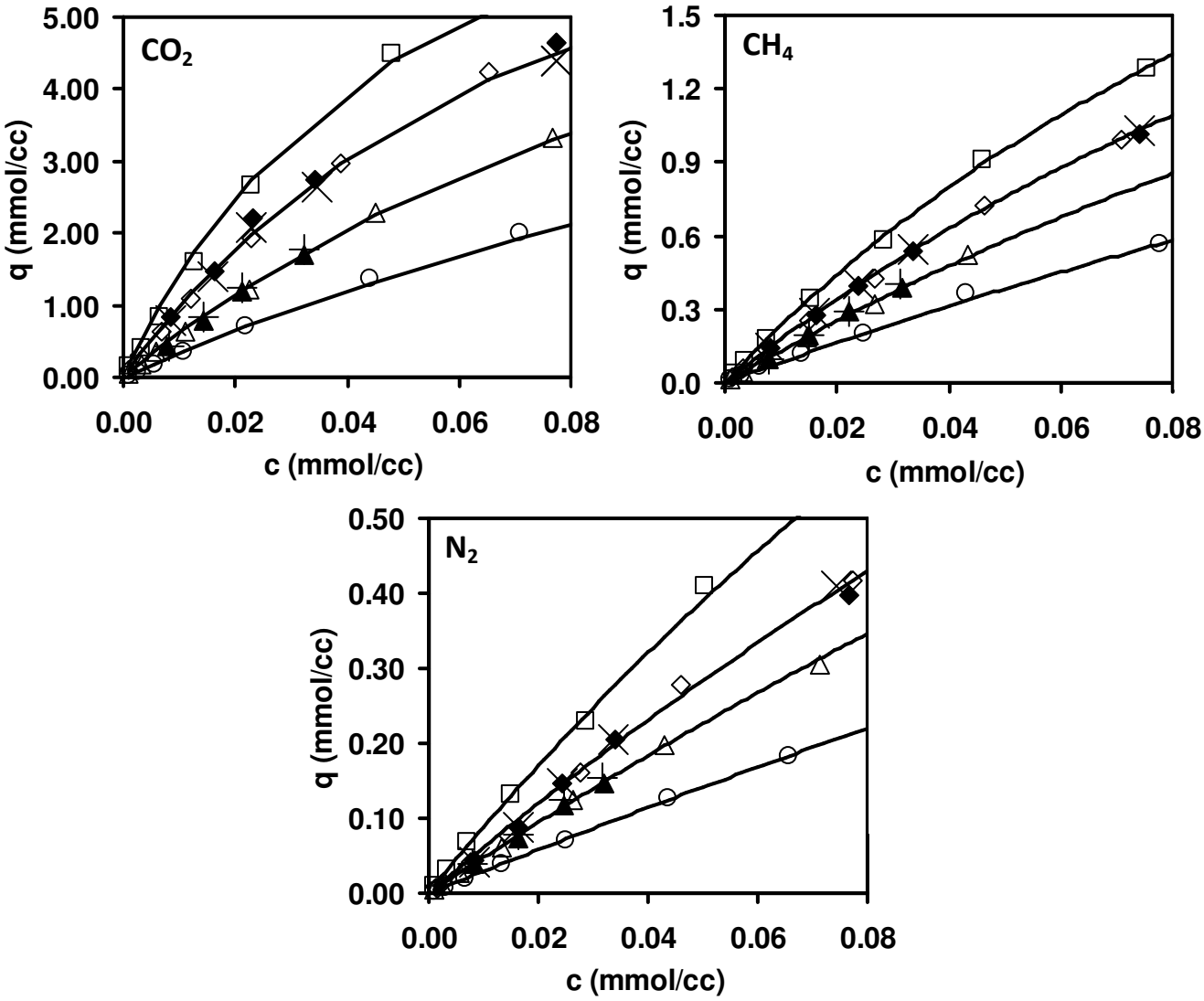

Figure 5.7. (□: 282.15 K, ◇,◆,×: 296.15 K, △,▲,+: 313.15 K, ○: 333.15 K) Comparison of equilibrium isotherms of CO_2, CH_4 and N_2 on Cu-BTC sample S2 obtained from the constant volume and breakthrough measurements. The open symbols are experimental data obtained from the constant volume apparatus. Filled symbols and ×/+ represent the experimental equilibrium capacity obtained from adsorption and desorption breakthrough measurements, respectively. The continuous lines are Langmuir isotherm fits.

5.2.1 Model equations for adsorber breakthrough simulation

The mathematical model for a dynamic column breakthrough process consists of the following components: (1) fluid-phase mass balance, (2) overall mass balance, (3) energy balance equations (4) mass transfer rate, and (5) adsorption equilibrium isotherm. The following assumptions were made to simulate breakthrough experiments conducted in this study:

1) Ideal gas law was applicable.

2) Column wall temperature was constant and equal to the water bath temperature.

3) The adsorber inlet pressure was constant and the pressure drop along the column was negligible.

4) An axially dispersed plug flow model represented the flow in the fluid phase with axial dispersion coefficient independently estimated from a widely used correlation.

5) A Linear Driving Force (LDF) model was used to represent the fluid-solid mass transfer rate where the LDF constant was a fitted parameter.

6) The Langmuir isotherm represented single component equilibrium for all the gases used with parameters obtained from the best fits of the equilibrium data measured in this study.

7) A one-dimensional heat balance equation was used. The fluid and adsorbent were in thermal equilibrium. There were thermal dispersion and convection in the axial direction, and a lumped heat transfer coefficient at the wall accounted for the radial heat transfer.

The mass and energy balance equations for a single component system, subjected to the above assumptions, are presented below.

Component mass balance and boundary conditions:

$$\frac{\partial c}{\partial t} = -\frac{\partial N}{\partial z} - \frac{(1-\varepsilon_b)}{\varepsilon_b}\frac{\partial \bar{q}}{\partial t} \qquad (5-10)$$

where

$$N = -C\ D_L \frac{\partial y}{\partial z} + y\ N \qquad (5-11)$$

Substituting 5-11 in 5-10, the following equation is obtained:

$$-D_L \frac{\partial^2 c}{\partial z^2} + \frac{\partial (v\, c)}{\partial z} + \frac{1-\varepsilon_b}{\varepsilon_b} \frac{\partial \bar{q}}{\partial t} = -\frac{\partial c}{\partial t} \qquad (5-12)$$

In the above equations, *N* is the flux of the adsorbable component, $\bar{q}$ is the average adsorbate concentration in the solid phase at any location along the column length. D_L is the axial dispersion coefficient, z is axial distance measured from the column inlet, and t represents time. *C* is the total concentration (or density, ρ_g) of the feed gas, which can be obtained from the ideal gas law.

Substituting the above assumptions in Equation (5-12), the component mass balance equation for a non-isothermal system takes the following form:

$$\frac{\partial y}{\partial t} = D_L \left[\frac{\partial^2 y}{\partial z^2} - \frac{1}{T} \frac{\partial y}{\partial z} \frac{\partial T}{\partial z} \right] - v \frac{\partial y}{\partial z} + (y-1) \frac{(1-\varepsilon_b) R_g T}{\varepsilon_b P} \frac{\partial \bar{q}}{\partial t} \qquad (5\text{-}13)$$

Equation (5-13) reduces to Equation (5-14) for an isothermal system:

$$\frac{\partial y}{\partial t} = D_L \frac{\partial^2 y}{\partial z^2} - v \frac{\partial y}{\partial z} + (y-1) \frac{(1-\varepsilon_b) R_g T}{\varepsilon_b P} \frac{\partial \bar{q}}{\partial t} \qquad (5-14)$$

For both non-isothermal and isothermal systems, the Danckwerts boundary conditions for dispersed plug flow apply:

$$D_L \left. \frac{\partial y}{\partial z} \right|_{z=0} = -v_0 \left(y|_{z=0^-} - y|_{z=0^+} \right) \qquad (5-15)$$

$$\left. \frac{\partial y}{\partial z} \right|_{z=L} = 0 \qquad (5-16)$$

Overall mass balance:

$$\frac{\partial C}{\partial t} = -\frac{\partial (C v)}{\partial z} - \frac{1-\varepsilon_b}{\varepsilon_b} \frac{\partial \bar{q}}{\partial t} \qquad (5-17)$$

which, for an isobaric non-isothermal system, can be expanded and rearranged to the following form:

$$\frac{\partial v}{\partial z}=\frac{v}{T}\frac{\partial T}{\partial z}-\frac{1}{T}\frac{\partial T}{\partial t}-\frac{(1-\varepsilon_b)}{\varepsilon_b}\frac{R_g T}{P}\frac{\partial \bar{q}}{\partial t} \qquad (5-18)$$

In the isothermal limit, the above equation reduces to:

$$\frac{\partial v}{\partial z}=-\frac{(1-\varepsilon_b)}{\varepsilon_b}\frac{R_g T}{P}\frac{\partial \bar{q}}{\partial t} \qquad (5\text{-}19)$$

Energy balance and boundary conditions:

$$\frac{1-\varepsilon_b}{\varepsilon_b}\left(\rho_s C_{ps}\frac{\partial T}{\partial t}+C_{pa}\frac{\partial\left(\bar{q}T\right)}{\partial t}\right)+\left(C_{pg}\right)\frac{\partial\left(CT\right)}{\partial t}=\frac{K_z}{\varepsilon_b}\frac{\partial^2 T}{\partial z^2}-C_{pg}\frac{\partial\left(CvT\right)}{\partial z}$$
$$+\frac{1-\varepsilon_b}{\varepsilon_b}\left[\left(-\Delta H\right)\right]\frac{\partial \bar{q}}{\partial t}-\frac{2h_i}{\varepsilon_b r_i}\left(T-T_w\right) \qquad (5\text{-}20)$$

The simplified form of the above equation is:

$$\left[\frac{1-\varepsilon_b}{\varepsilon_b}\left(\rho_s C_{ps}+C_{pa}q\right)+\rho_g C_{pg}\right]\frac{\partial T}{\partial t}=\frac{K_z}{\varepsilon_b}\frac{\partial^2 T}{\partial z^2}-C_{pg}\rho_g v\frac{\partial T}{\partial z}$$
$$+\frac{1-\varepsilon_b}{\varepsilon_b}\left(\left(-\Delta H\right)+\left(C_{pg}-C_{pa}\right)T\right)\frac{\partial \bar{q}}{\partial t}-\frac{2h_i}{\varepsilon_b r_i}\left(T-T_w\right) \qquad (5-21)$$

In the above equation, C_{pg}, C_{ps} and C_{pa} represent the specific heat capacities of the adsorbent, the gas phase, and the adsorbed phase, respectively. C_{pa} was assumed to be equal to C_{pg} in this study. K_z is the effective gas thermal conductivity, h_i is the inside heat transfer coefficient, and r_i is inside radius of the column, and ΔH is the enthalpy of adsorption. T_w is the column wall temperature which is equal to the water bath temperature.

The following boundary conditions for the energy balance equation are the analogous forms of Dankwerts boundary conditions:

$$K_z\left.\frac{\partial T}{\partial z}\right|_{z=0}=-v_0 C_{pg}\rho_g\left(T\big|_{z=0^-}-T\big|_{z=0^+}\right) \qquad (5-22)$$

$$\left.\frac{\partial T}{\partial z}\right|_{z=L}=0 \qquad (5-23)$$

Mass transfer rate

$$\frac{\partial \bar{q}}{\partial t} = k\left(q^* - \bar{q}\right) \qquad (5-24)$$

q^* is equilibrium solid loading calculated from Langmuir isotherm model given by Equation (4-6) to (4-8). k is the LDF rate constant.

In Equation (5-21), ΔH is related to ΔU by the following equation:

$$\Delta H = \Delta U - R_g T \qquad (5-25)$$

5.2.2 Parameter Estimation

Operating conditions, weighted average physical properties of carrier and adsorbate gases, axial dispersion coefficient, D_L, adsorbent heat capacity, C_{ps}, effective bed thermal conductivity, K_z, and Langmuir isotherm parameters were inputs to the simulation model. In the absence of some physical property information, such as C_{ps} and K_z, properties of other MOFs with similar framework as Cu-BTC were used. The column was assumed to be in equilibrium with the water bath temperature. The LDF rate constant, k, and the inside heat transfer coefficient, h_i, were varied to fit the corrected exit concentration and mid-column temperature profiles from the experiments. It was observed that the simulated concentration breakthrough profiles were not very sensitive to h_i in the range over which it was varied. Hence, for each run the measured mid-column temperature profile was fitted first by varying h_i, which was kept constant while finding the k value that fitted the corrected concentration breakthrough profile. The fitted h_i values were in the range 20-50 $\frac{W}{m^2.K}$.

The axial dispersion coefficient, D_L, has been estimated from the following correlation:

$$D_L = \gamma_1 D_m + 2\gamma_2 R_p v \qquad (5-26)$$

In the above equation, D_m is the molecular diffusivity of the adsorbate (N_2, CH_4 or CO_2) in the carrier gas (He for single component breakthrough measurements in this study) which can be obtained from the Chapman-Enskog theory (Chapman and Cowling, 1990) at the operating pressure and feed temperature. The coefficient γ_1 is related to the tortuosity of the packed bed, and is a function of bed voidage, ε_b. Wicke recommended the following correlation (Ruthven, 1984):

$$\gamma_1 = 0.45 + 0.55\varepsilon_b \qquad (5-27)$$

The coefficient γ_2 depends on the ratio of the column length to the column diameter, $\frac{L}{d}$, particle size, R_p, and bed voidage (Hsu and Haynes, 1981; Edwards and Richardson, 1968). Edwards and Richardson (1968) have suggested Equation (5.28) for calculating γ_2 at intermediate Reynolds number.

$$\gamma_2 = \frac{1}{Pe'_\infty\left(1+\beta\gamma_1\frac{D_m}{2R_p v}\right)} \qquad (5-28)$$

Pe'_∞ is the limiting value of Peclet number at high Reynolds number. For particles ≤ 0.3 cm in diameter, which is the case in the present study, Pe'_∞ is given by Equation (5.29) (Ruthven, 1984).

$$Pe'_\infty \approx \frac{1}{3.35R_p} \qquad (5-29)$$

β is a constant in Equation (5-28) and it was obtained by fitting the breakthrough responses in the same adsorption column packed with glass beads of the same size as Cu-BTC particles. This was the best experiment that could be conducted to get an independent estimate of axial dispersion in the column used for studying breakthrough of gases in Cu-BTC. β was

obtained by simultaneously fitting three breakthrough responses conducted with glass beads at three different pressures. Representative results are shown in Figure 5.8. The first term on the right hand side in Equation (5-26) is directly proportional to molecular diffusivity and hence inversely proportional to the operating pressure. As may be seen from Figure 5.8, the spread due to axial dispersion decreased with increasing pressure in the experiments, as expected. The fact that the effect was not very pronounced further confirms that the contribution from the second term was dominant. Therefore, fitting β was appropriate. In the analysis of breakthrough experiments with Cu-BTC, the axial dispersion coefficient was estimated from Equations (5-26) to (5-29) together with $\beta = 0.43$, the best fit value obtained by minimizing the sum of squares of the residuals.

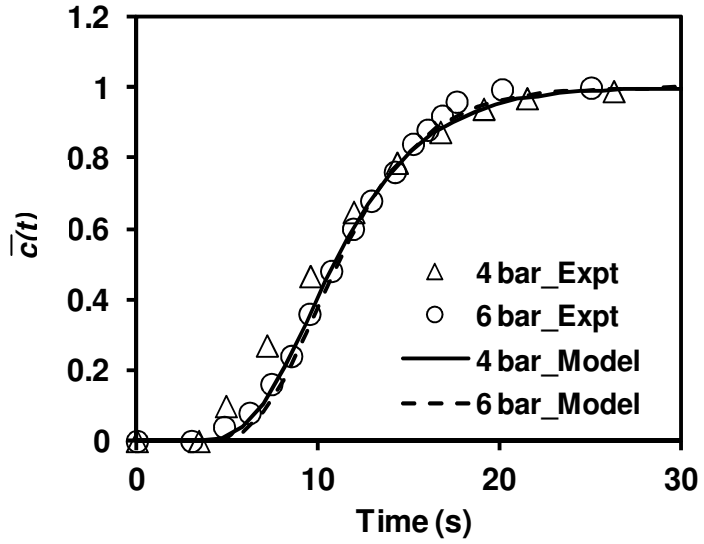

Figure 5.8. Non-adsorbing experiments with glass beads of the same size as Cu-BTC particles in the same breakthrough column. Symbols represent the experimental data and the solid lines represent best fit ($\beta = 0.43$) of Equation (5.28).

The LDF rate constant, k, in Equation (5-24) is the overall effective mass transfer coefficient, which is related to its possible constituents in an adsorption process by Equation (5-28):

$$\frac{1}{k}=\frac{R_p q_f^*}{3k_{film}c_f}+\frac{1}{k_{macro}}+\frac{1}{k_{micro}}=\frac{R_p q_f^*}{3k_{film}c_f}+\frac{R_p^2 q_f^*}{15\varepsilon_b D_e c_f}+\frac{r_c^2}{15D_c} \qquad (5-30)$$

The three terms on the right hand side of the above equation represent the linear driving force representation of the external film, macropore and micropore resistances, respectively.

In Equation (5.28), k_{film} is the mass transfer coefficient across the external film around the adsorbent particles. It can be estimated from the well known correlation of Wakao and Funazkri (1978) for mass transfer in packed beds:

$$Sh=2.0+1.1Re^{0.6}Sc^{1/3} \qquad (5-31)$$

The dimensionless groups in the above equation are defined below:

Sherwood number, $Sh=\frac{2R_p k_f}{D_m}$ $(5-32)$

Reynolds number, $Re=\frac{2R_p \rho_g u}{\mu}$ $(5-33)$

Schmidt number, $Sc=\frac{\mu}{\rho_g D_m}$ $(5-34)$

In the above equation, u is the superficial velocity and μ is the viscosity of the feed (carrier-adsorbate mixture), calculated from Equation (5-35):

$$\mu_{mix}=\frac{\left[\left(y_1\mu_1 M_1^{0.5}\right)+\left(y_2\mu_2 M_2^{0.5}\right)\right]}{\left[\left(y_1 M_1^{0.5}\right)+\left(y_2 M_2^{0.5}\right)\right]} \qquad (5-35)$$

In the above equation, subscripts 1 & 2 represent adsorbate and carrier, respectively, M is the molecular weight and $y_2=1-y_1$.

In Equation (5-30), D_e is the effective macropore diffusivity which consists of contributions from molecular and Knudsen diffusion, surface diffusion and poiseuille flow. Among these

possible contributions to macropore diffusion, the molecular diffusion is most significant for a system where the experiments are conducted at above atmospheric pressure, the pressure drop is negligible, and the adsorption capacity is in the crystal micropores. Therefore,

$$k_m = \frac{15\varepsilon_p D_m}{\tau R_p^2}\frac{c_0}{q_0^*} \qquad (5-36)$$

In this study, $\frac{\varepsilon_p}{\tau}$ was fixed at 0.1, which is a value typically used in the absence of more precise information.

Molecular diffusivity of each adsorbate in helium was calculated from Chapman-Enskog (1990) equation. Micropore diffusivity, D_c, in Equation (5-30) cannot be estimated from other known physical properties. Presence of significant micropore resistance will result in a fitted *k* which cannot be fully explained by the external film and macropore contributions. Micropore diffusivity is a strong increasing function of the adsorbate concentration in the micropores. Hence the important characteristic of a micropore controlled breakthrough process will be an increase in the fitted *k* values with increasing adsorbate partial pressure in the feed. This was not the case in the present study.

The effective gas thermal conductivity, K_z, was estimated from the following correlation (Wencai et al., 1999; Reid et al., 1977; Malek and Farooq, 1996; Suzuki, 1990):

$$K_z = K_{z0} + K_g \delta Pr Re \qquad (5-37)$$

$$K_{z0} = K_g\left(\varepsilon_b + \frac{1-\varepsilon_b}{\psi + 2/3\left(K_g/K_p\right)}\right) \qquad (5-38)$$

$$\psi = \psi_2 + (\psi_1 - \psi_2)\left(\frac{\varepsilon_b - 0.26}{0.216}\right) \qquad (5-39)$$

$\delta = 0.75$, $\psi_1 = 0.25$ and $\psi_2 = 0.13$ were used in this study. The weighted average values of thermal conductivities, K_g, and specific heat capacities, C_{pg}, of the carrier and adsorbate gases were used. In the absence of specific heat capacity and thermal conductivity values for Cu-BTC, these properties available for comparable MOF structures were used. The heat capacity, C_{ps}, was obtained by modifying the reported specific heat capacity for Mg-BTC based on the molecular weights of the two MOFs. The thermal conductivity was assumed equal to that of MOF-5 reported in the literature (Huang et al., 2005; Song et al., 2009).

A Cu-BTC pellet of known dimension was regenerated overnight at 423 K under vacuum and then quickly weighted to prevent any moisture adsorption. The pellet density calculated from the measured volume and weight was ~1 gm/cc. The bed voidage, ε_b, was calculated from the adsorber volume, weight of the adsorbent packed and measured pellet density. All of the input parameters have been compiled in Table 5.1.

5.2.3 Numerical Simulation

The model equations (5-11 to 5-24) were made dimensionless by introducing appropriate scaling factors. The dimensionless equations were discretized in space by applying the finite difference technique (Figure 5.9). The finite difference method discretized the space derivaties and converted the partial differential equations to ordinary differential equations and the ordinary differential equation (overall mass balance) to algebraic equation at each node point.

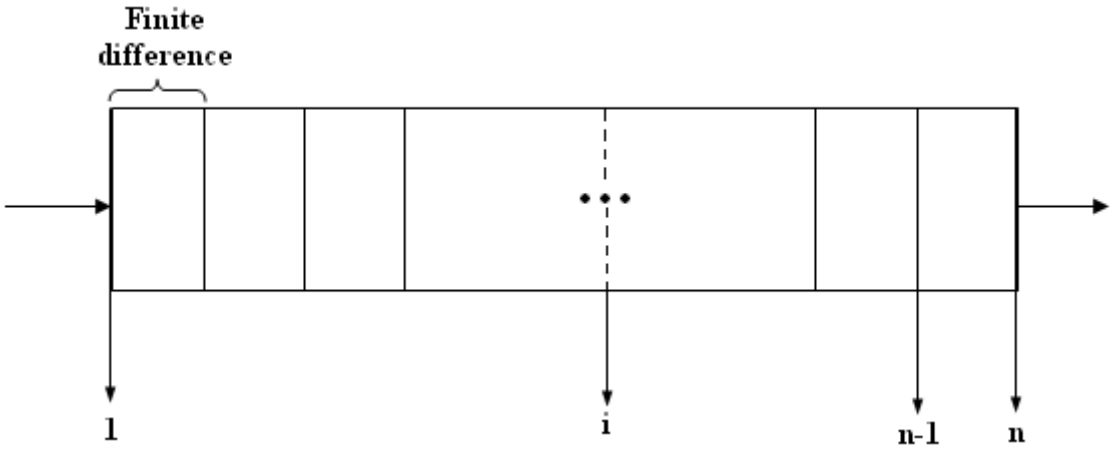

Figure 5.9. Schematic of a column discretized in finite difference.

The resulting system of ordinary differential equations (ODE), subjected to the initial and boundary conditions of the breakthrough operation, were integrated in time in MATLAB® using its ODE solver 15s. The algebraic equations gave explicit expressions for calculating dimensionless interstitial fluid velocity at every node. 300 internal node points were used. Starting from 100 node points, the number was gradually increased until there was no further change in the solution. Representative solutions for increasing different grid points are shown in Figure 5.10. The complete breakthrough is not shown to highlight the region where the solutions differed. It is clear that the solutions for 300 and 500 points were practically overlapping. Hence, 300 grod points were chosen to carry out the simulations presented in this chapter.

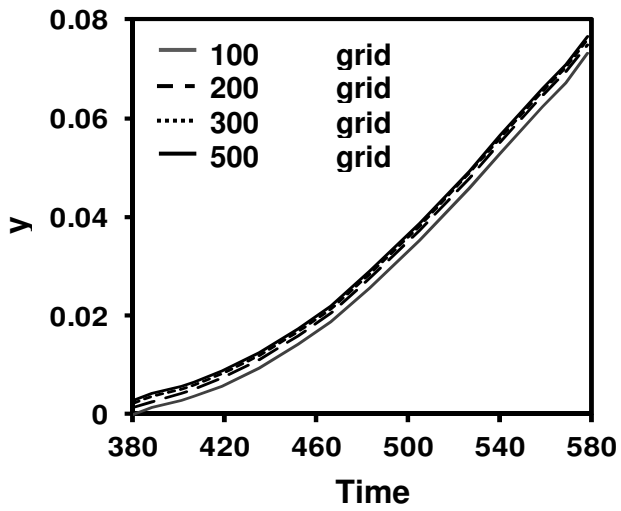

Figure 5.10. Breakthrough model solution using different grid points.

Table 5.1. Input parameters used in breakthrough simulation.

Bed parameters				Operating conditions	
$L\ (m)$		0.1		$T\ (K)$	296.15 and 313.15
$r_i\ (m)$		0.01		$P\ (bar)$	2-8
ε_b		0.44		$v_0 (m/s)$	0.005-0.015
Physical properties					
Adsorbates				Adsorbent	

Gas	D_m [a] $(m^2 s^{-1})$	K_g [b] $\left(\frac{W}{m.K}\right)$		C_{pg} [c] $\left(\frac{J}{mol.K}\right)$		μ [c] $(Poise)$		$R_p\ (m)$	$\rho_p \left(\frac{kg}{m^3}\right)$	K_p at 300K [d] $\left(\frac{W}{m.K}\right)$	C_{ps} [e] $\left(\frac{J}{kg.K}\right)$
		296.15K	313.15 K	296.15K	313.15 K	296.15K	313.15 K				
CO_2	6.12e-5	1.63e-2	1.76e-2	37.33	38.51	1.50e-4	1.57e-4	1.47e-3	1000	0.28	820
CH_4	6.75e-5	3.36e-2	3.59e-2	36.59	37.42	1.09e-4	1.14e-4				
N_2	6.87e-5	2.57e-2	2.70e-2	28.44	28.51	1.78e-4	1.82e-4				
He	-	1.48e-1	1.53e-1	20.79	20.79	2.11e-4	2.16 e-4				

a. Molecular diffusivity of the adsorbate gases in He at 1 bar and 298.15 K
b. McCabe et al., 1993.
c. Perry and Green, 2008.
d. Huang et al., 2005.
e. Song et al., 2009.

Mole fraction of the adsorbable component and fluid velocity at the column exit $(z/L=1)$, and dimensionless bed temperature in the middle of the column $(z/L=0.5)$, computed as functions of time, were used to analyze the experimental breakthrough responses.

5.3 Unary Breakthrough Results

In this study, a total of 54 single component adsorption and desorption runs were conducted for the three adsorbate gases, CO_2, CH_4 and N_2, at two temperatures, four total pressures and two adsorbate mole fractions. The experimental breakthrough profiles were measured at the detector and, the temperature profiles were measured at the middle of the column. Reproducibility was confirmed by repeating several of these runs. Reproducible runs for N_2 at 313.15 K and 2 bar are shown in Figure 5.11. Representative experimental breakthrough results and the corresponding isothermal and non-isothermal model predictions are shown in Figure 5.12 to 5.14.

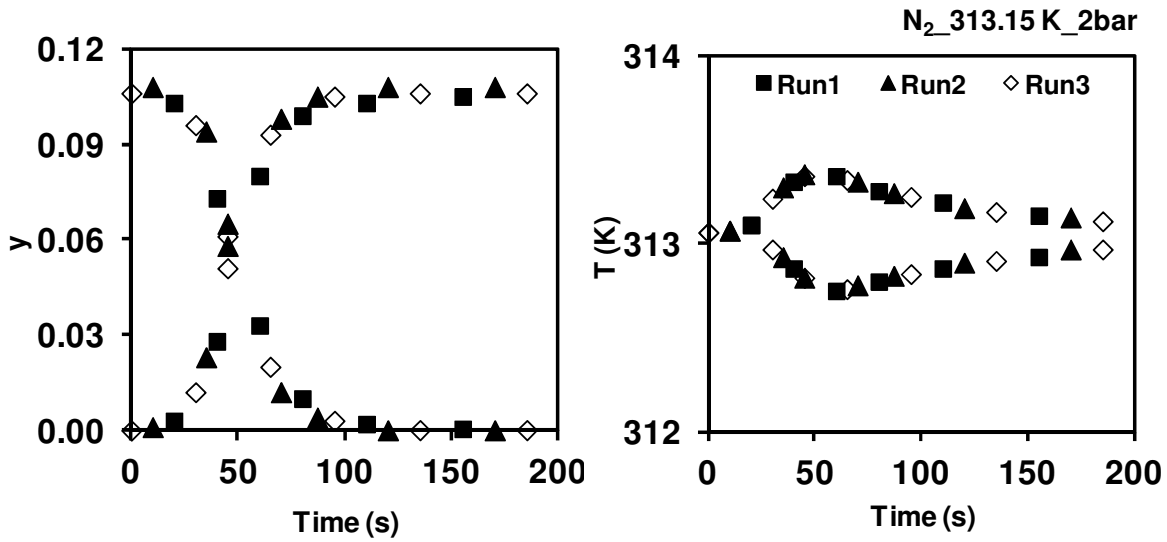

Figure 5.11. Several experimental adsorption-desorption breakthrough runs and corresponding temperature profile.

The predictions from isothermal and non-isothermal simulation models are very close to each other when the temperature change due to the adsorption or desorption is not very high

(Figure 5.13 and 5.14). However, non-isothermal model can predict the experimental data better in case of CO_2 breakthrough which the temperature change is much larger than the other two gases.

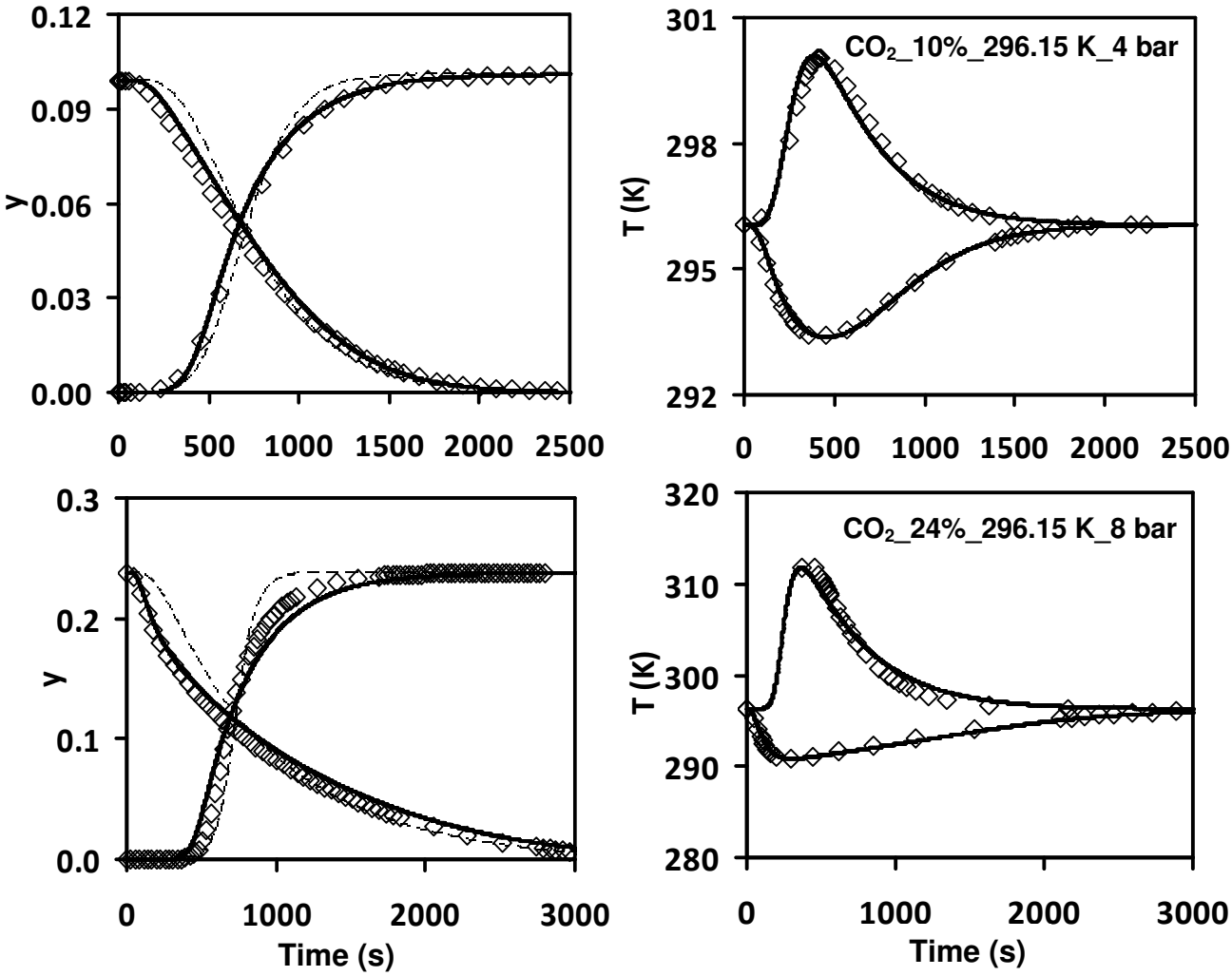

Figure 5.12. Breakthrough and temperature profile for adsorption and desorption of CO_2. Open symbols, solid lines and dashed lines show the experimental results, non-isothermal model and isothermal model, respectively.

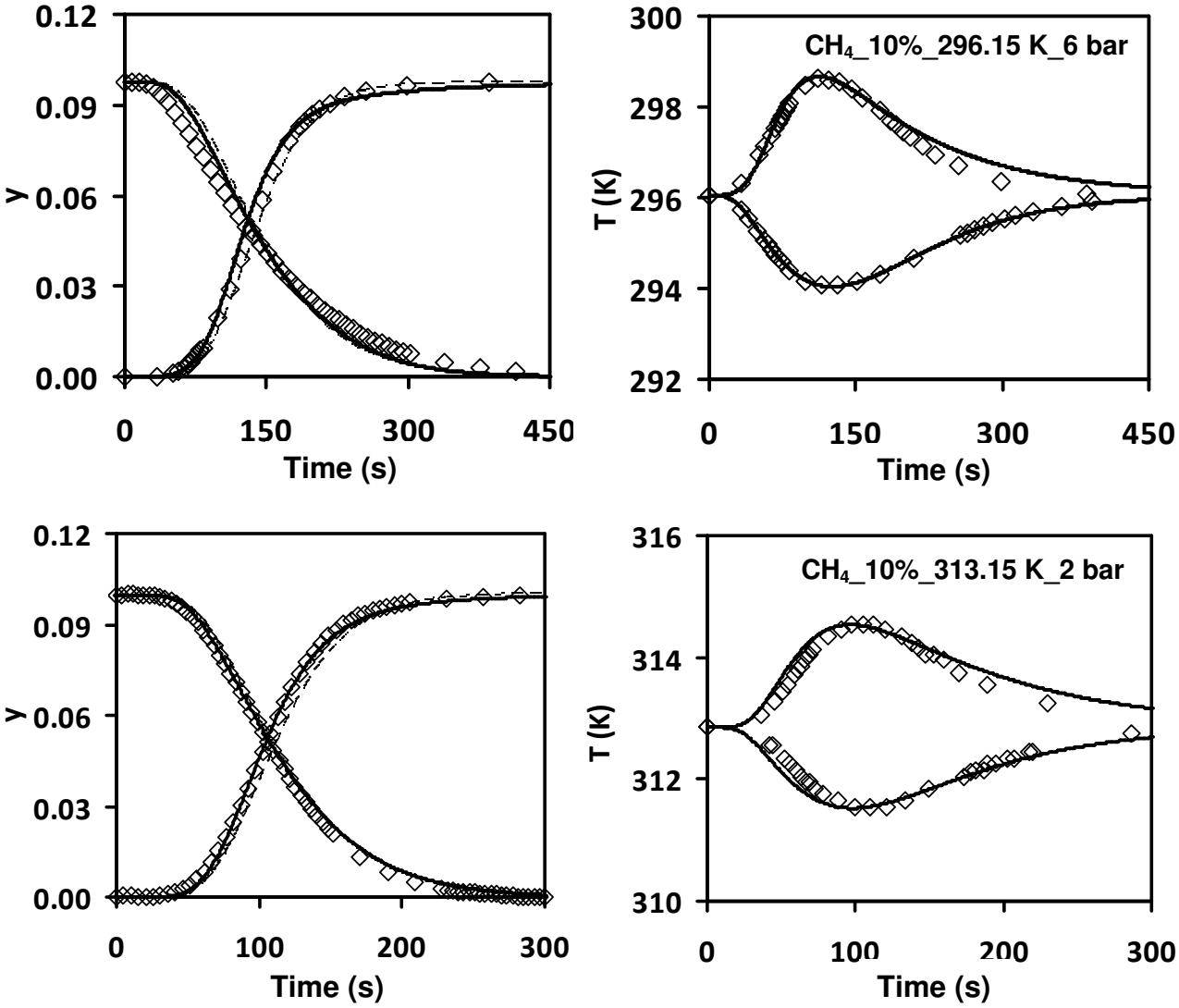

Figure 5.13. Breakthrough and temperature profile for adsorption and desorption of CH_4. Open symbols, solid lines and dashed lines show the experimental results, non-isothermal model and isothermal model, respectively.

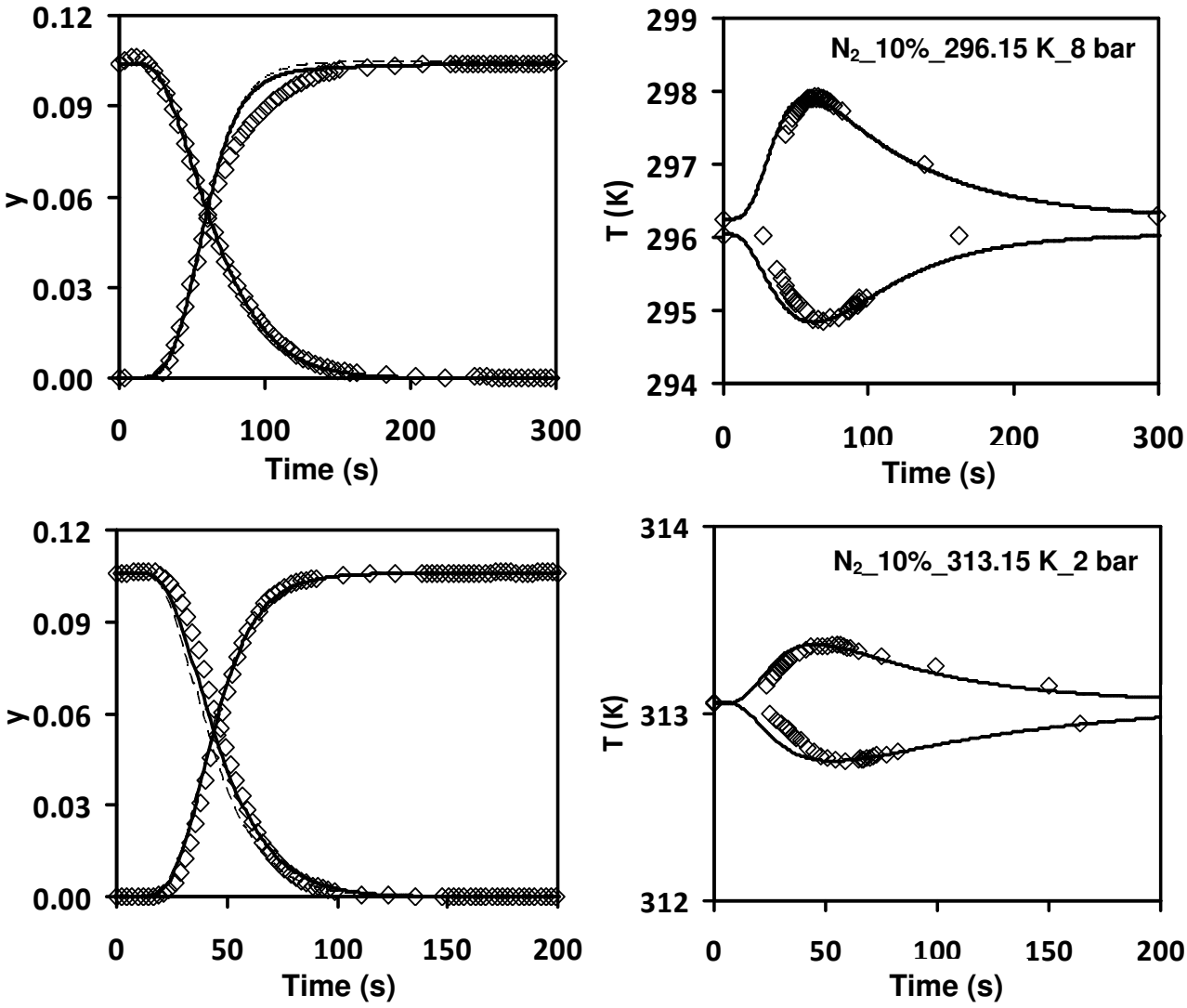

Figure 5.14. Breakthrough and temperature profile for adsorption and desorption of N_2. Open symbols, solid lines and dashed lines show the experimental results, non-isothermal model and isothermal model, respectively.

5.3.1 Prediction of Gas Transport Mechanism in Cu-BTC

It was observed that the fitted LDF constant, k_{fitted}, decreased with increasing pressure for all the three gases, which was a clear indication that the macropore and external film resistances were important and micropore resistance was not dominating. In order to confirm the controlling transport mechanism, the inverse of the fitted LDF constant, $1/k_{fitted}$, obtained from the simulations were plotted against $1/k_{macro}$ and $(1/k_{macro} + (R_p K)/3k_{film})$ and the results are shown in Figure 5.15. It is clear that the mass transfer mechanism for all three gases was dominated by molecular diffusion in macropores with some contribution from transport across the external film around the adsorbent particles.

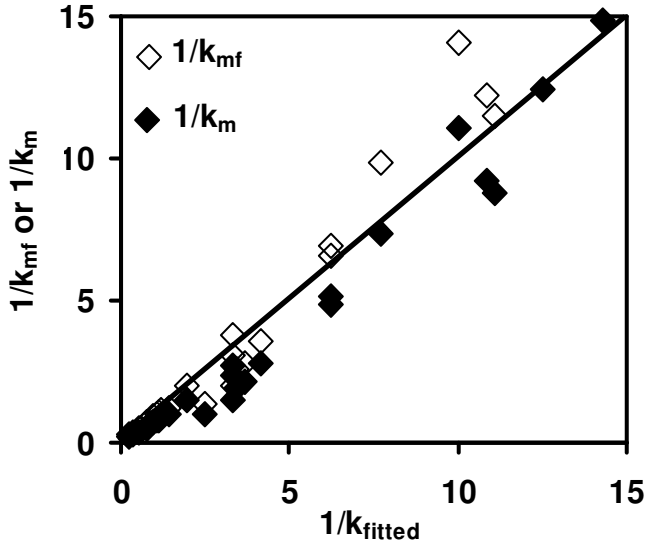

Figure 5.15. Fitted mass transfer resistances obtained from breakthrough experiments compared with estimated resistances assuming macropore molecular diffusion control and a combined macropore molecular diffusion and external film control.

$$\frac{1}{k_m} = \frac{1}{k_{macro}} ; \frac{1}{k_{mf}} = \frac{1}{k_{macro}} + \frac{R_p q_f^*}{3 k_{film} c_f}$$

5.4 Chapter summary

A total of 54 adsorption and desorption breakthrough experiments for the three adsorbate gases, CO_2, CH_4 and N_2, at two temperatures, four total pressures and two adsorbate mole fractions were conducted with the in-house Cu-BTC sample. Two methods, point by point

(PBP) and tanks-in-series (TIS), were applied to correct the experimental breakthrough responses for the dead volume in the system including the detector. The TIS model was experimentally verified to be the correct and reliable method for blank correction.

The breakthrough responses were analyzed in details using a simulation model developed in this study that allowed for the heat effect due to adsorption/desorption, axial dispersion in the fluid phase and finite mass transfer rate between fluid and adsorbent particles represented by LDF approximation. It is confirmed from the analyses that the transport of all three gases is controlled by a combination of molecular diffusion in the adsorbent macropores and diffusion across the external fluid film around the particles.

CHAPTER 6

DEVELOPMENT OF AN EQUILIBRIUM BASED VACUUM SWING ADSORPTION (VSA) PROCESS FOR CO_2 CAPTURE AND CONCENTRATION FROM POST-COMBUSTION FLUE GAS

Encouraging equilibrium selectivity for CO_2/N_2 and CO_2/ CH_4 separations on Cu-BTC were reported in chapter 4 (Figure 4.10), which makes the adsorbent a potential candidate for CO_2 capture and concentration from flue gas, and upgrading of natural gas and biogas – all relevant to clean energy applications highlighted in chapter 1. After having established single component equilibrium isotherm parameters and transport mechanism of the aforementioned gases in Cu-BTC in chapters 4 and 5, the adsorbent is evaluated for its suitability for CO_2 capture and concentration from post combustion flue gas in this chapter.

A detailed simulation model is developed for a 4-step vacuum swing adsorption (VSA) cycle. The model uses binary extensions of the equilibrium and kinetic models established from single component experiments. The binary extensions of the equilibrium and kinetic models are validated with binary breakthrough experiments before conducting process simulations. The performance of Cu-BTC is compared with that of 13X zeolite, an adsorbent studied in the literature for CO_2 capture from post combustion flue gas (Sayari et al., 2011).

As mentioned in the introductory chapter, The CO_2 concentration on dry basis in coal based post combustion power plant flue gas is around 15% which is considered in our simulation. Most of the adsorbents with high affinity and selectivity for CO_2 also strongly adsorbed

moisture. Therefore, it is not practical to remove both CO_2 and water from flue gas simultaneously. To overcome this problem, a suitable desicant such as 3A zeolite can be used to remove the moisture followed by the capture and concentration of CO_2 from dry flue gas.

6.1 VSA Simulation

A four-step VSA process consisting of pressurization, adsorption, forward blowdown and reverse evacuation steps have been studied. The schematic of the process is shown in Figure 6.1. In the presssurization step, the feed gas (CO_2 in N_2) is introduced into the column at z=0 keeping the other end closed. The column pressure increases from low pressure (P_L) to high pressure (P_H) during this step. In the adsorption step, the end at z=L is opened and feed continues to flow in at z=0. The more strongly adsorbing component (CO_2) is retained in the column while the lighter product (N_2 depleted in CO_2) is obtained as the raffinate product withdrawn at z=L. In the blowdown step, the column pressure is reduced to an intermediate vacuum pressure (P_{int}). i.e., the end at z=0 is closed and vacuum is pulled at z=L. The purpose of this step is to remove as much co-adsorbed N_2 as possible from the bed without losing CO_2. Finally, the bed is evacuated to P_L in the reverse direction and the desired concentrated CO_2 product is withdrawn at z=0 while the end at z=L is kept closed. In the VSA process, the steps constituting the cycle are repeated continuously in the same sequence. Since the effluent from one step is not a feed for another step, the columns in a multi-bed arrangement, necessary to make the process continuous, are uncoupled. Therefore, in the four-step cycle under study here, it is sufficient to simulate just one bed in order to capture the process dynamics and evaluate its preformance.

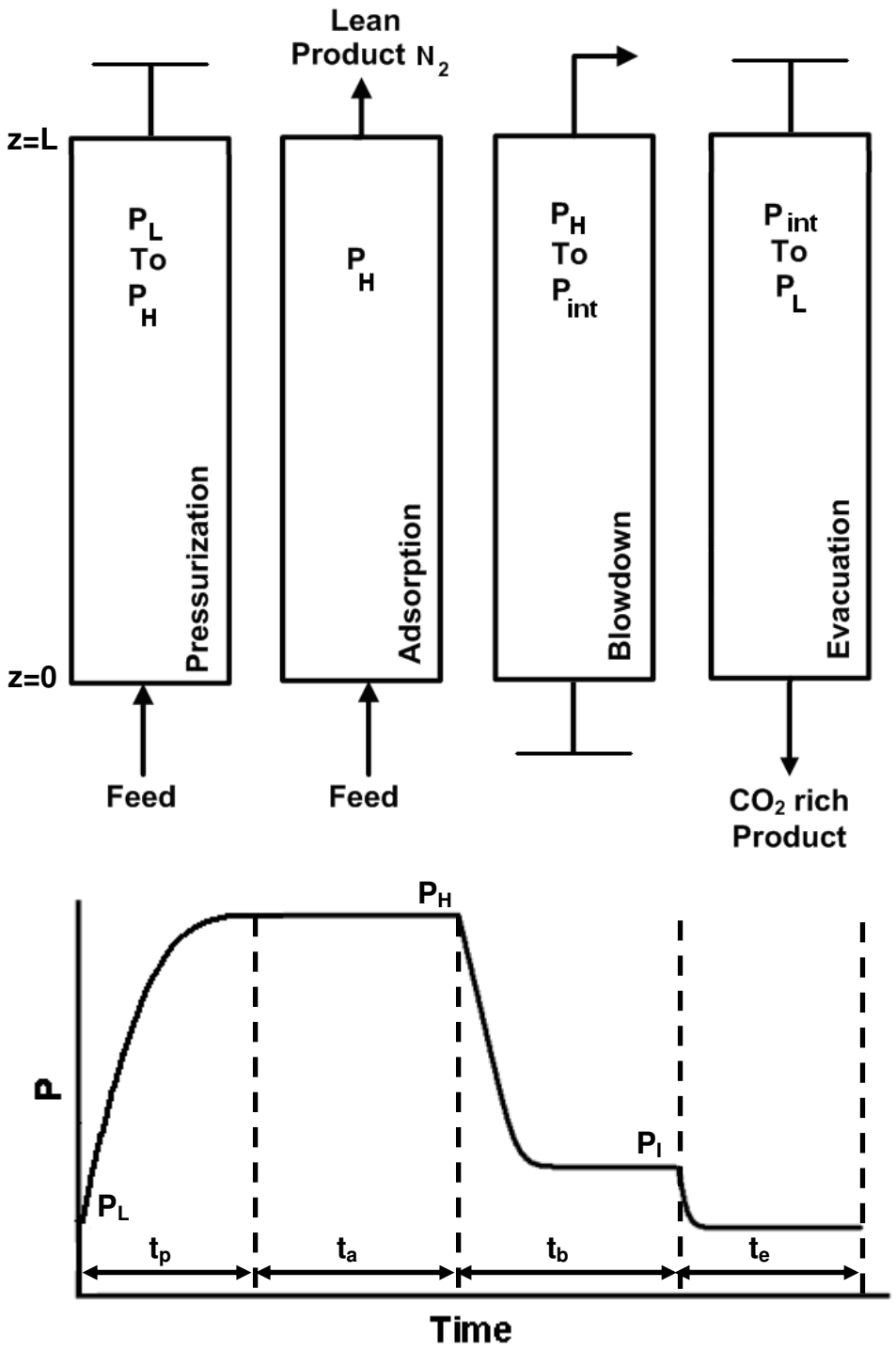

Figure 6.1. Schematic diagram of the four steps VSA cycle.

6.1.1 Model Equations for the Four-Step VSA Cycle

A mathematical model for a four-step vacuum swing adsorption (VSA) process was developed. The following assumptions were made:

1) Ideal gas law applies.

2) Column wall temperature is constant and equal to the water bath temperature for the binary breakthrough experiments

3) Frictional pressure drop along the column length in the direction of flow follows Darcy's law.

4) An axially dispersed plug flow model represents the flow in the fluid phase with axial dispersion coefficient independently estimated from a widely used correlation, which was calibrated with glass bead experiments in chapter 5.

5) A Linear Driving Force (LDF) model is used to represent the rate between the fluid and slid phases. The LDF coefficient is estimated from a combination of external film and macropore molecular diffusion controlled transport adjusted for a binary system.

6) The extended Langmuir isotherm with single component isotherm parameters applies for binary equilibrium

7) A one-dimensional heat balance equation is used. The fluid and adsorbent are assumed to be in thermal equilibrium. There are thermal dispersion and convection in the axial direction. A lumped heat transfer coefficient at the wall accounts for the heat loss through the column wall in the radial direction in the breakthrough experiments. Adiabatic assumption is more appropriate for pilot to industrial scale process operations.

The mass and energy balance equations for a binary system (in a VSA cycle), subjected to the above assumptions, are presented below. The boundary conditions for each step are also reported below.

Component mass balance for a non-isothermal and non-isobaric system:

$$\frac{\partial (C\, y_i)}{\partial t} = D_L \frac{\partial \left(C \frac{\partial y_i}{\partial z} \right)}{\partial z} - \frac{\partial (y_i C v)}{\partial z} - \frac{(1-\varepsilon_b)}{\varepsilon_b} \frac{\partial \bar{q}_i}{\partial t} \qquad (6-1)$$

In the above equation, $C = \frac{P}{R_g T}$ and therefore:

$$\frac{\partial y_i}{\partial t} = \frac{y_i}{T}\frac{\partial T}{\partial t} - \frac{y_i}{P}\frac{\partial P}{\partial t} + \frac{T}{P} D_L \frac{\partial(\frac{P}{T}\frac{\partial y_i}{\partial z})}{\partial z} - \frac{T}{P}\frac{\partial(\frac{y_i P}{T} v)}{\partial z} - \frac{R_g T}{P}\frac{(1-\varepsilon)}{\varepsilon}\frac{\partial \bar{q}_i}{\partial t} \qquad (6\text{-}2)$$

The overall mass balance equation takes the following form:

$$\frac{\partial P}{\partial t} = P\frac{\partial T}{\partial t} - T\frac{\partial(\frac{P}{T} v)}{\partial z} - \frac{(1-\varepsilon_b)}{\varepsilon_b} R_g T \sum_{i=1}^{n} \frac{\partial \bar{q}_i}{\partial t} \qquad (6-3)$$

The energy balance equation in presence of pressure drop is given by:

$$\left[\frac{(1-\varepsilon_b)}{\varepsilon_b}\left(\rho_s C_{ps} + C_{pa}\sum_{i=1}^{n}\bar{q}_i\right)\right]\frac{\partial T}{\partial t} = \frac{K_z}{\varepsilon_b}\frac{\partial^2 T}{\partial z^2} - \frac{C_{pg}}{R_g}\frac{\partial(v P)}{\partial z} - \frac{C_{pg}}{R_g}\frac{\partial P}{\partial t} + \frac{(1-\varepsilon_b)}{\varepsilon_b}\sum_{i=1}^{n}((-\Delta H_i - C_{pa}T)\frac{\partial \bar{q}_i}{\partial t}) - \frac{2h_i}{\varepsilon_b r_i}(T - T_w) \qquad (6-4)$$

Mass transfer rate:

$$\frac{\partial \bar{q}_i}{\partial t} = k_i\left(q_i^* - \bar{q}_i\right) \qquad (6-5)$$

Equilibrium isotherm for obtaining q_i^*:

$$\frac{q_i^*}{q_{si}} = \frac{\frac{P}{R_g T}(b_i y_i)}{1 + \frac{P}{R_g T}\sum_i (b_i y_i)} \qquad (6-6)$$

The velocity is obtained from Darcy equation:

$$v = \frac{-4}{150\mu}\left(\frac{\varepsilon_b}{1-\varepsilon_b}\right)^2 R_p^2 \frac{\partial P}{\partial z} \qquad (6-6)$$

Boundary conditions necessary to solve the above differential equations are different in each step of a VSA cycle. The boundary conditions for pressurization, adsorption, blowdown and evacuation step are listed below.

Pressurization step:

$$D_L \left.\frac{\partial y_i}{\partial z}\right|_{z=0^+} = -v_0 \left(y_{i,feed} - y_i \big|_{z=0^+} \right) \qquad (6-7a)$$

$$\left.\frac{\partial y_i}{\partial z}\right|_{z=L^-} = 0 \qquad (6-7b)$$

$$K_z \left.\frac{\partial T}{\partial z}\right|_{z=0^+} = -\varepsilon_b v_0 \rho_g C_{pg} \left(T_{feed} - T \big|_{z=0^+} \right) \qquad (6-7c)$$

$$\left.\frac{\partial T}{\partial z}\right|_{z=L^-} = 0 \qquad (6-7d)$$

Since the velocity is a function of pressure gradient through the Darcy's law, the overall mass balance equation (6.3) is, in fact, second order in P and requires two boundary conditions. Since the velocity at the z=L is zero in this step, the following pressure boundary condition is:

$$\left.\frac{\partial P}{\partial z}\right|_{z=L} = 0 \qquad (6-7f)$$

The other boundary condition comes for the assumed exponential change in pressure at the inlet, given by the equation below:

$$P\big|_{z=0^+} = f(t) = P_H + (P_L - P_H)\exp(-\alpha_p t) \qquad (6-7e)$$

In the above equation, P_H and P_L represent the high pressure adsorption step pressure and evacuation pressure, respectively. $\alpha_p \left(s^{-1}\right)$ is a constant that determines rate of the pressure change, which was fixed to 0.5 in this study.

Adsorption step:

$$D_L \left.\frac{\partial y_i}{\partial z}\right|_{z=0^+} = -v_0 \left(y_{i,feed} - y_i \big|_{z=0^+} \right) \qquad (6-8a)$$

$$\left.\frac{\partial y_i}{\partial z}\right|_{z=L^-} = 0 \qquad (6-8b)$$

$$K_z \left.\frac{\partial T}{\partial z}\right|_{z=0^+} = -\varepsilon_b v_0 \rho_g C_{pg} \left(T_{feed} - T \big|_{z=0^+} \right) \qquad (6-8c)$$

$$\left.\frac{\partial T}{\partial z}\right|_{z=L^-} = 0 \qquad (6-8d)$$

$$P\big|_{z=L} = P_H \qquad (6-8f)$$

Inlet pressure is calculated from the Darcy's law since the inlet velocity (feed velocity) is known in adsorption step:

$$v_0 = \frac{-4}{150\mu}\left(\frac{\varepsilon_b}{1-\varepsilon_b}\right)^2 R_p^2 \left.\frac{\partial P}{\partial z}\right|_{z=0} \Rightarrow \left.\frac{\partial P}{\partial z}\right|_{z=0} = -\frac{150\mu v_0 (1-\varepsilon_b)^2}{4\varepsilon_b^2 R_p^2}$$

Blowdown step:

$$\left.\frac{\partial y_i}{\partial z}\right|_{z=0^+} = 0 \qquad (6-9a)$$

$$\left.\frac{\partial y_i}{\partial z}\right|_{z=L^-} = 0 \qquad (6-9b)$$

$$\left.\frac{\partial T}{\partial z}\right|_{z=0^+} = 0 \qquad (6-9c)$$

$$\left.\frac{\partial T}{\partial z}\right|_{z=L^-} = 0 \qquad (6-9d)$$

Since the velocity at the z=0 is zero in this step, the following pressure boundary condition isat this end:

$$\left.\frac{\partial P}{\partial z}\right|_{z=0} = 0 \qquad (6-9e)$$

An exponential change in pressure is assumed at the outlet, given by Equation (6-9*f*), which gives the other boundary condition:

$$P|_{z=L^-} = f(t) = P_I + (P_H - P_I)\exp(-\alpha_p t) \qquad (6-9f)$$

Evacuation step:

$$\left.\frac{\partial y_i}{\partial z}\right|_{z=0^+} = 0 \qquad (6-10a)$$

$$\left.\frac{\partial y_i}{\partial z}\right|_{z=L^-} = 0 \qquad (6-10b)$$

$$\left.\frac{\partial T}{\partial z}\right|_{z=0^+} = 0 \qquad (6-10c)$$

$$\left.\frac{\partial T}{\partial z}\right|_{z=L^-} = 0 \qquad (6-10d)$$

The velocity at the z=L is zero in evacuation step. Therefore, the following pressure boundary condition is used for this end:

$$\left.\frac{\partial P}{\partial z}\right|_{z=L} = 0 \qquad (6-10e)$$

Similar to the other pressure changing steps, an assumed exponentially changing pressure, given by Equation (6-10*e*), is used as the boundary condition at the other end:

$$P|_{z=0} = f(t) = P_L + (P_I - P_L)\exp(-\alpha_p t) \qquad (6-10f)$$

In the above equation, all the variables have the same definitions as in chapter 5. They are not repeated here.

6.1.2 Finite Volume Method

Many numerical techniques such as finite difference (Carter and Wyszynski, 1983), finite element (Kikkinides and Yang, 1993), orthogonal collocation (Raghavan and Ruthven, 1983) and finite volume (Webley and He, 2000; Todd et al., 2001; Cruz et al., 2005) methods have been used to solve the coupled non-linear partial differential equations (PDEs) of a PSA/VSA process model.

It is desirable that the VSA process simulator is robust and computationally very efficient. A robust simulator is necessary to explore separation performance over a wide range of operating conditions. Computational efficiency allows undertaking a detailed search of the preferred performance regimes within a short time. All the numerical techniques work well when equilibrium isotherms have modest curvature and the mass transfer resistance is large, both of which result in a broad mass transfer zone with gentle slopes of the concentration/temperature profiles that evolve along the length of the adsorber in a cyclic PSA/VSA process. The finite difference method, used in chapter 5 for breakthrough simulation, requires very fine discretization in space to capture very sharp mass transfer fronts that develop in the adsorber when the equilibrium isotherm is strongly curved and the mass transfer resistance is not high (Medi and Amanullah, 2011). Equilibrium controlled CO_2 capture from flue gas falls in this category. Fine discretization increases the number of differential equations to be integrated in time, which in turn increases the computational time. The effect is felt more in PSA/VSA process simulation where the cyclic calculations of the steps are repeated several times until cyclic steady state is reached. The finite volume method is used in this chapter for VSA process simulation due to its ability to handle sharp changes in slopes of the various wave fronts with relatively less number of volume elements.

Simulations of an experimental breakthrough response using the finite difference and finite volume techniques are compared in Figure 6.2. It took 30 elements and 16.09 s CPU time for the finite volume method to attain the same accuracy that required 300 grid points 43.68 s in the finite difference method. The computational time required for simulating 100 cycles of the VSA process for a given set of operating conditions using finite volume and finite difference techniques were 3,700 s and 14,000 s, respectively These computations were carried out in an Acer TravelMate 6292 laptop with the following specifications of the processor: Intel® Core™2 Duo CPU; processor speed : 2 GHz.

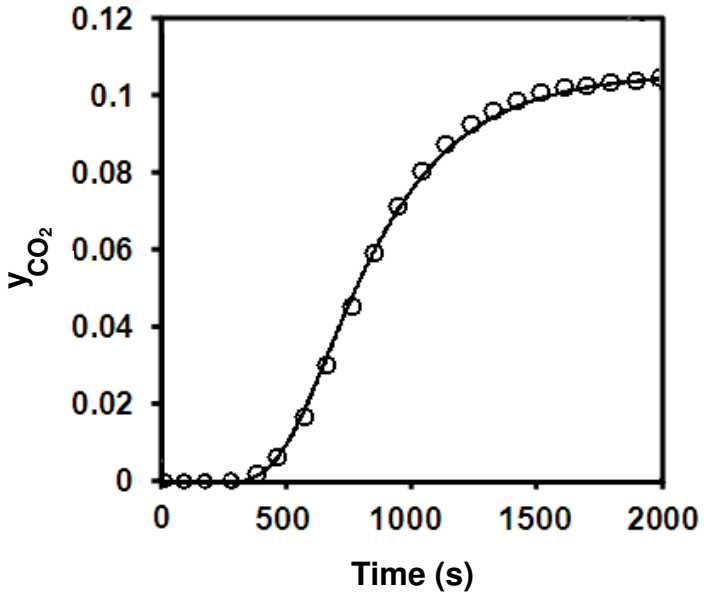

Figure 6.2. Breakthrough response for CO_2 at 2 bar and 296.15 K. Symbols, solid line and broken line represent experimental data, finite volume solution with 30 volume elements and finite difference solution with 300 grid points, respectively.

The finite volume method is based on integral form of the governing conservation equations, unlike the differential forms of the equations used in the other numerical methods mentioned earlier. The integral forms of the equations allow better conservation of mass, energy and momentum. The partial differential equations are valid at all points in the domain which can be considered as infinitesimal volumes and, the integral conservation law is enforced for

small control volumes on a meshed geometry. As it was shown in Figure 6.3.a, the column is discretized into “n” segments.

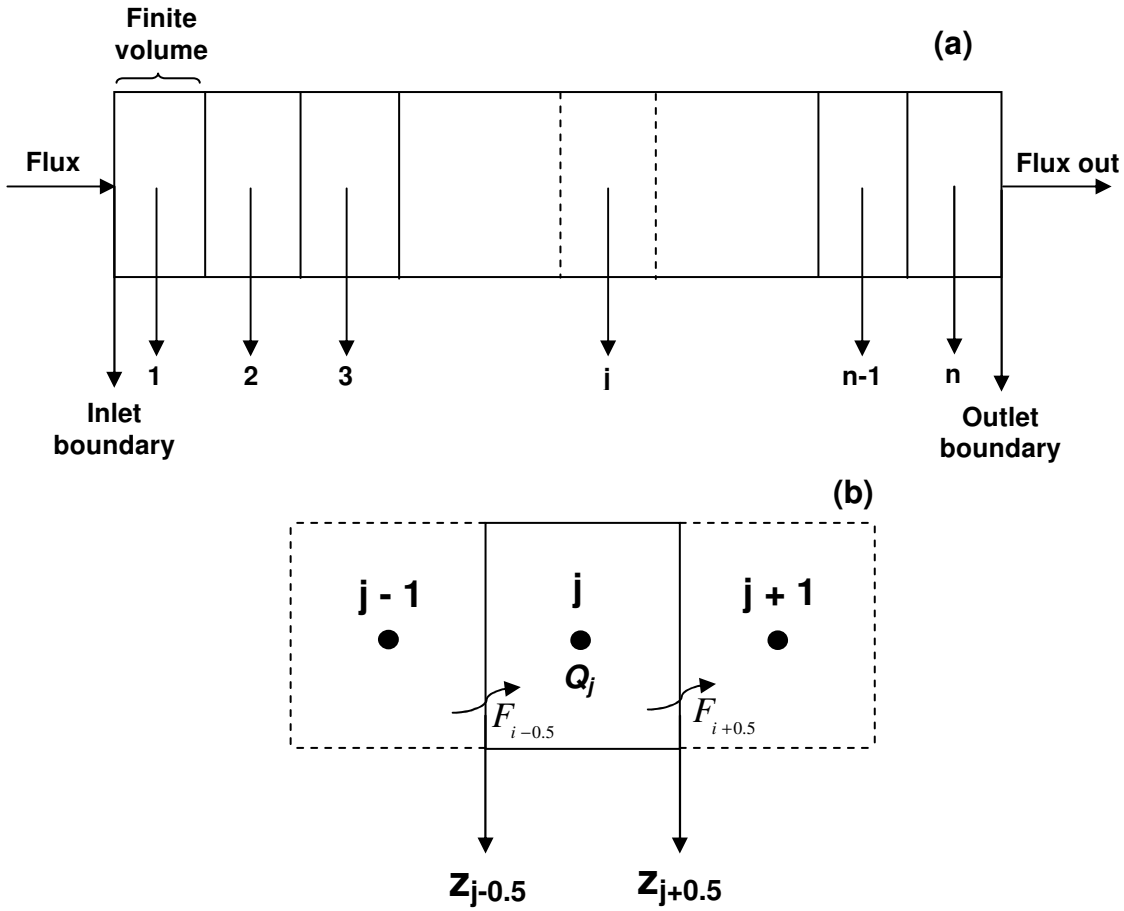

Figure 6.3. (a) Schematic of a column discretized in finite volume, (b) edge fluxes at the inlet and exit of the j^{th} cell.

"Finite volume" or “grid cell” refers to the small volume and the node point is placed exactly in the middle of that the volume element. The value of variable Q_j in Figure 6.3(b) approximates the average value over the j^{th} interval:

$$Q_j \approx \frac{1}{\Delta z}\int_{z_{j-0.5}}^{z_{j+0.5}} q(z)dz \qquad (6-11)$$

where $\Delta z = z_{j+0.5} - z_{j-0.5}$ is the length of the cell and, generally, uniform grid is assumed for

simplicity. The integral in Equation (6-1) can be replaced by the value of q at the midpoint j only if $q(z)$ is a smooth function. However, it is easier to use the cell average properties which are especially important in conservation law in deriving numerical methods (Leveque, 2002).

For hyperbolic problems, the information within the cell spreads with finite speed. Therefore, flux term at the boundary can be obtained from the cell average on either side of the interface as follows:

$$F_{j-0.5} = G\left(Q_{j-1}, Q_j\right) \quad \& \quad F_{j+0.5} = G\left(Q_j, Q_{j+1}\right) \tag{6-12}$$

where G is some numerical flux function. A first attempt to define the average flux at $z_{j-0.5}$ or $z_{j+0.5}$ might be the simple arithmetic average:

$$F_{j-0.5} = G\left(Q_{j-1}, Q_j\right) = \frac{1}{2}\left[g\left(Q_{j-1}\right) + g\left(Q_j\right)\right] \tag{6-13}$$

and

$$F_{j+0.5} = G\left(Q_j, Q_{j+1}\right) = \frac{1}{2}\left[g\left(Q_j\right) + g\left(Q_{j+1}\right)\right] \tag{6-14}$$

Unfortunately, this method (arithmetic averaging) is commonly unstable for most of the hyperbolic problems. Thus, more accurate estimation should be implemented to find the edge values. Therefore, the combination of any low-order flux formula $G_L\left(Q_{j-1}, Q_j\right)$ and high-order flux formula $G_H\left(Q_{j-1}, Q_j\right)$ is considered and named as flux-limiter method as follows:

$$F_{j-0.5} = G_L\left(Q_j, Q_{j+1}\right) + \phi_{j-0.5}\left[G_H\left(Q_j, Q_{j+1}\right) - G_L\left(Q_j, Q_{j+1}\right)\right] \tag{6-15}$$

If $\phi_{j-0.5}=0$, then $F_{j-0.5}$ reduces to the low-order (slope limiter) method and if $\phi_{j-0.5}=1$, high-order (flux limiter) method is obtained (Leveque, 2004; Boris and Book, 1973). In case sharp discontinuity is present in the system, high resolution total diminishing (TVD) or weighted essentially non-oscillatory (WENO) method are used (Randall, 2002). Flux limiters are actually used to eliminate the effect of non-physical oscillations and limit the solution gradient near shocks or discontinuities. van Leer and Superbee are two types of TVD scheme. The edge fluxes of the j^{th} cell (Figure 6.4.b) can be obtained using these schemes. The detail structure of van Leer and WENO schemes are discussed in the following paragraphs.

In van Leer method, which was first developed by Bram van Leer (1979), the edge fluxes can be obtained by the following equations:

$$F_{j+0.5}=F_j+\frac{1}{2}\phi\left(r_{j+0.5}\right)\left(F_{j+1}-F_j\right) \qquad (6-16)$$

$$r_{j+0.5}=\frac{F_j-F_{j-1}+\delta}{F_{j+1}-F_j+\delta} \qquad (6-17)$$

$$\phi\left(r_{j+0.5}\right)=\frac{r_{j+0.5}+\left|r_{j+0.5}\right|}{1+\left|r_{j+0.5}\right|} \qquad (6-18)$$

For inlet boundary:

$$r_{1+0.5}=\frac{2\left(F_1-F_{0.5}\right)+\delta}{F_2-F_1+\delta} \qquad (6-19)$$

The first WENO scheme was constructed by Lin et al. (1994) for a one dimensional problem and, it was further improved by Hu and Shu (1999). The WENO method can be applied in a one dimensional system using the following equations:

$$F_{j+0.5}=0.5\,\frac{\alpha_{0,j}}{\alpha_{0,j}+\alpha_{1,j}}\left(F_j+F_{j+1}\right)+\frac{\alpha_{1,j}}{\alpha_{0,j}+\alpha_{1,j}}\left(1.5F_j+0.5F_{j-1}\right) \qquad (6-20)$$

$$\alpha_{1,j} = \frac{2/3}{\left(F_{j+1} - F_j + \delta\right)^4} \qquad (6-21)$$

$$\alpha_{0,j} = \frac{1/3}{\left(F_j - F_{j-1} + \delta\right)^4} \qquad (6-22)$$

In this study, it was observed that in both WENO and van Leer methods, the bed profiles in VSA simulation did not show any detectable change beyond 30 volume elements. However, WENO required less computer time than van Leer. The simulation time for modeling of a VSA process with 100 cycles using WENO method was about 3700s while, the same simulation using van Leer method took about 4500s in the same computer mentioned earlier. Therefore, the WENO scheme was used for finite volume modeling in this study. Bed profiles after reaching cyclic steady state obtained by the WENO method for 10, 20, 30 and 50 volume elements have been shown in Figure 6.4 (a). The breakthrough model solution using different numbers of volume elements are also shown in Figure 6.4 (b).

The dimensionless equations for the four-step process and related boundary conditions for each step, discretized in space according to the finite volume scheme, are given in Table 6.1.

Table 6.1. Dimensionless equations for a four-step VSA cycle.

Non-dimensional variables
$t_s = \frac{L}{v_f} \Rightarrow t^* = \frac{t}{t_s}$, $v_s = v_0 \Rightarrow v^* = \frac{v}{v_s}$, $z_s = L \Rightarrow z^* = \frac{z}{z_s}$, $P_s = P_H \Rightarrow P^* = \frac{P}{P_s}$ $q_s = q_s\left(\text{saturation capacity}\right) \Rightarrow \left(q^*\right)^* = \frac{q^*}{q_s}$, $T_s = T_w \Rightarrow T^* = \frac{T}{T_s}$
Dimensionless groups and constants

Table 6.1 (continued)

$$Pe_T = \frac{L v_s}{K_z} \qquad Pe_y = \frac{L v_s}{D_L} \qquad \pi_1 = \frac{1}{Pe_y} \qquad \pi_2 = \frac{R(1-\varepsilon_b) q_s T_s}{\varepsilon_b P_s} \qquad \pi_3 = C_s + C_{pa} q_s \sum_j \bar{q}_j^*$$

$$\pi_4 = \frac{K_Z}{v_s (1-\varepsilon_b) L} = \frac{1}{Pe_T (1-\varepsilon_b)} \qquad \pi_5 = \frac{C_{pg} \varepsilon_b P_s}{T_s (1-\varepsilon_b) R_g} \qquad \pi_6 = \frac{2 h_{in} L}{(1-\varepsilon_b) r_{in} v_s} \qquad \pi_7 = \frac{2 h_{in} L}{(1-\varepsilon_b) r_{in} v_s}$$

$$\pi_8 = \frac{P_s}{v_s L \mu} \qquad \pi_9 = \frac{4}{150} \left(\frac{\varepsilon_b}{1-\varepsilon_b} \right)^2 R_p^2 \qquad \pi_{10} = \frac{P_s}{R_g T_s} = \frac{\pi_5 (1-\varepsilon_b)}{C_{pg} \varepsilon_b}$$

Component mass balance

$$\left(\frac{\partial y_i}{\partial t^*} \right)_j = \left(\frac{y_i}{T^*} \frac{\partial T^*}{\partial t^*} \right)_j - \left(\frac{y_i}{P^*} \frac{\partial P^*}{\partial t^*} \right)_j + \frac{\pi_1}{\Delta z^*} \left(\frac{T^*}{P^*} \right)_j \left[\left(\frac{P^*}{T^*} \right)_{j+0.5} \left(\frac{(y_i)_{j+1} - (y_i)_j}{\Delta z^*} \right) - \left(\frac{P^*}{T^*} \right)_{j-0.5} \left(\frac{(y_i)_j - (y_i)_{j-1}}{\Delta z^*} \right) \right]$$

$$- \frac{T_j^*}{\Delta z^* P_j^*} \left[\left(\frac{y_i P^* v^*}{T^*} \right)_{j+0.5} - \left(\frac{y_i P^* v^*}{T^*} \right)_{i-0.5} \right] - \pi_2 \left(\frac{T^*}{P^*} \right)_j \left(\frac{\partial \bar{q}_i^*}{\partial t^*} \right)_j$$

Total mass balance

$$\left(\frac{\partial P^*}{\partial t^*} \right)_j = \left(\frac{P^*}{T^*} \right)_j \left(\frac{\partial T^*}{\partial t^*} \right)_j - \frac{T_j^*}{\Delta z^*} \left[v^*_{j+0.5} \left(\frac{P^*}{T^*} \right)_{j+0.5} - v^*_{j-0.5} \left(\frac{P^*}{T^*} \right)_{j-0.5} \right] - \pi_2 T_j^* \sum_i \left(\frac{\partial \bar{q}_i^*}{\partial t^*} \right)_j$$

Energy balance

$$\left(\frac{\partial T^*}{\partial t^*} \right)_j = \frac{\pi_4}{\pi_3 \Delta z^{*2}} - \frac{\pi_5}{\pi_1} \left(\frac{\partial P^*}{\partial t^*} \right)_j - \frac{\pi_6}{\pi_3 \Delta z^*} \left[\left(v^* P^* \right)_{j+0.5} - \left(v^* P^* \right)_{j-0.5} \right]$$

$$- \frac{q_s}{\pi_3} \sum_i \left(\frac{\Delta H_i}{T_s} + C_{pa} T_j^* \right) \left(\frac{\partial \bar{q}_i^*}{\partial t^*} \right)_j - \frac{\pi_7}{\pi_3} \left(T_j^* - \frac{T_w}{T_s} \right)$$

Velocity (Darcy equation)

$$v^*_{j+0.5} = \frac{-\pi_8}{\Delta z^*} \pi_9 \left(P^*_{j+1} - P^*_j \right)$$

Mass transfer rate

$$\left(\frac{\partial \bar{q}_i^*}{\partial t^*} \right)_j = k_i t_s \left(\left(q_i^* \right)^* - \bar{q}_i^* \right)_j$$

Equilibrium isotherm

Table 6.1 (continued)

$$\frac{\left(\left(q_i^*\right)^*\right)_j}{q_{si}} = \frac{\frac{\pi_{10} P_j^*}{T_j^*}\left(b_i y_i\right)_j}{1+\frac{\pi_{10} P_j^*}{T_j^*}\sum_i \left(b_i y_i\right)_j}$$		
Boundary conditions		
Step	$z^*=0$	$z^*=1$
Pressurization	$\left.\frac{\partial y_i}{\partial z^*}\right\|_{z=0^+} = -Pe_y\, v_0^*(y_{i,feed} - y_{i,0.5})$ $\Rightarrow \quad y_{i,0.5} = \frac{y_{i,1} + y_{i,feed}\frac{Pe_y v_0^* \Delta z^*}{2}}{1+\frac{Pe_y v_0^* \Delta z^*}{2}}$ $\left.\frac{\partial T^*}{\partial t^*}\right\|_{z=0^+} = -Pe_T\, v_0^*(T_{feed} - T_{0.5})$ $\Rightarrow \quad T_{0.5}^* = \frac{T_1^* + T_{feed}^*\frac{Pe_T v_0^* \Delta z^*}{2}}{1+\frac{Pe_T v_0^* \Delta z^*}{2}}$ $P_{0.5}^* = P_H^* + \left(P_L^* - P_H^*\right)\exp\left(-\alpha t^* t_s\right)$ from Darcy's law: $v_{0.5}^* = \frac{-2\pi_8}{\Delta z^*}\pi_9\left(P_1^* - P_{0.5}^*\right)$	$\left.\frac{\partial y_i}{\partial z^*}\right\|_{z=1^-} = 0$ $\Rightarrow \quad y_{i,n+0.5} = y_{i,n}$ $\left.\frac{\partial T^*}{\partial t^*}\right\|_{z=1^-} = 0$ $\Rightarrow \quad T_{n+0.5}^* = T_n^*$ $v_{n+0.5}^* = 0 \Rightarrow \left.\frac{\partial P^*}{\partial z^*}\right\|_{z^*=L^-} = 0$ $\Rightarrow \quad P_{n+0.5}^* = P_n^*$
Adsorption	$\left.\frac{\partial y_i}{\partial z^*}\right\|_{z=0^+} = -Pe_y\, v_0^*(y_{i,feed} - y_{i,0.5})$ $\Rightarrow \quad y_{i,0.5} = \frac{y_{i,1} + y_{i,feed}\frac{Pe_y v_0^* \Delta z^*}{2}}{1+\frac{Pe_y v_0^* \Delta z^*}{2}}$ $\left.\frac{\partial T^*}{\partial t^*}\right\|_{z=0^+} = -Pe_T\, v_0^*(T_{feed} - T_{0.5})$ $\Rightarrow \quad T_{0.5}^* = \frac{T_1^* + T_{feed}^*\frac{Pe_T v_0^* \Delta z^*}{2}}{1+\frac{Pe_T v_0^* \Delta z^*}{2}}$	$\left.\frac{\partial y_i}{\partial z^*}\right\|_{z=1^-} = 0$ $\Rightarrow \quad y_{i,n+0.5} = y_{i,n}$ $\left.\frac{\partial T^*}{\partial t^*}\right\|_{z=1^-} = 0$ $\Rightarrow \quad T_{n+0.5}^* = T_n^*$ $P_{n+0.5}^* = 1$

Table 6.1 (continued)

	$P_{0.5} = P_1 + \dfrac{\Delta z^*}{\pi_8 \pi_9}$	
Blowdown	$\left.\dfrac{\partial y_i}{\partial z^*}\right\|_{z=0^+} = 0$ $\Rightarrow \quad y_{i,0.5} = y_{i,1}$ $\left.\dfrac{\partial T^*}{\partial t^*}\right\|_{z=0^+} = 0$ $\Rightarrow \quad T^*_{0.5} = T^*_1$ $v^*_{0.5} = 0 \Rightarrow \left.\dfrac{\partial P^*}{\partial z^*}\right\|_{z^*=0^+} = 0$ $\Rightarrow \quad P^*_{0.5} = P^*_1$	$\left.\dfrac{\partial y_i}{\partial z^*}\right\|_{z=1^-} = 0$ $\Rightarrow \quad y_{i,n+0.5} = y_{i,n}$ $\left.\dfrac{\partial T^*}{\partial t^*}\right\|_{z=1^-} = 0$ $\Rightarrow \quad T^*_{n+0.5} = T^*_n$ $P^*_{n+0.5} = P^*_I + \left(P^*_H - P^*_I\right)\exp\left(-\alpha t^* t_s\right)$ from Darcy's law: $v^*_{n+0.5} = \dfrac{-2\pi_8}{\Delta z^*}\pi_9\left(P^*_{n+0.5} - P^*_n\right)$
Evacuation	$\left.\dfrac{\partial y_i}{\partial z^*}\right\|_{z=0^+} = 0$ $\Rightarrow \quad y_{i,0.5} = y_{i,1}$ $\left.\dfrac{\partial T^*_j}{\partial t^*}\right\|_{z=0^+} = 0$ $\Rightarrow \quad T^*_{0.5} = T^*_1$ $P^*_{0.5} = P^*_L + \left(P^*_I - P^*_L\right)\exp\left(-\alpha t^* t_s\right)$ from Darcy's law: $v^*_{0.5} = \dfrac{-2\pi_8}{\Delta z^*}\pi_9\left(P^*_1 - P^*_{0.5}\right)$	$\left.\dfrac{\partial y_i}{\partial z^*}\right\|_{z=1^-} = 0$ $\Rightarrow \quad y_{i,n+0.5} = y_{i,n}$ $\left.\dfrac{\partial T^*}{\partial t^*}\right\|_{z=1^-} = 0$ $\Rightarrow \quad T^*_{n+0.5} = T^*_n$ $v^*_{n+0.5} = 0 \Rightarrow \left.\dfrac{\partial P^*}{\partial z^*}\right\|_{z^*=1^-} = 0$ $\Rightarrow \quad P^*_{n+0.5} = P^*_n$

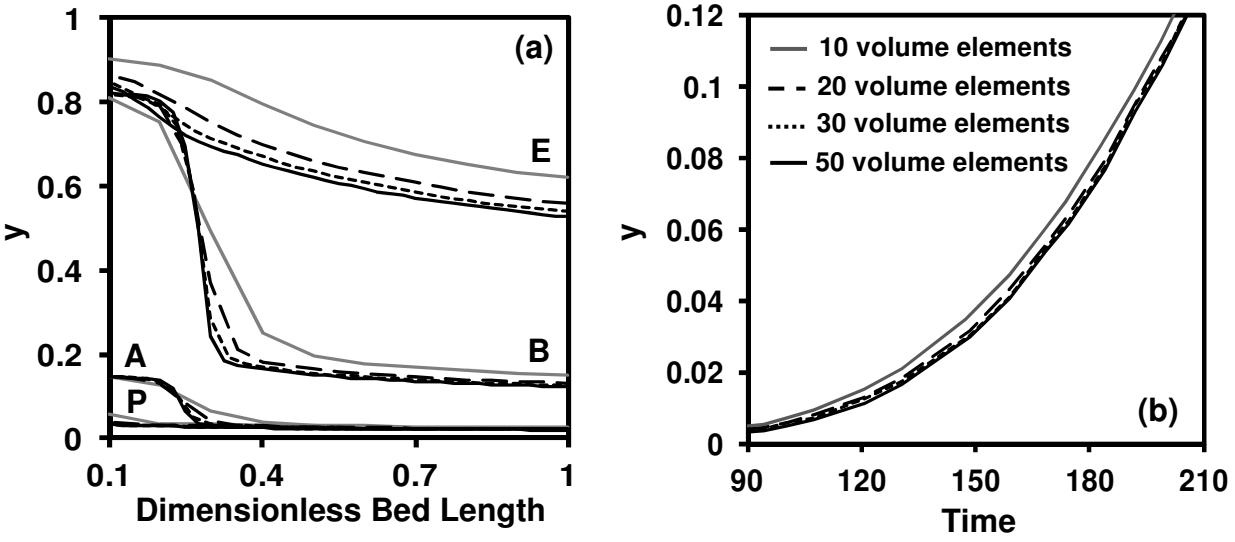

Figure 6.4 (a) Simulated VSA process bed profiles using different number of volume elements. P, A, B and E represent pressurization, adsorption, blowdown and evacuation steps, respectively. (b) Breakthrough finite volume model solution using different number of volume elements. These results are for CO_2/N_2 mixture in Cu-BTC.

6.2 Binary Breakthrough Study

Two important assumptions used in VSA simulation are (i) use of binary extension of the equilibrium isotherm using single component parameters in Table 4.3 and (ii) macropore molecular diffusion and film resistance controlled transport mechanism established from single component experiments to be valid under binary conditions. Limited binary breakthrough experiments were conducted for 30:70 and 50:50 CO_2/N_2 and CH_4/N_2 mixtures at 2 bar and 296.15 K to validate these assumptions. The same experimental set-up and adsorption column used for single component breakthrough study, detailed in chapter 5, was used. The adsorbents properties used in the simulations were same as those in Table 5.1. Various physical properties of the binary mixtures used in the simulations are compiled in Table 6.2 and bed parameters and operating conditions are presented in Table 6.3. The experimental breakthrough results and non-isothermal model predictions are shown in Figure 6.5, 6.6, 6.7 and 6.8. Moreover, the experimental and model predictions of the column midpoint temperatures are also shown in the same figures. The model equations for the high

pressure adsorption step, detailed earlier and solved numerically using the finite volume method, were directly applicable for the breakthrough study.

Table 6.2. Physical properties of adsorbate mixtures used in the breakthrough and VSA simulations.

Physical properties						
Adsorbates						
Gas	D_m [a] $\left(m^2 s^{-1}\right)$	K_g [b] $\left(\frac{W}{m.K}\right)$		C_{pg} [c] $\left(\frac{J}{mol.K}\right)$		μ [c] $(Poise)$
		296.15K	313.15 K	296.15K	313.15 K	296.15K
N_2:CO_2	8.05e-6	1.63e-2	1.76e-2	37.33	38.51	1.67 e-4
N_2:CH_4	1.10e-5	3.36e-2	3.59e-2	36.59	37.42	1.58 e-4

Table 6.3. Bed parameters and operating conditions in VSA simulation.

Bed parameters		Operating conditions	
$L\ (m)$	1.00	$T\ (K)$	296.15
		$P_H\ (bar)$	1*1.013
$r_i\ (m)$	14.45e-2	$P_I\ (bar)$	(0.07-0.25)*1.013
		$P_L\ (bar)$	(0.005-0.05)*1.013
ε_b	0.37	$t_p(s)$	37.47
		$v_f\ (m/s)$	0.40

a.Molecular diffusivity of the adsorbate gases in He at 1 bar and 298.15 K
b. McCabe et al., 1993. c. Perry and Green, 2008.
d. Huang et al., 2005. e. Song et al., 2009.

For the results in Figure 6.5, the bed was first saturated with pure N_2 and then the CO_2/N_2 mixture was introduced to monitor the breakthrough of CO_2. The amount of adsorbed N_2 that

was in excess due to reduction in its partial pressure in the feed and competition from CO_2 was desorbed while CO_2 was adsorbed. Since the amount of CO_2 adsorbed was much higher than the amount of N_2 desorbed and the former has a higher heat of adsorption, the result was a net increase in temperature. After the bed was saturated with the mixture, the feed was changed back to pure nitrogen and desorption of CO_2 from the bed was monitored. This being the reverse of the previous run, there was a net decrease in the temperature, as expected.

The results in Figure 6.7 are for the breakthrough of CO_2 from 50:50 CO_2:N_2 feed mixture in a bed saturated with 30:70 CO_2:N_2 mixture, and the reverse. Since the net adsorption and desorption amounts are less in these runs compared to those for the runs in Figure 6.6, the temperature changes are comparatively less.

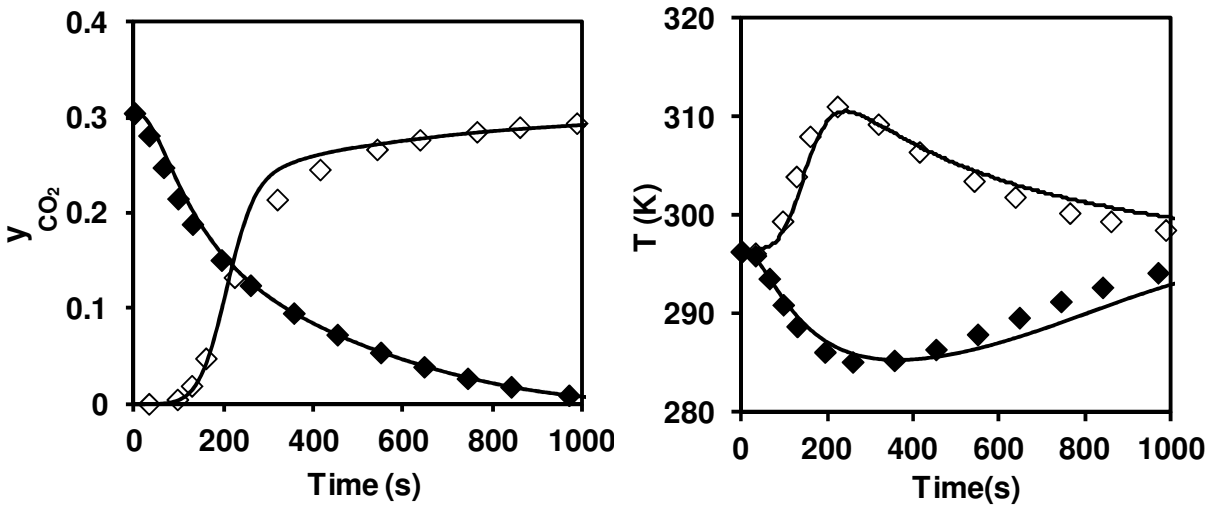

Figure 6.5. Binary breakthrough of CO_2/N_2 mixture in Cu-BTC sample S2 at 2 bar and 296.15 K. The open symbols are experimental results for adsorption breakthrough of CO_2 from a 30:70 CO_2:N_2 mixture fed at 2 bar and 296.15 K to a bed initially saturated with N_2 at 2 bar and 296.15 K. The closed symbols are experimental results for CO_2 desorption when pure N_2 is fed to the bed after saturating it with the mixture. The solid lines are the non-isothermal model predictions.

Although CH_4/N_2 separation was not investigated in this study, still binary breakthrough experiments with mixtures of these two gases in different proportions were carried out to further validate the mixture equilibrium and kinetic models used in the VSA simulation.

CH_4/N_2 mixture breakthrough results, similar to the CO_2/N_2 runs in Figure 6.5, and corresponding model predictions are shown in Figures 6.7 and 6.10 for two different feed compositions. Details are given in the figure captions. Since CH_4 has lower capacity and heat of adsorption compared to CO_2, the temperature changes due to adsorption/desorption seen in Figure 6.7 for 30% CH_4 in the feed were expectedly less than those in Figure 6.5. The temperature changes were higher when the CH_4 amount in the feed was increases to 70%, as may be seen from Figure 6.8.

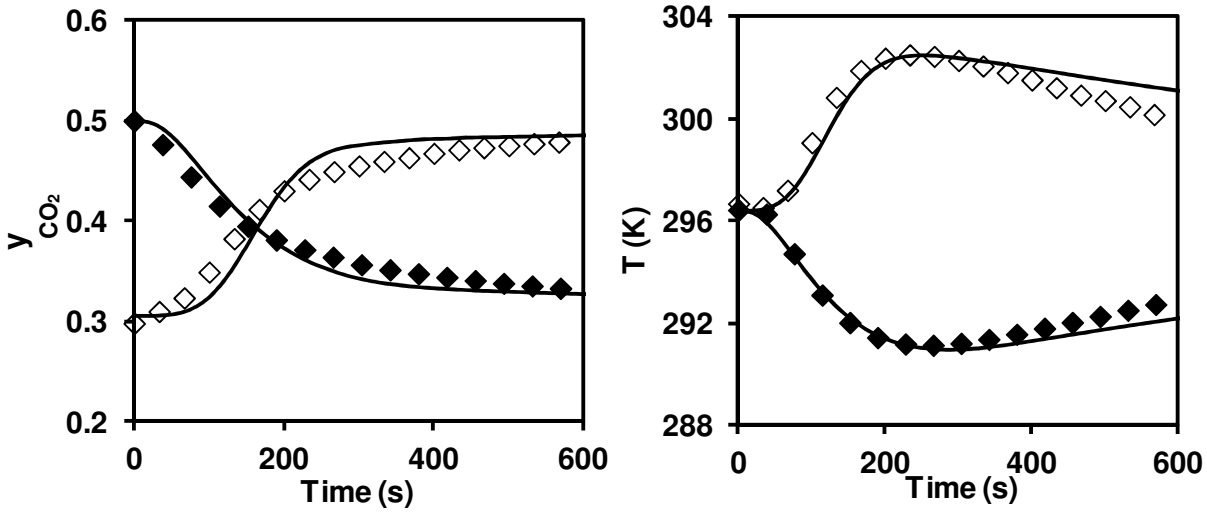

Figure 6.6. Binary breakthrough of CO_2/N_2 mixture in Cu-BTC sample S2 at 2 bar and 296.15 K. The open symbols are experimental results for adsorption breakthrough of CO_2 from a 50:50 CO_2:N_2 mixture fed at 2 bar and 296.15 K to a bed initially saturated with CO_2:N_2 30:70% at 2 bar and 296.15 K. The closed symbols are experimental results for CO_2 desorption when pure N_2 is fed to the bed after saturating it with the mixture. The solid lines are the non-isothermal model predictions.

The simulated and experimentally measured breakthrough and temperature profiles are in good agreement. In addition to using the extended Langmuir isotherm for calculating binary equilibrium, estimation of the LDF mass transfer coefficient for macropore molecular diffusion controlled transport also requires binary equilibrium information at the operating conditions. The good agreements between the simulated and experimental profiles provide some degree of confidence that the two important assumptions used in VSA simulations, mentioned earlier, are indeed reasonable.

6.3 Important Definitions in VSA Process

Before proceeding to PSA/VSA process simulation Some important process performance indicators are defined first for capture and concentration of CO_2 from flue gas , which is obtained as the raffinate product in the evacuation step.

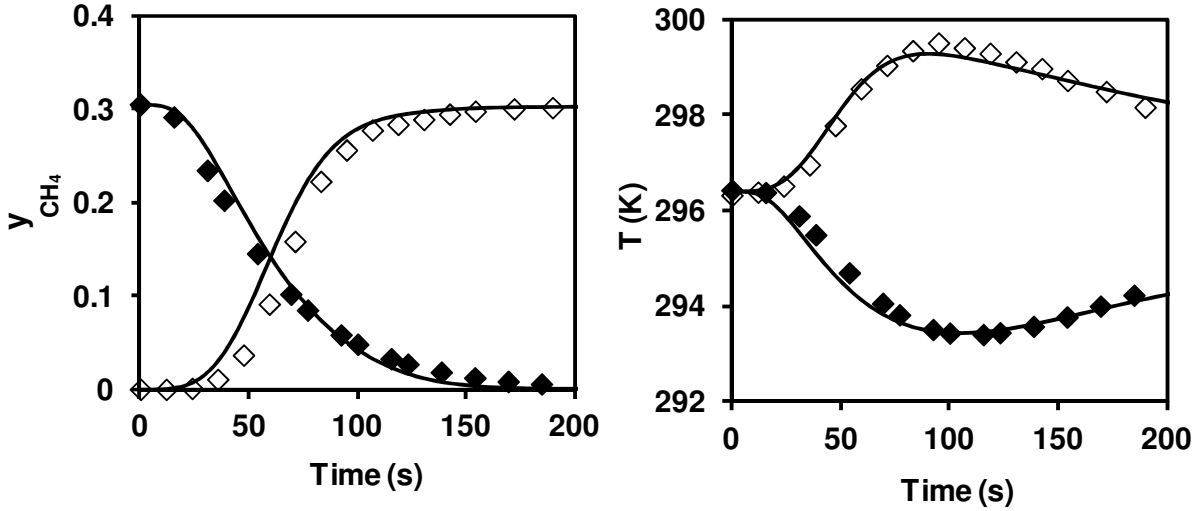

Figure 6.7. Binary breakthrough of CH_4/N_2 mixture in Cu-BTC sample S2 at 2 bar and 296.15 K. The open symbols are experimental results for adsorption breakthrough of CH_4 from a 30:70 CH_4:N_2 mixture fed at 2 bar and 296.15 K to a bed initially saturated with N_2 at 2 bar and 296.15 K. The closed symbols are experimental results for CH_4 desorption when pure N_2 is fed to the bed after saturating it with the mixture. The solid lines are the non-isothermal model predictions.

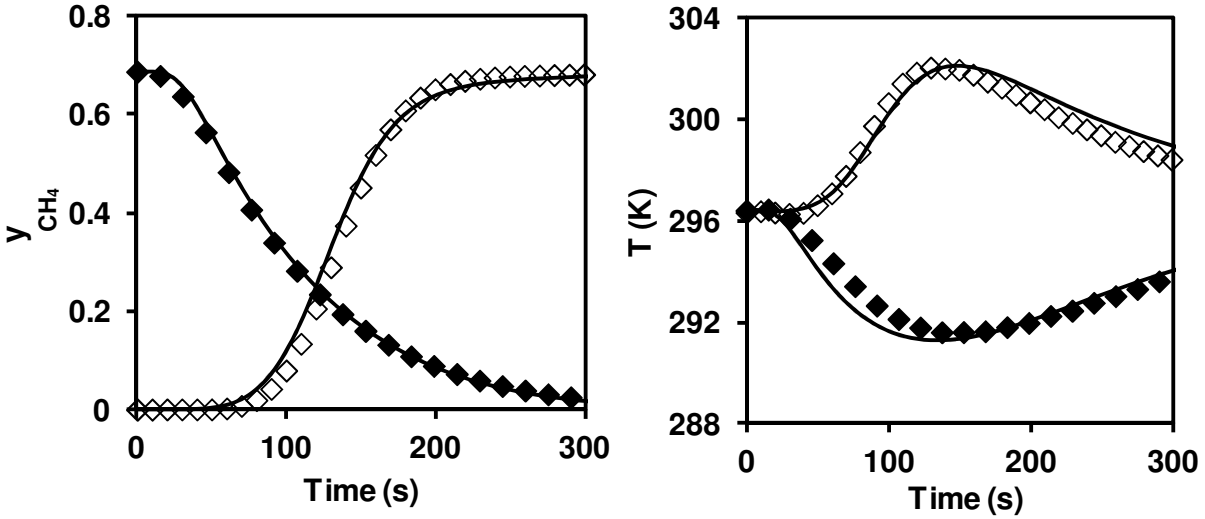

Figure 6.8. Binary breakthrough of CH_4/N_2 mixture in Cu-BTC sample S2 at 2 bar and 296.15 K. The open symbols are experimental results for adsorption breakthrough of CH_4 from a 70:30 CH_4:N_2 mixture fed at 2 bar and 296.15 K to a bed initially saturated with N_2 at 2 bar and 296.15 K. The closed symbols are experimental results for CH_4 desorption when pure N_2 is fed to the bed after saturating it with the mixture. The solid lines are the non-isothermal model predictions.

$$\sum \text{Moles in } CO_2 = \text{Moles in } CO_2\big|_{\text{p}} + \text{Moles in } CO_2\big|_{\text{a}} \qquad (6-23)$$

$$\sum \text{Moles out } CO_2 = \text{Moles out } CO_2\big|_{\text{a}} + \text{Moles out } CO_2\big|_{\text{b}} + \text{Moles out } CO_2\big|_{\text{e}} \qquad (6-24)$$

$$\text{Moles in } CO_2 = \pi_{10} v_s \varepsilon_b A \int_0^{t^*} v_{0.5}{}^*\left(t^*\right) \frac{y_{feed} P_{0.5}{}^*\left(t^*\right)}{T_{0.5}{}^*\left(t^*\right)} dt^* \qquad (6-25)$$

$$\text{Moles out } CO_2 = \pi_{10} v_s \varepsilon_b A \int_0^{t^*} v_{n+0.5}{}^*\left(t^*\right) \frac{y_{n+0.5} P_{n+0.5}{}^*\left(t^*\right)}{T_{n+0.5}{}^*\left(t^*\right)} dt^* \qquad (6-26)$$

$$\text{for reverse evacuation} \Rightarrow \text{Moles out } CO_2 = \pi_{10} v_s \varepsilon_b A \int_0^{t^*} v_{0.5}{}^*\left(t^*\right) \frac{y_{0.5} P_{0.5}{}^*\left(t^*\right)}{T_{0.5}{}^*\left(t^*\right)} dt^*$$

$$\Rightarrow \text{Total Moles out} = \pi_{10} v_s \varepsilon_b A \int_0^{t^*} v_{0.5}{}^*\left(t^*\right) \frac{P_{0.5}{}^*\left(t^*\right)}{T_{0.5}{}^*\left(t^*\right)} dt^* \qquad (6-27)$$

$$\text{Purity}(\%) = \frac{\text{moles of } CO_2 \text{ in the evacuation stream}}{\text{Total moles of gas in the evacuation stream}} * 100\% \qquad (6-28)$$

$$\text{Recovery}(\%) = \frac{\text{moles of } CO_2 \text{ in the evacuation stream}}{\text{moles of } CO_2 \text{ entering the pressurization and adsorption steps}} * 100\% \qquad (6-29)$$

6.4 Parametric Study of the VSA Process

As it was mentioned in the previous section, the performance of VSA process was investigated in terms of common indicators such as purity and recovery of CO_2. The simulation runs were conducted up to a large number of cycle (100 cycles in this study) in order for the system to reach cyclic steady state. Mass balance error less than 0.5% was the criteria used to confirm steady state condition. Mass balance error in this study was obtained from the following equation:

$$\text{Mass balance error}(\%) = \qquad (6-30)$$

$$\frac{\left(\text{Moles in } CO_2\big|_{\text{a}} + \text{Moles in } CO_2\big|_{p}\right) - \left(\text{Moles out } CO_2\big|_{a} + \text{Moles out } CO_2\big|_{\text{b}} + \text{Moles out } CO_2\big|_{\text{e}}\right)}{\left(\text{Moles in } CO_2\big|_{\text{a}} + \text{Moles in } CO_2\big|_{p}\right)} * 100$$

The adsorbent parameters given in Table 5.1 and physical properties of the CO_2/N_2 mixture compiled in Table 6.2 were also used in the VSA simulations. The input bed parameters and the range of process parameters investigated are listed in Table 6.3 The interstitial feed velocity and column size given in this table are representative of a pilot plant study on a commercial adsorbent currently in progress in our research group.

The effects of various independent process parameters, namely, adsorption time (t_a), blowdown time (t_b), evacuation time (t_e), system intermediate pressure (P_I) and system low pressure (P_L) on the performance of the VSA process are discussed in the following sections. The study was carried out by varying one parameter at a time while keeping the other parameters fixed.

6.4.1 Adsorption Time (t_a)

The duration for the adsorption step was increased from 37 to 150 seconds. The simulation results of purity and recovery of CO_2 are plotted as a function of adsorption time (t_a) in Figure 6.9. The purity increased monotonically with increasing adsorption time, but the recovery first increased with increasing adsorption time reaching a maxima before beginning to drop with further increase in the adsorption time. By increasing adsorption time, CO_2 front penetrates deeper into the adsorber leaving less capacity for co-adsorbed N_2, which explains the monotonic rise in CO_2 purity in the evacuation step. Deeper penetration of CO_2 with increasing adsorption time also increases CO_2 loss in the forward blowdown step. Further, spreading of the CO_2 front during the forward blowdown step also increases CO_2 loss in the high pressure adsorption step. These losses lead to the declining part of the recovery vs. t_a plot in Figure 6.9. The gas phase bed profiles for each step after reaching the cyclic steady state are shown in Figure 6.10 for different adsorption step durations. Deeper penetration of the CO_2 front at the end of the adsorption step and increasing losses (indicated by higher CO_2

mole fraction at the column exit) during forward blowdown step with increasing adsorption step duration are clearly seen in the figure. The increasing loss of CO_2 in the adsorption step is also clear from the insert showing the exit CO_2 mole fraction at the end of this step plotted with a magnified y axis as a function of the adsorption time.

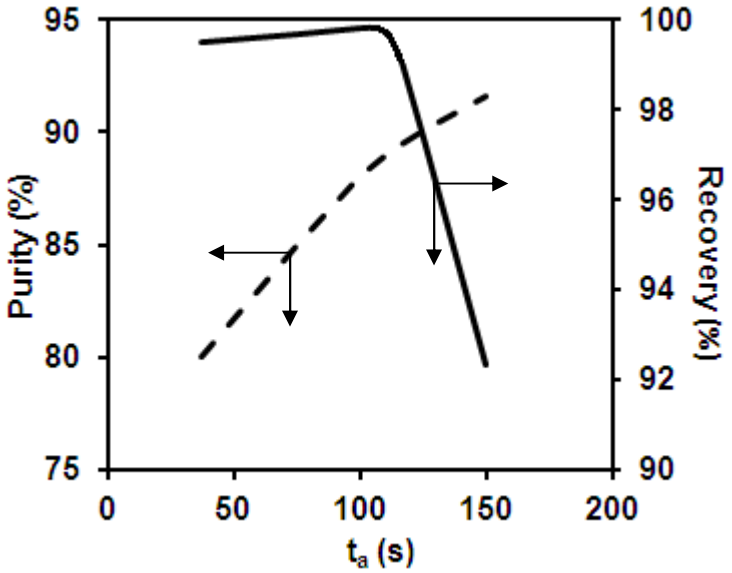

Figure 6.9 Effect of adsorption time (t_a) on simulated purity and recovery of CO_2 in VSA process using Cu-BTC (sample S2) adsorbent. The other process parameters are $t_b = 74.94s$, $t_e = 74.94s$, $P_I = 0.14bar$ and $P_L = 0.01bar$.

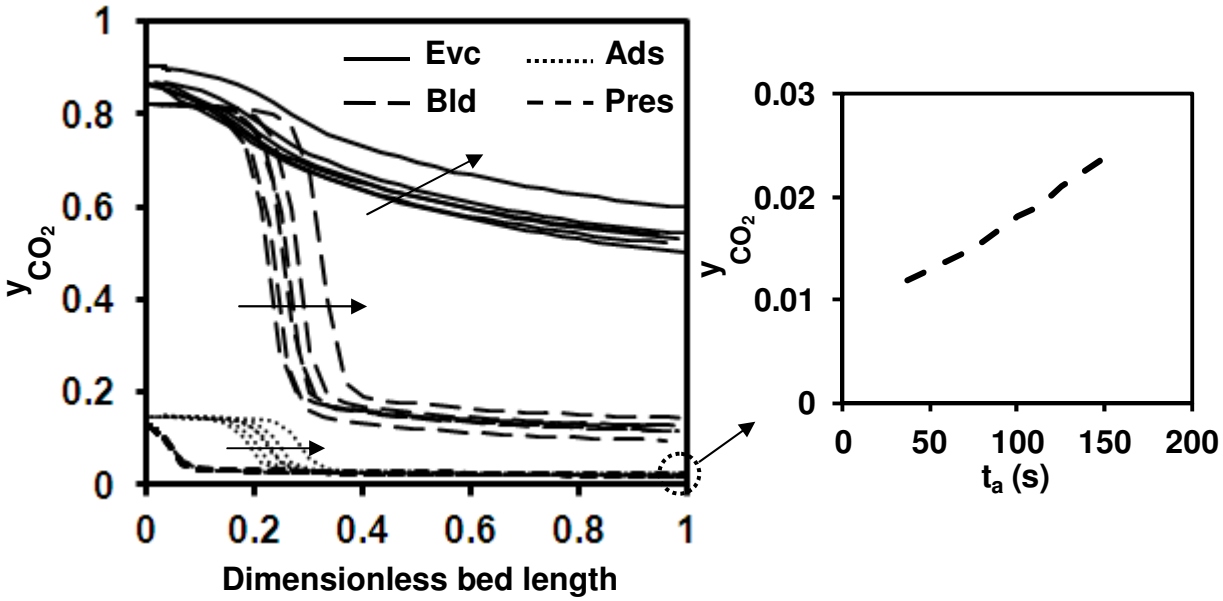

Figure 6.10. Gas phase bed profiles after reaching the cyclic steady state. The arrows show the direction of increasing t_a. The process parameters are $t_b = 74.94s$, $t_e = 74.94s$, $P_I = 0.14bar$ and $P_L = 0.01bar$. The insert shows exit CO_2 mole fraction at the end of the adsorption step plotted on a magnified y axis as a function of adsorption time.

6.4.2 Blowdown Time (t_b)

The best parameters (except t_b) obtained from the previous section, which simultaneously gave the purity and recovery of more than 90%, were fixed, and the effect of changing the blowdown step time was studied. Blowdown step duration was increased from 50 to 125 seconds. The negligible effect on purity and recovery are shown in Figure 6.11 The reason is the minimum time of 50 seconds used for blowdown step was long enough for the desorption (due to a change in pressure from 1 to 0.14 bar) to be nearly complete. Further increasing the duration of this step did not significantly change the loading of either N_2 or CO_2, which is evident from the steady state adsorbed phase profiles shown in Figure 6.12. As a result, both purity and recovery remained practically unchanged by changing the blowdown step duration in the range 50 to 125 seconds.

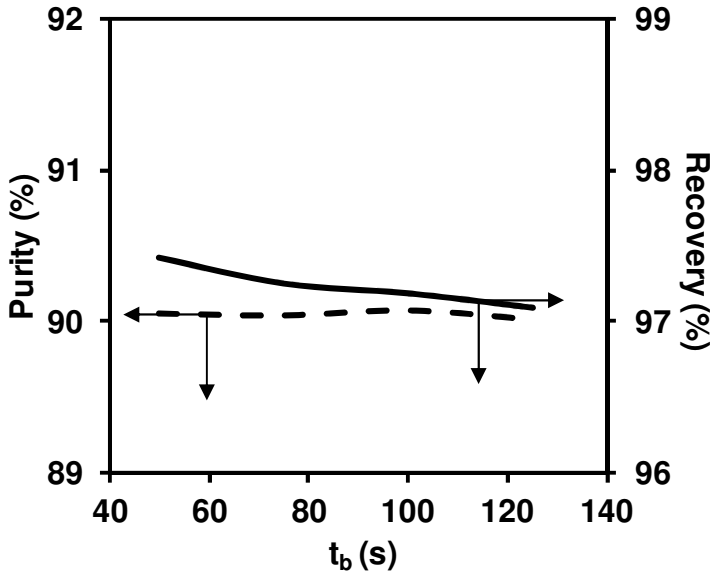

Figure 6.11. Effect of blowdown time (t_b) on simulated purity and recovery of CO_2 in VSA process using sample S2 adsorbent. The other process parameters are $t_a = 124.9s$, $t_e = 74.94s$, $P_I = 0.14bar$ and $P_L = 0.01bar$.

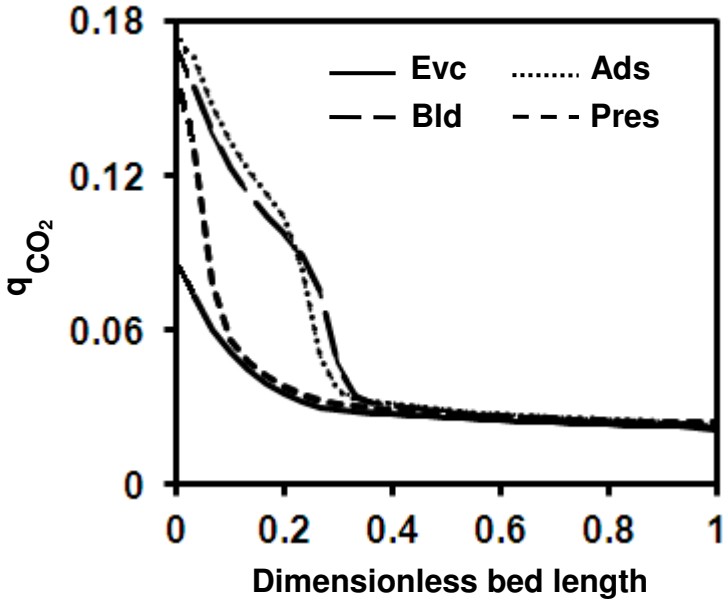

Figure 6.12. Adsorbed phase bed profiles after reaching the cyclic steady state. Four t_b cases (50, 74.9, 100 and 125 seconds) are shown here and the profiles are not significantly changed. The process parameters are $t_a = 124.9s$, $t_e = 74.94s$, $P_I = 0.14bar$ and $P_L = 0.01bar$.

6.4.3 Evacuation Time (t_e)

In the evacuation step the raffinate product, CO_2, is obtained by evacuating the column to a very low pressure, P_L. At a given low pressure, the effect of increasing the evacuation time from 50 to 150 seconds on purity and recovery was simulated. The results are shown in Figure 6.13. Since the CO_2 isotherm is quite nonlinear at its partial pressure in the feed, its desorption is slow. Hence, providing longer time allows more CO_2 to be desorbed resulting in increased recovery, but the increase is not very large. The increase in purity is even less. Mole fraction of CO_2 in the evacuation stream is shown as a function of time for different t_e in Figure 6.14. As may be seen from the figure, by increasing the evacuation time from 50 seconds onward, the CO_2 mole fraction in the evacuation stream does not change much.

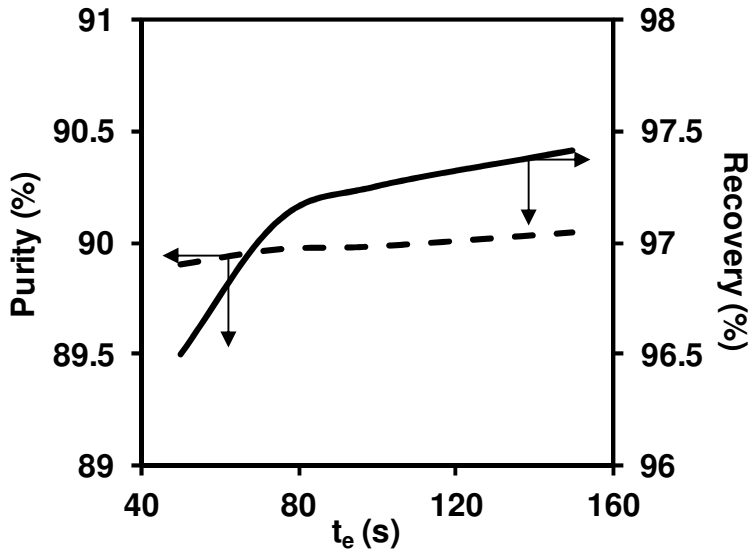

Figure 6.13. Effect of evacuation time (t_e) on simulated purity and recovery of CO_2 in VSA process using sample S2 adsorbent. The other process parameters are $t_a = 124.9s$, $t_b = 74.94s$, $P_I = 0.14bar$ and $P_L = 0.01bar$.

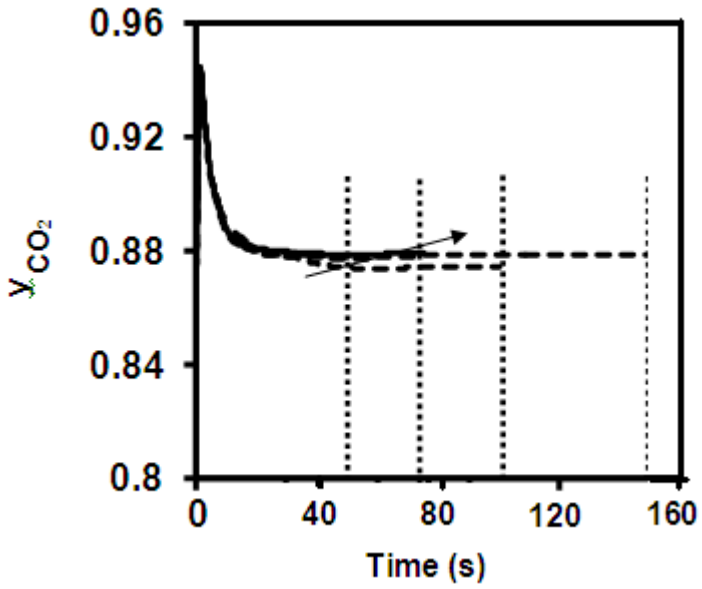

Figure 6.14. CO_2 mole fraction in the evacuation stream as a function of time. The arrow shows the direction of increasing t_e (50, 75, 100 and 150 seconds). The process parameters are $t_a = 124.9s$, $t_b = 74.94s$, $P_I = 0.14bar$ and $P_L = 0.01bar$.

6.4.4 Blowdown Pressure (P_I)

The role of the blowdown step is to remove as much of the co-adsorbed N_2 as possible while minimizing loss of CO_2. Such a delicate balance is necessary to ensure high purity and recovery of CO_2 in the evacuation step. There are two operating variables for the blowdown

step, its duration and the pressure level at the end of this step, P_I. It has been shown in Figure 6.11 that the purity and recovery are not very sensitive to the step duration beyond 50 seconds. The effect of blowdown pressure on purity and recovery of CO_2 is shown in Figure 6.15. As expected, CO_2 purity increases and its recovery decreases with decreasing blowdown pressure. This is because by decreasing the blowdown pressure more and more CO_2 is lost along with N_2 removal from the bed, which is clear from the plot of CO_2 mole fraction in the gas leaving the bed during blowdown plotted as a function of time in Figure 6.16.

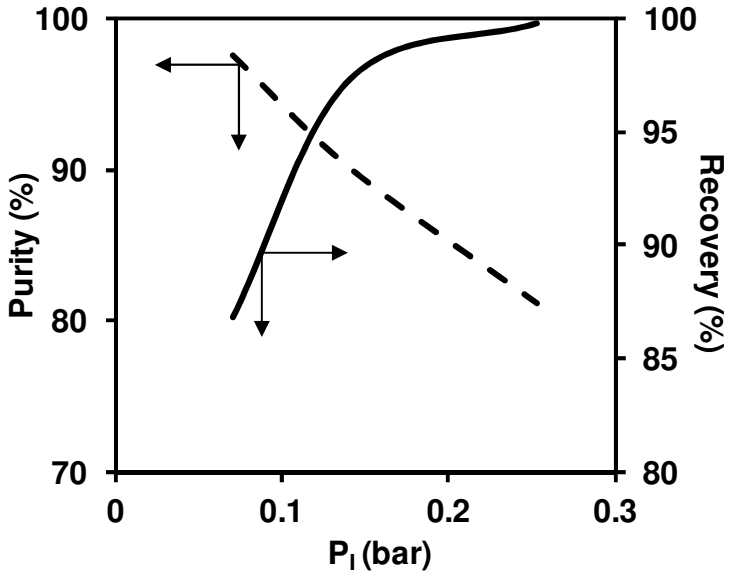

Figure 6.15. Effect of blowdown pressure (P_I) on simulated purity and recovery of CO_2 in VSA process using sample S2 adsorbent. The other process parameters are $t_a = 124.9s$, $t_b = 74.94s$, $t_e = 74.94s$ and $P_L = 0.01bar$.

6.4.5 Evacuation Pressure (P_L)

The CO_2 purity, recovery plots and its gas concentration profiles along the bed length obtained by changing the evacuation from pressure 0.005 to 0.05 bars are shown in Figures 6.17 and 6.18, respectively.

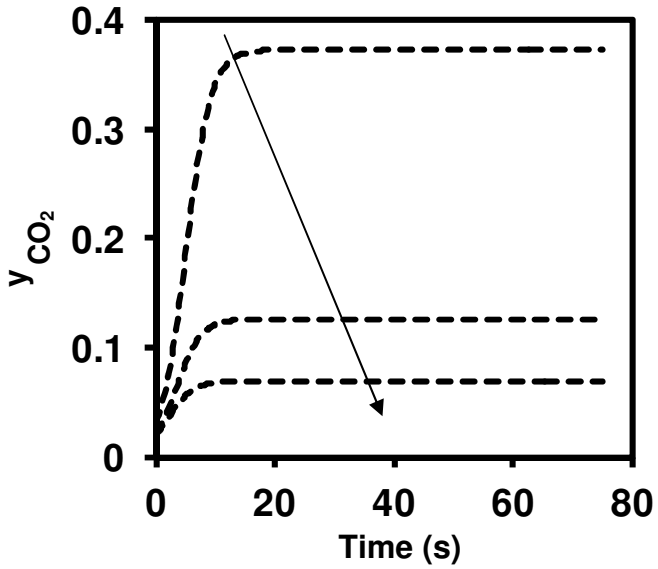

Figure 6.16. CO_2 mole fraction in the evacuation stream. The arrow gives the direction of increasing P_I $(0.07, 0.14 \text{ and } 0.25 bar)$. The process parameters are $t_a = 124.9s$, $t_b = 74.94s$, $t_e = 74.94s$ and $P_L = 0.01 bar$.

The recovery of CO_2 is affected by changing the evacuation pressure. CO_2 recovery first increases by lowering the evacuation and then decreases upon further reduction. This means that there is an optimum for evacuation pressure in this case. It is clear from Figure 6.18 that increasing evacuation pressure keeping everything else constant leads to deeper penetration of the CO_2 front leaves less N_2 in the bed, which increases CO_2 purity. However, it is also clear from Figure 6.18 that CO_2 mole fraction at the exit of the column also increases with increasing P_L during the high pressure adsorption step leading to loss of CO_2 during the blowdown step. As such, the recovery initially increases but further increase in P_L leads to excessive loss of CO_2 from the other end of the bed causing the recovery to drop.

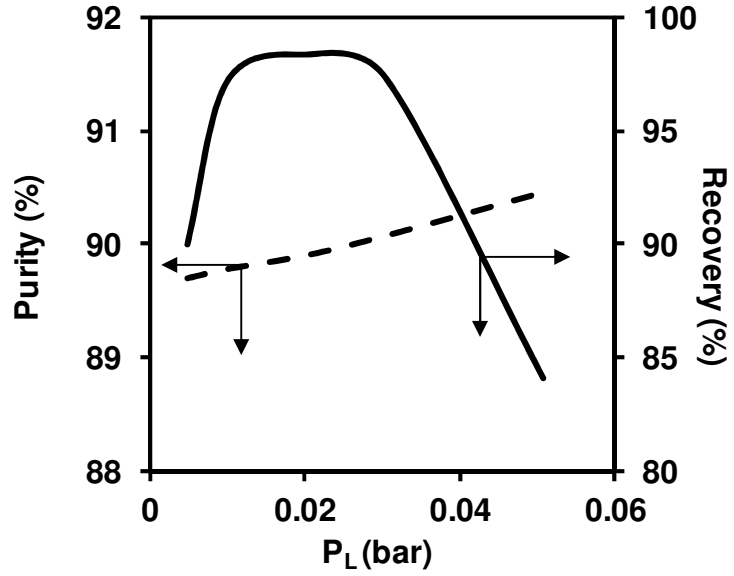

Figure 6.17. Effect of blowdown pressure (P_I) on simulated purity and recovery of CO_2 in VSA process using sample S2 adsorbent. The other process parameters are $t_a = 124.9s$,$t_b = 74.94s$, $t_e = 74.94s$ and $P_I = 0.14bar$.

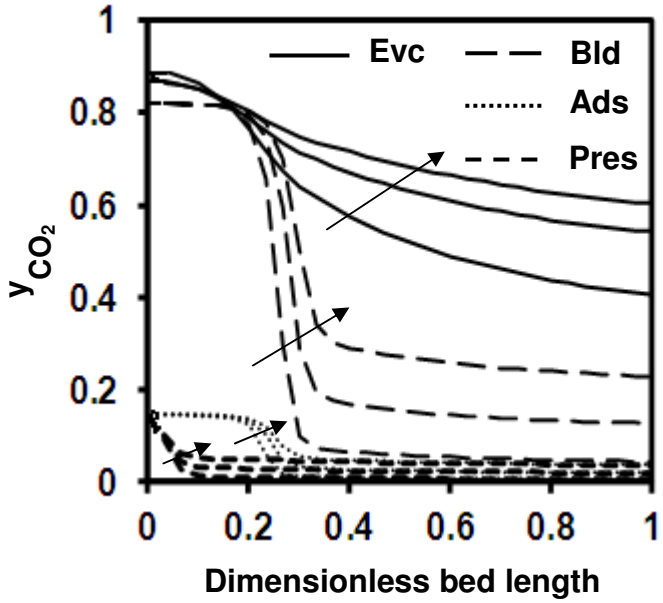

Figure 6.18. Gas phase bed profiles after reaching the cyclic steady state (100 cycles in this case). The arrows show the direction of increasing P_L (0.01, 0.03 and 0.05 bar). The process parameters are $t_a = 124.9s$, $t_b = 74.94s$, $t_e = 74.94s$ and $P_I = 0.14bar$.

6.5 Comparison of Cu-BTC and 13X VSA simulation results

In this section, the performance of two adsorbents, namely 13X zeolite and Cu-BTC, are compared for CO_2 capture and concentration from post combustion coal fired power plant

flue gas in the four-step VSA studied in the previous section. 13X zeolite was chosen because it is currently considered as the best commercial adsorbent for CO_2 capture from flue gas.

The 13X simulation results are adopted from the optimization study by Haghpanah et al. (2013) who used the same four-step VSA CO_2 capture process used in this study. Dual site Langmuir model was used in their study to fit the experimental equilibrium data. LDF model was used to describe the rate equation in their study. They assumed that mass transfer mechanism was controlled by macropore molecular diffusion. They used a non-isothermal, non-isobaric model to fully optimize the process in order to maximize purity and recovery, subject to the following bounds on six process decision variables (P_L: 0.005-0.05 bar, P_I: 0.05-0.5 bar > P_L +*0.01 bar,* t_a: 20-100 s, t_b: 30-200 s, t_e: 30-200 s and v_{feed}: 10-200 cm.s^{-1}). The process parameters shown in Table 6.4 have been chosen from the Pareto of 13X to cover the full spectrum. The run numbers are sorted based on the lowest simulated purity to the highest one in both samples. The purity-recovery results for Cu-BTC computed for these process parameters are compared with the Pareto values of 13X in Figure 6.19.

According to the simulated results shown in Figure 6.19, the performance of Cu-BTC adsorbent is comparable with 13X adsorbent in a four-step VSA cycle under similar operating conditions. CO_2 purity and recovery of about 90% and above (dashed area in Figure 6.19) can be achieved using both adsorbents' parameters in VSA process simulation.

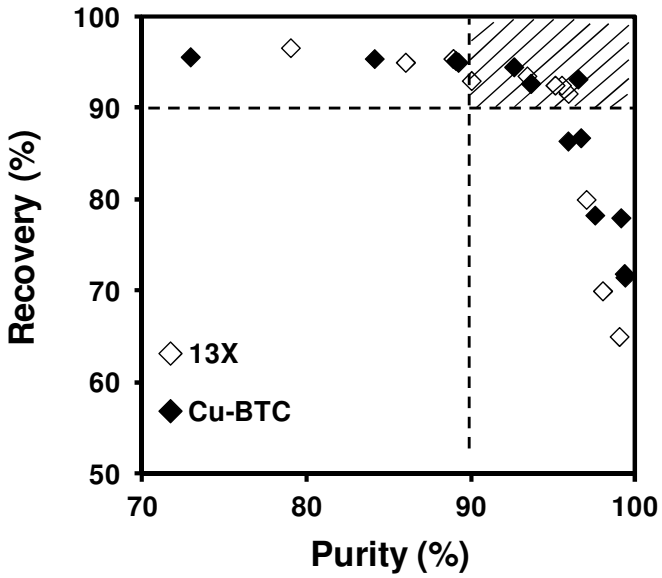

Figure 6.19. Comparison of simulated CO_2 purity-recovery in VSA process using parameters in Table 6.3. Open symbols show 13X and close symbols show Cu-BTC results, respectively.

Table 6.4. VSA simulation parameters for CO_2:N_2 separation process using 13X and Cu-BTC.

Run no.	$t_p(s)$	$t_a(s)$	$t_b(s)$	$t_e(s)$	$P_I(bar)$	$P_L(bar)$	$v_{feed}(m.s^{-1})$
1	18.84	72.21	100.47	109.89	0.231	0.010	0.318
2	18.86	89.61	165.06	89.61	0.118	0.011	0.212
3	19.46	83.90	74.18	162.94	0.096	0.010	0.822
4	19.29	93.26	135.07	90.04	0.089	0.010	0.311
5	19.89	74.58	99.44	170.70	0.099	0.010	0.603
6	19.92	74.99	99.60	171.08	0.099	0.010	0.853
7	19.78	71.94	86.33	196.04	0.073	0.010	0.556
8	20.24	72.11	86.03	180.91	0.083	0.011	0.790
9	19.68	84.33	115.25	75.89	0.116	0.011	0.356
10	20.51	77.73	124.15	199.71	0.067	0.011	0.926
11	19.77	73.83	69.87	171.39	0.087	0.011	1.517
12	20.63	51.57	138.20	169.14	0.109	0.010	0.485
13	20.11	79.85	60.34	160.91	0.099	0.010	1.641

The energy consumption for capturing CO_2 is very important to evaluate an adsorbent for carbon capture and concentration process. The following equations used by Haghpanah et al., (2013) were used to compute energy consumption for each step and the whole cycle for Cu-BTC.

$$W_{p\,or\,a} = \frac{1}{\eta}\,\varepsilon_b\,A\,v_s\,P_s\,\frac{\gamma}{\gamma-1}\int_{t=0}^{t=t_{p\,or\,a}}\left(v_{0.5}{}^{*}\,P_{0.5}{}^{*}\right)\left[\left(\frac{P_s\,P_{0.5}{}^{*}}{P_{flue\,gas}}\right)^{\frac{\gamma-1}{\gamma}}-1\right]dt \qquad (6-31)$$

$$W_b = \frac{1}{\eta}\,\varepsilon_b\,A\,v_s\,P_s\,\frac{\gamma}{\gamma-1}\int_{t=0}^{t=t_b}\left(v_{n+0.5}{}^{*}\,P_{n+0.5}{}^{*}\right)\left[\left(\frac{P_{atm}}{P_s\,P_{n+0.5}{}^{*}}\right)^{\frac{\gamma-1}{\gamma}}-1\right]dt \qquad (6-32)$$

$$W_e = \frac{1}{\eta}\,\varepsilon_b\,A\,v_s\,P_s\,\frac{\gamma}{\gamma-1}\int_{t=0}^{t=t_e}\left(v_{0.5}{}^{*}\,P_{0.5}{}^{*}\right)\left[\left(\frac{P_{atm}}{P_s\,P_{0.5}{}^{*}}\right)^{\frac{\gamma-1}{\gamma}}-1\right]dt \qquad (6-33)$$

$$W_{cycle}\left(\frac{kWh}{tonne\ of\ CO_2\ captured}\right) = \frac{\left(W_p+W_a+W_b+W_e\right)}{3.6*10^6*\text{Moles out }CO_2\big|_e}*\frac{10^6}{44} \qquad (6-34)$$

In the above equations, A, $\eta(=0.72)$ and $\gamma(=1.4)$ are the column cross sectional area, compression efficiency and the adiabatic constant, respectively. Subscripts *p*, *a*, *b* and *e* represent pressurization, adsorption, blowdown and evacuation steps, respectively. In this study, the power consumption in blowdown and evacuation steps are dominant due to the presence of vacuum pump.

The energy consumption for two adsorbents for the purity-recovery results in Figure 6.19 is compared in Figure 6.20. For all of the cases, 13X adsorbent has higher energy consumption compared to Cu-BTC.

A fair comparison will be to study the full optimization of the four-step VSA process for both the adsorbents to minimize energy and maximize productivity with the constraints that purity-recovery must be at least 90%. The energy-productivity Pareto thus obtained can only confirm which one between 13X and Cu-BTC will have a better energy advantage.

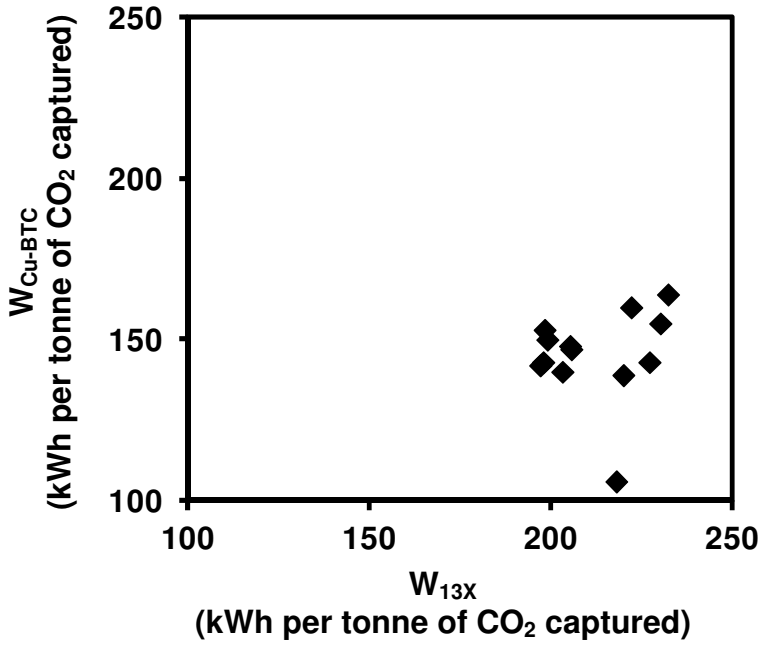

Figure 6.20. Comparison of simulated energy consumption of VSA process using parameters in Table 6.3.

6.6 Chapter Summary

The advantages of using finite volume method over finite difference method in solving the partial differential equations were discussed in details in this chapter. A mathematical model for a four-step vacuum swing adsorption (VSA) process was developed and the model equations were solved using the finite volume method and suitable ODE solver from MATLAB to simulate the cyclic process. Important model assumptions related to the prediction of mixture equilibrium and kinetics using single component parameters were validated with limited binary breakthrough experiments

Detailed parametric studies were carried out for CO_2 capture from post combustion power plant flue gas by a four-step VSA process on the Cu-BTC adsorbent synthesized and characterized in this study. Finally, the performance of Cu-BTC for CO_2 capture has been compared with 13X zeolite, a commercial adsorbent and a leading candidate for pilot plant studies. While Cu-BTC gave comparable purity-recovery with 13X under similar operating conditions, the energy advantage of the former could not be established within the scope of the present simulation study. The full optimization study necessary for a definite conclusion is recommended for a future undertaking.

CHAPTER 7

CONCLUSIONS AND RECOMMENDATIONS

In this chapter, the major findings and conclusions obtained from experimental, modeling and simulation studies conducted on adsorption and diffusion of gases in synthesized Cu-BTC adsorbent are presented. In addition, some recommendations for future work are also discussed.

7.1 Conclusions

Based on the experimental, modeling and simulation studies carried out in this project, the following conclusions are drawn:

1. Five samples of Cu-BTC, a member of the MOF adsorbent family, were synthesized following synthesis routes that represent some modifications of published recipes. These recipes differed in the proportion of reagents, mixing of the organic and inorganic solutions before the reaction, duration and temperature of the reaction, and solvents used. The XRD patterns obtained matched well with published reports. Some samples contained very small amount of CuO or Cu_2O as impurity. It was found that longer reaction duration and higher concentration of precursors increased the formation of trace impurity like CuO. It was also observed that higher reaction temperature led to increased Cu_2O impurity.

2. Pre-mixing of the solutions containing the precursors, modest reaction temperature and duration, and higher dilution of the precursors gave the most stable sample (S2), which gave stable CO_2 adsorption capacity after several adsorption-desorption cycles used as

the screening test. The optimum regeneration temperature was determined to be 423.15 K (150°C) for both in-house and Basolite® C300 samples.

3. In view of very low yield from these recipes, a new constant volume apparatus was designed, constructed and implemented that gave reproducible equilibrium data with only a few grams of adsorbent. Experimental isotherms of CO_2, CH_4 and N_2 were measured over a wide range pressure and temperature ranges on the shortlisted synthesized Cu-BTC sample (S2) and its commercial analogue, Basolite® C300. Langmuir isotherm model was able to adequately capture the experimental isotherm data. By analyzing the isosteric heats of adsorption (ΔU_s), it was confirmed that both the Cu-BTC samples are energetically homogeneous for the adsorption of CO_2, CH_4 and N_2 in the pressure range covered in this study.

4. The dynamic column breakthrough (DCB) apparatus, redesigned in this study to reduce dead volume, was successfully used to yield meaningful breakthrough results with small adsorber containing about 17g of the chosen Cu-BTC sample. The composite breakthrough responses were corrected to obtain the true responses using TIS model in this work. For the first time in the literature, the tank in series (TIS) model was experimentally verified to be the correct and reliable method for blank correction. The corrected experimental breakthrough responses were analyzed in details using the simulation model developed in MATLAB in this study. It was confirmed that the transport of all three gases is controlled by a combination of molecular diffusion in the adsorbent macropores and diffusion across the external fluid film around the particles.

5. A mathematical model for a four-step VSA process including co-current pressurization, co-current adsorption, co-current blowdown and counter-current evacuation was developed and numerically solved in MATLAB using the finite volume method. Important model assumptions related to the prediction of mixture equilibrium and kinetics using single component parameters used in the VSA simulation was verified with limited binary breakthrough experiments.

6. A parametric study of the VSA process for CO_2 capture from dry, post-combustion flue gas from a coal fired power plant using Cu-BTC adsorbent revealed that the evacuation pressure was the most sensitive parameter affecting the attainment of at least 90% purity-recovery requirements. It was found that the purity-recovery requirements could be easily achieved using both Cu-BTC and 13X at an evacuation pressure of 0.01 bar. In addition, the energy advantage of Cu-BTC could not be established within the scope of the present simulation study.

7.2 Recommendations for Future Work

Besides the experimental and simulation work conducted in this study, some recommendations are made for future consideration:

1. Some of the metal organic framework materials such as MOF-177 and IRMOF-1 have been recently commercialized by BASF Company, which claim to have higher selectivity for CO_2 compared to Cu-BTC. A comprehensive evaluation of these MOFs, following the methodology proposed and demonstrated in this study, could be undertaken to investigate their process suitability.

2. It will be instructive to further validate the transport mechanism of gases in Cu-BTC with gravimetric/volumetric experiments using particles of at least two different sizes. As discussed in chapter 5, breakthrough experiments with larger particle size may not be as effective as gravimetric/volumetric experiments due to interference from axial dispersion.

3. Some acid gases exist in natural and flue gas streams, such as H_2S and SO_2. In general, very few studies are known in the literature where the adsorption and diffusion of these gases in various adsorbents have been studied. Understanding equilibrium and transport of these gases in Cu-BTC and other adsorbents will be an interesting area for future work. However, adequate precautions will be necessary to carry out necessary experiments.

4. A detailed optimization study to generate energy-productivity Paretos subjected to purity-recovery constraints should be undertaken for the 4-step VSA cycle using Cu-BTC in order to fairly compare its energy performance with that of 13X. Similar comparative evaluation may also be extended to other cycle configurations. Experimental validation should be considered if the results from the optimization study look promising.

BIBLIOGRAPHY

Achmann S., Hagen G., Kita J., Malkowsky I. M., Kiener C. and Moos R. Metal-Organic Frameworks for Sensing Applications in the Gas Phase, Sensors 2009, 9, 1574-1589.

Aprea P., Caputo D., Gargiulo N., Iucolano F. and Pepe F. Modeling Carbon Dioxide Adsorption on Microporous Substrates: Comparison between Cu-BTC Metal-Organic Framework and 13X Zeolitic Molecular Sieve, Journal of Chemical and Engineering Data 2010, 55 (9), 3655-3661.

Babarao R., Jiang J. and Sandler S. I. Molecular Simulations for Adsorptive Separation of CO2/CH4 Mixture in Metal-Exposed, Catenated, and Charged Metal-Organic Frameworks, Langmuir 2009, 25 (9), 5239-5247.

Bae Y. S., Farha O. K., Spokoyny A. M., Mirkin C. A., Punatahnam S., Hupp J. T., Snurr Q. R. Carborane-based Metal-Organic Frameworks as Highly Selective Sorbents for CO_2 over Methane, Chemical Communications 2008, 35, 4135-4137.

Bai R. and Yang R. T. Heterogeneous Extended Langmuir Model with Multiregion Surfaces for Adsorption of Mixtures, Journal of Colloid and Interface Science 2002, 253, 16-22.

Bai R. and Yang R. T. A Thermodynamically Consistent Langmuir Model, Journal of Colloid and Interface Science 2001, 239, 296-302.

Barman S., Furukawa H., Blacque O., Venkatesan K., Yaghi O. M., Jinc G. X. and Berke H. Incorporation of Active Metal Sites in MOFs via In Situ Generated Ligand dDeficient Metal-Linker Complexes, Chemical Communications 2011, 47, 11882-11884.

Bhadra S. J. and Farooq S. Separation of Methane-Nitrogen Mixture by Pressure Swing Adsorption for Natural Gas Upgrading, Industrial and Engineering Chemistry Research 2011, 50 (24), 14030-1404.

Boris, J. P. and Book, D. L. Flux-Corrected Transport. 1. SHASTA, A Fluid Transport Algorithm That Works, Journal of Computational Physics 1973, 11 (1), 38-69.

Bourrellya S., Serreb C., Vimontc A., Ramsahyed N. A. , Maurind G., Daturic M., Filinchuke Y., Féreyb G. and Llewellyna P. L. A multidisciplary approach to understanding sorption induced breathing in the metal organic framework MIL53(Cr), From Zeolites to Porous MOF Materials - the 40th Anniversary of International Zeolite Conference, 2007.

van Leer B. Towards the ultimate conservative difference scheme V: a second order sequel to Godunov' method, Journal of Computational Physics 1979, 32, 101-136.

Brieva G. B., Martin J. M. C., Al-zahrani S. M. and Fierro J. L. G. Removal of Refractory Organic Sulfur Compounds in Fossil Fuels using MOF Sorbents, Global NEST Journal 2010, 12 (3), 296-304.

Brieva G. B., Martin J. M. C., Al-zahrani S. M. and Fierro J. L. G. Effectiveness of Metal-Organic Frameworks for Removal of Refractory Organo-Sulfur Compound Present in Liquid Fuels, Fuel 2011, 90, 190-197.

Cambridge Structure Database (CSD) as of 2005.

Carter, J. W. and Wyszynski M. L. The Pressure Swing Adsorption Drying of Compressed Air, Chemical Engineering Science 1983, 38 (7), 1093-1099.

Castillo J. M., Vlugt T. J. H. and Calero S. Understanding Water Adsorption in Cu-BTC Metal-Organic Frameworks. Journal of Physical Chemistry C, 2008, 112 (41), 15934-15939.

Cavenati S., Grande C. A. and Rodrigues A. E. Metal Organic Framework Adsorbent for Biogas Upgrading, Industrial and Engineering Chemistry Research 2008, 47, 6333-6335

Chae H. K., Siberio-Pe´rez D. Y., Kim J., Go Y. B., Eddaoudi M., Matzger A. J., O'Keeffe M. and Yaghi O. M. A Route to High Surface Area, Porosity and Inclusion of Large Molecules in Crystals. Nature 2004, 427, 523-527.

Chapman, S., and Cowling, T. G. The Mathematical Theory of Non-Uniform Gases: An Account of the Kinetic Theory of Viscosity, Thermal Conduction, and Diffusion in Gases, Cambridge University Press 1990.

Chen, S., Zhang, J., Wu, T., Feng, P., Bu, X. J. Multiroute Synthesis of Porous Anionic Frameworks and Size-Tunable Extraframework Organic Cation-Controlled Gas Sorption Properties, Journal of the American Chemical Society 2009, 131 (44), 16027-16029.

Chowdhury P., Bikkina C., Meister D., Dreisbach F. and Gumma S. Comparison of Adsorption Isotherms on Cu-BTC Metal Organic Frameworks Synthesized from Different Routes. Microporous and Mesoporous Materials 2009, 117, 406-413.

Chui S. S.-Y., Lo S. M.-F., Charmant J. P. H., Orpen A. G. and Williams I. D. A Chemically Functionalizable Nanoporous Material $[Cu_3(TMA)_2(H2O)_3]_n$., Science 1999, 283, 1148-1150.

Cruz P., Santos J. C., Magalh˜aes F. D. and Mendes A. Simulation of Separation Processes Using Finite Volume Method. Computers and Chemical Engineering 2005, 30(1), 83-98.

Dathe, H., Peringer, E., Roberts, V., Jentys, A. and Lercher, J. A. Metal Organic Frameworks based on Cu2+ and Benzene-1,3,5-tricarboxylate as Host for SO_2 Trapping Agents, Comptes Rendus Chimie 2005, 8, 753-763.

Do D. D. Adsorption Analysis: Equilibria and Kinetics. London: Imperial College Press, 1998.

DOE (2011): *http://fossil.energy.gov/programs/powersystems/gasification/gasificationpioneer.html*

Dybtsev D. N., Chun H. and Kim K. Rigid and Flexible: A Highly Porous Metal-Organic Framework with Unusual Guest-Dependent Dynamic Behavior, Angewandte Chemie International Edition 2004, 43, 5033-5036.

Eddaoudi M., Kim J., Rosi N., Vodak D., Wachter J., O'Keeffe M., and Yaghi O. M. Systematic Design of Pore Size and Functionality in Isoreticular MOFs and their Application in Methane Storage, Science 2002, 295, 469-472.

Edwards M. F. and Richardson J. F. Gas Dispersion in Packed Beds, Chemical Engineering Science 1968, 23, 109-l23.

Farooq S. and Ruthven D. M. A Diffusion Model for a Pressure Swing Adsorption Bulk Separation Process: Importance of the Concentration Dependence of Micropore Diffusivity, Chemical Engineering Science 1991, 46 (9), 2213-2224.

Farooq S., Rathor M. N. and Hidajat K. A. A Predictive Model for a Kinetically Controlled Pressure Swing Adsorption Process, Chemical Engineering Science 1993, 48, 4129-4141.

Ferreira A. F. P., Santos J. C., Plaza M. G., Lamia N., Loureiro José M. and Rodrigues A. E. Suitability of Cu-BTC Extrudates for Propane-Propylene Separation by Adsorption Processes, Chemical Engineering Journal 2011, 167, 1-12.

Finsy V., Ma L., Alaert L., De Vos D. E., Baron C. V. and Denayer J. F. M. Separation of CO_2 Mixtures with the MIL-53(Al) Metal-Organic Framework, Microporous and Mesoporous Materials 2009, 120, 221-227.

Furukawa H. and Yaghi O. M. Storage of Hydrogen, Hethane, and Carbon Dioxide in Highly Porous Covalent Organic Frameworks for Clean Energy Applications, Journal of American Chemical Society 2009, 131, 8875-8883.

Furukawa H., Ko N., Go Y. B., Aratani N., Choi S. B., Choi E., Yazaydin A. O., Snurr R. Q., O'Keeffe M., Kim J. and Yaghi O. M. Ultrahigh Porosity in Metal-Organic Frameworks, Science 2010, 329, 424-528.

Garcı´a-Pe´rez E., Gasco´n J., Morales-Flo´rez V., Castillo J. M., Kapteijn F., and Calero S. Identification of Adsorption Sites in Cu-BTC by Experimentation and Molecular Simulation. Langmuir 2009, 25, 1725-1731.

Gascon J., Aktay U., Hernandez-Alonso M. D., Klink G. P.M. and Kapteijn F. Amino-Based Metal-Organic Frameworks as Stable, Highly Active Basic Catalysts. Journal of Catalysis, 2009, 261, 75-87.

Glueckauf E. and Coates J. I. E. Theory of Chromatography, Part 4. The Influence of Incomplete Equilibrium on the Front Boundary of Chromatogram and on the Effectiveness of Separation, Journal of the Chemical Society 1947, 1315-1321.

Golden T. C. and Sircar S. Gas Adsorption on Silicalite, Journal of Colloid and Interface Science 1994, 162, 182-188.

Haghpanah R., Majumdar A., Nilam R., Rajendran A., Farooq S., Karimi I. A. and Amanullah M. Multiobjective Optimization of a Four-Step Adsorption Process for Postcombustion CO_2 Capture Via Finite Volume Simulation, Industrial and Engineering Chemistry Research 2013, 52, 4249-4265.

Hamon L., Jolimaıˆtre E. and Pirngruber G. D. CO_2 and CH_4 Separation by Adsorption Using Cu-BTC Metal-Organic Framework, Industrial and Engineering Chemistry Research 2010, 49, 7497-7503.

Hamon L., Llewellyn P. L., Devic T., Ghoufi A., Clet G., Guillerm V., Pirngruber G. D., Maurin G., Serre C., Driver G., van Beek W., Jolimaıˆtre E., Vimont A., Daturi M. and Fe´rey G. Co-Adsorption and Separation of CO_2-CH_4 Mixtures in the Highly Flexible MIL-53(Cr) MOF, Journal of the American Chemical Society 2009, 131, 17490-17499

Hartmann M. and Kevan L. Transition-Metallons in Aluminophosphate and Silicoaluminophosphate Molecular Sieves: Location, Interaction with Adsorbates and Catalytic Properties, Chemical Reviews 1999, 99, 635-663.

Hartmann M., Kunz S., Himsl D. and Tangermann O. Adsorptive Separation of Isobutene and Isobutane on $Cu_3(BTC)_2$. Langmuir 2008, 24, 8634-8642.

Hsu L. -K. P. and Haynes H. W. Effective Diffusivity by the Gas Chromatography Technique: Analysis and Application to Measurements of Diffusion of Various Hydrocarbons in Zeolite NaY. AIChE Journal 1981, 27 (1), 81-91.

Hu C. and Shu C. W. Weighted Essentially Non-oscillatory Schemes on Triangular Meshes 1, Journal of Computational Physics 1999, 150, 97-127.

Huang, B.L., Ni b, Z., Millward, A., McGaughey, A.J.H., Uher, C., Kaviany, M. and Yaghi, O. Thermal Conductivity of a Metal-Organic Framework (MOF-5): Part II. Measurement, International Journal of Heat and Mass Transfer 2005, 50, 405-411.

Hwang Y. K., Chang J. S., Park S. E., Kim D. S., Kwon Y. U., Jhung J. S., Hwang J. S. and Park M. S. Microwave Fabrication of MFI Zeolite Crystals with a Fibrous Morphology and their Applications, Angewandte Chemie International Edition 2005, 44 (4), 556-560.

IPCC, Special Report on Carbon Capture and Storage, 2005, Prepared by Working Group III of the Intergovernmental Panel on Climate Change, Geneva, Switzerland.

IPCC, Managing the risks of extreme events and disasters to advance Climate Change adaptation, 2012, A special report of working group I and II of the intergovernmental Panel on Climate Change.

Jeremiah J. G., Furukawa H., Smaldone R. A., Forgan R. S., Botros Y. Y., Yaghi O. M. and Stoddart J. F. Strong and Reversible Binding of Carbon Dioxide in a Green Metal-Organic Framework, Journal of the American Chemical Society 2011, 133, 15312-15315.

Kapoor, A., Yang, R. T. Kinetic Separation of Methane-Carbon Dioxide Mixture by Adsorption on Molecular Sieve Carbon, Chemical Engineering Science 1989, 44, 1723-1733.

Karra R. J. and Walton S. K. Effect of Open Metal Sites on Adsorption of Polar and Nonpolar Molecules in Metal-Organic Framework Cu-BTC, Langmuir 2008, 24, 8620-8626.

Karra R. J. and Walton S. K. Molecular Simulations and Experimental Studies of CO_2, CO, and N_2 Adsorption in Metal-Organic Frameworks. Journal of Physical Chemistry C 2010, 114, 15735-15740.

Khalighi M., Farooq S. and Karimi I. A. Non-Isothermal Pore Diffusion Model for a Kinetically Controlled PSA Process, Industrial and Engineering Chemistry Research 2012, 51, 10659-10670.

Kikkinides E. S. and Yang R. T. Effects of Bed Pressure Drop on Isothermal and Adiabatic Adsorber Dynamics, Chemical Engineering Science 1993, 48 (9), 1545-1555.

Kitagawa S., Kitaura R. and Noro S. Functional Porous Coordination Polymers, Angewandte Chemie International Edition 2004, 43 (18), 2334-2375.

Knaebel K. S. and Reinhold H. E. Landfill Gas: From Rubbish to Resource, Adsorption 2003, 9, 87-94.

Komarneni S., Rjha R. K. and Katsuki H. Microwave-Hydrothermal Processing of Titanium Dioxide, Material Chemistry and Physics 1999, 61 (1), 50-54.

Krungleviciute V., Lask K., Migone A.D., Lee J.-Y. and Li J. Kinetics and Equilibrium of Eas Adsorption on RPM1-Co and Cu-BTC Metal-Organic Frameworks: Potential for Gas Separation Applications. AIChE Journal 2008, 54, 918-923.

Lamia N., Jorge M., Granato M. A., Paz F. A. A., Chevreau H. and Rodrigues A. E. Adsorption of Propane, Propylene and Isobutene on a Metal-Organic Framework: Molecular Simulation and Experiment, Chemical Engineering Science, 2009, 64, 3246-3259.

Lee J. Y., Li J. and Jagiello J. Gas Sorption Properties of Microporous Metal Organic Frameworks, Journal of Solid State Chemistry 2005, 178, 2527-2532.

Leveque R. Finite Volume Methods for Hyperbolic Problems. Cambridge University Press, 2002.

Li H., Eddaoudi M., O'Keeffe M. and Yaghi O. M. Design and Synthesis of an Exceptionally Stable and Highly Porous Metal-Organic Framework. Nature 1999, 402, 276-279.

Li P. and Tezel F. H. Equilibrium and Kinetic Analysis of CO_2-N_2 Adsorption Separation by Concentration Pulse Chromatography, Journal of Colloid and Interface Science 2007, 313, 12-17.

Liang Z., Marshall M. and Chaffee A. L. CO_2 Adsorption-Based Separation by Metal Organic Framework (Cu-BTC) versus Zeolite (13X), Energy & Fuels 2009, 23, 2785-2789.

Lin S. J., Chao W. C., Sud Y. C. and Walker G. K. A class of the van Leer-type Transport Schemes and its Applications to the Moisture Transport in a General Circulation Model, Monthly Weather Review 1994, 122, 1575-1593.

Lin W. Metal-Organic Frameworks for Asymmetric Catalysis and Chiral Separations. MRS Bulletin 2007, 32, 544-548.

Liu J., Culp J. T., Natesakhawat S., Bockrath B. C., Zande B., Sankar S. G., Garberoglio G. and Johnson J. K. Experimental and Theoretical Studies of Gas Adsorption in $Cu_3(BTC)_2$: An Effective Activation Procedure. Journal of Physical Chemistry C 2007, 111, 9305-9313.

Liu Y., Her J., Dailly A., Ramirez-Cuesta A. J., Neumann D. A. and Brown C. M. Reversible Structural Transition in MIL-53 with Large Temperature Hysteresis. Journal of the American Chemical Society 2008, 130, 11813-11818.

Livage C., Forster P. M., Guillou N., Tafoya M. M., Cheetham A. K. and Ferey G. Effect of Mixing of Metal Cations on the Topology of Metal Oxide Networks, Angewandte Chemie International Edition 2007, 46, 5877-5879

Malek A. and Farooq S. Comparison of Isotherm Models for Hydrocarbon Adsorption on Activated Carbon, AIChE Journal 1996, 42 (11), 3191-3201.

Marathe R. P., Farooq S. and Srinivasan M. P. Effect of Ion Exchange and Dehydration Temperature on the Adsorption and Diffusion of Gases in ETS-4 Industrial and Engineering Chemistry Research 2004, 43, 5281-5290.

Marathe R. P., Farooq S. and Srinivasan M. P. Modeling Gas Adsorption and Transport in Small-Pore Titanium Silicates, Langmuir 2005, 21, 4532-4546.

McCabe W. L., Smith J. C. and Harriott P. Unit operation of chemical engineering, Singapore, 1993.

Medi B. and Amanullah M. Application of a Finite-Volume Method in the Simulation of Chromatographic Systems: Effects of Flux Limiters, Industrial and Engineering Chemistry Research 2010, 50 (3), 1739-1748.

Myers A. L. and Prausnitz J. M. Thermodynamics of Mixed-Gas Adsorption, AIChE Journal 1965, 11 (1), 121-127.

Ockwig N. W., Delgado-Friedrichs O., O'Keeffe M. and Yaghi O. M. Reticular Chemistry: Occurrence and Taxonomy of Nets, and Grammar for the Design of Frameworks, Accounts of Chemical Research 2005, 38, 176-182.

Pereira P. R., Pires J. and Brotas de Carvalho M. Zirconium Pillared Clays for Carbon Dioxide/Methane Separation. 1. Preparation of Adsorbent Materials and Pure Gas Adsorption, Langmuir 1998, 14, 4584-4588.

Perry R. H. and Green D. W Perry's chemical engineers' handbook. McGraw-Hill: New York, 2008.

Plaza M.G., Ferreira A.F.P., Santos J.C., Ribeiro A.M., Müller U., Trukhan N., Loureiro J.M. and Rodrigues A.E. Propane/Propylene Separation by Adsorption using Shaped Copper Trimesate MOF, Microporous and Mesoporous Materials 2012, 157, 101-111.

Raghavan N. S. and Ruthven D. M. Numerical Simulation of a Fixed-bed Adsorption Column by the Method of Orthogonal Collocation, AIChE Journal 1983, 29(6), 922-925.

Rajendran A., Kariwala V. and Farooq S. Correction Procedures for Extra-Column Effects in Dynamic Column Breakthrough Experiments, Chemical Engineering Science 2008, 63, 2696-2706.

Rama Rao V., Farooq S. and Krantz W. B. Design of a Two-Step Pulsed Pressure-Swing Adsorption-Based Oxygen Concentrator, AIChE Journal 2010, 56 (2), 354-370.

Rasi, S., Lantela, J., Veijanen, A. and Rintala, J. Landfill Gas Upgrading with Countercurrent Water wash, Waste Management 2008, 28, 1528-1534.

Reid R.C., Praunsnitz J.M. and Sherwood T.K. The Properties of Gases and Liquids. McGraw-Hill. NY, 1977.

Report of the Interagency Task Force on Carbon Capture and Storage, Aug 2010.

Rosi N. L., Kim J., Eddaoudi M., Chen B., O'Keeffe M., and Yaghi O. M. Rod Packings and Metal-Organic Frameworks Constructed from Rod-Shaped Secondary Building Units. Journal of the American Chemical Society 2005, 127, 1504-1518.

Rowsell J. L. C. and Yaghi O. M. Metal-Organic Frameworks: a New Class of Porous Materials, Microporous and Mesoporous Materials 2004, 73, 3-14.

Rowsell, J. L. C., Spencer, E. C., Eckert, J., Howard, J. A. K. and Yaghi, O. M. Gas Adsorption Sites in a Large-Pore Metal-Organic Framework, Science 2005, 309 (5739), 1350-1354.

Ruthven, D. M. Principles of Adsorption and Adsorption Processes, Wiley-Interscience: New York, 1984.

Ruthven D.M., Farooq S. and Knaebel K.S. Pressure Swing Adsorption, VCH Publishers: New York, USA, 1994.

Sayaria A., Belmabkhouta Y. and Serna-Guerrerob R. Flue Gas Treatment via CO_2 Adsorption, Chemical Engineering Journal 2011, 171, 760-774.

Schlichte, K., Kratzke, T. and Kaskel S. Improved Synthesis, Thermal Stability and Catalytic Properties of the Metal-Organic Framework Compound $Cu_3(BTC)_2$. Microporous and Mesoporous Materials 2004, 73, 81-88.

Schnobrich J. K., Koh K., Sura K. N. and Matzger A. J. A Framework for Predicting Surface Areas in Microporous Coordination Polymers, Langmuir 2010, 26 (8), 5808-5814.

Senkovska, I. and Kaskel, S. High Pressure Methane Adsorption in the Metal-Organic Frameworks $Cu_3(btc)_2$, $Zn_2(bdc)_2dabco$, and $Cr_3F(H_2O)_2O(bdc)_3$. Microporous and Mesoporous Materials 2008, 112, 108-115.

Seo Y. K., Hundal G., Jang I. T., Hwang Y. K., Jun C. H. and Chang J. S. Microwave Synthesis of Hybrid Inorganic-Organic Materials Including Porous $Cu_3(BTC)_2$ from Cu(II)-trimesate Mixture, Microporous and Mesoporous Materials 2009, 119, 331-337.

Shin H. S. and Knaebel K. S. Pressure Swing Adsorption: An Experimental Study of Diffusion-Induced Separation, AIChE Journal 1988, 34 (9), 1409-1416.

Sircar S. Excess Properties and Thermodynamics of Multi-Component Gas Adsorption, Journal of the Chemical Society Faraday Transactions I 1985, 81 (7), 1527-1540.

Sircar S. Basic Research Needs for Design of Adsorptive Gas Separation Process, Industrial and Engineering Chemistry Research 2006, 45, 5435-5448.

Sircar S., Golden T. C. and Rao M. B. Activated Carbon for Gas Separation and Storage, Carbon, 1996, 34 (1), 1-12.

Sircar, S. Influence of Adsorbate Size and Adsorbent Heterogeneity of IAST, AIChE Journal 1995, 41, 1135-1145.

Skarstrom C. W. Method and Apparatus for Fractionating Gaseous Mixtures by Adsorption, US Patent 2944627, 1960.

Skarstrom C. W. Recent Development in Separation Sciences (edited by Li N. N.), Vol. 2, pp. 95-106, CRC Press, Cleveland, Ohio, 1972.

Song L.F., Jiang, C.H., Zhang, J., Sun, L.X., Xu, F., Tian, Y.O., You, W.S., Cao, Z., Zhang, L. and Yang, D.W Heat Capacities and Thermodynamic Properties of MgBTC, Journal of Thermal Analysis and Calorimetry 2009, 101 (1) , 365-370.

Stein A., Keller S. W. and Mallouk T. E. Turning Down the Heat: Design and Mechanism in Solid-State Synthesis, Science 1993, 259, 1558-1564.

Suzuki, M. Adsorption Engineering, Kodansha Ltd., pp 193, 1990.

Todd R. S., He J., Webley P. A., Beh C., Wilson S., and Lloyd M. A. Fast Finite-Volume Method for PSA/VSA cycle Simulation-Experimental Validation, Industrial and Engineering Chemistry Research 2001, 40(14), 3217-3224.

Tomic E. A. Thermal Stability of Coordination Polymers, Journal of Applied Polymer Science 1965, 9, 3745-3752.

Tompsett G., Conner W.C. and Yngvesson K.S. Microwave Synthesis of Nanoporous Materials, ChemPhysChem 2006, 7 (2), 296-319.

Tranchemontagne D. J., Hunt J. R. and Yaghi O. M. Room Temperature Synthesis of Metal-Organic Frameworks: MOF-5, MOF-74, MOF-177, MOF-199, and IRMOF-0. Tetrahedron 2008, 64, 8553-8557.

Vishnyakov A., Ravikovitch P. I., Neimark A.V., Blow M. and Wang Q. M. Nanopore Structure and Sorption Properties of Cu-BTC Metal-Organic Framework, Nano Letters 2003, 3 (6), 713-718.

Volkringer C., Loiseau T., Guillou N., F´erey G., Elka¨ım E. and Vimont A. XRD and IR Structural Investigations of a Particular Breathing Effect in the MOF-Type Gallium Terephthalate MIL-53(Ga), Dalton Transactions 2009, 12, 2241-2249.

Wang Q. M., Shen D., Bülow M., Lau M. L., Deng S., Fitch F. R., Lemcoff N. O. and Semanscin J. Metallo-Organic Molecular Sieve for Gas Separation and Purification. Microporous and Mesoporous Materials 2002, 55, 217-230.

Wakao N. and Funazkri T. Effect of Fluid Dispersion Coefficients on Particle-to-Fluid Mass Transfer Coefficients in Packed Beds, Chemical Engineering Science 1978, 33, 1375-1384.

Webley P. A. and He J. Fast Solution-Adaptive Finite Volume Method for PSA/VSA Cycle Simulation, 1 Single Step Simulation, Computers and Chemical Engineering 2000, 23 (11-12), 1701-1712.

Wencai L., Farooq S. and Chi T. Estimation of Overall Effective Coefficient of Heat Transfer for Nonisothermal Fixed-Bed Adsorption, Chemical Engineering Science 1999, 54, 4031-4040.

Wilmer C. E., Leaf M., Lee C. Y., Farha O. K., Hauser B. G., Hupp J. T. and Snurr R. Q. Large-Scale Screening of Hypothetical Metal-Organic Frameworks, Nature Chemistry 2012, 4 (5), 83-89.

Xu T., Apps J. A. and Pruess K. Reactive Geochemical Transport Simulation to Study Mineral Trapping for CO_2 Disposal in Deep Arenaceous Formations, Journal of Geophysical Research 2003, 108 (B2), 2071-2084.

Yaghi O. M., O'Keeffe M., Ockwig N. W., Chae H. K., Eddaoudi M. and Kim J. Reticular Synthesis and the Design of New Materials, Nature 2003, 423, 705-714.

Yaghi, O.M., 2007. Metal-Organic Frameworks: a Tale of Two Entanglements, Nature Materials 6, 92.

Yang R. T. and Doong S. J. Gas Separation by Pressure Swing Adsorption: a Pore-Diffusion Model for Bulk Separation, AIChE Journal 1985, 31 (11), 1829-1841.

Yang Q., Xue C., Zhong C. and Chen J. F. Molecular Simulation of Separation of CO_2 from Flue gases in Cu-BTC Metal-Organic Framework, AIChE Journal 2007, 53 (11), 2832-2840.

Yang R. T. Gas Separation by Adsorption Processes, Butterworth Publisher: Boston, 1987.

Yang R. T. Adsorbents: Fundamentals and Applications, Wiley: New York, 2003.

Yang Q., Wiersum A. D., Jobic H., Guillerm V., Serre C., Llewellyn P. L. and Maurin G. Understanding the Thermodynamic and Kinetic Behavior of the CO_2/CH_4 Gas Mixture within the Porous Zirconium Terephthalate UiO-66(Zr): A Joint Experimental and Modeling Approach, Journal of Physical Chemistry C 2011, 115 (28), 13768-13774.

APPENDIX 1.

VOLUMETRIC EXPERIMENTAL EQUILIBRIUM DATA OF CO_2, CH_4 AND N_2 ON Cu-BTC

A1.1. Equilibrium Data on Synthesized Cu-BTC (S2)

CO_2

Temperature (K)	c (mmol/cc)	q (mmol/cc)	Temperature (K)	c (mmol/cc)	q (mmol/cc)
282.15	0.00112	0.14398	**296.15**	0.00100	0.08912
	0.00311	0.39565		0.00307	0.29206
	0.00658	0.84522		0.00673	0.62323
	0.01266	1.59946		0.01218	1.08814
	0.02278	2.67596		0.02271	1.92595
	0.04790	4.48514		0.03885	2.96957
	0.08134	5.80924		0.06537	4.23080
	0.11705	6.59427		0.10266	5.31720
	0.15746	7.09371		0.14914	6.08761
	0.20893	7.48244		0.19736	6.59856
313.15	0.00106	0.05948	**333.15**	0.00094	0.02800
	0.00311	0.18178		0.00253	0.08298
	0.00601	0.34580		0.00549	0.18419
	0.01118	0.63290		0.01074	0.35772
	0.02239	1.20709		0.02203	0.70898
	0.04519	2.27684		0.04400	1.35939
	0.07662	3.32930		0.07077	1.99382
	0.10648	4.08997		0.10299	2.62765
	0.14395	4.77338		0.14079	3.20222
	0.18749	5.37944		0.17941	3.66037

CH_4

Temperature (K)	c (mmol/cc)	q (mmol/cc)	Temperature (K)	c (mmol/cc)	q (mmol/cc)
282.15	0.00151	0.03879	**296.15**	0.00122	0.02192
	0.00372	0.09307		0.00326	0.06098
	0.00740	0.17974		0.00757	0.13751
	0.01538	0.34403		0.01486	0.25736
	0.02848	0.57880		0.02663	0.42728
	0.04599	0.90725		0.04630	0.72032
	0.07531	1.28580		0.07092	0.99582
	0.11568	1.75458		0.10981	1.36978
	0.16755	2.24043		0.16086	1.77006
	0.21351	2.64075		0.21988	2.16538
313.15	0.00099	0.01386	**333.15**	0.00106	0.01384
	0.00333	0.04461		0.00297	0.03001
	0.00753	0.09915		0.00626	0.06583
	0.01482	0.18765		0.01386	0.12282
	0.02674	0.31940		0.02471	0.20349
	0.04330	0.51953		0.04312	0.36831
	0.08804	0.85525		0.07768	0.56414
	0.13235	1.13917		0.11256	0.75519
	0.16951	1.34984		0.15398	0.93032
	0.20248	1.52135		0.18949	1.09244

N_2

Temperature (K)	c (mmol/cc)	q (mmol/cc)	Temperature (K)	c (mmol/cc)	q (mmol/cc)
282.15	0.00115	0.00979	**296.15**	0.00123	0.00643
	0.00330	0.03054		0.00279	0.01500
	0.00715	0.06759		0.00766	0.04119
	0.01504	0.13137		0.01443	0.07694
	0.02869	0.22816		0.02769	0.14339
	0.05039	0.40950		0.04615	0.26913
	0.08017	0.57913		0.07730	0.40811
	0.12017	0.77724		0.11606	0.56098
	0.16759	0.97961		0.16760	0.72974
	0.21390	1.16535		0.21041	0.88744
313.15	0.00087	0.00427	**333.15**	0.00097	0.00271
	0.00242	0.01160		0.00284	0.00810
	0.00571	0.02772		0.00668	0.01895
	0.01345	0.06146		0.01336	0.03781
	0.02625	0.12323		0.02492	0.06977
	0.04316	0.19864		0.04358	0.12668
	0.07120	0.30426		0.06556	0.18276
	0.11209	0.42185		0.10422	0.26061
	0.15769	0.53323		0.14444	0.32502
	0.19936	0.62913		0.00097	0.00271

A1.2. Equilibrium Data on Commercial Cu-BTC (Basolite® C300)

CO_2

Temperature (K)	c (mmol/cc)	q (mmol/cc)	Temperature (K)	c (mmol/cc)	q (mmol/cc)
282.15	0.00079	0.13684	**296.15**	0.00089	0.09516
	0.00227	0.35737		0.00261	0.26760
	0.00539	0.74941		0.00668	0.60139
	0.01245	1.45628		0.01327	1.04063
	0.02379	2.26834		0.02345	1.61026
	0.04344	3.23450		0.04020	2.30567
	0.06859	3.95821		0.06306	3.03244
	0.09301	4.47526		0.08824	3.55825
	0.12055	4.82460		0.11723	3.98617
	0.14572	5.04931		0.14865	4.33036
	0.17360	5.25214		0.18371	4.58518
	0.19796	5.40805		0.21541	4.75310
	0.22817	5.53835			
313.15	0.00073	0.03558	**333.15**	0.00054	0.02020
	0.00252	0.12699		0.00222	0.07970
	0.00555	0.27064		0.00504	0.17376
	0.01119	0.51645		0.01112	0.36220
	0.01973	0.81612		0.01892	0.57225
	0.02881	1.14069		0.03115	0.84980
	0.04258	1.59393		0.04689	1.19903
	0.06417	2.12264		0.07116	1.61155
	0.08820	2.58924		0.09977	1.99341
	0.11259	2.96923		0.13496	2.36933
	0.14076	3.31960			
	0.17385	3.62404		0.17861	2.68107
	0.20446	3.84883			

CH_4

Temperature (K)	c (mmol/cc)	q (mmol/cc)	Temperature (K)	c (mmol/cc)	q (mmol/cc)
282.15	0.00103	0.02376	**296.15**	0.00087	0.01368
	0.00379	0.08642		0.00250	0.04124
	0.00883	0.19097		0.00594	0.09757
	0.01777	0.34853		0.01196	0.18660
	0.02916	0.52542		0.02017	0.29868
	0.04681	0.78185		0.02946	0.40715
	0.07100	1.02465		0.04605	0.60947
	0.09966	1.27409		0.06879	0.79522
	0.13483	1.54041		0.09763	0.99474
				0.12919	1.18169
	0.17487	1.82452		0.16703	1.37043
				0.20782	1.54077
313.15	0.00078	0.00909	**333.15**	0.00074	0.00503
	0.00234	0.02960		0.00217	0.01223
	0.00539	0.06332		0.00532	0.02968
	0.01133	0.12687		0.01124	0.06445
	0.01922	0.20225		0.01822	0.10282
	0.02872	0.28615		0.02693	0.14675
	0.04411	0.44135		0.04117	0.24311
	0.06560	0.58054		0.06229	0.33289
	0.09274	0.72957		0.08751	0.42828
	0.12608	0.89041		0.11551	0.51718
	0.16129	1.02941		0.14961	0.60679
	0.19837	1.15127		0.18487	0.69243

N_2

Temperature (K)	c (mmol/cc)	q (mmol/cc)	Temperature (K)	c (mmol/cc)	q (mmol/cc)
282.15	0.00097	0.00669	**296.15**	0.00078	0.00460
	0.00331	0.01937		0.00256	0.01286
	0.00701	0.04253		0.00751	0.03620
	0.01373	0.08240		0.01553	0.07275
	0.02306	0.13922		0.02696	0.12584
	0.03668	0.26165		0.04303	0.20483
	0.05638	0.37098		0.06430	0.28644
	0.08134	0.51205		0.09559	0.38175
	0.11124	0.64326		0.13095	0.48965
	0.14493	0.77779		0.16871	0.59414
	0.18616	0.93027		0.20884	0.69787
	0.22286	1.06747			
313.15	0.00072	0.00332	**333.15**	0.00059	0.00216
	0.00248	0.00953		0.00237	0.00473
	0.00598	0.02086		0.00530	0.01097
	0.01267	0.04479		0.01091	0.02561
	0.01984	0.07102		0.02008	0.04315
	0.02891	0.10022		0.03242	0.05662
	0.04521	0.17956		0.05491	0.09535
	0.07112	0.24511		0.08234	0.12361
	0.09802	0.30835		0.11082	0.15996
	0.13163	0.37385		0.14463	0.18804
	0.16459	0.43346		0.18341	0.22302
	0.19981	0.48914			

APPENDIX 2.

CALIBRATION PROCEDURES, CALIBRATION CURVES

A2.1 Pressure Transducer Calibration

The two pressure transducers were calibrated carefully with a pressure calibrator (FLUKE 716, 700P07, Range 500 psi) in the range 0-10 bar. The calibration equations for the whole pressure range are given in Table A2.1.

Table A2.1. Calibration curves for pressure transducers.

P (bar)	Calibration equation	
	Pressure Transducer 1	Pressure Transducer 2
0-10	$P = 2.6352V^{*} - 1.3124$	$P = 2.6244V^{*} - 1.296$

* Voltage unit: *volts (v)*

A2.2 Flow Controller / Meter Calibration

The mass flow controllers at the inlet of the column and the mass flow meter (Brooks 5860i 2 SLPM) which is placed at the column outlet to monitor the flow change due to the adsorption-desorption, were calibrated for different gases against a digital flow meter (Agilent Technologies, ADM 1000). The calibration curves for three gases are shown in Table A2.2.

MFC-1 was used for He flow (carrier gas in single breakthrough measurements) and, MFC-2 was used for adsorbable gases. Q represents the flow rate *(ml/cc)* and, V and SP represent the voltage *(v)* and set point indicator, respectively.

Table A2.2. Calibration curves for mass flow meters and mass flow controller.

Gas	Calibration curve	
	MFC	MFM
He	$Q = 1043.7\ SP + 60.938 \quad (SP \le 0.24)$	$Q = 559.43V + 16.431 \quad (SP \le 0.24)$
	$Q = 1338.6\ SP - 7.1935 \quad (0.24 < SP)$	$Q = 711.71V - 66.812 \quad (0.24 < SP)$
CO_2	$Q = 25.973\ SP + 0.5629$	$Q = 298.25V + 9.7908$
CH_4	$Q = 26.595\ SP + 1.8639$	$Q = 308.71V + 11.905$
N_2	$Q = 34.458\ SP + 2.007$	$Q = 388.33V + 16.153$

According to the manual of the mass flow controllers and mass flow meter, a scale shift would occur in the calibration curves if the controller or meter was operated on a gas other than the gas it was calibrated with. This scale shift is because of difference in heat capacities of two gases and, it can be approximated by using the ratio of molar heat capacities of gases. This ratio was calculated for some of the gas pairs pointed in the manuals of the flow controller and meter under the name of "sensor conversion factor". The ratio of sensor conversion factor of the new gas to the factor of the calibrated gas is multiplied by the output reading that is obtained from the controller or meter. The product will be the actual gas flow rate. The sensor conversion factor for a gas mixture is obtained by the following formula in Equation (A2-1):

$$SCF_{mix} = \frac{1}{\sum_{1}^{n} \frac{y_i}{SCF_i}} \qquad (A2-1)$$

$$\sum_{1}^{n} y_i = 1 \qquad (A2-2)$$

In the above equations, *SCF* represent the sensor conversion factor which was provided by the manufacturer for each gas. y is the gas mole fraction. Sensor conversion factors of

experimental gases in both mass flow controllers and mass flow meter are shown in Table A2.3. The flow rate equations for different gas pairs in Table A2.4 were obtained from equation (A2-1) and the sensor conversion factors in Table A2.3.

Table A2.3. Mass flow controller and mass flow meter sensor conversion factor for different gases.

Gas	Sensor conversion factor (N_2 based)
He	1.387
CO_2	0.778
CH_4	0.808
N_2	1.000

Table A2.4. Flow rate equations for different gas pairs.

Gas pair	**Flow rate equation ($SP_{He} \leq 0.24$)**	**Flow rate equation ($0.24 < SP_{He}$)**
He:CO_2	$Q = \frac{435.24V + 12.7833}{0.609\ y_{CO_2} + 0.778}$	$Q = \frac{553.71V - 51.98}{0.609\ y_{CO_2} + 0.778}$
He:CH_4	$Q = \frac{452.02V + 13.28}{0.579\ y_{CH_4} + 0.808}$	$Q = \frac{575.06V - 53.98}{0.579\ y_{CH_4} + 0.808}$
He:N_2	$Q = \frac{559.43V + 16.431}{0.387\ y_{N_2} + 1}$	$Q = \frac{711.71V - 66.812}{0.387\ y_{N_2} + 1}$
N_2:CH_4	$Q = \frac{313.771V + 13.052}{0.192\ y_{CH_4} + 0.808}$	
N_2: CO_2	$Q = \frac{302.121V + 12.567}{0.222\ y_{CO_2} + 0.778}$	

In the above equations in Table A2.4, the first three rows are the equations that we used for calculating the flow rate in single component breakthrough measurements. He is an inert gas and, therefore, is not adsorbed in Cu-BTC. The last two rows are the equations for binary gas mixtures. These equations give gas flow rate at any time of the breakthrough where both sensor voltage and gas composition are changing.

A2.3 TCD Calibration

The Thermal Conductivity Detector (TCD) which is shown in Figure A2.1 is a dual channel detector which works based on measuring the difference in thermal conductivity between carrier gas flowing through a reference channel and adsorbable gas which is along with a portion of carrier gas flowing through an analytical channel. The aim of TCD calibrating is to find a correlation between the voltage signal obtained from the detector and the concentration of carrier and adsorbable gas. Some parameters such as signal attenuation, system offset value, system pressure, flow rate entering the detector and adsorbable gas concentration are affected the calibration curve. The calibration curves for different gases at different pressures and concentration range are in Table A2.5 and A2.6.

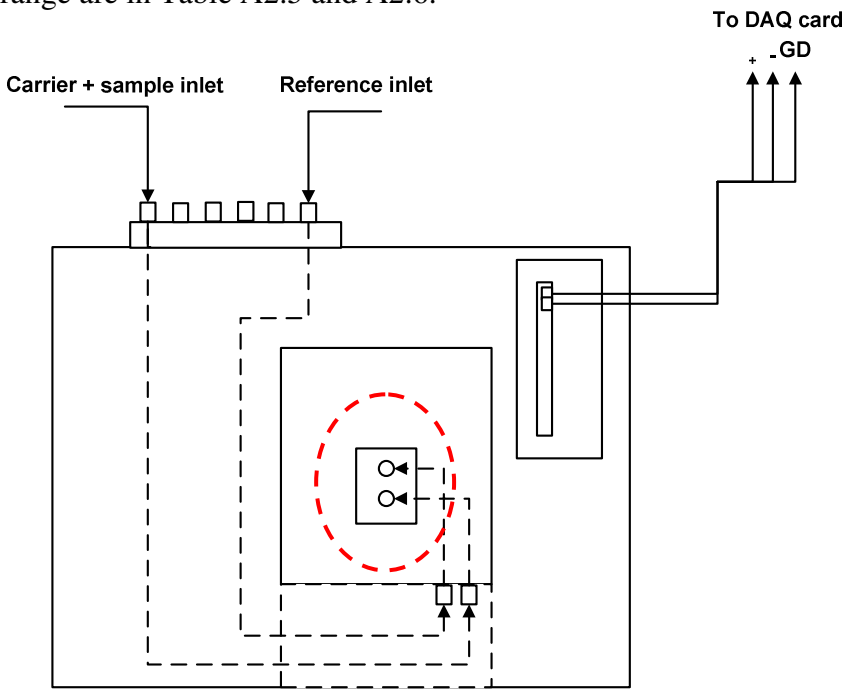

Figure A2.1. Schematic view of TCD from the top.

Table A2.5. TCD calibration for single component breakthrough measurements.

P (bar)	He:CO_2	He:CH_4	He:N_2
2 $(y \leq 10\%)$	$y = 2.5167\ \Delta V$	$y = 3.474\ \Delta V$	$y = 3.1338\ \Delta V$
4 $(y \leq 10\%)$	$y = 2.4404\ \Delta V$	$y = 3.3758\ \Delta V$	$y = 3.0214\ \Delta V$
6 $(y \leq 10\%)$	$y = 2.3736\ \Delta V$	$y = 3.2817\ \Delta V$	$y = 2.7644\ \Delta V$
8 $(y \leq 10\%)$	$y = 2.1955\ \Delta V$	$y = 2.9048\ \Delta V$	$y = 2.5921\ \Delta V$
8 $(y \leq 30\%)$	$y = -2.01\ \Delta V^{2} + 2.3402\ \Delta V$	$y = 2.9245\ \Delta V$	$y = -2.1258\ \Delta V^{2} + 2.6933\ \Delta V$

Table A2.6. TCD calibration for binary breakthrough measurements.

P (bar)	N_2: CO_2	N_2:CH_4
2	$y = -0.4211 \Delta V^{2} + 1.2441\ \Delta V$	$y = 0.9295\ \Delta V^{2} + 0.7809\ \Delta V$